

Residual Stresses
in Thick Bi-metallic Fusion Welds:
a Neutron Diffraction Study

PROEFSCHRIFT

ter verkrijging van de graad van doctor
aan de Technische Universiteit Delft,
op gezag van de Rector Magnificus prof. ir. K.C.A.M. Luyben,
voorzitter van het College voor Promoties,
in het openbaar te verdedigen op dinsdag 12 november 2013 om 10.00 uur

door

Carsten OHMS

Diplom-Physiker
Christian-Albrechts-Universität zu Kiel, Duitsland
geboren te Kiel, Schleswig-Holstein, Duitsland

Dit proefschrift is goedgekeurd door de promotor:
Prof.dr. I.M. Richardson

Samenstelling promotiecommissie:

Rector Magnificus,	voorzitter
Prof.dr. I.M. Richardson,	Technische Universiteit Delft, promotor
Dr. H. Schut,	Technische Universiteit Delft, copromotor
Dr. ir. R. Delhez,	Technische Universiteit Delft
Prof.dr. C. Pappas,	Technische Universiteit Delft
Prof.dr. P.J. Bouchard,	The Open University, Milton Keynes, UK
Prof.dr. D. Smith,	University of Bristol, UK
Prof.dr.ir. J. Sietsma,	Technische Universiteit Delft



Residual Stresses in Thick Bi-metallic Fusion Welds: a Neutron Diffraction Study
C. Ohms
PhD thesis of Delft University of Technology - with summary in Dutch
ISBN 978-94-6191-960-1

Key words: Neutron diffraction, residual stresses, dissimilar metal welding, micro-structure, grain size, texture, uncertainty assessment

Copyright © 2013 by C. Ohms

All rights reserved. No part of the material protected by this copyright notice may be reproduced or utilised in any form or by any means, electronic or mechanical, including photocopying, recording or by any information storage and retrieval system, without written permission from the author.

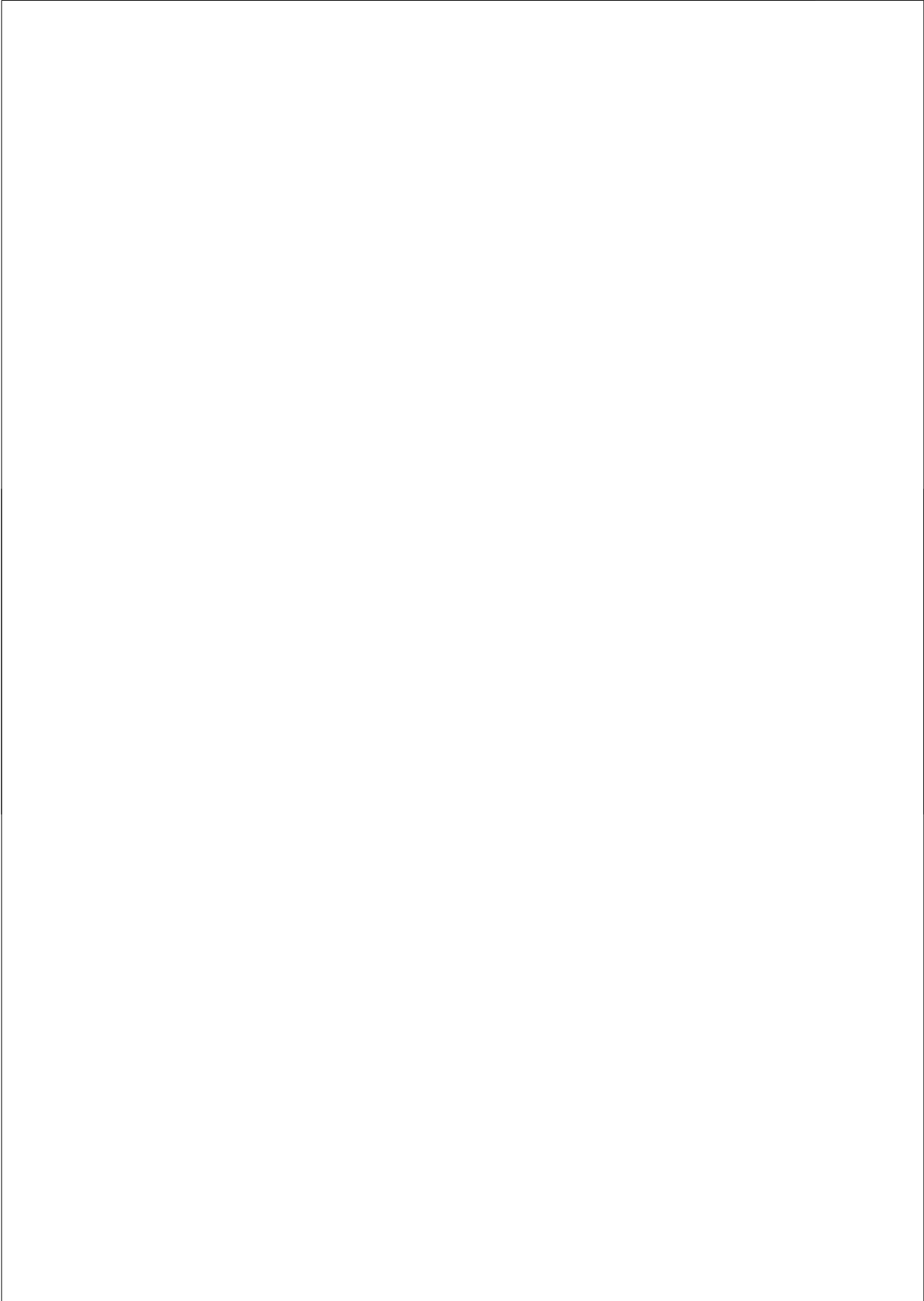
Printed in The Netherlands.

Contents

Nomenclature	vii
1 Introduction	1
2 Residual stresses	9
2.1 Definitions and mathematical concepts for applied stresses	9
2.2 Residual stresses and their characteristics	10
2.3 Stress-strain relationships	13
2.4 Origin of residual stresses	15
2.5 Effects of residual stresses	17
3 Measurement of residual stress	19
3.1 Techniques for measurement of stress and strain	19
3.1.1 Strain relaxation techniques	20
3.1.2 Diffraction based techniques	21
3.2 Residual stress measurement by neutron diffraction	22
3.2.1 Measurement of lattice strain	22
3.2.2 Stress from strain	23
3.2.3 Measurement geometry	27
3.2.4 Monochromatic instruments	30
3.2.5 Time-of-flight methods	30
3.3 Measurement equipment	32
3.3.1 Neutron source	32
3.3.2 Wavelength selection	33
3.3.3 Definition of the sampled gauge volume	33
3.3.4 Collimating elements	34
3.3.5 Specimen positioning table	34
3.3.6 Neutron detector	35
3.4 The Large Component Neutron Diffraction Facility	35

4	Welding	39
4.1	Definitions / welding methods	39
4.1.1	Fusion welding techniques	41
4.1.2	Fusion welding techniques for nuclear applications	42
4.2	Welding and residual stresses	43
4.2.1	Residual stresses	43
4.2.2	Distortion	47
4.3	Welding microstructures and their influence on diffraction stress measurement	47
5	Residual stresses in a thin dissimilar metal pipe weld	53
5.1	Introduction	53
5.2	Description of the component	54
5.3	Neutron diffraction measurements	58
5.4	Neutron diffraction results	62
5.4.1	Residual strains	62
5.4.2	Residual stresses	65
5.4.3	Assessing the results	66
5.5	Comparison to finite element modeling results	69
6	Residual stresses in a clad component	73
6.1	Introduction	73
6.2	Description of the component	74
6.3	Experimental approach	75
6.4	Results	78
6.4.1	Peak positions	78
6.4.2	Residual strains	81
6.4.3	Residual stresses	81
6.4.4	Consistency assessment of the results	83
6.5	Comparison with other measurement techniques and modeling	84
6.5.1	Deep hole drilling	84
6.5.2	Ring core method	85
6.5.3	Numerical modeling	88
7	Residual stresses in a thick dissimilar metal pipe weld	91
7.1	Introduction	91
7.2	The component and the reference specimens	92
7.2.1	The component and its manufacturing	92
7.2.2	Preparation of the neutron diffraction specimens	94
7.3	Neutron diffraction measurements	99
7.4	Neutron diffraction results	102
7.4.1	Residual strains	103

7.4.2	Residual stresses	114
7.4.3	Brief assessment of the results	116
7.5	Comparison with other measurement techniques and modeling	119
7.5.1	Surface hole drilling	119
7.5.2	Crack compliance method	120
7.5.3	Numerical modeling	123
8	Comparison and assessment of methods and results	133
8.1	Error propagation due to fitting uncertainties	133
8.2	Uncertainty of the diffraction elasticity constants	134
8.3	Instrumental and environmental uncertainty contributors	135
8.4	Specimen dependent uncertainty contributions	136
8.4.1	Chemistry variations and intergranular strains	137
8.4.2	Grain size effects	137
8.4.3	Magnitude of grain size effects	138
8.4.4	Analysis of the scatter in the measured data	142
8.4.5	Variability of grain size effects along the weld	147
8.5	Significance of instrument calibration	149
8.5.1	Uncertainty due to lack of calibration	149
8.5.2	Example	151
8.6	Overview of the uncertainty contributors	155
8.7	Comparison with other experimental methods	155
8.8	Modeling of residual stresses in welds	160
8.9	Validity of the experimental approaches presented	161
8.9.1	Introductory remarks	161
8.9.2	Efficiency of reference specimen design	164
8.9.3	Cutting of components prior to measurements	165
8.9.4	Measurements through 51 mm of steel	167
9	Conclusions	169
	References	173
	Summary	181
	Samenvatting	187
	Acknowledgements	193
	List of publications	195
	Curriculum Vitae	205

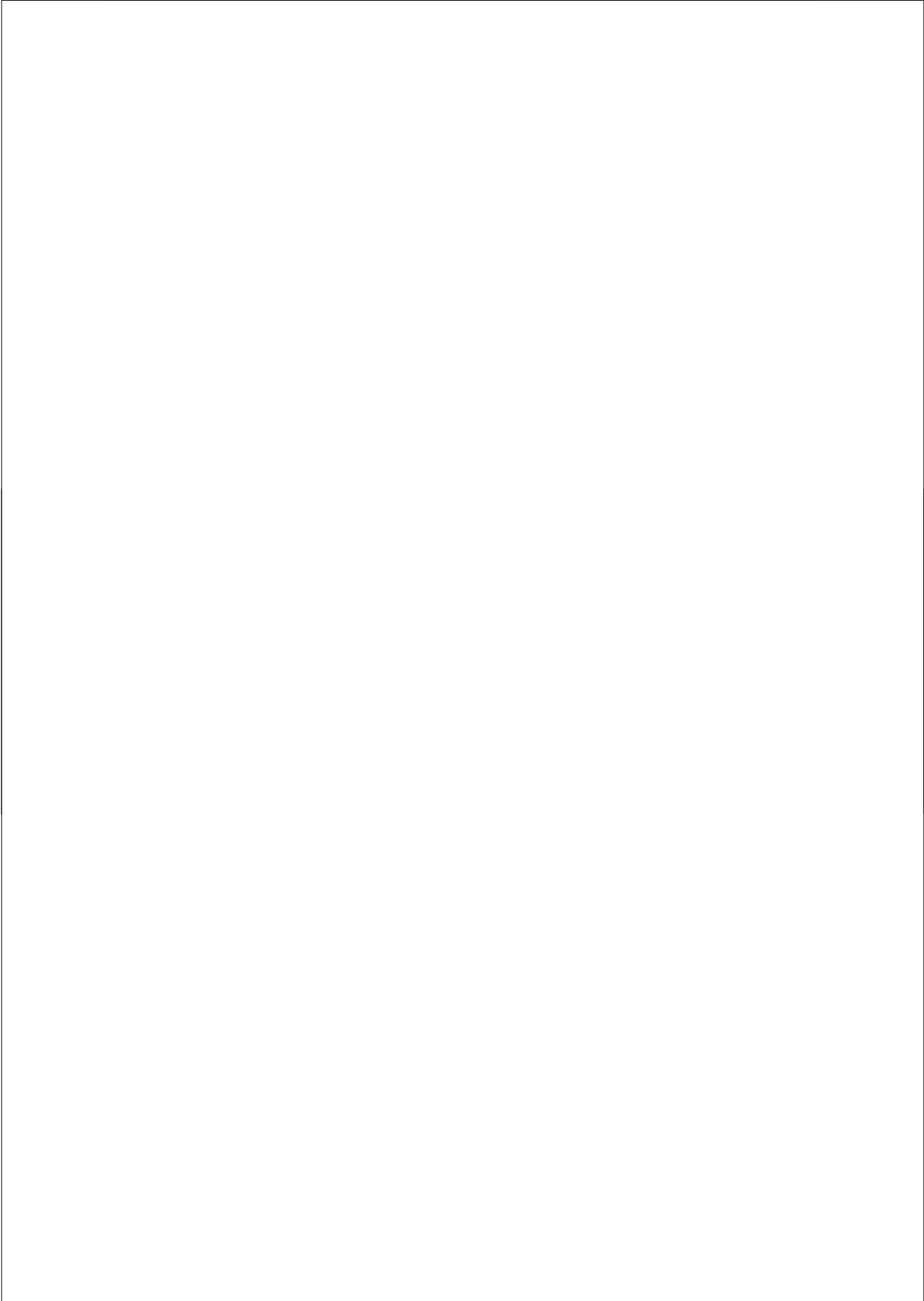


Nomenclature

Symbol	Description	Unit
A, dA	surface area, area element	m^2
d	lattice spacing	m
d_{hkl}	lattice spacing of hkl lattice plane	m
$d_{0,hkl}$	free of stress or reference lattice spacing of hkl lattice plane	m
E	Youngs modulus	Pa
E_{hkl}	diffraction elasticity constant corresponding to Youngs modulus	Pa
F	force	N
hkl	indices for a (set of) lattice plane(s)	-
$\underline{k}_i, \underline{k}_f$	wave vectors of incident and diffracted beams	m^{-1}
$l-l_0$	deformation	m
l_0	original length of deformed object	m
n	positive integer	-
\underline{Q}	scattering vector	m^{-1}
V, dV	volume, volume element	m^3
W	wall thickness	m
$X_1, X_2, X_3,$ X'_1, X'_2, X'_3	coordinate systems	-
x_1, x_2, x_3	coordinates	-

$\delta_{i,j}$	Kronecker delta	-
ε	strain	-
$\boldsymbol{\varepsilon}$	strain tensor	-
$\varepsilon_{i,j}, i, j \in \{1, 2, 3\}$	component of strain tensor	-
$\varepsilon_i, i \in \{1, 2, 3\}$	normal component of strain tensor	-
ε_{hkl}	lattice strain for hkl lattice plane	-
$\varepsilon_{\phi,\psi}$	normal strain observed in direction (ϕ, ψ)	-
2θ	peak position	degrees
$2\theta_{hkl}$	peak position obtained for hkl lattice plane at given wavelength	degrees
$2\theta_{0,hkl}$	peak position obtained for free of stress or reference hkl lattice plane at given wavelength	degrees
$\lambda, \Delta\lambda$	wavelength, bandwidth of wavelength	m
ν	Poissons ratio	-
ν_{hkl}	diffraction elasticity constant corresponding to Poissons ratio	-
$\underline{\sigma}$	mechanical stress, vector format	Pa
$\boldsymbol{\sigma}$	mechanical stress, tensor format	Pa
$\boldsymbol{\sigma}'$	mechanical stress, tensor format, in dashed coordinate system	Pa
$\sigma_{eq.}$	von Mises stress	Pa
$\sigma_{i,j}, i, j \in \{1, 2, 3\}$	component of stress tensor	Pa
$\sigma_i, i \in \{1, 2, 3\}$	normal component of stress tensor	Pa
$\sigma^I, \sigma^{II}, \sigma^{III}$	type I, II and III residual stresses	Pa
σ_n	normal stress component in a direction normal to a cross section or a surface	Pa
$\sigma_{\phi,\psi}$	stress observed in direction (ϕ, ψ)	Pa
τ	shear stress, vector format	Pa
ϕ, ψ	orientation angles with respect to the specimen	degrees

Abbreviation	Meaning
DEC	Diffraction Elasticity Constants
DHD	Deep Hole Drilling
EDM	Electrical Discharge Machining
FE	Finite Element
FEM	Finite Element Modeling
GTAW	Gas Tungsten Arc Welding
HB4	Horizontal Beam Tube 4
HFR	High Flux Reactor
JRC	Joint Research Centre
ND	Neutron Diffraction
RC	Ring Core (Method)
SMAW	Shielded Metal Arc Welding



Chapter 1

Introduction

In most industrial sectors welding represents an important family of manufacturing processes for both fabrication and repair, as it allows (metal) parts to be joined to form almost homogeneous units. Many industrial products and installations could not be achieved without the capability to make such joints. There are many reasons why welding techniques have become so widely used; the feasibility of a technical or engineering solution is one aspect, but economic considerations can also play an important role. Welding can be less labour intensive and more advantageous in terms of material consumption than competing joining techniques.

Welding can, however, involve aspects that are technically disadvantageous. This thesis will focus on one characteristic of almost all welding methods: residual stresses that develop in welded components; *i.e.*, stresses that are present in a structure in the absence of any external loads. These residual stresses can reach significant magnitudes, approaching or exceeding the yield strength of the material. In addition, it is in the nature of almost all welding processes that the material that is formed in the region of the joint has characteristics different from those of the base materials. This, combined with local tensile residual stresses, often leads to a higher susceptibility to the formation and propagation of cracks in the fusion and heat affected zones. As a result weld zones attract most of the attention when the integrity of a welded component is assessed.

Figure 1.1 gives an impression of the potential consequences of a weld failure. In this case, a small hydrogen induced crack in one of the welds led to the complete destruction of a pressure vessel during a hydraulic test performed to demonstrate fitness for service [1].

In many industrial sectors, and in particular in the aerospace and nuclear power industries, the consequences of component failure during operation can be severe, and failure probability must be kept to a minimum. In such cases, component integrity must be maintained in all foreseeable loading conditions. This generally leads to thorough regulatory supervision of equipment and plant operators, during the design, construction and operational phases. In the nuclear industry for example, detection of



Figure 1.1: Pressure vessel failure during hydraulic test [1].

flaws can necessitate an in-depth analysis of component integrity before authorization for continued use can be granted. An entire installation can therefore be taken out of service while such an analysis is taking place. In order to put this into an economic perspective, it is helpful to consider for example that the cost to the utility of an average day out of operation for a nuclear power plant in Europe is of the order $\text{€ } 10^6$.

In countries with relevant industrial installations, dedicated codes; *e.g.*, for structures containing defects or for components operating at high temperatures, are applied for integrity assessments. These assessments take into account both the static and dynamic loads acting on a component, and the associated stresses. Examples for such assessment codes are the R6 and R5 procedures [2; 3] that are used in the UK.

There are several types of loads and consequently stresses that have to be taken into consideration when a structure is designed. In the first place there can be service loads which may include pressures, thermal gradients, gravity and inertial forces. Further there can be environmental impacts from factors such as wind, rain, snow, ice, thermal gradients, running water, earthquakes *etc.* Residual stresses can add up with the stresses caused by external loads such that the maximum acceptable external load for a structure may be reduced.

It is therefore important to be able to quantify all stresses in a given structure. In most cases residual stresses are more difficult to evaluate or predict than external loads [4]. For this reason, it is often necessary to use upper bound residual stress profiles as input data for defect analyses; *i.e.*, to assume a worst case scenario as far as residual stresses are concerned. This approach forces engineers to apply conservative safety margins in the design of safety critical components.

Generally speaking, a structure with a large cross sectional area can support a higher load than a structure, made from the same material, with a smaller cross sectional area. Consequently, applying upper bound profiles for the residual stresses

results in thicker walls implemented in component designs. Knowledge of realistic residual stress distributions permits a fitness for purpose design approach instead of an overly conservative approach, which may generate economies in the construction and operation of safety critical installations. In addition, improved knowledge of the welding residual stresses could also lead to improved application of welding procedures and to safer and more economic operation of installations.

In order to validate the component integrity assessment models, experimental determination of residual stresses is needed. A number of techniques are available for this. Most of these techniques are categorized as either strain relaxation methods or as non-destructive techniques; the former measure the strain response due to unloading, achieved in most cases by cutting. The non-destructive techniques comprise the diffraction methods (X-ray and neutron), and the magnetic and ultrasonic techniques.

Neutron diffraction for stress analysis has only been available for the last 30 years [5], and was the first non-destructive technique capable of measuring spatially resolved strains and stresses in the bulk of a component. Nowadays in addition to neutron diffraction [6] synchrotron X-ray diffraction [7], deep hole drilling [8] and the contour method [9] are available for measuring bulk residual stresses. The availability of these new stress measurement techniques has triggered a significant increase in the number of applications to real engineering problems.

As with other diffraction based stress measurement techniques, neutron diffraction measures changes of lattice spacing; *i.e.*, lattice strain, caused by the presence of stresses. From multi-dimensional measurements of the lattice strain, the residual stress can be derived through formalisms based on a generalized Hooke's law [10]. Due to the high penetration power of neutrons, neutron diffraction is still the only technique capable of non-destructively measuring residual strains in three dimensions in the bulk of a component at a reasonable spatial resolution. The method is, however, only applicable to crystalline materials; *i.e.*, metals and ceramics.

Focus of the Present Work

In this work neutron diffraction is applied for the measurement of welding residual stresses in thick section components of primary systems of a pressurized water nuclear power installation. Figure 1.2 shows a cut through the reactor pressure vessel of a pressurized water reactor. Typically, for a 1000 MW plant such a vessel would be about 12 m high and about 5 m in diameter, with a wall thickness in the range 200 to 250 mm [11]. The vessel wall and the nozzles connecting the vessel to the primary piping system can be seen in the figure. Such a system contains a large number of welds. For example, the nozzles are welded into the vessel walls and the piping system is connected to the nozzles through girth welds. The vessels themselves are also welded structures, mostly made from low alloy steels. Such steels are prone to corrosion in the operating environment of a light water reactor. Therefore a clad layer of stainless steel, several millimetres thick, is welded over the entire inner surface of the vessel, including the nozzles.

Under normal operation conditions the primary system of a pressurized water

reactor is subject to pressures that can be in excess of 150 bar. In order to contain such pressures, thick walls are needed; as stated above the reactor pressure vessel wall is typically 200 to 250 mm in thickness, the piping walls of the primary coolant piping are in the range between 20 and 80 mm in thickness. In installations, where the primary piping systems are fabricated from austenitic stainless steels, joining these to the pressure vessel nozzles involves the application of dissimilar metal girth welds. Welding dissimilar metals introduces an additional source of residual stress through the mismatch of the thermo-mechanical properties of the materials.

The weld components investigated here were full-thickness mock-ups of real reactor components, representing pressure vessel nozzle to primary piping dissimilar metal girth welds (2 specimens), and a welded clad layer on the reactor pressure vessel wall. The structure and typical dimensions of a pressure vessel nozzle to a stainless steel primary piping joint as well as the location of the clad layer are illustrated in Figure 1.3. The welds investigated in this work were accomplished by multi-pass fusion welding using austenitic stainless steel consumables. The two piping components had a wall thickness of 25 and 51 mm and outer diameters of 168 and 453 mm, respectively. The thinner pipe was about 400 and the thicker pipe about 500 mm long. The clad component was a 200 by 225 mm block of 146 mm thickness with a 10 mm clad layer.

The neutron diffraction measurements were challenging because (i) the components were relatively thick and thus strongly attenuated the neutron beams, and (ii) the locations for the neutron stress measurements were difficult to access. These difficulties necessitated the development of dedicated cutting schemes to remove material to allow sufficient access for the neutron beams to the required measurement locations.

This work describes the experimental examination of the welding residual stresses in these three nuclear components. At the same time the suitability of the experimental approaches has been critically assessed. The experimental work comprises the development of the specimen cutting schemes, the execution of the neutron diffraction measurements, with subsequent analyses of the measurement data, and the design and preparation of the reference specimens to calibrate the stress measurements. In addition a thorough assessment of the strain measurement uncertainty is undertaken.

As stated earlier, reliable estimates of the residual stresses are essential for the assessment of the integrity of welded components. The residual stress measurements presented here thus formed part of larger research programmes addressing integrity related questions relevant to the respective components. These also involved residual stress simulations and the application of alternative stress measurement methods. While these latter investigations do not form part of the present research, the experimental and numerical data obtained are included for comparison with the neutron results in order to facilitate an assessment of the experimental approaches presented.

This thesis has the following structure: chapters 2, 3, and 4 provide the scientific/technical background for the work in a condensed form. This includes the concepts of stress and residual stresses and the associated formulae (chapter 2). In chapter 3 the technique for measurement of residual stresses by means of neutron diffraction

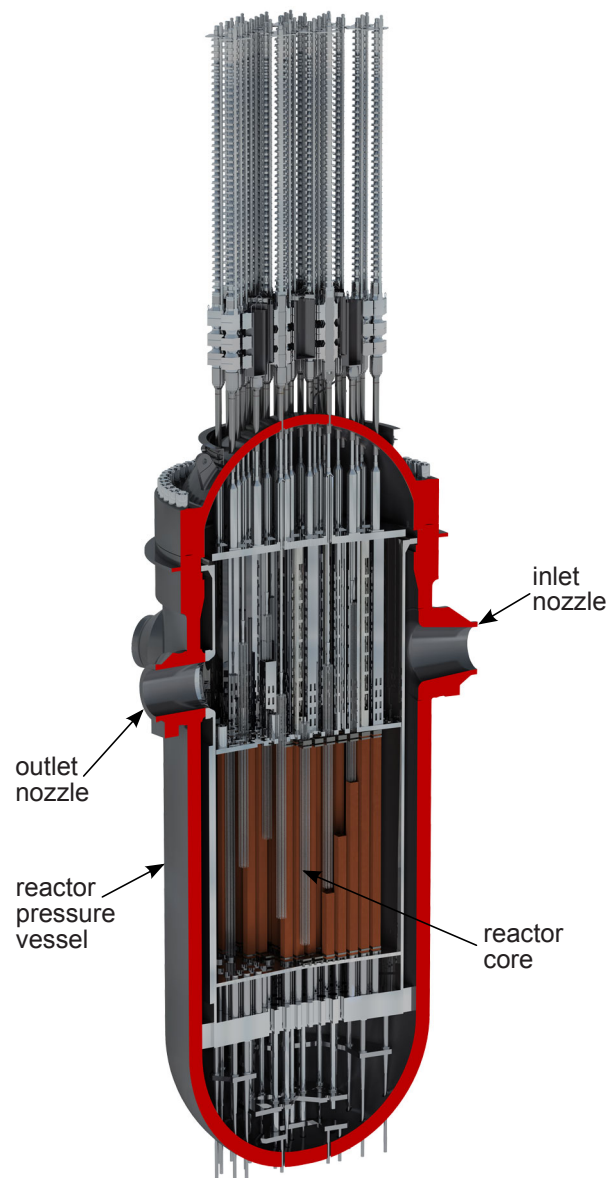


Figure 1.2: *Cut through a reactor pressure vessel (courtesy of B. Forssgren).*

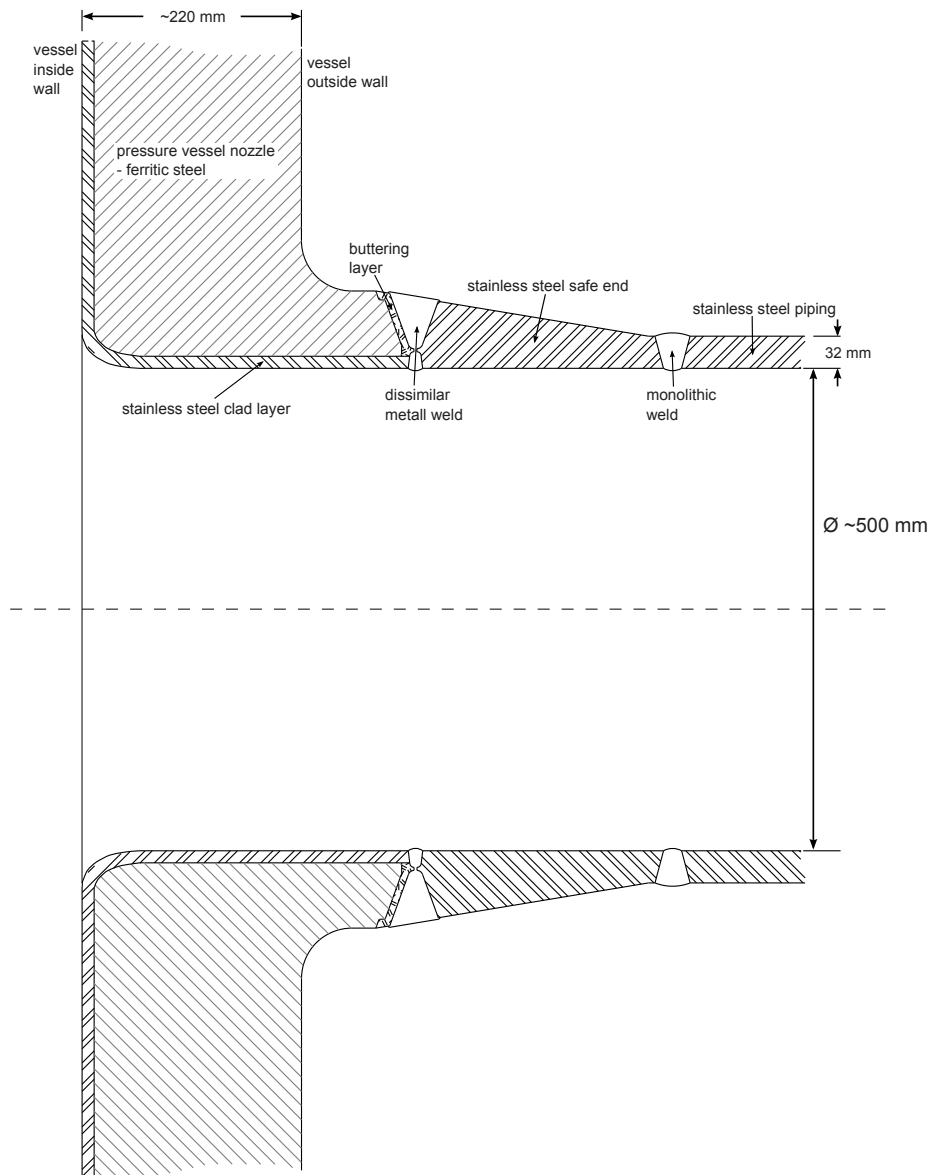


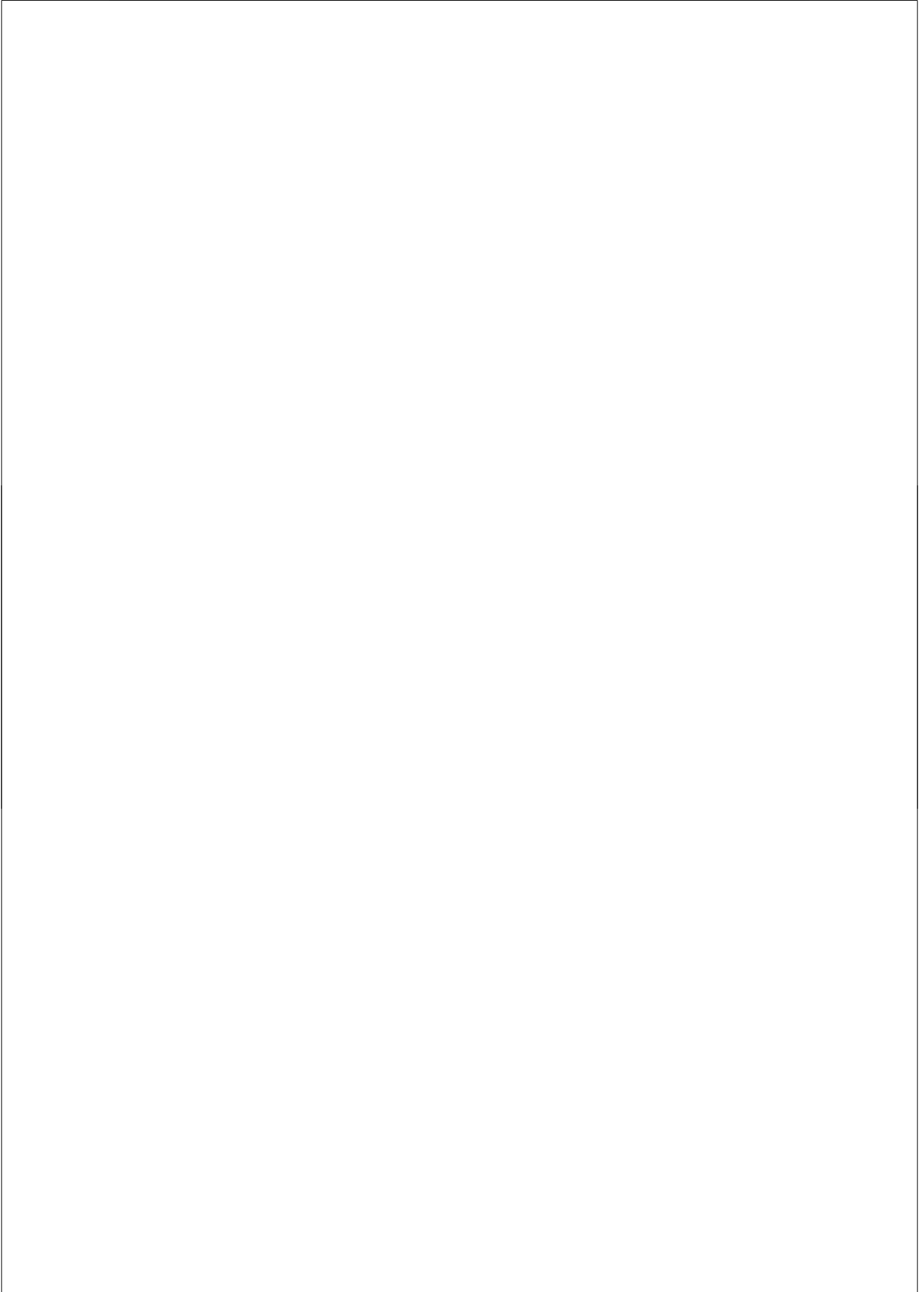
Figure 1.3: Cross section of a pressure vessel nozzle to primary piping connection representative of a VVER440 type reactor [12].

is explained and a brief overview of other stress measurement techniques is given. The neutron diffraction equipment is presented and details of the neutron diffractometer used in these investigations are provided. An introduction to welding is given in chapter 4, which covers the industrial relevance, a brief overview of welding techniques, and aspects relevant to this work, including residual stress generation and microstructural features of the welded materials.

Chapters 5, 6, and 7 present the residual stress investigations in a 25 mm thick bi-metallic piping weld, a clad layer specimen and a 51 mm thick bi-metallic piping weld, respectively. These three chapters also address the manufacturing of the welds themselves, the design of the neutron diffraction and reference specimens, the experimental arrangement, the measurement results and the comparisons with other measurement techniques and numerical analyses.

Chapter 8 provides a general discussion of the work, including the assessment of the measurement uncertainties, comparisons with results from other methods and from stress modelling, and an assessment of the experimental methods and specimen preparations used in this investigation.

The outcome of the work is presented in chapter 9 in the form of conclusions and general recommendations derived from these investigations.



Chapter 2

Residual stresses

In this chapter the engineering concepts of applied and residual stress are introduced. The relevant definitions for stresses are provided in the first two sections. Furthermore, mathematical descriptions are introduced and the most important rules governing the distributions of residual stresses in a component are explained. These rules are important in the appraisal of the quality of experimental and numerical assessments of residual stresses. The relationships between stress and strain that are relevant for the present work are presented in section 2.3. Finally, sections 2.4 and 2.5 give a brief overview of the possible origins of residual stresses and explain why these are important for the integrity of components.

2.1 Definitions and mathematical concepts for applied stresses

A material object of cross section, A , which could be a structure, a component, a specimen, a volume element within a test piece *etc.*, subjected to a force \underline{F} experiences a stress $\underline{\sigma}$ that is equal to the force divided by the surface area over which it is acting.

$$\underline{\sigma} = \frac{\underline{F}}{A} \quad (2.1)$$

A distinction is made between normal stresses $\underline{\sigma}$ generated by forces normal to the cross section under consideration, and shear stresses $\underline{\tau}$ generated by forces parallel to the observation plane. Figure 2.1 illustrates this.

Normal and shear stresses cannot be treated separately. If an observer would decide to use a different co-ordinate system to describe the force \underline{F} in Fig. 2.1, he/she would obtain a force component giving rise to a normal stress and another component giving rise to a shear stress within the object. Therefore, in order to completely describe a stress state, a co-ordinate system needs to be defined and the normal and shear components of the stress must be obtained.

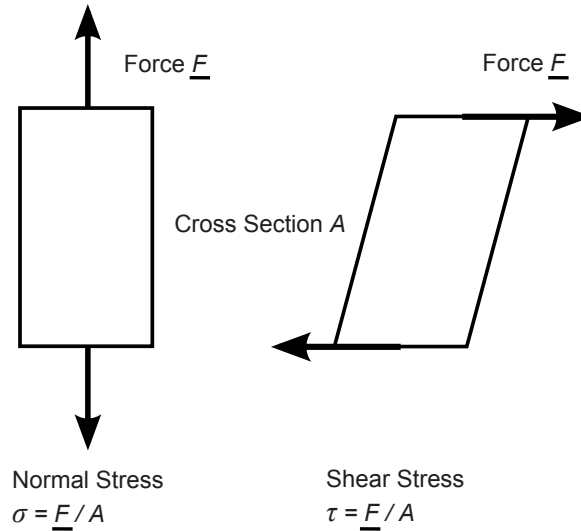


Figure 2.1: Normal and shear stresses

In three-dimensional space, a second rank tensor is obtained, describing the stress state at the location of interest within an object:

$$\sigma_{ij} = \begin{pmatrix} \sigma_{11} & \sigma_{12} & \sigma_{13} \\ \sigma_{21} & \sigma_{22} & \sigma_{23} \\ \sigma_{31} & \sigma_{32} & \sigma_{33} \end{pmatrix}. \quad (2.2)$$

Indices 11, 22, and 33 represent normal stresses, while the other combinations are used for the shear components. Figure 2.2 illustrates the situation. A force $\underline{F} = (F_1, F_2, F_3)$ defined in co-ordinate system (X_1, X_2, X_3) acting on a small cubical volume element at the location of interest, gives rise to a stress state at this location that can be described by the stress tensor in equation (2.2).

The normal stresses are classified as tensile or compressive, depending on whether the force causes the object to expand (tensile stress) or to contract (compressive stress) at the location of interest. Tensile stresses are quantified by positive numbers, while negative values describe compressive stresses.

2.2 Residual stresses and their characteristics

Residual stresses are stresses present inside a component or test piece in the absence of any externally applied load [6]. They are caused by the interaction of material elements within a component with the surrounding material. Through this they are

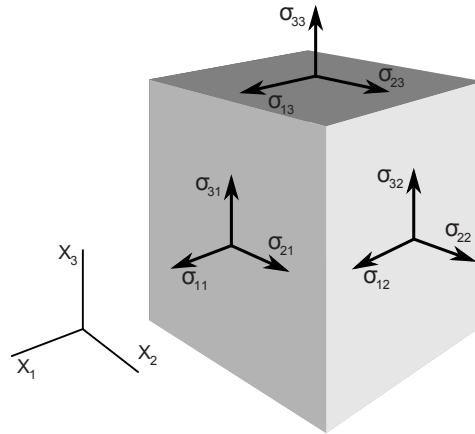


Figure 2.2: Components of the stress tensor σ in co-ordinate system (X_1, X_2, X_3) , (see also [13] or [10])

distinguished from applied stresses, which are caused by external loads acting on a component or test piece¹. Residual stresses can arise from many materials processing routes applied in manufacturing of components or structures [10]. Sometimes they can also be introduced locally after manufacture through proof testing and service loads.

In general, residual stresses vary with location. Depending on the length scales of these variations they are classified as type I, type II or type III stresses. Type I residual stresses, also called macrostresses, vary over a length scale comparable to the dimensions of a component. Residual stresses of type II vary in the range of the grain size of a poly-crystalline aggregate, and type III stresses are variable on the atomic scale [6]. Type II stresses are caused by differences in the thermo-mechanical properties of grains with different orientations or grains of different composition in a poly-crystalline material. Type III stresses are caused by crystal imperfections, such as dislocations, interstitial atoms, voids *etc.* Residual stresses of types II and III are often jointly described as microstresses. Attributing a common term to type II and III residual stresses makes sense, as there are basically no well-established techniques available for experimentally determining their magnitude independently of type I stresses. Nevertheless in recent years novel high resolution techniques have emerged based on; *e.g.*, electron backscattering diffraction [14] or high-energy X-ray diffraction [15], by which location, orientation and crystallographic strain of individual grains can be determined. Figure 2.3 illustrates the differences between type I, II and III residual stresses.

¹NB: The distinction between residual and applied stresses is not completely obvious, when it comes to stresses caused by the component's or structure's own weight. Stresses caused by an object's own weight are of interest only in cases where the supporting walls of an object are thin with respect to its length or height.

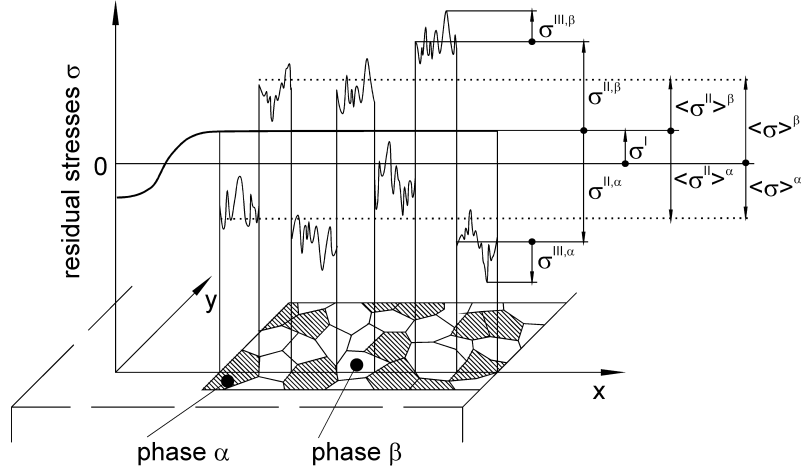


Figure 2.3: Residual stresses, σ , of types I, II and III in a poly-crystalline 2-phase material (courtesy of R. V. Martins).

For the following discussions, static equilibrium conditions and ambient temperatures are assumed.

Stresses inside a structure in equilibrium balance the externally applied forces. In the case of residual stresses, by definition no external forces are present, which means that all components of the residual stress tensor over the entire volume of a structure must integrate to 0 MPa [6].

$$\int_V \sigma_{ij} dV = 0 ; i, j \in \{1, 2, 3\}. \quad (2.3)$$

Equilibrium considerations lead to the balance of the normal stresses across any complete cross section of the structure [13]; *i.e.*,

$$\int_A \sigma_n dA = 0 , \quad (2.4)$$

with A being the area of a complete cross section through the structure and σ_n the residual stress component normal to cross section A . In stress measurements this condition is sometimes used as a check of consistency of the results. This check can only be rigorously applied when measurements of the normal component of the residual stress across an entire cross section have been obtained. This can rarely be achieved, as only few techniques offer the possibility for such measurements. Never-

theless, the criterion is sometimes used as a qualitative indicator for the consistency of a measurement.

Equilibrium considerations concerning moments require that the shear components sharing the same indices in reversed order are identical [13]; *i.e.*,

$$\sigma_{ij} = \sigma_{ji} , \quad i, j \in \{1, 2, 3\}. \quad (2.5)$$

Finally, residual stresses normal to a free surface of a component must be zero.

As stated in section 2.1, the residual stress tensor $\boldsymbol{\sigma}$ is based on the co-ordinate system (X_1, X_2, X_3) used. A different choice of co-ordinate system (X'_1, X'_2, X'_3) renders a different residual stress tensor $\boldsymbol{\sigma}'$ describing the same stress state in the new co-ordinate system. The transformation of the stress tensor follows the transformation rules for second rank tensors, involving the cosines of the angles between the old and the new co-ordinate axes. In the case of a residual stress tensor it is always possible to find a co-ordinate system such, that all components of shear stress σ_{ij} , $i \neq j$, are 0 MPa [10]. This process is called diagonalisation of the stress tensor. The normal stress components σ_{11} , σ_{22} and σ_{33} of this particular stress tensor are called the principal stresses. When residual stresses are measured, in many cases it is assumed that a good prediction of the directions of the principal stresses can be made and measurements are only performed in these directions.

Another possible consistency check for residual stress measurements is the comparison of the measured figures to the yield strength of the material concerned. According to the von Mises criterion a ductile material yields when the equivalent, or von Mises stress exceeds the material's yield stress [16]. Measured residual stress tensors could therefore be assessed against this criterion; *i.e.*, the equivalent stresses derived from the measured data should not exceed the yield value. For the purposes of this work the measured normal stresses are assumed to be principal stresses. The equivalent stress is then derived as follows:

$$\sigma_{eq.} = \sqrt{\frac{1}{2} \left((\sigma_{11} - \sigma_{22})^2 + (\sigma_{22} - \sigma_{33})^2 + (\sigma_{33} - \sigma_{11})^2 \right)}. \quad (2.6)$$

2.3 Stress-strain relationships

Stresses and strains [10] are the normalized quantities used in load-displacement assessment. A fundamental problem with the experimental determination of stresses is that they cannot be measured directly by any technique. The quantity that is measured in stress analyses based on diffraction methods is strain. In order to facilitate the calculation of stresses from the measured strains, stress-strain relationships are needed.

Strain, ε , is defined as deformation, $l - l_0$, per unit length, l_0 :

$$\varepsilon = \frac{l - l_0}{l_0} \quad (2.7)$$

In analogy to the stress tensor introduced in section 2.1, the strain tensor at a given location inside a material specimen is composed of normal strain components and shear strain components.

$$\varepsilon_{ij} = \begin{pmatrix} \varepsilon_{11} & \varepsilon_{12} & \varepsilon_{13} \\ \varepsilon_{21} & \varepsilon_{22} & \varepsilon_{23} \\ \varepsilon_{31} & \varepsilon_{32} & \varepsilon_{33} \end{pmatrix}, \quad i, j \in \{1, 2, 3\} \quad (2.8)$$

As for the stress tensor, the shear components are the non-diagonal components, representing the angular distortion at the location of interest caused by external forces or by residual stresses. The normal components represent the relative change in length (dilatation) of the material element under consideration.

In the elastic regime, for a material with isotropic elastic properties a normal stress gives rise to normal strains of magnitudes:

$$\varepsilon_{11} = \frac{1}{E} \sigma_{11}, \quad (2.9)$$

$$\varepsilon_{22} = \varepsilon_{33} = -\frac{\nu}{E} \sigma_{11}, \quad (2.10)$$

with E and ν as the applicable macroscopic linear elasticity constants, known as Young's modulus, and Poisson's ratio, respectively. Young's modulus is defined as the ratio of the uniaxial stress over the uniaxial strain in the range of stress in which Hooke's Law holds. Poisson's ratio is the negative of the ratio between the strains in directions orthogonal to this stress and the strain parallel to the stress. Taking both normal and transverse stresses into account, a normal component of a strain tensor is derived as:

$$\varepsilon_{11} = \frac{1}{E} \sigma_{11} - \frac{\nu}{E} (\sigma_{22} + \sigma_{33}). \quad (2.11)$$

A corresponding relationship applies for the normal strain components ε_{22} and ε_{33} .

The relationship between shear strains and shear stresses is characterized by the same elasticity constants E and ν that define the relationship between normal stresses and normal strains:

$$\varepsilon_{ij} = \frac{1 + \nu}{E} \sigma_{ij}, \quad i \neq j. \quad (2.12)$$

Combining (2.11) and (2.12) yields the following relationship between the stress and strain tensors:

$$\varepsilon_{ij} = \frac{1+\nu}{E}\sigma_{ij} - \delta_{ij}\frac{\nu}{E}(\sigma_{11} + \sigma_{22} + \sigma_{33}), \quad (2.13)$$

with δ_{ij} being Kronecker's delta. Rearranging to obtain the stresses at the left side of equation (2.13) yields:

$$\sigma_{ij} = \frac{E}{1+\nu}\varepsilon_{ij} + \delta_{ij}\frac{\nu E}{(1+\nu)(1-2\nu)}(\varepsilon_{11} + \varepsilon_{22} + \varepsilon_{33}). \quad (2.14)$$

2.4 Origin of residual stresses

Residual stresses are present in almost every object or structure [17]. As stated before, residual stresses are caused by the interaction of material elements within an object with the surrounding material. The surrounding material exerts a force on a volume element causing it to adopt a shape different from the shape it would have without the influence of its surroundings. There are a number of basic phenomena that lead to the generation of residual stresses, and at least one of them is involved in almost all material/structure fabrication processes [18; 19]; these phenomena are:

- a. Non-homogeneous plastic deformation of the material
- b. Temperature gradients within the material or between separate parts of the structure
- c. Phase transformation of a fraction of the material
- d. Mismatch of the thermo-mechanical properties of the constituents of composite materials

A distinction is made between plastic and elastic deformation and between single-phase and multi-phase materials. Plastic deformation occurs in ductile materials when loaded beyond their elastic limit. This type of deformation is in general irreversible; *i.e.*, the material does not return to its original shape once the load is removed. Elastic deformation on the other hand is recovered after removal of the load. Pure elastic deformation in a single part object from a monolithic material cannot give rise to residual stress. A monolithic material is composed of one single constituent, whereas in multi-phase materials there are constituents distinguished from one another by chemical composition, or different molecular, microstructural or material phases. The following examples illustrate the above mechanisms and how they lead to the generation of residual stresses.

- a. Permanent deformation of materials or structures is deliberately applied in many production processes for one of two reasons: it is either necessary in order to achieve a desired shape or it is applied in order to introduce a desirable residual stress state. Typical component shaping processes are cold rolling and bending. An

example for a residual stress distribution caused by a bending process is the diametrically compressed ring described in [20]. Examples for processes introducing beneficial compressive residual stresses in surface regions are peening processes, deep rolling or cold expansion of rivet holes.

Many machining processes, like grinding or milling introduce surface residual stresses into components without specifically aiming to do so.

b. Many production processes involve the application of heat. In most cases this leads to the formation of a thermal gradient when the structure undergoes differential cooling. Surface regions normally cool faster than the interior of the material. In extreme cases the thermal gradients can be sufficiently large that the material undergoes plastic deformation, leading to the development of residual stresses. In quenching processes this effect is further enhanced, mostly aiming at the introduction of beneficial compressive surface residual stresses.

With so-called interference fits, residual stresses are used to generate a stable connection between two otherwise separated component parts. In this case the outer part of the component, with an annular shape, is brought to an elevated temperature, while a slightly oversized insert is cooled down. The cold insert is then positioned inside the hot annular part, and the temperatures are left to equilibrate. The size mismatch between the two parts now generates residual stresses and the frictional forces generated by these residual stresses produce a firm connection of the two parts [21]. In this example, a purely elastic deformation leads to the formation of the residual stresses.

The most important example for the application of heat in production processes are welds. Most welding processes involve material melting in the area where the joint is generated, while the surrounding areas, outside of the heat affected zone, stay at relatively low temperatures, far below melting. In this way significant temperature gradients can be present during welding, giving rise to high residual stresses, as shown by the examples presented in this thesis.

c. Phase transformations are another possible cause of residual stresses. Two important examples are martensitic transformation of low alloy carbon steels causing the volume of the crystallographic cell to increase rapidly by about 3.5% [22], and the transformation of low alloy steels from a body centered cubic (bcc) to a face centered cubic (fcc) structure at high temperatures and vice versa, which again corresponds to a rapid change of the specific volume of the crystallographic cell. Both phenomena generate residual stresses, particularly in the presence of other material phases.

Solid state phase transformations strongly influence the residual stress field around welds in ferritic steels. With better knowledge of the behaviour of the materials involved, tailoring of such stress fields by making use of the phase transformations could be considered in future welding applications [23].

d. Composite and multi-phase materials are functional materials making use of a combination of the attractive features of their constituents. In most cases the joining of these constituents involves the application of high temperatures. When cooling down to room temperature different coefficients of thermal expansion lead to a shape mismatch of the constituents at room temperature and therefore to residual stress.

Typical examples are fibre-reinforced materials, metal or ceramic matrix composites and duplex steels.

One of several possible classifications of residual stresses [19] is by the manufacturing process that generated them. Such a classification employs terms, such as welding residual stresses, bending residual stresses, quenching residual stresses, *etc.* Other distinctions, such as normal and shear stresses, or Type I, II and III stresses have already been introduced in section 2.2.

2.5 Effects of residual stresses

In section 2.2 residual stresses are defined as stresses present in a structure, component or test piece in the absence of external loads. A state of mechanical and thermal equilibrium is considered in this definition. Where they are present, residual stresses by themselves do not have any additional effects on the components. However, this can change (rapidly) when additional thermal or mechanical loads are applied, or when the material properties change, for example by hydrogen embrittlement, irradiation embrittlement or thermal ageing.

Applied and residual stresses in a component simply add up as long as the sum of the stresses does not lead to plastic deformation or crack formation/failure. In the case of plastic deformation in a ductile material, able to sustain a considerable amount of plastic deformation, the residual stresses after removal of the external load differ from the original distribution. The same holds for brittle materials developing cracks or complete failure with little or no tolerance for stresses in excess of the elastic limit. Also in such materials the residual stress distribution is different after removal of the external load. Hence in (quasi-)static loading conditions residual stresses are of much more concern for brittle materials than for ductile materials, because in the latter case residual stresses are re-distributed (relaxed to a certain degree) before the material fails [24].

In the dynamic regime, cyclic loads are applied to a component in service, leading in the long run to fatigue damage; *i.e.*, crack formation, even in cases where the combined service and residual stresses never reach the static elastic limit. It makes a significant difference whether the residual stress at the crack location is tensile or compressive. Tensile residual stresses open the crack and support its propagation through the material, while compressive stresses in the surface region counteract and delay crack growth and are therefore generally considered beneficial to the fatigue life of a component [25]. This is the main reason for the implementation of processes such as surface peening, deep rolling and others, which introduce significant compressive residual stresses in the surface region.

Residual stresses by themselves can cause deformation of a component, when it is cut or material is removed from it. In accordance with equation (2.3) residual stresses equilibrate over the entire volume of a component. When parts of the material, which contain residual stresses, are removed, the stresses become imbalanced, which

is compensated by a (small) deformation of the component. This effect of residual stresses is most disturbing in surface finishing of components manufactured within small tolerances [26]. Conversely, this very same effect is employed for measurement of residual stresses using strain relaxation methods (see also chapter 3).

Residual stresses are in many cases deliberately used to stabilize a structure or component, an example of this is the interference fit discussed in section 2.4. Another example is a bicycle wheel, where the radial tension, applied to the rim by the spokes, thus generating compression in the circumferential direction, gives stiffness to the rim, which would not be there without the stresses applied.

Another effect associated with residual stresses is stress-corrosion-cracking [27]. This phenomenon can occur when a susceptible material constantly experiencing applied or residual tensile stresses is exposed to a corrosive environment. Cracks normally initiate at intergranular locations and propagate in a direction more or less normal to the stress. The phenomenon does not occur in the absence of tensile stresses or in a non-aggressive environment. However, in the presence of both conditions, stress-corrosion-cracking can become the prevailing failure mode, because it can occur at stress levels significantly below yield [28]. Stress-corrosion-cracking can be a particular threat to welded components in corrosive environments, because welded components often exhibit significant tensile residual stresses at their surfaces.

Residual stresses can also contribute to is the development of creep cracking. In austenitic stainless steel welds residual stresses can be a contributor to the initiation of creep cracking; and where this phenomenon occurs during stress relieving heat treatments - in the absence of applied loads - residual stresses are even its only driver [29]. In the case of welded 9-12 wt-% ferritic-martensitic steels residual stresses are also considered to be one of the drivers of a form of creep cracking that has frequently been observed in the heat affected zones around the welds [30].

Chapter 3

Measurement of residual stress

This chapter provides information on how residual stresses can be determined experimentally. A brief overview of existing measurement techniques is given in section 3.1, followed by a detailed description of the neutron diffraction technique in section 3.2. Here, the underlying concepts of the technique are outlined and the principal measurement geometries are discussed. The two principles (monochromatic and time-of-flight) are presented followed by an explanation of the different methods for converting strain into stress. Subsequently, the equipment typically used in neutron diffraction stress measurements is described, and the HFR Large Component Neutron Diffraction Facility that has been used for these investigations is presented.

3.1 Techniques for measurement of stress and strain

There are several basic principles that can be used for the determination of stresses in materials and components. The most commonly used classes of measurement techniques are the strain relaxation methods and the diffraction methods. Other existing techniques exploit the magnetic, acoustic or optical properties of materials.

Strain relaxation techniques record the strain developing after cutting into the specimen. Stresses can be derived from such strain data recorded in various directions. Diffraction techniques employ the Bragg principle [31; 32] to measure changes in lattice spacing. Again, stresses can be inferred when such changes have been recorded for several measurement directions.

A few important strain relaxation and diffraction techniques for measurement of stress are briefly described in the following sections.

3.1.1 Strain relaxation techniques

It is common to these techniques that they measure strain relaxation due to material removal. Stresses are subsequently derived from the strain data. Depending on the technique used it is possible to derive stresses 1-, 2- or 3-dimensionally.

Strain gauge based methods: hole drilling, ring core, crack compliance etc.

These techniques measure strain relaxation due to material removal using strain gauges applied on the surface of the specimen. For surface hole drilling and the ring core method strain gauge rosettes with three strain gauges are applied on the specimen. In hole drilling, material is removed in the centre of the rosette by electro discharge machining (EDM) or mechanical drilling [33]. With the ring core method, an annular groove is cut around the strain gauges [34]. Stress analysis, which is essentially two-dimensional, is then based on the readings of all three strain gauges. Originally, hole drilling was only applied to measure uniform near surface stresses, but later incremental approaches were developed that facilitated determination of non-uniform stress vs. depth profiles as well [35]. The test resolution in the drilling direction can be as high as 0.1 mm, but is limited in the other directions by the size of the strain gauges applied. A rosette diameter of one centimetre is typical. A measurement range of several millimetres depth from the surface can be covered.

The crack compliance method [36] measures in one direction only, but facilitates the establishment of stress distributions through somewhat thicker test pieces. It can actually be applied to specimens of different geometries, including circular cross sections. Strain gauges can be applied on either surface of the test piece; then an artificial crack is applied stepwise by means of EDM. The stress distribution is derived from the recorded strains.

Deep hole drilling

The deep hole drilling technique is related to conventional hole drilling and the ring core method. Here, a reference hole is drilled through the entire thickness of the component using a gun-drill. The diameter of the hole is measured using an air probe system at several angles around the axis of the hole and in pre-selected steps along the axis of the hole. Afterwards, a larger cylinder, co-axial with the original hole, is cut from the test piece by EDM. The distortion of the hole diameter, caused by strain relaxation in the surrounding material after extraction of this cylinder, is measured by repeating the measurement sequence previously performed with the air probe. The data are corrected for thermal effects caused by EDM, and subsequently stresses in the planes normal to the drilling axis are calculated using elasticity theory [8]. The method can measure through thickness stress distributions through thick components. Test pieces of more than half a meter have been investigated. The achievable spatial resolution is similar to that of the surface hole drilling and ring core methods.

Contour method

The contour method [9] allows for high-resolution 1-dimensional stress mapping across entire cross sections of test pieces. It is applied in three basic steps. First, the component is cut by EDM into two pieces along the cross-section, where the measurement is taken. Then the deflections caused by residual stresses are measured across the cut surface by means of a co-ordinate measurement machine. Finally, by analytical or numerical methods, the residual stress field is derived that would force the cut surface back into the shape it had before cutting, namely flat. This way a high-resolution map of the stresses normal to the cut is obtained. The method can not easily be applied on components with complex shapes.

3.1.2 Diffraction based techniques

Diffraction techniques apply the Bragg principle to measure the change in lattice spacings, from which subsequently stresses can be derived. Synchrotron X-rays, laboratory X-rays and neutrons are the probes that can be used. The latter technique is described in detail in sections 3.2 and 3.3 as it is the measurement technique used in this study.

Synchrotron X-ray diffraction

Synchrotron X-ray diffraction uses a high energy X-ray beam extracted from a synchrotron source. Because of the brilliance of the source and the energy of the photons considerable penetration of materials can be achieved. For example, at the European Synchrotron Radiation Facility in Grenoble, beams with photon energies in excess of 100 keV can penetrate several centimetres of steel.

The high photon energies, and hence the short wavelengths, result in the application of small diffraction angles, typically in the range 3° to 20° . For this reason normally only 2-dimensional measurements can be obtained because of unacceptably long beam paths through the material for the third measurement direction.

The source brilliance facilitates the application of small sampling volumes, sometimes with linear dimensions in the order of 0.1 mm or less. It is also possible to work with short testing times in the order of seconds.

Laboratory X-ray diffraction

In X-ray diffraction based on laboratory photon sources, one of the characteristic lines of the anode material of the X-ray tube is used for the incoming radiation. Typical photon wavelengths are in the range 0.1 to 0.2 nm and typical diffraction angles are between 70° and 180° .

Normally beam penetrations are limited to a few tens of micrometres into most materials of interest. Stress measurements can thus only be performed at surfaces and the $\sin^2 \psi$ method [10] is usually applied.

The necessary equipment is available at many laboratories worldwide. There are even portable X-ray diffractometers for residual stress applications.

3.2 Residual stress measurement by neutron diffraction

3.2.1 Measurement of lattice strain

All diffraction methods for residual stress analysis are based on the Bragg principle [31; 32]. It relates the lattice spacing of a crystalline material to the positions of the diffraction peaks in the scattering pattern. For a given wavelength, λ , of the incident radiation and a given family of lattice planes, (hkl) , the Bragg equation is

$$2d_{hkl} \sin \theta_{hkl} = n\lambda , \quad (3.1)$$

with θ_{hkl} being the diffraction angle for this particular family of lattice planes. The lattice spacing, d_{hkl} , can thus be determined by measuring the angle of diffraction provided the wavelength is accurately known and the angular response of the diffractometer has been calibrated against a certified standard.

The presence of residual stresses will cause the lattice spacing, d_{hkl} , to deviate from its stress-free value, $d_{0,hkl}$. Such deviations will be reflected in shifts of the diffraction peak positions. The (residual) strains are then obtained via the definition of lattice strain:

$$\varepsilon_{hkl} = \frac{d_{hkl} - d_{0,hkl}}{d_{0,hkl}} . \quad (3.2)$$

A measurement is obtained from the test piece exhibiting residual stress and a corresponding measurement for d_0 from the same material that is free of stress. Combination of eqs. (3.1) and (3.2) yields:

$$\varepsilon_{hkl} = \frac{\sin \theta_{0,hkl}}{\sin \theta_{hkl}} - 1 , \quad (3.3)$$

which suggests that the lattice strain, ε_{hkl} , can be measured by diffraction methods without actually determining any lattice spacing. In order for this "self-calibrating" approach to be reliable, measurements from the test piece containing residual stress and from the stress free materials must be obtained using identical instrument settings; *i.e.*, the wavelength, λ and the angular settings of the detector must be the same. Furthermore, the angular position of the neutron detector needs to be known to within 1° or 2° [37]. When such conditions cannot be fulfilled, lattice spacings for the stress free material and the stressed specimen must be measured using a fully calibrated diffractometer, and subsequently lattice strain can be determined using eq. (3.2).

3.2.2 Stress from strain

In chapter 2 stress has been introduced as a 2nd rank tensor quantity. Because of the associated stress-strain relationships, it is not possible to derive the local residual stress state from a single measurement of strain. In general, strains are determined in several directions in order to enable the calculation of the stress. Three methods for stress determination are presented here:

a) Measurement of strain in three mutually orthogonal directions

In this case the generalized Hooke's law is applicable in the following form:

$$\sigma_i = \frac{E}{1 + \nu} \varepsilon_i + \frac{\nu E}{(1 + \nu)(1 - 2\nu)} (\varepsilon_1 + \varepsilon_2 + \varepsilon_3), \quad (3.4)$$

with $i \in \{1, 2, 3\}$, representing the three orthogonal measurement directions X_1 , X_2 , and X_3 . Equation (3.4) corresponds to the previously derived eq. (2.14) with the difference being that eq. (3.4) does not consider the shear terms of the stress and strain tensors. Normally the measurement directions are chosen to have a relation to the specimen geometry; *e.g.*, parallel to the edges in a rectangular specimen, or the circumferential, axial and radial directions in a cylindrical specimen. The elasticity constants used for the strain to stress conversion can be determined by measuring the strains during a load experiment, but for many materials there are literature values available. When the strain measurement is based on a single diffraction peak, the corresponding diffraction elasticity constants for this peak are used [38; 39].

In cases where X_1 , X_2 , and X_3 represent the directions of principal stress, the stress components represent all non-vanishing components of the stress tensor; *i.e.*, the complete stress state at this location has been determined [39]. When this is not the case, the values thus determined for σ_1 , σ_2 and σ_3 are still correct, but they only represent the normal stresses at the test location and the shear terms remain unknown.

This method is most commonly used in stress determination by neutron diffraction and has been used for all investigations presented in this work.

b) The $\sin^2 \psi$ method

The $\sin^2 \psi$ method is mostly applied in X-ray diffraction, but the principle is also used occasionally in neutron diffraction. It is based on the co-ordinate transformations described briefly in chapter 2.2. A detailed account on the principles is given in [10]. The method represents a simplified approach for obtaining stress information experimentally when measurements in three mutually orthogonal directions are not practicable. Figure 3.1 illustrates the principle. In an isotropic material, measurements of normal strain in a direction ($\phi\psi$) relative to a chosen co-ordinate system (X_1, X_2, X_3) are performed. Based on co-ordinate transformation the measured strain is related to the stress tensor defined in (x_1, x_2, x_3) by:

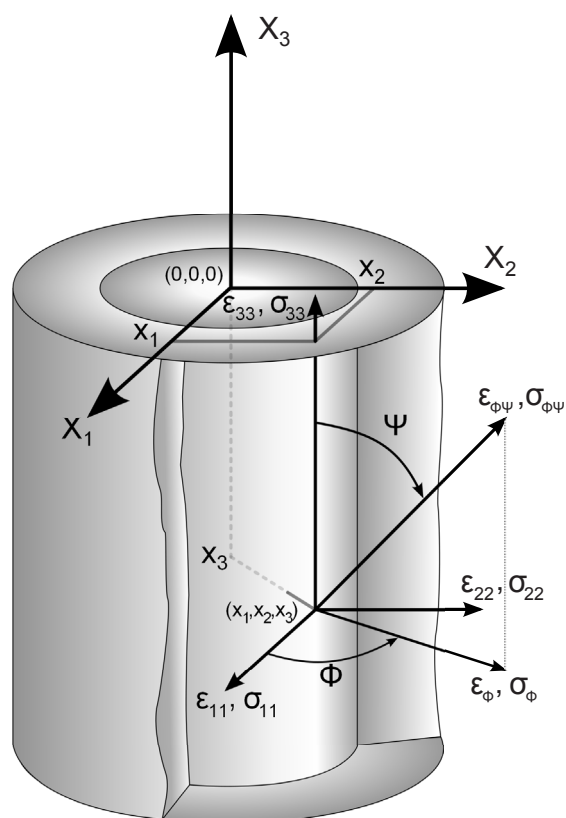


Figure 3.1: Stress and strain components at a measurement point (x_1, x_2, x_3) in the specimen co-ordinate system (X_1, X_2, X_3) [39].

$$\begin{aligned}
\varepsilon_{\phi\psi} &= \frac{1+\nu}{E}(\sigma_{11} \cos^2 \phi + \sigma_{12} \sin 2\phi + \sigma_{22} \sin^2 \phi - \sigma_{33}) \sin^2 \psi \\
&+ \frac{1+\nu}{E}\sigma_{33} - \frac{\nu}{E}(\sigma_{11} + \sigma_{22} + \sigma_{33}) \\
&+ \frac{1+\nu}{E}(\sigma_{13} \cos \phi + \sigma_{23} \sin \phi) \sin 2\psi .
\end{aligned} \tag{3.5}$$

Subscripts 12, 13 and 23 correspond to the shear components of stress. If the choice of the co-ordinate system is such that X_1 , X_2 , and X_3 correspond to the principal stress directions at the measurement location, eq. (3.5) simplifies as follows:

$$\begin{aligned}
\varepsilon_{\phi\psi} &= \frac{1+\nu}{E}(\sigma_{11} \cos^2 \phi + \sigma_{22} \sin^2 \phi - \sigma_{33}) \sin^2 \psi \\
&+ \frac{1+\nu}{E}\sigma_{33} - \frac{\nu}{E}(\sigma_{11} + \sigma_{22} + \sigma_{33}) .
\end{aligned} \tag{3.6}$$

In the case where the orientation angle ϕ can be chosen to coincide with the X_1 -axis, the problem is reduced even further:

$$\begin{aligned}
\varepsilon_{0\psi} &= \frac{1+\nu}{E}(\sigma_{11} - \sigma_{33}) \sin^2 \psi \\
&+ \frac{1+\nu}{E}\sigma_{33} - \frac{\nu}{E}(\sigma_{11} + \sigma_{22} + \sigma_{33}) .
\end{aligned} \tag{3.7}$$

Accordingly, in the case where ϕ coincides with the X_2 -axis:

$$\begin{aligned}
\varepsilon_{90\psi} &= \frac{1+\nu}{E}(\sigma_{22} - \sigma_{33}) \sin^2 \psi \\
&+ \frac{1+\nu}{E}\sigma_{33} - \frac{\nu}{E}(\sigma_{11} + \sigma_{22} + \sigma_{33}) .
\end{aligned} \tag{3.8}$$

When measuring the normal strain at various angles of inclination ψ , stress information can be obtained from the slope and the axis intercept of the strain as a function of $\sin^2 \psi$ -curve. In the optimum situation the entire stress tensor could be determined from measurements based on eqs. (3.7) and (3.8). In the case of standard X-ray diffraction, applicable only on the surface of the test piece where σ_{33} is 0 MPa, the slope of the $\sin^2 \psi$ -curves render directly the magnitudes of σ_{11} and σ_{22} .

c) Full stress tensor determination based on multiple direction measurement of strain

In order to determine the complete stress state at a given location, measurements of normal strain in at least six independent orientations are necessary [39]. The

principle of co-ordinate transformation is again applicable. The stress components can thus be derived by solving the following linear equation based on the strains measured in directions $\phi\psi$:

$$\begin{aligned} \varepsilon_{\phi\psi} = & \frac{1+\nu}{E} [(\sigma_{11} \cos^2 \phi + \sigma_{22} \sin^2 \phi + \sigma_{12} \sin 2\phi) \sin^2 \psi \\ & + \sigma_{13} \cos \phi \sin 2\psi + \sigma_{23} \sin \phi \sin 2\psi + \sigma_{33} \cos^2 \psi] \\ & - \frac{\nu}{E} [\sigma_{11} + \sigma_{22} + \sigma_{33}] . \end{aligned} \quad (3.9)$$

Again, subscripts 12, 13 and 23 correspond to the shear components of stress. Figure 3.1 illustrates the situation. Full stress tensor determination is rarely done by neutron diffraction. It is a complicated and time consuming procedure, which would in many cases only provide limited additional information, in particular when the directions of principal stress can be predicted.

Diffraction elasticity constants

The relationship between stresses and strains involve the elasticity constants E and ν . The elasticity constants are material and treatment specific and can be determined experimentally; for example, through tensile tests. In non-diffraction experimental stress determination, as well as in numerical modeling, bulk elasticity constants are normally used to describe the stress-strain relationship.

Diffraction based measurement of stresses employs crystallites with a distinct crystallographic orientation as "internal strain gauges". In general, grains of different crystallographic orientation exhibit a different strain response to an external load, even if embedded in a matrix of grains with randomly distributed orientations [38; 39]. This means that the amount of strain observed in a diffraction experiment depends on the crystallographic plane, on which the measurement was undertaken. To account for these differences in stress determination, diffraction, rather than bulk, elasticity constants need to be used for the strain to stress conversion. Diffraction elasticity constants can be determined experimentally during tensile tests; *i.e.*, making lattice strain and mechanical strain measurements as a function of an applied load. The tensile test specimens have to be manufactured from the same materials as the stressed specimens under investigation. Lattice strains need to be determined by the diffraction process itself, and the crystallographic orientation relevant to the envisaged experiment must be used.

Elasticity constants can also be derived analytically or numerically from single crystal elasticity constants. For polycrystalline materials, methods proposed by Voigt and Reuss [40; 41] in the late 1920s are used frequently. The Voigt method is based on the assumption of identical strain across all grains and grain orientations, whereas Reuss based his concept on the assumption of identical stresses. Another concept involved the usage of the average values of results obtained from the Voigt and Reuss methods [42]. Kröner developed a method to calculate diffraction elasticity constants

Table 3.1: *E*-modulii for the (111) and (200) crystallographic orientations obtained for several similar stainless steels by the Voigt-Reuss average and by a neutron diffraction measurement; the bulk modulus for such a steel would normally be in the range 200 GPa to 210 GPa.

Austenitic steel, 18% Cr, 12% Ni, Voigt-Reuss average [38]	Austenitic steel, 18% Cr, 8% Ni, Voigt-Reuss average [18]	Experimental (neutron diffraction) values for austenitic steel 18.25% Cr, 13.5% Ni [45]
$E_{111} = 247$ GPa	$E_{111} = 259$ GPa	$E_{111} = 261$ GPa
$E_{200} = 139$ GPa	$E_{200} = 138$ GPa	$E_{200} = 155$ GPa

by considering individual grains as single crystalline, elastically anisotropic elliptical inclusions in a homogeneous, isotropic matrix [43]. Subsequently developed methods are often derivatives of the Kröner method (for example [44] on the influence of morphological texture). Eigenmann and Macherauch [18; 38] gave an overview of such analytically derived diffraction elasticity constants for a number of different materials. For example, Table 3.1 shows the diffraction elasticity constants for the "stiffest" and the "most compliant" crystallographic orientations for austenitic steels, which differ by a factor of almost 2 in their *E*-modules.

The differences between the crystallographic orientations demonstrate that in materials with pronounced elastic anisotropy it is indispensable to employ diffraction elasticity constants in diffraction based stress analysis, and to avoid using bulk elasticity constants.

3.2.3 Measurement geometry

The basic geometry of a measurement of lattice spacing, d , following the Bragg principle is shown in Fig. 3.2. The left part of the figure (a) indicates how the Bragg equation (3.1) is derived from the geometric concept. The path difference between two waves scattered from neighbouring lattice planes with distance d under scattering angle θ , is $2 \cdot d \cdot \sin\theta$. When this path difference is a multiple of the wavelength λ of the radiation, constructive interference is obtained and a diffraction peak can be observed in that direction (*cf.* eq. 3.1).

Figure 3.2 (b) shows how the diffraction geometry is normally presented in neutron strain measurements. Incident and diffracted radiation are represented by the wave vectors, \underline{k}_i and \underline{k}_f . The length of these vectors is inversely proportional to the wavelength of the radiation. The lattice spacing is determined in the direction of the scattering vector, Q , which is the difference of the diffracted and incident wave vectors, and, by default, is in the direction normal to the lattice planes [46]. The angle that is recorded is the angle between the direction of the incident beam and that of the diffracted beam. This corresponds to 2 times the Bragg angle θ and one should note that the measurements of the scattering angles reported in this work are cited in accordance with Fig. 3.2 (b).

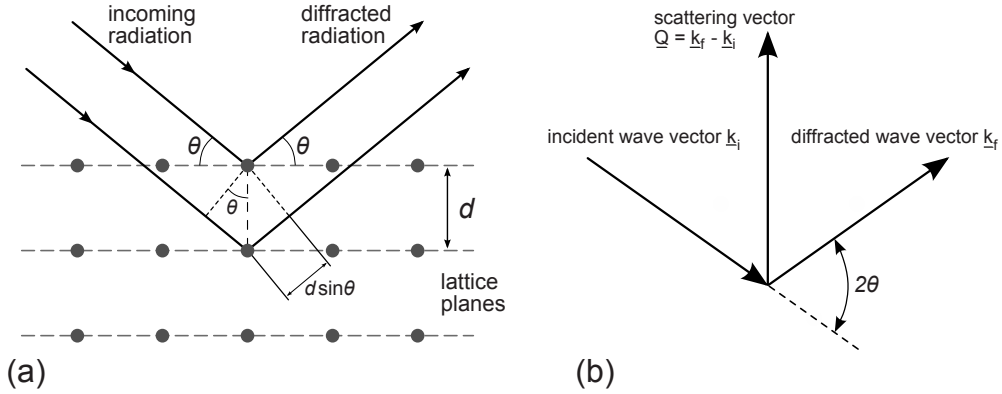


Figure 3.2: Geometry of Bragg diffraction.

A schematic of a neutron diffraction set-up is shown in Figs. 3.3 (a) - (c). The wave vectors are replaced by the incident and diffracted neutron beams. The measurement direction bisects the angle between the orientations of these two beams. The intersection of the incident and diffracted beams is called the sampling volume. This is the volume in space, from which the diffraction signal is obtained. In Fig. 3.3 (a) the measurement direction is normal to the long side of a rectangular shaped specimen.

As the incident beam is strongly linked to the source, which has to be either a nuclear reactor or a spallation source, the beam cannot be moved; and because, in general, the detector also has a fixed position, the position and orientation of the beams is fixed. In order to change the location of measurement, or its direction with respect to the specimen orientation, one needs to change the position (b) or orientation (c), of the specimen with respect to the incident and diffracted beams. These changes are normally facilitated by a sophisticated positioning system supporting the specimen.

In order to illustrate the above, a few typical dimensions applicable to neutron diffraction stress analysis are given:

The lattice spacings of relevant crystalline engineering materials; *i.e.*, metals and ceramics, that can be investigated, ranges from ~ 0.1 nm to ~ 0.35 nm. Normally, neutrons in the wavelength range 0.12 nm to 0.3 nm are used. These wavelengths, in accordance with the de Broglie principle [47], correspond to a kinetic energy range of ~ 55 meV to ~ 9 meV. Neutrons in this energy range are generally called thermal neutrons, because the kinetic energy of particles at room temperature (~ 25 meV) also falls into this range.

The width of the incident and diffracted neutron beams is chosen in accordance with the desired spatial measurement resolution and the thickness of and attenuation through the material to be investigated. Typical widths are in the range 1 to 5 mm, for very thick components the experimenter might choose to go up to 10 mm. The beam height, the dimension normal to the drawing plane in Fig. 3.3, will also be

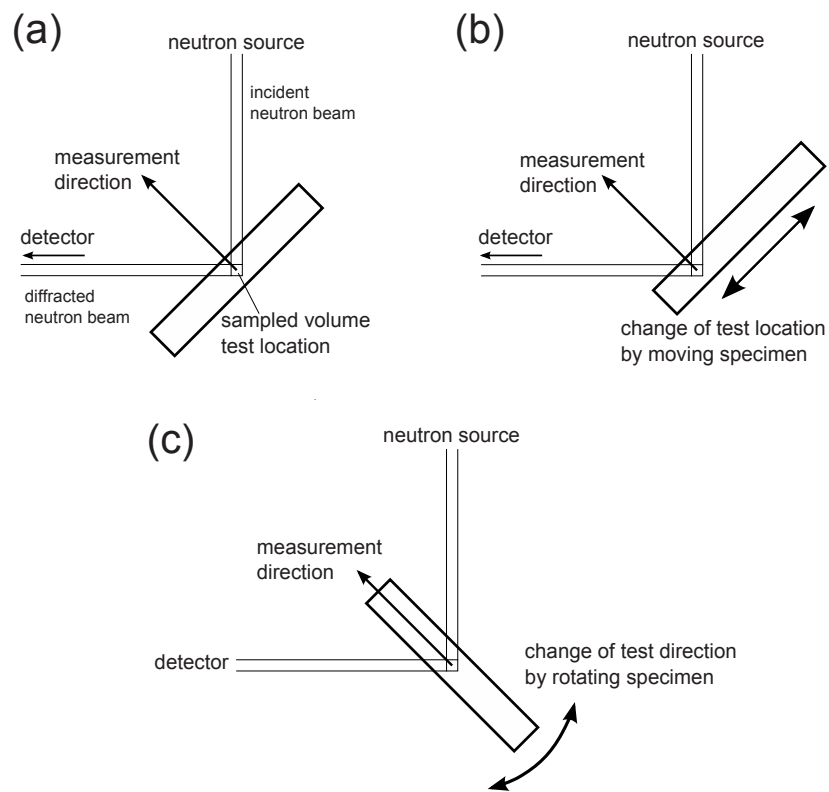


Figure 3.3: Schematic of neutron diffraction stress measurement: (a) basic set-up of a measurement, the average lattice spacing is measured over the sampled volume at the test location in a direction normal to the long side of the specimen; (b) in order to change the test location, the specimen is moved with respect to the neutron beams; (c) in order to change the measurement direction, the specimen is rotated.

chosen based on the desired spatial and strain resolution and material thickness, but it could actually be up to 50 mm (matchstick shaped sampling volume), in cases where no significant variation of stress is to be expected along this dimension of the sampling volume.

For the purposes of neutron stress measurement, neutron path lengths through steels of up to 70 or 80 mm can be attained, through aluminium alloys up to a few hundred mm and through nickel alloys up to 30 or 40 mm.

3.2.4 Monochromatic instruments

It is typical at steady state sources; *i.e.*, sources with a constant flux of neutrons, such as reactors, to perform stress measurements on monochromatic instruments. On a monochromatic stress diffractometer, a neutron beam containing neutrons with a small bandwidth of energies ($\Delta\lambda/\lambda \approx 10^{-3}$ to 10^{-4}) is directed to the specimen. The wavelength can be selected by a crystal monochromator based on the Bragg principle. The specimen is located in the direction of the beam diffracted from the monochromator. For a given wavelength of the neutrons scattered, the lattice spacing of the lattice plane, (hkl), chosen for the measurement, prescribes the diffraction angle in accordance with eq. (3.1).

Figure 3.4 shows an example of a neutron diffraction peak obtained from a monochromatic instrument, together with a Gaussian fit to the measurement data. Fitting parameters in this case are the angular position of the peak (corresponding to 2θ), the amplitude, the width and the level of the background. In addition, the fitting provides an estimate of the uncertainty for these quantities. The quantity, relevant for strain determination, eqs. (3.1)-(3.3), is the peak position. Peak width, height and peak height to background ratio play an important role for the fitting uncertainties that can be attained. The rule of thumb is that the uncertainty is inversely proportional to the peak amplitude and directly proportional to the square of the peak width [48]. For this reason it can be beneficial to sacrifice intensity in favour of peak width; for example, by installing a different monochromator or using a different monochromator reflection plane.

3.2.5 Time-of-flight methods

Next to the monochromatic instruments for neutron diffraction there are installations operating on the time-of-flight principle. Such machines do not only measure the location where the neutron impinges on the detector, but also the time the neutron has traveled before reaching the detector. This flight time is associated with the neutron wavelength via the de Broglie principle [47]. Time-of-flight methods generally facilitate the measurement of multiple peak diffraction spectra, unlike the monochromatic instruments presented above. For an overview of the time-of-flight technique see [6].

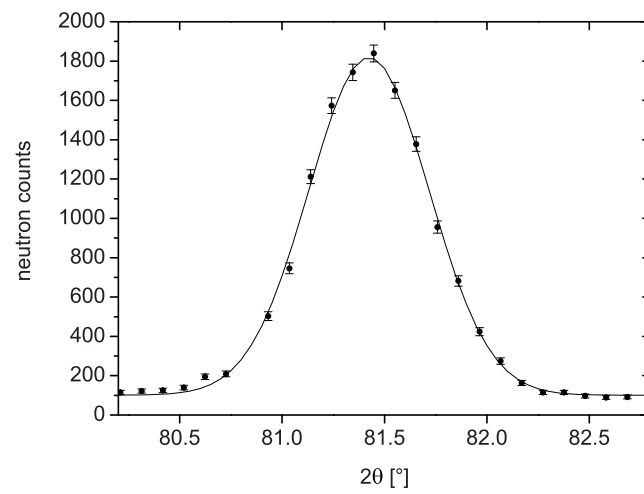


Figure 3.4: Example of a Bragg peak from a steady state source based diffractometer. The data obtained have been fitted with a Gaussian distribution and a constant background.

3.3 Measurement equipment

The neutron diffraction technique for residual stress measurement is still relatively young. Krawitz [5] published an overview of its early history. According to him, the possibility to apply neutron diffraction for strain measurement was first considered in the mid 1970s in the USA. The first journal article on neutron strain measurements was only published in the early 1980s by a UK based group [49]. The same principles had been applied in X-ray diffraction for stress analysis and in neutron diffraction structural analysis (powder diffraction) decades before. In the early days the corresponding neutron diffractometers were therefore derivatives of powder diffraction facilities. In principle, there are only two characteristics that fundamentally distinguish the diffractometer for residual stresses from the powder diffractometer: a) the sampling volume, *i.e.* the volume, from which scattered neutrons reach the detector, needs to be carefully selected by means of beam defining optics (mostly neutron masks and/or collimators) in the incident and diffracted beams, and b) a sample positioning stage, facilitating the positioning of the sampling volume and of the orientation of the scattering vector with respect to the sample. Since the early 1980s the performance of residual stress diffractometers has improved considerably. The development of position sensitive and multi-detectors allowed simultaneous measurement of complete diffraction peaks; dedicated instruments featured incoming beam optics optimized for resolution or intensity (*e.g.*, no second order filtering, dedicated monochromators, beam focusing *etc.*); and heavy sample manipulation tables with large ranges for linear displacement facilitated investigations of large engineering components. In the early 1990s the introduction of time-of-flight methods; *e.g.*, at pulsed spallation sources, gave access to simultaneous observation and analysis of complete diffraction spectra, allowing new insights into material response to mechanical loads.

The following components are common to all neutron diffractometers for residual stress analysis operating in the world today.

3.3.1 Neutron source

A neutron source has to offer a medium to high flux of thermal neutrons ($10^9 - 10^{12}$ n/m²s) at a considerable distance from the source itself. This distance, mostly in the range 5 m to 50 m, facilitates the availability of a low divergence beam and helps to reduce the background neutron count. The typical thermal neutron flux at the core of a suitable research reactor is in the range $10^{16} - 10^{19}$ n/m²s. To date such neutron fluxes cannot be offered by portable neutron sources, which means that the technique can only be applied at nuclear research reactors and spallation neutron sources, both being large research infrastructures.

At a reactor, neutrons are produced by fission, normally of U-235. Among the fission products of one uranium atom in a light-water reactor there are on the average 2.4 free neutrons [50]. One of these neutrons is needed to sustain the chain reaction, and some of the remaining free neutrons reach the beam ports of the facility.

At a spallation source a heavy metal target (tungsten, mercury, uranium *etc.*)

is bombarded with high energy protons from an accelerator. The impact of a high energy proton on a heavy nucleus causes the latter to disintegrate into several smaller nuclei. This reaction releases, on the average, 20 to 30 free neutrons [51], some of which again becoming available for the neutron beams.

In both cases the free neutrons emanating directly from the source, are fast neutrons, *i.e.* their energy is too high and their wavelength too short for diffraction measurements. Slowing down of neutrons is accomplished by moderators, like water or methane, which are very effective in slowing neutrons down because of the mass equivalence between the abundant hydrogen nuclei and the neutrons.

3.3.2 Wavelength selection

With a continuous neutron beam containing a white spectrum of neutron energies impinging directly onto the specimen under investigation, the experimenter would not be able to obtain distinguishable diffraction peaks. For this reason the following types of "beam conditioning" are applied:

- At steady state sources in most cases the neutron beam is monochromatised. This leads to a neutron beam with a narrow band of neutron wavelengths being directed to the specimen and the response of one chosen diffraction plane is studied in the experiment.
- At pulsed sources the flight time of neutrons between the source and the neutron detector is accurately measured. Through this technique measurements with a "white" neutron beam are possible and complete diffraction spectra are obtained.

3.3.3 Definition of the sampled gauge volume

In stress measurements it is important that the signal is obtained from a defined volume in space that contains part of the specimen material. This is achieved by placing beam defining apertures in the incoming and diffracted beams, either in the form of slits, or in the form of radial collimators. Such apertures define size and shape of and flux distribution in the beams. Such equipment is manufactured from materials with a very high absorption cross section for thermal neutrons. There are in principle four elements with isotopes having such a high cross-section: gadolinium, cadmium, boron and lithium (given in order of decreasing neutron absorption cross section) [51]. For collimators, in most cases, materials containing gadolinium are applied, for slits it is often cadmium. Cadmium has the advantage that a thickness of 1 to 2 mm suffices for a neutron mask. In addition, cadmium is relatively easy to machine and to deform.

The shape of the gauge volume is also defined by the diffraction angle 2θ chosen. Preferred diffraction angles for residual stress analysis by neutron diffraction are as close as possible to 90° ; and it is advisable not to use angles outside of the range 60° to 120° . This requirement is related to the geometries shown in Fig. 3.3. When the

measurement angle is too far from 90° , the sampling volume becomes skewed with its diagonals too different from each other. This causes the sampling volumes for different testing directions to occupy different parts of the specimen material, hence compromising the reliability of 3-dimensional stress measurements. In addition, the neutron path through the specimen material then becomes very long in at least one of the test directions.

3.3.4 Collimating elements

Collimation is necessary to ensure that the beam impinging on the specimen is sufficiently parallel, or that the sampling volume seen by a particular element of the neutron detector is sufficiently small. This is usually achieved by linear collimators for the incoming beam; the diffracted neutrons are usually collimated by a linear collimator for a "point" detector, whereas radial collimators can be applied in front of a position sensitive detector. In many cases the collimation secured by the geometry of the instrument suffices, and no dedicated collimation equipment is necessary for successful execution of stress measurements. For example, a monochromator width of 50 mm and a slit of 2 mm at 2.5 m from the monochromator already render a maximum angular range of admissible neutron flight paths of only $\pm 0.6^\circ$, which is sufficient for the execution of stress measurements without using extra equipment for beam collimation.

3.3.5 Specimen positioning table

Positioning table assemblies are an important part of neutron diffraction stress measurement facilities. Such an assembly facilitates linear specimen translation along three mutually orthogonal axes, and specimen rotation about at least one axis through the centre of the sampling volume. Different capabilities in terms of weight capacity and movement ranges distinguish facilities from one another.

With modern positioning equipment linear movement in the range 100 to 500 mm, with a resolution of 0.01 mm is easily available. Clever guidance of the cables can facilitate rotation ranges bigger than 270° needed for the selection of multiple orientations of the specimen without remounting. The motor and encoder assembly can render a stepping resolution of 0.01° or better.

The whole set-up has to be able to carry and position the weight of the specimen and the auxiliary equipment installed together with the specimen. Nowadays there are instruments that can handle specimens of the order of 10^3 kg (for example at Paul Scherrer Institute, Institut Laue-Langevin, ISIS, Los Alamos Neutron Science Center, Joint Research Centre). A small weight capacity and/or a small range of linear movement constitute a substantial limitation to the application for stress measurements in engineering components.

3.3.6 Neutron detector

The neutrons that are diffracted from the specimen are detected in a neutron detector that is normally located at the horizontal level of the incoming beam at a given distance from the sampling volume at the diffraction angle chosen for the particular measurement.

Various detector types can be applied, but the most common are gas chambers (He-3) and scintillator arrangements.

Nowadays position sensitive detectors are in use covering one or several complete diffraction peaks in a single measurement, while in the past, measurements were performed by scanning a single wire detector over the diffraction peak. At some instruments (*e.g.* SALSa at Institut Laue-Langevin or E3 at Helmholtz Zentrum Berlin), the detectors used are position sensitive in two dimensions; this permits visualization of grain size effects and the umbrella effect [52] for scattering angles deviating strongly from 90° . With this information available, these effects can be taken into account in data analysis or for adapting the measurement procedure. Two-dimensional detectors with sensitive areas as big as 30 by 30 cm² are installed at some monochromatic instruments; *e.g.*, E3 at Helmholtz Zentrum Berlin. Larger detectors sample larger fractions of the diffracted neutrons, enabling better counting statistics. Conversely, a large detector collects neutrons from a wide range of scattering angles, which is only acceptable within certain limits in a stress measurement. Many instruments offer a range of $\pm 10^\circ$ to $\pm 15^\circ$ for the acceptance angle of the neutron detector; *e.g.*, E3 (see above) or ENGIN-X at ISIS [53].

At time-of-flight instruments, scintillator detectors are mostly used. Also in this case one and two dimensional detectors are applied. Two dimensional detector arrays can cover an area considerably bigger than that quoted above for the detectors at monochromatic instruments, although the same limitation in acceptance angle also applies. The major difference compared to the steady state instrument is that the flight time of the neutrons is recorded in addition to the angle of scattering. As a consequence, at a time-of-flight instrument, the entire detector surface contributes to the diffraction signal, while at a monochromatic instrument, only the detector area covered by the diffraction peak contributes.

3.4 The Large Component Neutron Diffraction Facility

At the HFR in the late 1990s the author of this thesis coordinated the development of the Large Component Neutron Diffraction Facility. The facility has replaced the older dedicated stress diffractometer at beam tube HB4, of which the monochromator and some other components were maintained.

The objective of this development was to produce a novel type of diffractometer, suitable for performing measurements in heavy engineering components, and offering an extended range for linear specimen positioning. The choice has been made to

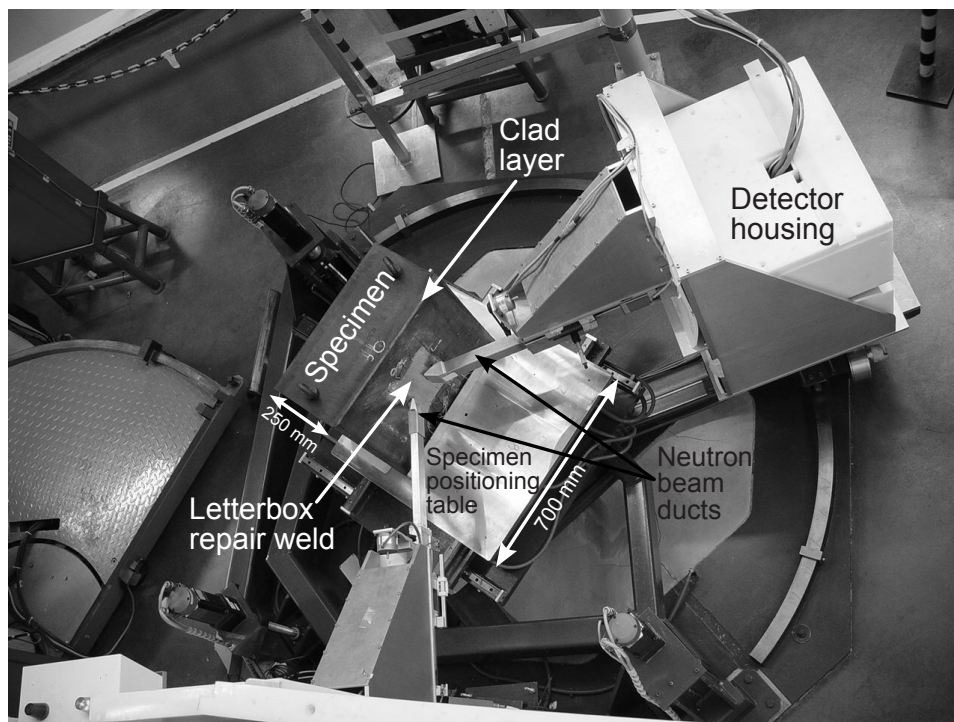


Figure 3.5: *The Large Component Neutron Diffraction Facility at the HFR during strain measurements on a 25 cm thick 600 kg block of ferritic steel featuring a clad layer and a letterbox repair weld.*

develop a double frame facility, where the horizontal positioning stages and the specimen rotation stage are carried by the inner frame lifted by three heavy ball bearing spindles, which facilitate vertical specimen positioning (see Fig. 3.5).

Similar spindles and wide frames with sliding bearings enable a linear positioning range of 400 mm in the X and Y directions.

In view of the considerable size of the equipment, new beam-defining apertures and shielded beam path encapsulation had to be designed, which are mechanically supported from the top, rather than the bottom. Beam defining apertures are exchangeable cadmium masks available in the range from 1 mm to 1 cm width.

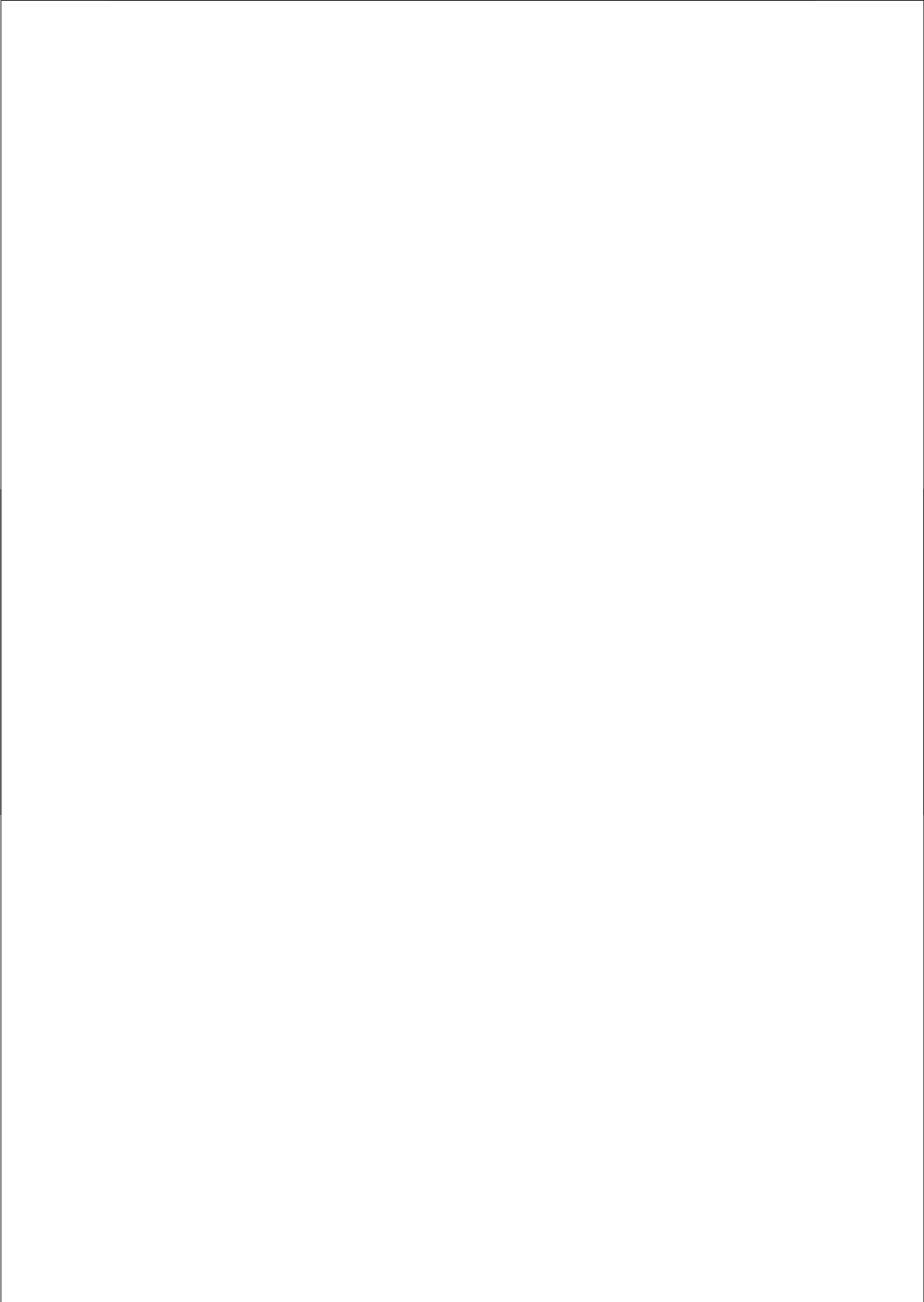
The detector is a 32-wire multi-detector (He-3 at 8 atm), positioned at a distance of 1110 mm from the sampling volume, offering a resolution of about 0.1° per wire and a total detector acceptance angle of about 3° . The detector is shielded from background neutron radiation by about 20 cm of polyethylene and 2 cm of borated polyethylene.

The instrument was first operated in 1999, at that time the first facility in the world with a specimen weight capacity of 1000 kg. Since then several facilities offering

similar or even bigger specimen weight capacity have been commissioned at other neutron scattering facilities. The picture (Fig. 3.5) shows the heaviest specimen that has been tested at the facility to date. It was a 600 kg low-alloy steel block with a welded austenitic cladding layer and a repair type of weld in its centre.

The monochromator installed at this facility is a pyrolytic graphite (PG) double monochromator. It is oriented for use of the (002) reflection. This arrangement gives the experimenter a considerable flexibility in the choice of neutron wavelength. In addition, the wavelength can be varied without changing the location of the sampling volume. For the present investigations the monochromator has been oriented for the (004) reflection. Experience has shown that more accurate and reliable measurements of strain and stress are obtained with this setting. This observation is likely to result from a better angular resolution and higher symmetry of the diffraction peaks obtained with the (004) orientation.

The weight carrying capacity, the long translation ranges of the specimen table and the flexibility in the choice of wavelength make this facility a suitable instrument for the investigations undertaken in the context of this study.



Chapter 4

Welding

The term welding is used for many techniques applied for joining components or materials. Welding is distinguished from other joining techniques, such as soldering, adhesive bonding, bolting or riveting, by the formation of a continuous metallurgical bond. The reasons why welding has become important in manufacturing are manifold, and the choice of joining process depends on the individual application. Table 4.1 gives a brief overview of factors to be considered when making the choice for or against welding.

In this chapter, a definition is provided for the term welding and a brief overview of modern welding techniques is given. Important industrial applications of welding are listed together with considerations governing process selection. Several fusion-welding methods applied in nuclear power installations are relevant to this work and these are briefly described. The final sections describe specific weld features that influence residual stress measurements.

4.1 Definitions / welding methods

There are many differently worded definitions of the term welding. According to ISO 857-1 [54], the term is used for “fabrication processes involving irreversible joining of components using heat and/or pressure with or without the addition of consumables”. Welding can generally be applied to metallic materials as well as to glasses and thermoplastics.

On a microscopic level welding processes create inter-atomic bonds over large areas, where these have not been before. This can be achieved either by melting of materials or by applying mechanical forces at the surfaces where the bond is to be created. In most cases, input of energy is necessary to create a welded joint.

During welding, additional material in the form of a consumable rod, wire or insert is often needed. This is the case when the size, arrangement and geometry of the surfaces to be joined are prohibitive for directly joining the components at

Table 4.1: *Factors to consider when selecting a joining technique.*

<i>Economical</i>	<ul style="list-style-type: none"> • Labour cost • Capital cost of equipment • Process duration • Material cost • Energy cost • Size, shape and weight of the final structure • Maintenance and surveillance effort • Probability of flaws
<i>Technical</i>	<ul style="list-style-type: none"> • Joint properties similar to those of the base materials. - facilitating service load scenarios possibly not conceivable with other joining techniques. • Permanence. • Applicability in view of size, shape and thickness of the component(s) to be manufactured. • Considerations related to regulatory requirements, if any.
<i>Structural Integrity</i>	<ul style="list-style-type: none"> • Response to applied loads. • Failure mechanisms and susceptibility to failure; <i>e.g.</i>, cracking and crack propagation. • Residual stresses. • Impact of ambient conditions.

their (prepared) surfaces. The use of a consumable generally implies that the process involves material melting.

While welding techniques have been in existence for a few thousand years, the precursors of today's welding methods have been developed relatively recently. For example, the first arc welding techniques were only invented in the 19th century [55], and it subsequently took another few decades before coated electrodes or shielded gas welding became available. Gases produced from coatings or added separately reduce the oxidation of the consumables and parent materials at the high temperatures applied. More recent developments in welding technology include laser beam welding, electron beam welding and friction stir welding.

Welding is applied in a large number of industrial sectors, and an overview lies outside of the scope of the present work. Examples of sectors where welding constitutes an important part of the manufacturing/construction process are the construction, petro-chemical, shipbuilding and the automotive industries. In certain areas of aircraft construction, welding is becoming increasingly accepted. Notably, welding is often employed in safety critical applications, such as the nuclear installations considered in this work.

Nowadays more than 100 welding techniques have been developed [56]. These can in general be classified into two major categories: solid-state welding and fusion welding. Examples of solid state welding techniques are friction welding, pressure welding and extrusion welding. For the applications considered in the present work, only fusion welding techniques are relevant.

4.1.1 Fusion welding techniques

Fusion welding techniques involve the application of heat to the components to be welded and, if applicable, to the welding consumable added. In fusion welding, part of the base material in the region of the joint and the consumable used are melted and the bond is generated by the solidification of the material during cooling.

Resistance welding is an important process as it is widely used in car manufacturing. In this process heat is generated by passing an electric current through the parts to be joined at the location of the joint. The high electrical resistance at the interface of the joint generates the heat necessary for the parts to be joined either in a fusion or solid-state process; *i.e.*, resistance welding is not exclusively a fusion welding process. Spot welding is a typical example of a resistance welding process.

Other important welding techniques involving material melting are the energy beam techniques. Examples for these are laser welding and electron beam welding. In these processes the necessary energy is transferred to the materials to be melted *via* the respective laser or electron beams. The nature and geometry of these beams allow for the generation of narrow and at the same time also for deep penetration welds.

Oxy-fuel welding is a process that might be most familiar to the layman. It involves metal melting through the heat generated by a flame torch directed onto the base material and the consumable. In order to reach the necessary temperatures to

melt many metals, the flame needs to be fueled by a gas producing a sufficiently hot flame, often acetylene combined with oxygen [55]. Oxy-fuel welding does not play a significant role in industrial manufacturing processes, but is often used in small workshops or on remote construction sites.

Today arc-welding is an important industrial welding process [55; 57]. It involves the transfer of heat *via* an electric arc between the base material(s) and an electrode. Through this heat the welding consumable, if present, and parts of the base materials are melted and upon solidification, the fusion joint is generated. The material surfaces subjected to the heat are protected against oxidation by a shielding gas atmosphere and/or by slag generated by the molten coating of the added consumable. Two techniques used for the present work are: Shielded Metal Arc Welding and Gas Tungsten Arc Welding [57].

Shielded Metal Arc Welding uses an electric arc struck between a consumable electrode and the base material. The consumable electrode material is a coated metal rod with a composition compatible with the base material. Due to its finite length, the consumable electrode must be replaced on a regular basis between successive weld passes. The coating of the electrode generates the environment protecting the hot metal from oxidation. The slag emanating from the coating needs to be removed at the end of the process, and prior to the application of the following weld layer.

The slower Gas Tungsten Arc Welding technique uses a non-consumable refractory electrode made from tungsten. A consumable may be fed independently in the form of a rod or wire if required. Shielding is provided by feeding an inert gas into the weld zone. Gas Tungsten Arc Welding is suitable for the welding of thin sheets and is often used for the first layers of a multi-layer weld, because it facilitates control of weld pool penetration and dilution of the consumable in the parent material. It is a flexible process in that the energy input can be adjusted to a large extent independently of the amount of consumable added [58].

4.1.2 Fusion welding techniques for nuclear applications

Welds of considerable dimensions are applied for the construction of pressure vessels and for piping installations of the primary and secondary cooling circuits of nuclear power reactors. Reactor pressure vessels of light water reactors can have wall thicknesses in the order of 200 to 300 mm; the primary piping wall thickness is in the range of 20 to 80 mm. Such a pressure vessel consists of a large steel cylinder closed at both ends. The cylinder itself is assembled by welding cylindrical sections, and welding is used to attach the penetrations (nozzles) to the vessel as well.

In this work, two dissimilar metal welds and a welded clad layer have been investigated. The dissimilar metal welds connect ferritic steel pressure vessel nozzles to austenitic steel piping sections. These welds have been made using arc-welding in multi-pass circumferential welding arrangements. In both cases austenitic steels have been used as consumables.

The clad layer specimen is representative of an austenitic steel clad layer welded on the inside surface of a low alloy steel pressure vessel. This clad layer protects the

low alloy steel from the corrosive attack of the water inside the vessel. This lowers the risk for stress corrosion cracking. At the same time it also reduces the dissolution of metal atoms limiting the level of radioactivity in the primary system. The number of weld layers to be applied depends on the process and the total thickness of the clad layer. Typical clad layer thicknesses are in the range 5 to 10 mm. In the example presented in this work a clad layer of 10 mm is applied in 3 layers of welding.

Similar applications also exist in other industrial sectors, for example in the petrochemical industry or in boilers in non-nuclear electric power generation.

4.2 Welding and residual stresses

4.2.1 Residual stresses

During welding the localized application of thermal and/or mechanical energy leads to the presence of strong temperature gradients. The evolution of temperature gradients leads to local (cyclic) plastic deformation, which eventually leaves the component under a localised residual stress. It is not unusual that residual stress levels reach the yield stress of the material. During multi-pass welding these processes occur repeatedly, which complicates the formation (and hence prediction) of the final residual stress field. Actually, in multi-pass welding partial stress relief annealing will occur at the same time as new stresses are generated.

Phase transformations that occur for example in ferritic steels during welding are another influencing factor in the generation of residual stresses. Rapid volume changes of the transforming material can result in localized plastic deformation and hence in and additional contribution to the stress formation.

The magnitude and distribution of residual stresses depend on a number of factors, such as energy input, restraint during welding, pre-heating, welding speed, cooling rate, interpass temperature *etc.* The temperature dependence of the material properties determines the relative impact of these influences.

An example of a temperature distribution in space and time is given in Fig. 4.1. The figure shows the result of a numerical thermal analysis of the application of a single weld bead on a stainless steel plate by Gas Tungsten Arc Welding [59; 60]. The plate was 180 mm long, 120 mm wide and 17 mm thick. A single weld bead of 60 mm length was applied on one surface in the centre of the plate. The travel speed of the welding torch was 2.27 mm/s. Figure 4.1 (a) shows the temperature distribution along a line running beneath the weld bead 2 mm below the plate surface at times when the weld torch has traversed about half the length of the bead and when it has reached the end of the bead. The higher peak temperature at the end of the bead is mainly related to a short dwell of the torch at this position. Figure 4.1 (b) shows the temperature distribution along a line across the weld bead, 2 mm below the surface, when the torch passes the mid-length position of the bead.

The figures give an impression of the temperature distribution in the material in time and space in the directions along and transverse to the weld bead. They also illustrate at what rate the material cools down after the passing of the weld torch.

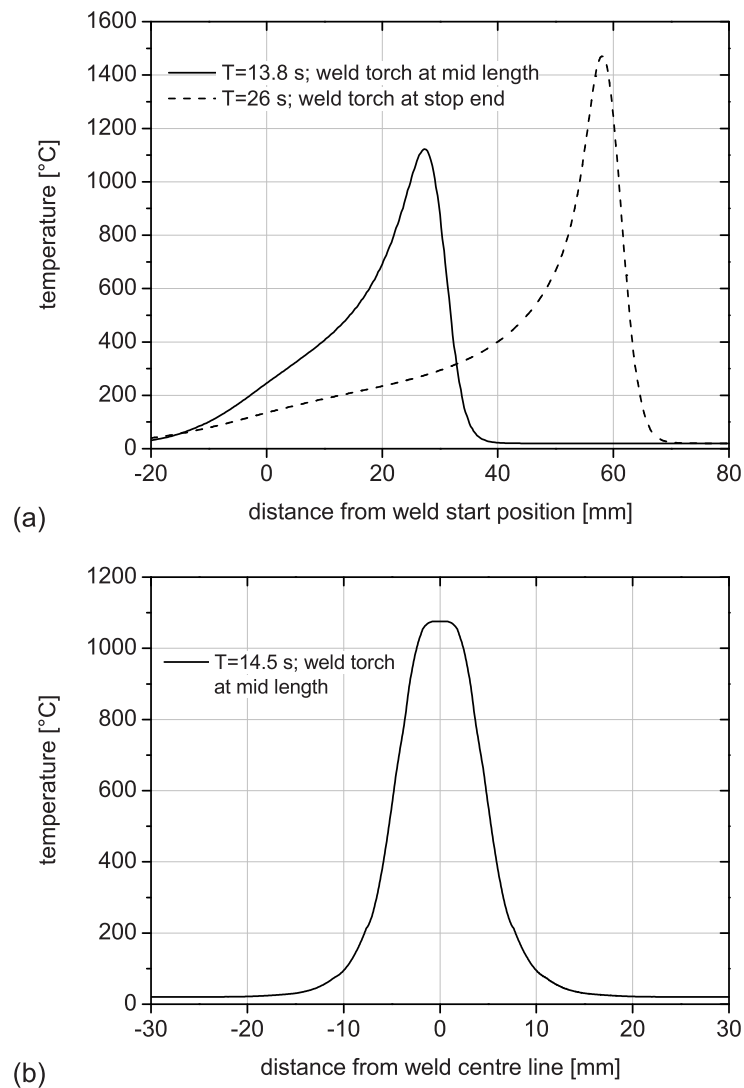


Figure 4.1: Predicted temperature distributions along lines 2 mm below the surface during application of a single weld bead on a stainless steel plate; (a) along the weld bead underneath its centre when the torch is at mid length of the bead (solid line) and when the torch is at the end of the bead (dashed line), (b) along a line across the weld at mid length of the bead at the moment when the torch passes over this position; data courtesy of K. Decroos [60].

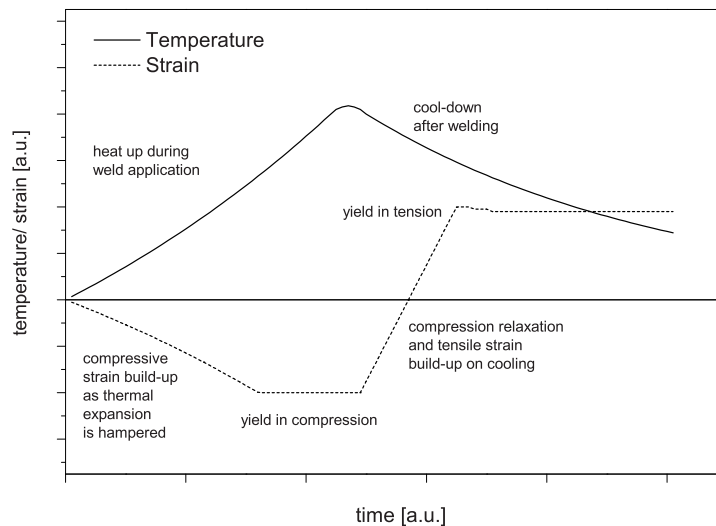


Figure 4.2: *Sketched evolution of local strain/stress in the heat-affected zone or nearby base material due to thermal expansion during welding cycle.*

It can be seen that the temperature on the sides of the weld bead drops from about $1100\text{ }^{\circ}\text{C}$ to less than $200\text{ }^{\circ}\text{C}$ within less than 10 mm . Concerning the time evolution, Fig. 4.1 (a) shows that temperatures drop from about $1100\text{ }^{\circ}\text{C}$ to a level in the range of $250\text{ }^{\circ}\text{C}$ to $300\text{ }^{\circ}\text{C}$ after 12 to 13 seconds (corresponding to 30 mm of torch travel).

What happens mechanically under such inhomogeneous thermal loads is that the hot material is restrained in its thermal expansion by the surrounding colder material. The thermal gradients are such that the material yields plastically while expanding. Upon cooling, the opposite happens: the material is restrained in its thermal contraction by the surrounding material undergoing much smaller temperature changes, and again plastic yielding occurs. When cooled down to room temperature, the material in areas where contraction was hampered remains under tensile stress, and applies forces on the surrounding material to leave the latter under compressive stress. Figure 4.2 shows a qualitative sketch of this evolution due to a single thermal cycle.

Bar models as described in [61] explain the principle in a simple, but illustrative manner. The different zones in the welded component are represented by individual bars solidly connected at their ends. In these models, the evolution of the yield strength of the material, which decreases with increasing temperature, is taken into account. The prediction is similar to that indicated in Fig. 4.2, resulting in a high tensile residual stress in the region of the weld after cooling to room temperature.

Figure 4.3 shows a comparison of averaged experimental residual stress data with 4 different FEM predictions. The figure provides a suggestion as to how the plate ma-

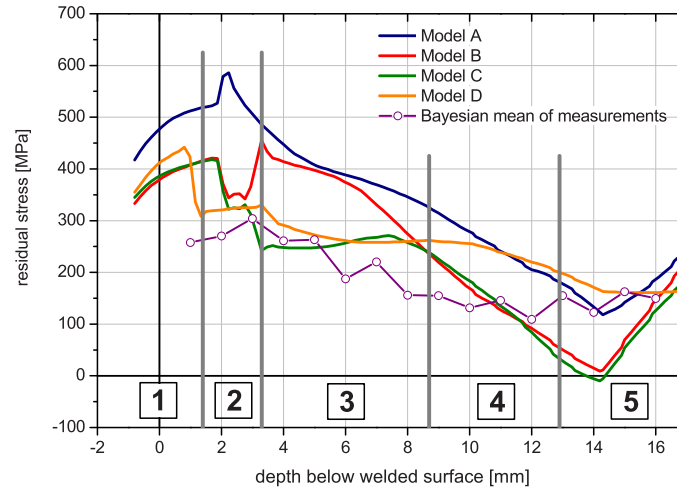


Figure 4.3: Residual stresses as a function of distance from the weld surface for different FE models compared to averaged experimental data (data courtesy of M. Smith and P.J. Bouchard from EdF Energy).

terial underneath the single weld bead may be divided into zones, where the thermal load applied through welding leads to different mechanical deformations. In zone 1, corresponding to the molten material, consisting of a mixture of molten base material and added weld material, only the cooling of the material contributes to the stress formation. Zones 2, 3 and 4 experience heating and cooling without material melting, but with material yielding through thermal expansions and contractions. The material in zone 5 does not undergo any plastic deformation; however the residual stress distribution here is predicted to be quite sensitive to the amount of heat (expressed in energy per unit of length of the weld bead) put into the material. [62]

The figure also gives an indication how complicated modeling of welding stress actually is, even in this “relatively simple” case. A number of different models are shown and these exhibit a considerable variety of stress distributions. Input parameters, such as the amount of thermal energy put into the system; *i.e.*, the welding efficiency, the hardening law used, material properties chosen, incorporation of annealing effects *etc.*, have a significant impact on the final outcome of a numerical welding stress analysis.

In model A the welding efficiency is calibrated in a way different from the other models, giving the highest predicted stresses. Model B applies non-linear kinematic hardening for the weld material only, whereas model C uses this hardening law for the entire specimen. The resulting stresses differ in region 3, where model B predicts

significantly higher stresses. In the other regions these two models produce almost identical longitudinal stress estimates. Model D uses a different hardening law, which renders similar stresses to model C in regions 1, 2 and 3, but considerably higher stresses in regions 4 and 5. Nevertheless, the different models presented here render a similar overall trend for the longitudinal stresses and all show that the predicted stresses are tensile along this line through the thickness of the plate.

4.2.2 Distortion

Another important aspect of welding is the distortion induced in the component. In the process of local heating and cooling, material expands and shrinks, as described above. The volumetric expansions and contractions lead to distortions in shape and size of the welded component. Figure 4.4 shows an example [63] of angular distortion of a plate after application of a groove weld along its centre.

The extent of welding distortions can be influenced in different ways. For example, mechanical restraints can be used to reduce the extent of such distortions. The edges of the plate shown could have been fixed on a supporting table during welding, reducing the final angular distortion. However, as already stated above, the prevention of distortion comes at the cost of higher residual stress levels [61] and/or additional plastic deformation of the material. Component geometries themselves can form mechanical restraints. For example, the angular distortion shown in Fig. 4.4 is hardly possible in a circumferential pipe weld configuration.

4.3 Welding microstructures and their influence on diffraction stress measurement

The repeated processes of heating and cooling, material melting and solidification have a significant impact on the microstructure of the material. The region of a weld is generally characterized by heterogeneous material; a fusion zone and a heat-affected zone surrounded by unaffected base material. In a micrograph of a weld these different material zones can often be identified.

Other, important aspects of welding are welding errors or flaws. All welds contain some flaws, such as lack of fusion, lack of penetration, undercutting, macroscopic and/or microscopic inclusions, gas pores, hot cracking, reheat cracking, cold cracking, lamellar tearing and others [58; 64]. These flaws represent discontinuities in the material, and are therefore in many cases potential locations at which failure can initiate.

The heat-affected zone comprises regions that have not been molten, but the crystallite structures have clearly been influenced by the temperature to which these regions have been subjected. It is possible to differentiate between the coarse and the fine-grained heat-affected zones, the latter being formed further away from the fusion zone. Here the maximum temperatures reached have been high enough to initiate recrystallization of the base material that might have undergone a prior work

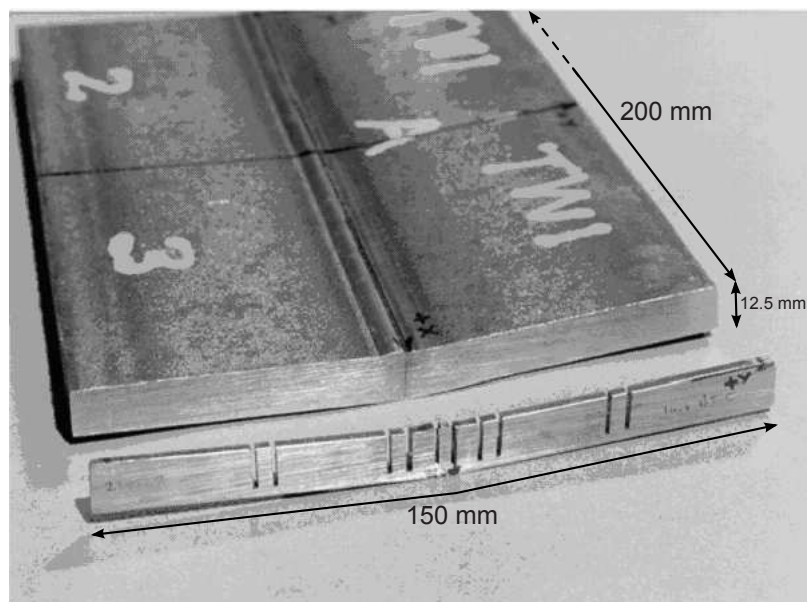


Figure 4.4: A ferritic steel weld specimen used for a neutron diffraction round robin, showing angular distortion due to welding. The 3 mm thin strip in the foreground was used for measurement of the free of stress reference values.

hardening process; *e.g.*, cold rolling [65]. Under certain circumstances precipitation of carbides can be found in the fine-grained heat-affected zone. Closer to the weld the higher temperatures give rise to grain growth. Hence, the heat-affected zone close to the fusion zone is characterized by rather large grains [65]. In multi-pass welding recrystallization of weld material through subsequent weld beads can occur, such that every bead generates its own heat-affected zone in the material underneath [66].

The fusion zone is the region where material has been molten and subsequently solidified again. The fused material includes both added consumable and base material. Often the fusion zone is characterized by a relatively large grain size (in a polycrystalline material) and by the dendritic growth of the crystallites following the directions of the thermal gradients. The size of the grains in the fusion zone, the direction of their growth and their crystallographic structure and orientation depend on the temperature gradient at the solidification front and the speed of solidification [58]. Furthermore, the type of material welded and the amount of alloying elements play a role. As these parameters can vary strongly from weld to weld, fusion zone microstructures can be very different in appearance. The microstructure formed by material production treatments, such as (cold and/or hot) rolling, and the mechanical properties of the material, are completely changed after melting and resolidification. In general, the fusion zone is characterized as having an "as-cast" structure.

The fusion and heat-affected zones of the joint are therefore characterized by different structural and mechanical properties compared to the base metal. The material around the fusion zone generally has been subject to yielding; *i.e.*, plastic deformation during welding, and diffusion processes may have changed the chemical composition of the material. Experience shows that heat-affected zones and fusion zones often exhibit preferential corrosion and/or cracking in service. The combination with high tensile residual stresses leads to welds becoming regions of increased concern for structural integrity.

Generally speaking, welding fusion zones exhibit microstructures that differ substantially from those of the parent materials. The influences that play a role here are manifold. Solidification in the case of a weld starts from the existing unmelted material, and solidification rates and crystallographic growth directions are regulated by factors such as heat input and travel speed of the welding torch. In cubic materials, such as steels, crystal growth predominantly takes place along a $\langle 100 \rangle$ -axis. At the same time growth occurs in the direction of the temperature gradient. Depending on the cooling rate these two effects can cause significant textures to be present in weld material.

The shape and size and orientation of crystallites in the weld metal, the partially molten zone, the heat-affected zone and the base metal are often quite different. As an example, Fig. 4.5 shows the microstructure across a fusion boundary of a multi-pass stainless steel weld from this work. The coarse dendritic structure of the unrefined weld material is seen in the upper part, whereas the lower part displays the grain structure in an earlier deposited bead. The latter structure is refined through the thermal impact of the deposition of the subsequent bead. The visible length of the dendrites in the coarser grained structure is several hundred micrometers. The picture

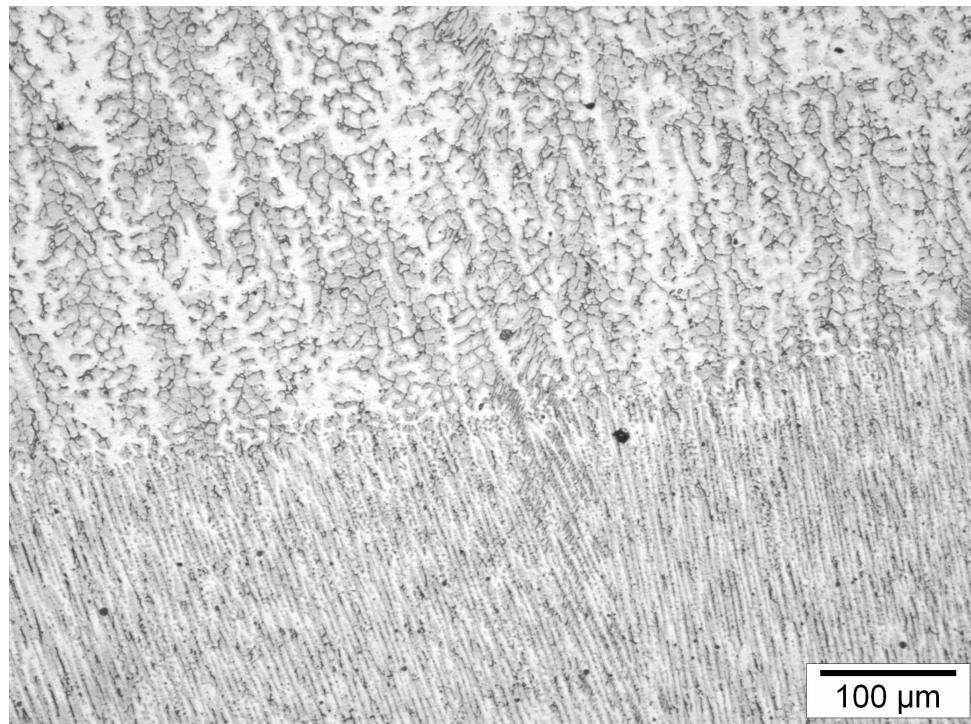


Figure 4.5: *Micrograph across a fusion boundary between two weld beads within a multi-pass stainless steel weld. The coarse dendritic structure of the unrefined weld material is seen at the top, and the lower part displays the refined structure in material deposited earlier.*

also suggests that the dominant growth direction of the grains is maintained across the fusion boundary. This observation is in agreement with a simple grain growth model for a stainless steel multi-pass weld suggested in [67]. Figure 4.6 gives an overview of the predicted grain growth directions across the entire cross-section of a sample 40-pass groove weld configuration in a stainless steel grade 316, suggesting a strong dominance of growth in a direction perpendicular to the respective fusion boundary.

In general, zones with an average grain size bigger than 75 to 100 μm , which is the case for the length of the grains in Fig. 4.5, present a measurement problem for diffraction stress analysis because a non-homogeneous distribution of the diffracting grains may influence the angular position of a diffraction peak. This effect is superimposed upon the peak shifts caused by lattice strains. An analysis of the impact of the grain size on the scatter of neutron diffraction data has been published in [68]. This phenomenon is further discussed in chapter 8.

Depending on the presence of alloying elements and cooling rates, various material phases can develop in steel welds. One important contributor to this is the carbon

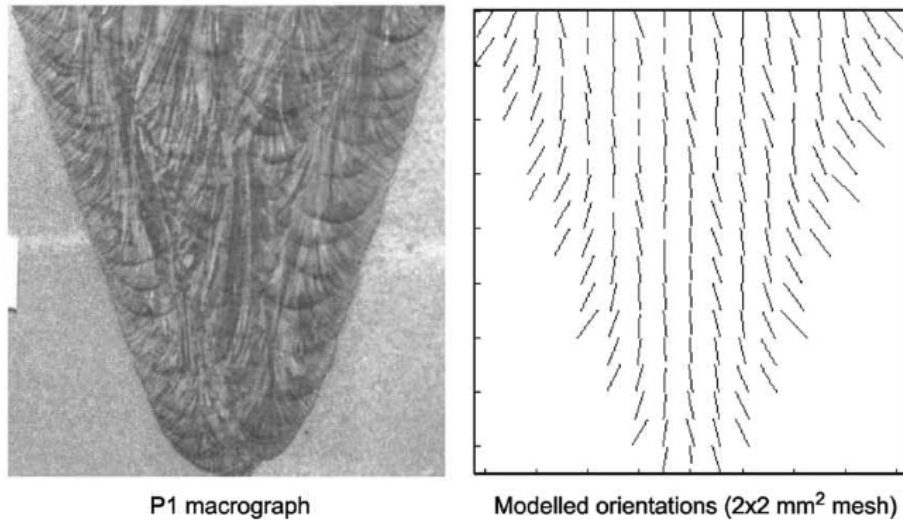
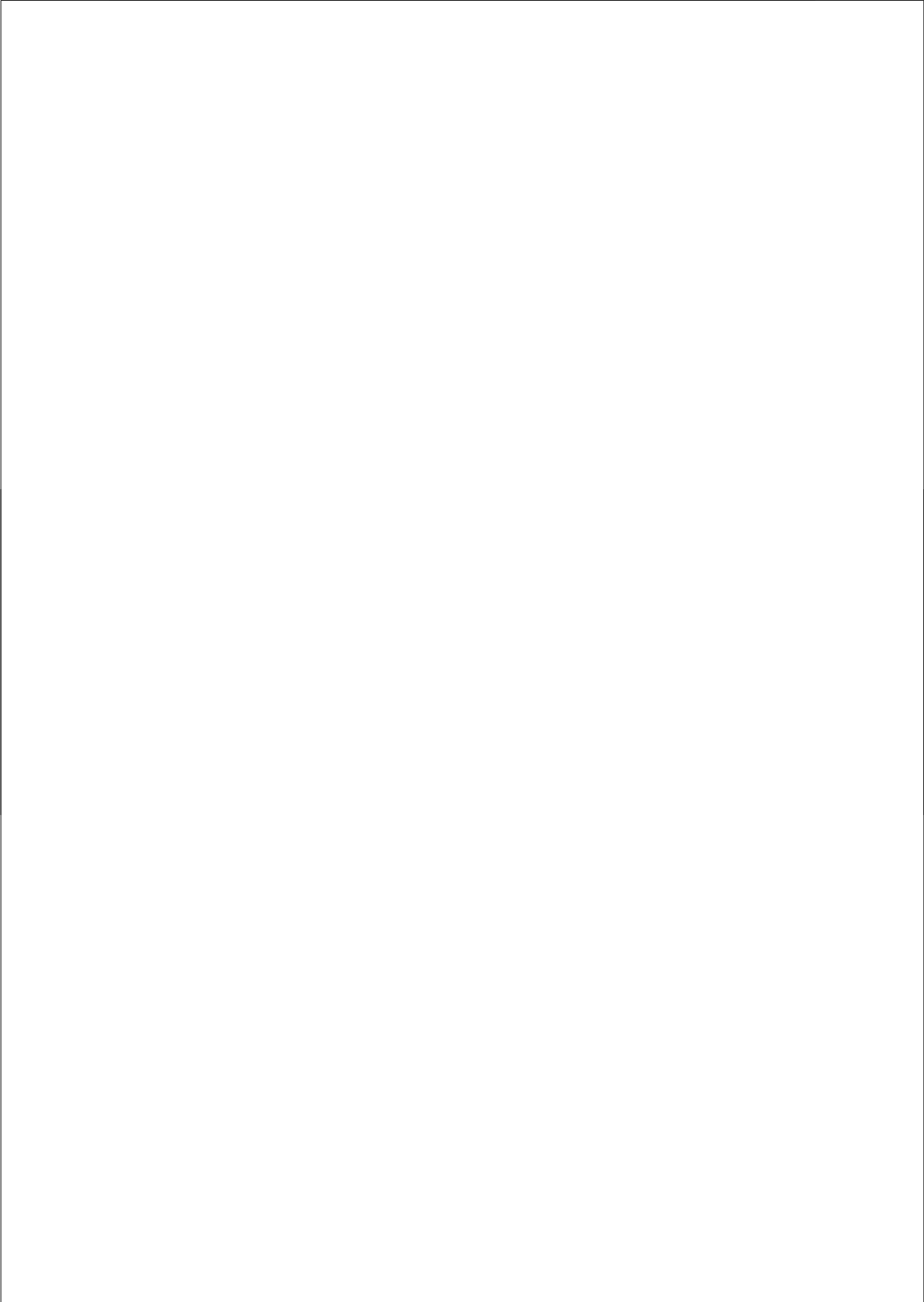


Figure 4.6: *Macrograph of a 40-pass groove weld and the predicted grain growth direction for this weld (from [67]).*

content, which can influence, for example, the formation of martensite, especially at high cooling rates. In general, welding consumables and the base material do not have the same chemical composition. This in itself makes the weld material different from the base material. In addition, the heat involved might cause certain alloying elements to diffuse through the material and concentrate; *e.g.*, near grain boundaries or inclusions, or even to form precipitates. In multi-pass welding all this occurs repetitively.

The phenomena described result in a high probability that measurements of the stress free reference values, which are so important for diffraction based stress analysis (see eq. 3.3), will vary with location in the fusion and heat-affected zones of welded components, and that they will almost certainly differ significantly from the value obtained for the base metal. In the fusion welds under investigation in the context of this thesis, it is therefore necessary to measure the reference parameter per location and per direction in a macroscopically stress free condition.



Chapter 5

Residual stresses in a thin dissimilar metal pipe weld

5.1 Introduction

Welding of dissimilar materials is used, for example, in nuclear power installations to join ferritic components to austenitic piping systems. Welded joints are more susceptible to cracking than the pure base material regions, and in addition, the presence of different materials complicates inspection of the weld regions [69]. When a flaw is detected in such nuclear components, a defect assessment is performed in order to establish whether the component is safe for continued use. As, for obvious reasons, destructive examination does not normally serve the purpose, non-destructive examination is required and/or one has to rely on computational predictions of the remaining life of a defective component. Such assessments have to take into account a component's thermal and mechanical operational loads, its geometry, material properties, operational history, and also the residual stresses present.

The primary objective of the present study is to assess and validate analysis methods for a model case representing a dissimilar metal weld joining a ferritic steel pressure vessel nozzle to a stainless steel piping section [70]. By artificially introducing a large defect into the component and by initiating crack propagation through the application of a bending force, experimental verification of different numerical approaches for assessing the fracture behaviour was performed.

Residual stress data were obtained in this context in order to serve as one set of input data for these fracture assessments. The regions of interest were the fusion zone and the surrounding base material. Neutron diffraction was chosen as it provides a non-destructive means for measuring residual stresses in the bulk of a component.

5.2 Description of the component

The component was a pipe of ~ 400 mm length, with 168 mm outer diameter and 25 mm wall thickness. It was made from two parts each of ~ 200 mm length, one of ferritic steel grade A508 and the second of stainless steel grade 304L, joined by means of a circumferential butt weld using stainless steel as a filler material. Joining of dissimilar materials almost invariably leaves the user with potential problems arising from the mismatch of thermo-mechanical properties. This leaves the component under a significant residual stress in the as manufactured condition.

This particular geometry was not meant to represent any particular pipe connection in a nuclear plant, but rather served as a model case for different kinds of bi-metallic piping joints in the primary system of a light water reactor. Furthermore this investigation was a precursor to the assessment of a full scale mock-up of a pressure vessel to primary piping joint.

Component manufacturing

Manufacturing of the test component [71] started with the application of a buttering layer on the ferritic pipe. The pipe edge to be welded was machined to a bevel angle of 25° (see Fig. 5.1). This preparation was also applied on the austenitic pipe end. Prior to buttering the ferritic pipe was preheated to 120°C , which reduces the risk of hydrogen embrittlement in ferritic welds. The first buttering layer was applied by shielded metal arc welding (SMAW). This layer was laid down in the form of 9 circumferential beads; the maximum permissible interpass temperature near the weld was 175°C . Temperature monitoring was facilitated by thermocouples attached to the component. The first layer was deposited with an overalloyed steel (309L-16) having an increased Cr and Ni content in order to reduce the risk of martensite formation near the fusion boundary [72]. Martensite would increase the brittleness of the material and therefore its susceptibility to rapid cracking. Subsequently another 3 layers of buttering were built up with almost the same welding parameters. The difference was that for those layers stainless steel grade 308L-15 was used as the filler material. Tables 5.1 and 5.2 show the chemical compositions of the weld filler materials and the welding parameters, respectively.

The ferritic pipe with the buttering layer was subjected to a post-weld heat treatment, during which it was kept at $\sim 600^\circ\text{C}$ for one hour. The heating and cooling rates were kept below 50°C/h in the range 400°C to 600°C . After cooling down, the pipe was machined to its prescribed inner and outer diameters of 118 mm and 168 mm, respectively.

Ferritic and austenitic steels generally have different thermo-mechanical properties. Hence, the heat-treated buttered pipe was expected to exhibit significant residual stresses after cooling to room temperature. These stresses have not been experimentally determined; therefore it is not possible to give an estimate of their magnitude.

The buttered ferritic and the stainless steel halves of the test component were machined prior to welding to form a 50° included angle V-groove in accordance with Fig. 5.2.

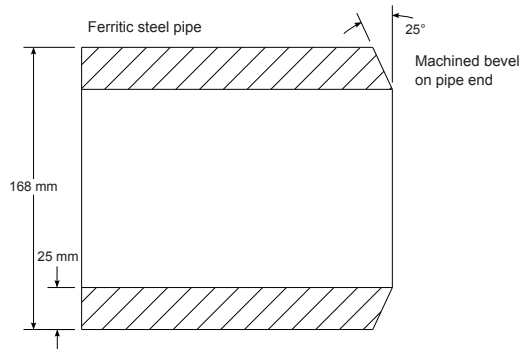


Figure 5.1: Geometry of ferritic pipe with machined end beveling.

Table 5.1: Chemical composition of weld consumables used for the buttering layer [in wt%].

Consumable	C	Mn	Si	P	S	Cr	Ni	Mo	V	Co	Ti	Nb	Cu	N
309 L-16	0.019	0.81	0.82	0.02	0.012	23.7	12.5	0.04	0.08	0.06	0.01	0.004	0.06	0.05
308 L-15	0.02	1.62	0.22	0.021	0.004	19.5	10.0	0.05	0.07	0.05	0.013		0.044	0.03

Remainder is assumed to be Fe

Table 5.2: Prescribed welding parameters for application of the buttering layer.

Pass	Welding process	Filler material	Diameter [mm]	Amperage range [A]	Voltage range [V]	Travel speed
1	SMAW	309 L	4	110 - 140	23 - 28	Not presc.
2 - 4	SMAW	308 L	4	110 - 140	23 - 28	Not presc.

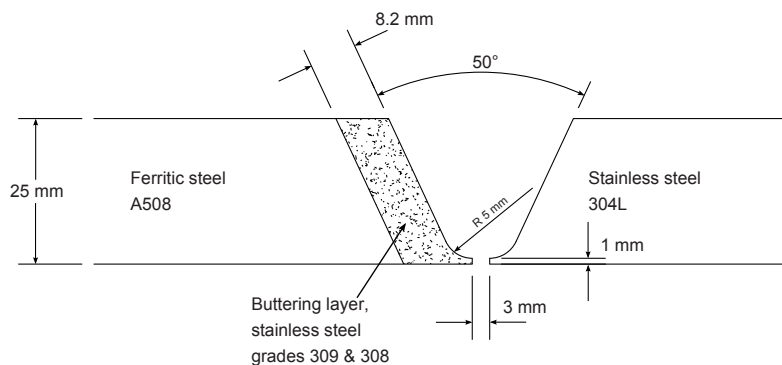


Figure 5.2: V-butt weld preparation for bi-metallic steel piping weld after application of the buttering layer to the ferritic steel part of the pipe.

Table 5.3: Chemical composition of weld consumables used for the V-butt weld [in wt%].

Consumable	C	Mn	Si	P	S	Cr	Ni	Mo	V	Co	Ti	Nb	Cu	N
ER 308 L	0.023	1.65	0.37	0.018	0.013	19.7	9.8	0.26	0.054	0.064	<	<	0.12	0.049
E 308 L	0.02	1.62	0.22	0.021	0.004	19.5	10.0	0.05	0.07	0.05	0.013		0.044	0.03

Remainder is assumed to be Fe

Table 5.4: Prescribed welding parameters for application of the V-butt weld.

Pass	Welding process	Filler material	Diameter [mm]	Amperage range [A]	Voltage range [V]	Travel speed
1 - 7	GTAW	ER 308 L	1.2	70 - 120	8 - 15	Not presc.
8 - 32	SMAW	E 308 L	4	110 - 160	22 - 26	Not presc.

The V-butt welding was performed without pre-heating the components. The first seven beads were laid down by gas tungsten arc welding (GTAW) using an ER 308 L filler material, and subsequently the groove was filled by an additional 25 beads applied by SMAW (filler E 308 L). Also for this weld, the maximum permissible interpass temperature was 175 °C. After cooling of the component, the cap and root reinforcements of the weld were machined away. No post-weld heat treatment took place, as it was not considered necessary for the purposes of stress relief in the context of these investigations. Tables 5.3 and 5.4 show the chemical compositions of the weld filler materials and the welding parameters, respectively.

Ultrasonic, dye-penetrant and X-ray radiographic inspections of the weld and the buttering layer were performed at various stages of the process to insure an acceptable quality of the component. X-ray radiography was performed at the JRC Radiographic Laboratory, where in total 11 defective areas distributed over the circumference of the weld were found. These were tungsten inclusions and gas pores of 1 mm or less in size, with the tungsten inclusions appearing in clusters in a few cases. In addition one gas pore with a 5 mm crack was found [73]. Based on these results a test location was chosen in the component for neutron diffraction measurements where no flaws had been detected in the weld.

A substantial amount of material needed to be removed from the component in order to facilitate access of the neutrons and the neutron beam ducts to the measurement locations around the fusion zone. Figure 5.3 shows the "windows" that were cut in the neutron diffraction component. While the windows at the outer ends of the component were milled, electro-discharge machining (EDM) was used to cut the window at mid-length of the tube. A special type of EDM technique was used, where copper plates were driven through the material along the edges of the desired hole. This way the material loss by the cutting process was limited to less than 3 mm around the edges and the removed piece of material was left intact to be used as reference material for the neutron diffraction investigations and for materials testing.

In the determination of the residual stresses present, variations in the stress free lattice spacing in the weld had to be taken into account. To determine these variations

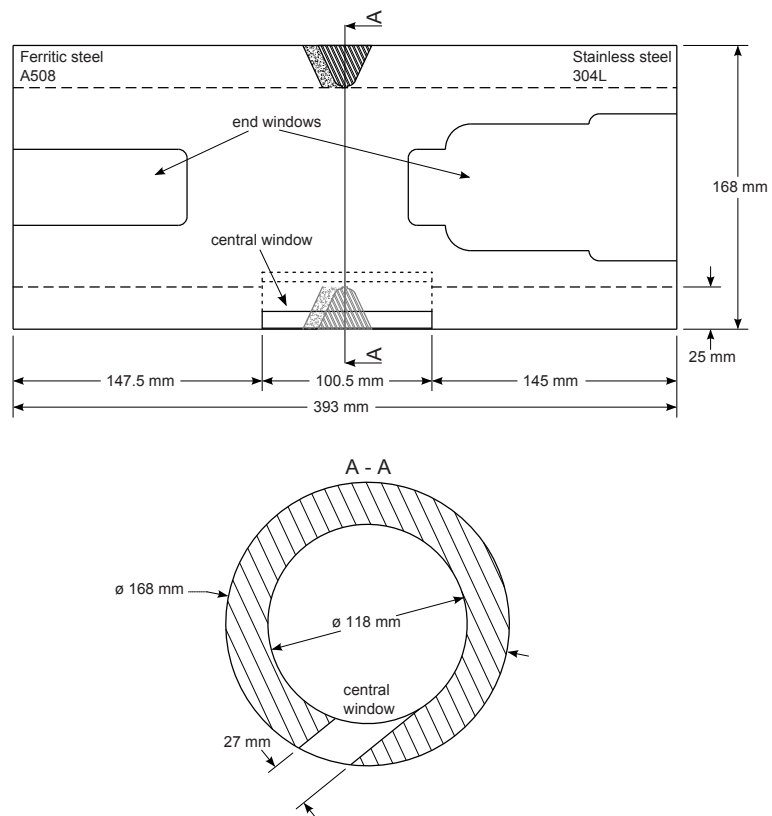


Figure 5.3: Final geometry of component for neutron diffraction stress measurement. The windows that were cut to facilitate the measurements are shown.

reference specimens were cut from the material extracted from the central window. First, a radial slice of 6 mm thickness was cut from the window material. The cut surface was polished and etched in order to make the fusion zone visible. The specimen was then cut into two pieces, as closely as possible along the interface between the buttering layer and the remainder of the fusion zone. Finally, three cuts in the piping axial direction were applied in each of the two pieces, which generated long "teeth" of material, which were subsequently used to do measurements of the reference scattering angles. Figure 5.4 illustrates the manufacturing of the reference specimens and shows the two reference specimens, one containing the buttered layer and the ferritic steel base material and the other containing the remainder of the fusion zone and the stainless steel base material.

5.3 Neutron diffraction measurements

The Large Component Neutron Diffraction Facility described in chapter 3 was chosen for these investigations. This instrument facilitates accurate positioning of this relatively heavy component in the neutron beam. In addition the facility has an adjustable double monochromator, allowing the performance of measurements using different neutron wavelengths.

The first consideration for investigations in this component was the size of the gauge volume to be chosen. An elongated matchstick shape was no option, because no usable plane of symmetry existed in the region where the measurements were to be made. The component wall thickness was 25 mm. In order to keep the measurement time acceptably short; *i.e.*, no more than 4 to 6 hours for the longest individual measurements, a relatively large gauge volume size was chosen.

For the piping axial and radial directions it was possible to use a gauge volume of $4 \times 4 \times 10 \text{ mm}^3$. In this way the spatial resolution was not high, and it was not possible to obtain valid measurement results within 1 mm of the buttering ferrite interface.

Measurements in the circumferential direction required a smaller vertical gauge volume dimension than those in the axial and radial directions. The reason for this is the orientation of the interfaces between the weld and base materials during measurements in the circumferential direction. A gauge volume of 10 mm height would cut across an interface at many test locations. Hence, in this case a volume of $4 \times 4 \times 5 \text{ mm}^3$ was selected.

Based on the size of the chosen gauge volume in relation to the component geometry, it was decided to obtain measurements along lines at four different depths in the wall, namely 3 mm (line A), and 9.3 mm from the outer surface (line B), and 9.3 mm (line C) and 3 mm from the inner surface (line D). Figure 5.5 shows the measurement locations over the buttering and weld fusion zones and the base materials.

It was decided to perform all measurements with the same detector position. This was necessary for two reasons. In the first place this was done because otherwise the central window would have needed an individual shape for every material zone to be investigated; and secondly, keeping the detector position fixed, minimized inaccuracies

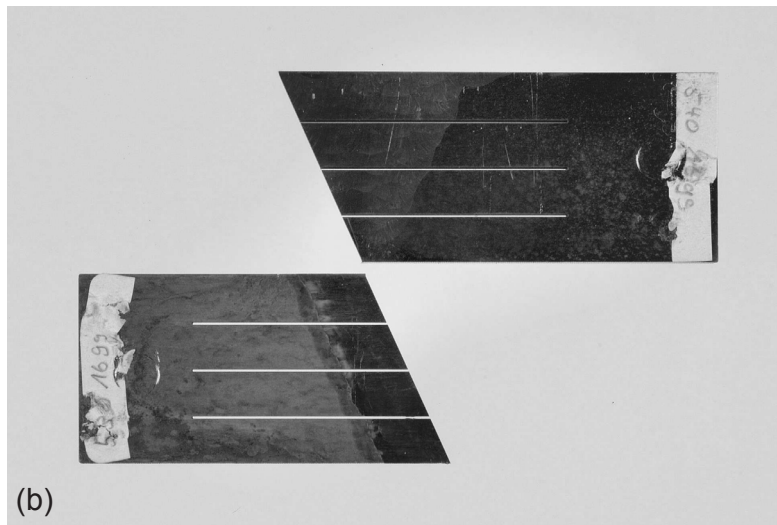
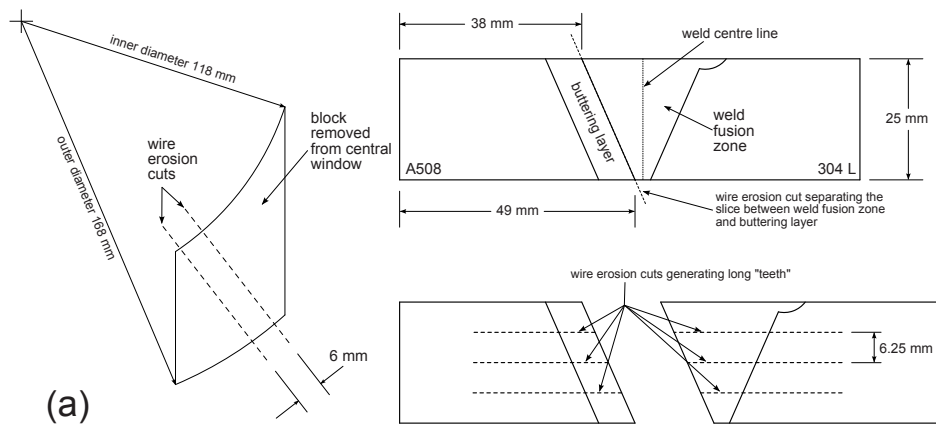


Figure 5.4: Reference specimens: (a) left: slice extracted from block of material removed from the central window; top right: slice cut into two trapezoidal pieces along the buttering-butt weld interface; bottom right: additional cuts in each piece producing long "teeth"; (b) photograph of the final reference specimens; on the bottom left the ferritic steel and the buttering layer, and on the top right the fusion weld and the stainless steel base material.

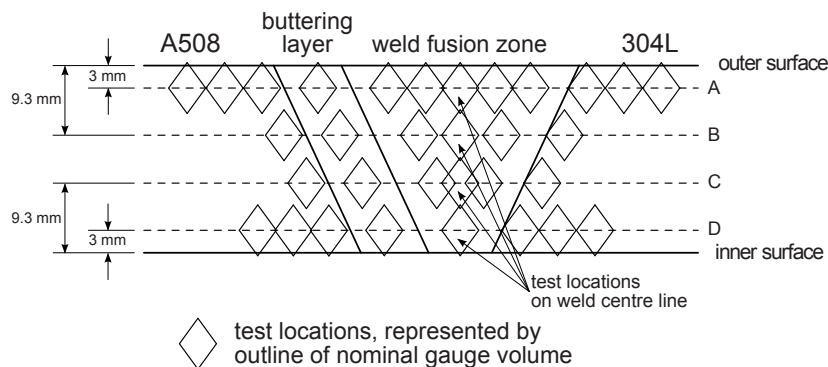


Figure 5.5: Locations of stress measurements in and around the fusion zone of the bi-metallic weld component.

associated with detector positioning. The choice was made to perform all measurements at a fixed detector position of 76.15° . This particular angle corresponds to a measurement of the austenitic steel (111)-reflection plane at a neutron wavelength of 0.257 nm.

As there were three material zones, namely the stainless steel base material, the fusion zone including the buttering layer (exhibiting a strong (200) texture), and the ferritic steel base material, it was necessary to adjust the neutron wavelength using the double monochromator.

The measurements were thus executed using the instrument settings and crystallographic lattice planes shown in Table 5.5. Because of the sensitivity of the (200)-reflection planes to plastic strain, these planes are normally not the preferred choice for measurements in austenitic steel. In these investigations, however, the (200)-planes had to be used because they rendered substantially higher peak intensities than the (111)-planes. Other crystallographic planes were not accessible because of the high neutron wavelengths at the diffractometer used.

Measurements were performed in all three directions for all test locations shown in Fig. 5.5. Figure 5.6 depicts the gauge volumes and neutron beam orientations for measurements in the three different directions. Because the neutron wavelength was changed every time a new material zone was investigated, it was chosen to perform measurements on the welded component and the corresponding reference specimen in the corresponding orientation in direct succession, such that an intermediate change and resetting of the wavelength would not be necessary.

Figure 5.7 depicts the bi-metallic component on the neutron diffractometer during measurements in the circumferential direction. It can be seen that the duct of the incoming beam enters the component through the window at mid-length. In addition, the interface between the buttering layer and the ferritic part is visible on the component outer surface. The reference specimen for the determination of the reference lattice spacings can be seen at the bottom in front of the component.

Table 5.5: *Important parameters of neutron diffraction measurements.*

Gauge volume:	4 × 4 × 10 mm ³ (radial and axial) 4 × 4 × 5mm ³ (circumferential)
Detector position:	76.15° (for all measurement directions)
Crystallographic reflections:	ferrite {110} austenite {200} in the weld and the buttering layer austenite {111} in base material 304 L
Neutron wavelengths:	0.252 nm for {110}-ferrite 0.223 nm for {200}-austenite 0.257 nm for {111}-austenite
Counting times:	between 15 minutes and 4 hours

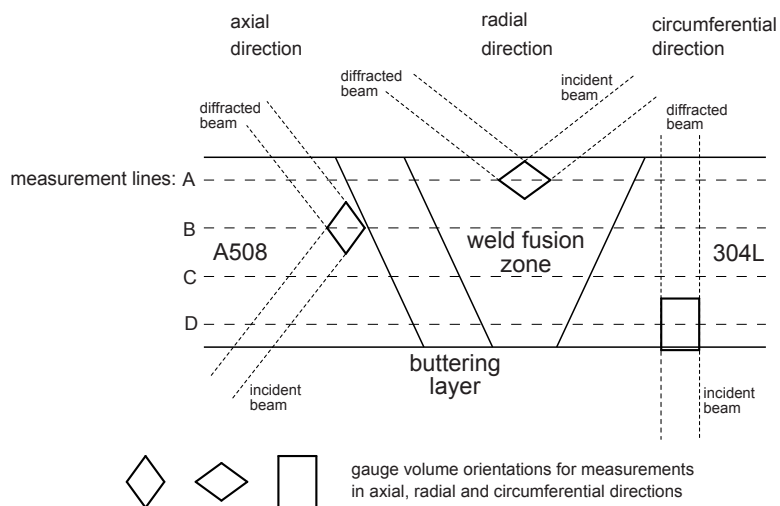


Figure 5.6: *Orientation of the gauge volumes and beam paths for the three measurement directions.*

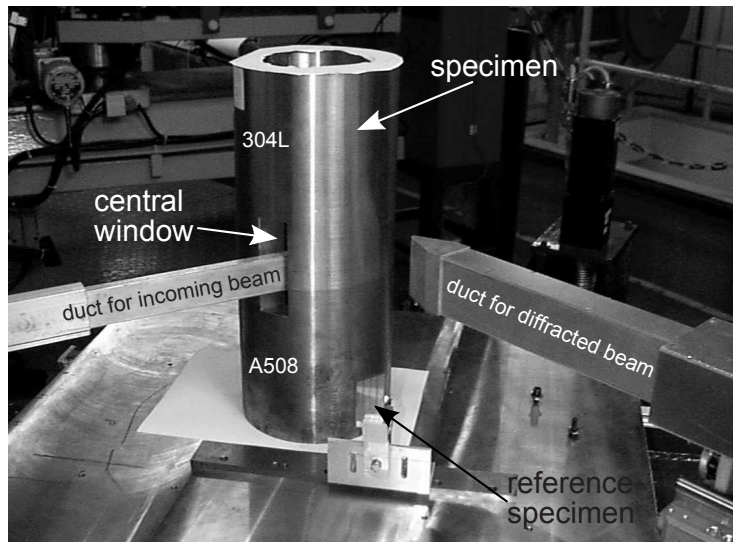


Figure 5.7: *Bi-metallic welded component and reference specimen (at the bottom in front of the component) during neutron diffraction measurements in the circumferential direction; the duct of the incident beam is on the left, the duct of the diffracted beam is on the right.*

5.4 Neutron diffraction results

The results of the neutron diffraction measurements are presented here. Gaussian functions were fitted to the raw data using a commercially available fitting routine (PeakFit [74]). Weighting of the data was applied. The centre of the fitted Gaussian and the reported fitting error form the basis of the strain results and their measurement uncertainty. Strains were calculated by inserting the peak position for the component and the corresponding peak position for the reference test piece into equation (3.3).

5.4.1 Residual strains

Figures 5.8 through 5.10 show the residual strains, and their uncertainties, measured in the bi-metallic welded pipe for the piping circumferential, axial and radial directions as a function of the distance from the weld centre line, respectively.

The left hand sides of the plots correspond to the test locations in the ferritic steel. All circumferential strains measured in ferrite are compressive (Fig. 5.8). A sharp strain gradient marks the transition from the ferrite into the buttering layer. The buttering layer and the weld exhibit high tensile strains, except for the locations near the inner surface where these strains are slightly compressive. Along line A the strain reaches values of about $2000 \mu\text{m}/\text{m}$. In the austenitic base material the tensile

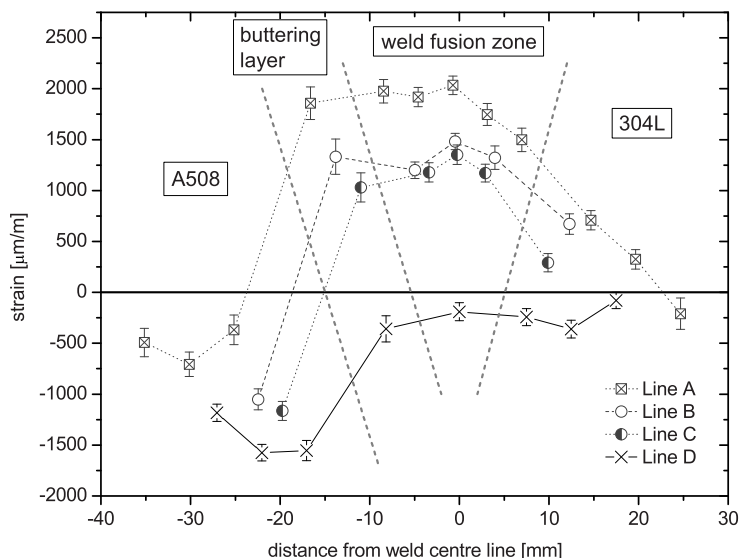


Figure 5.8: Circumferential residual strains measured along the 4 lines shown in Figs. 5.5 and 5.6.

strains remain below $1000 \mu\text{m}/\text{m}$ at all measurement locations, and they decrease even into compression at the test location furthest away from the weld. This considerable difference in maximum strains can be attributed to the difference between the lattice planes used for the measurements. In the buttering layer and the weld, measurements have been taken from the (200) lattice planes, whereas in the austenitic base material the (111) planes have been used. Grains with the (200) orientation in the load direction exhibit a bigger strain in response to a stress than grains oriented in the much stiffer (111) direction.

The strains in the axial and radial directions generally do not reach values as high in tension and compression as observed in the circumferential direction, where $1700 \mu\text{m}/\text{m}$ are found in compression in the ferrite and $2000 \mu\text{m}/\text{m}$ in tension in the fusion zone. In the axial direction (Fig. 5.9) the highest strains are observed in the ferrite near the outer surface of the pipe. The highest compressive strains are in the ferrite and the buttering layer near the inner surface. In general, there is a trend from tension to compression from the outer to the inner surface. In the radial direction (Fig. 5.10), compressive strains of up to $1500 \mu\text{m}/\text{m}$ in the fusion zone are found near the outer surface, and tensile strains of up to $1000 \mu\text{m}/\text{m}$ in the fusion zone near the inner surface. The trend is opposite to the axial direction, from compression near the outer surface to tension near the inner surface.

In general, the strain uncertainties derived from the fitting errors are sufficiently small for observation of the variations in strain and for the identification of regions

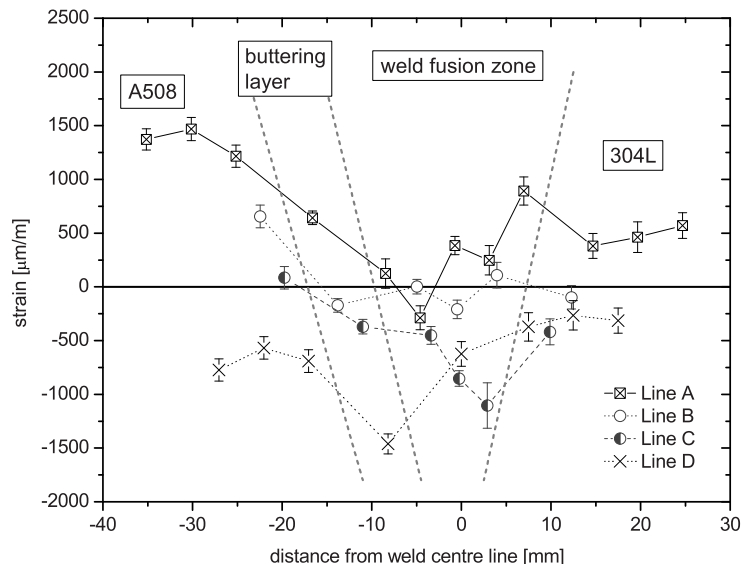


Figure 5.9: Axial residual strains measured along the 4 lines shown in Figs. 5.5 and 5.6.

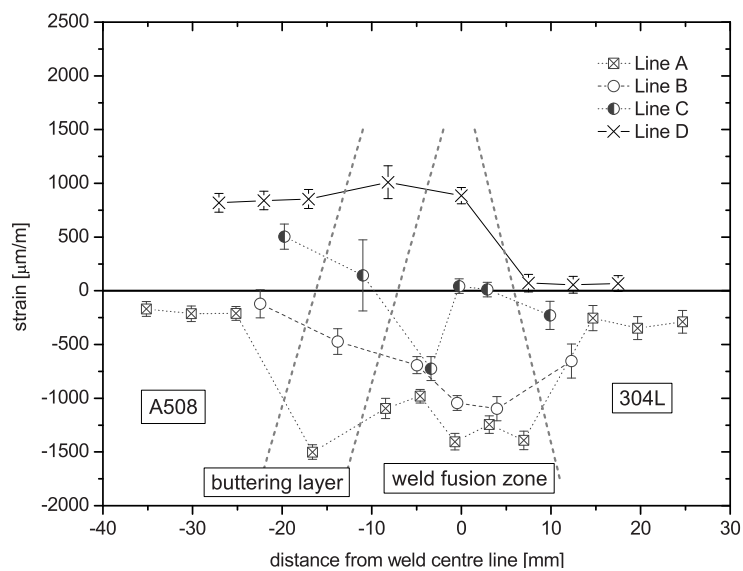


Figure 5.10: Radial residual strains measured along the 4 lines shown in Figs. 5.5 and 5.6.

where the scatter of the strain data goes beyond the effects of measurement statistics. Conversely, for some test locations in the fusion zone, relatively large uncertainties have been obtained, which can be caused by a less favourable texture or the presence of a subset of large grains with an unfavourable orientation at these particular locations.

5.4.2 Residual stresses

Residual stresses were calculated from the measured strains based on equation (3.4). Diffraction elasticity constants were taken from the literature [38]. In this case the values had been calculated based on an approach combining the Reuss and Voigt methods. The applied elasticity constants were:

For the ferritic parent material:

$$E_{110} = 220 \text{ GPa}$$

$$\nu_{110} = 0.28$$

For the buttering layer and weld:

$$E_{200} = 139 \text{ GPa}$$

$$\nu_{200} = 0.35$$

For the austenitic parent material:

$$E_{111} = 247 \text{ GPa}$$

$$\nu_{111} = 0.24$$

The uncertainties presented in the plots were derived from the uncertainties of the strains based on standard error propagation theory [75]. No uncertainty contribution from the elasticity constants was taken into account.

Stresses in the circumferential direction

In the circumferential direction, which corresponds to the welding longitudinal direction in this component, compressive residual stresses are derived for the ferritic side of the joint, while tensile residual stresses dominate the fusion zone and the austenitic steel base material (Fig. 5.11). Only near the inner surface there are small compressive stresses in the fusion zone and in the austenitic steel base material.

The strongest compression of about -400 MPa exists in the ferritic steel near the inner surface of the pipe, while at the outer surface the stress in the ferritic steel is close to zero.

The highest tensile stresses in the fusion zone are found near the outer surface of the sample, reaching about 350 MPa. At the inner surface a small compression of up to -130 MPa has been measured. Tensile stresses decrease when moving from the fusion zone into the austenitic base material. At the test location furthest away from the weld a small compressive stress is found.

The data indicate that there is a discontinuity in the circumferential stress at the ferrite-buttering interface, but the available spatial measurement resolution does not allow for measurements sufficiently close to the interface to confirm or refute this

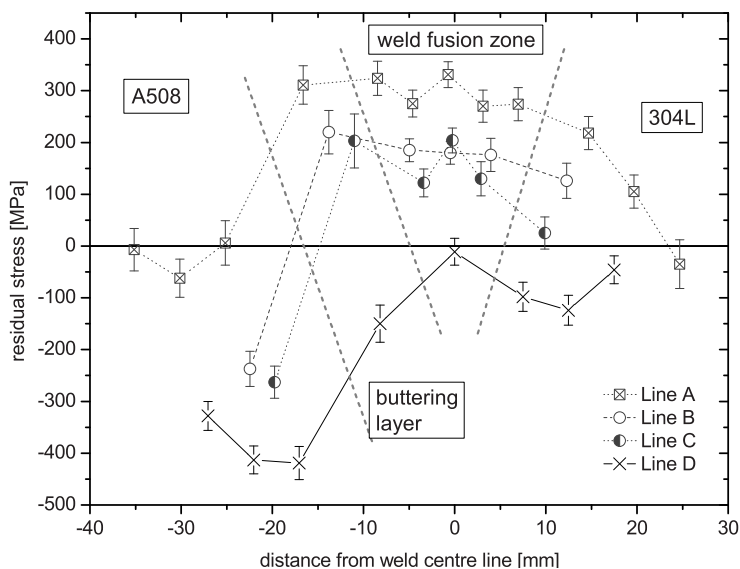


Figure 5.11: Circumferential residual stresses measured along the 4 lines shown Figs. 5.5 and 5.6.

possibility.

Stresses in the piping axial direction

In the piping axial direction tensile stresses are found near the outer surface in all material zones, and near the inner surface compressive stresses have been measured, with the stresses in the centre of the component thickness falling in between (Fig. 5.12). The highest values for tension and compression are found in the ferritic steel with a maximum of ~ 300 MPa in tension and ~ -250 MPa in compression. In the buttering layer, stresses range from $+200$ to -300 MPa, in the fusion zone from $+150$ to -100 MPa and in the austenitic base material from $+200$ to -150 MPa.

Stresses in the piping radial direction

Residual stresses in the radial direction, which corresponds to the through thickness direction of the piping wall, are within a substantially smaller range than the stresses found in the other two directions (Fig. 5.13). Almost all measurements lie within the range ± 100 MPa, with most of the outliers actually located in the fusion zone.

5.4.3 Assessing the results

For an assessment of the quality of the residual stress data obtained in these investigations, it is necessary to establish a set of criteria to test the data against. Such

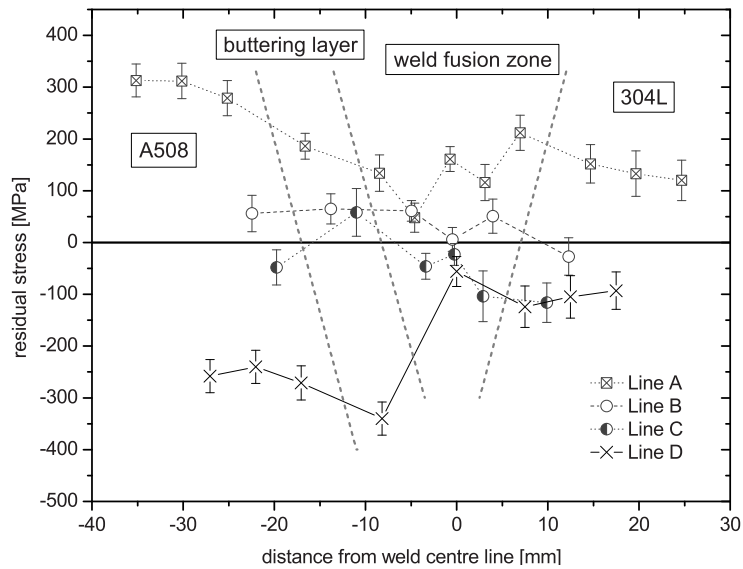


Figure 5.12: Axial residual stresses measured along the 4 lines shown in Figs. 5.5 and 5.6.

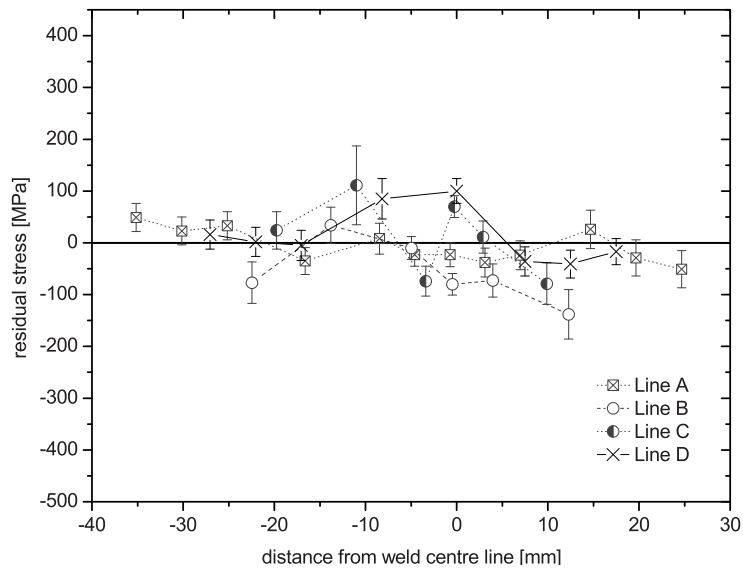


Figure 5.13: Radial residual stresses measured along the 4 lines shown in Figs. 5.5 and 5.6.

Table 5.6: Yield stresses and ultimate tensile strengths of the materials involved [69].

Material	Yield stress [MPa]	Tensile strength ¹ [MPa]
Ferritic steel (SA 508)	584	671
Buttering (309 L)	373	615
Buttering, weld (308L)	364	636
Austenitic steel (304 L)	322	not reported

criteria can be derived from the characteristics of residual stress distributions outlined in section 2.2. The following criteria are applied here:

- Are the residual stress results in compliance with stress balance (eq. 2.4)?
- Do the von Mises stresses derived from the measured residual stresses (eq. 2.6) exceed the applicable yield stress at any of the measurement locations?
- Are the residual stresses in the radial direction close to 0 MPa near the free surfaces; *i.e.*, along lines A and D?

Concerning stress balance, the available measurement data do not facilitate a rigid consistency check. The best possibility for such a check is the axial stresses based on the assumption of an axi-symmetric distribution. However, there are only 4 test locations through the wall thickness, and these are in most cases not at the same axial positions. Furthermore, the impact of the window in the middle of the component on the stress distribution is also not known. Nevertheless, the available data do not reflect an unbalanced situation; *i.e.*, there is no obvious inconsistency.

Table 5.6 lists the yield stresses measured for the constituent materials of this specimen. Additionally, measured figures for the tensile strengths of similar materials used in a follow up project (see also chapter 7) are given.

For all measurement locations in all material zones, the von Mises stresses derived from the measured residual stresses (Figs. 5.11, 5.12 and 5.13) remain well below the corresponding yield stresses. Only for one of the measurement locations, in the buttering layer close to the inner piping surface, the von Mises stress is nearly equal to the applicable yield value (368 MPa vs. 373 MPa). Therefore the residual stresses found are consistent with respect to the yield stresses.

The residual stresses in the radial direction (Fig. 5.13) remain within ± 100 MPa at almost all measurement locations. This range is significantly smaller than the range of -450 MPa to +350 MPa covered by the circumferential and axial stresses. Since the manufacturing process and the geometry of the specimen would not be expected to give rise to the formation of significant radial residual stresses, the observed low stress levels are in line with the expectations.

Along lines A and D, 3 mm from the outer and inner surfaces of the specimen, respectively, the radial residual stresses should be nearly 0 MPa because of the proximity to the free surface. The average value of radial stress for all 20 measurement

¹Quoted figures are from the same report, but measured on similar materials used in a follow-up project (see chapter 7)

positions along lines A and D is 1 MPa, well within the average uncertainty of 29 MPa.

There are 12 measurement positions along lines A and D in base material and the remaining 8 positions lie within weld material. For 7 out of the 12 positions (58%) in the base materials, the measured stresses lie within the magnitude of the corresponding uncertainty based on counting statistics. For all of these 12 positions the measured stresses are within two times the uncertainty. In the weld material the measured residual stresses are within their corresponding uncertainties for 3 out of the 8 measurement positions (37.5%), and within two times the uncertainty for 6 out of 8 (75%). Therefore, statistically the measured radial stresses in the parent materials support the assumption of no radial residual stresses along lines A and D. For the weld material it is found that the scatter of the measured data is larger than expected based on the errors derived from counting statistics.

Because the stress data is derived from strain measurements in three directions the observations made on the radial stress data also reflect the validity of the stress results for the other two directions.

5.5 Comparison to finite element modeling results

Despite the unique features of neutron diffraction as a tool to measure residual stresses as described in chapter 3, the method is still sensitive to effects that are not related to residual stress, such as chemical variations, grain size, texture, material inhomogeneities, *etc.* Some of these features can affect a neutron diffraction measurement and the accuracy of such measurements needs to be assessed carefully.

The results of different and/or complementary methods for residual stress assessment in the weld specimens are included in this section and in sections 6.5 and 7.5. In this way additional information is given concerning to what extent neutron diffraction can be used to validate numerical stress estimations, and to what extent other stress measurement techniques can be used to independently validate such estimations.

For the 25 mm thick bimetallic piping weld no alternative stress measurement methods have been applied. At the time of these investigations, the most appropriate complementary technique, deep hole drilling, was not available and no other technique could provide bulk stress measurements non-destructively.

Three different groups have undertaken a numerical assessment of this weld by FEM. Brief descriptions of these models are given below and their results are compared to the neutron diffraction stress measurements.

At the time of the measurements, between 1998 and 2000, AREVA NP has performed a simplified FEM analysis on this problem in order to generate residual stress input data for a model used to assess the fracture behaviour of this weld [76]. The assumption is made that this simplified model only estimated stresses developing during cooling down after a fictitious post weld heat treatment.

Keppas and Katsareas from the University of Patras [77; 78] have studied the 25 mm bi-metallic weld several years later making use of advances in computation

technology. They have performed a number of parametric studies in order to develop models that are economic in terms of computation time. A number of key parameters of their models are presented here.

The simulations were based on uncoupled thermal and mechanical analyses, whereby the temperature fields derived from the thermal analyses were used as input loads in the subsequent quasi-static mechanical analyses. For the generation of the weld beads the “birth of element” technique was used, whereby beads not yet deposited, were modeled as if not present by reducing the thermal conductivity or mass. Upon deposition, the corresponding elements were activated by setting these properties back to realistic values. A multi-linear kinematic hardening law with a prescribed temperature approach was used to simulate the heat input during welding. The energy input was determined by the size of the bead, its prescribed temperature of 1450 °C and the time over which this temperature was held. Cooling after deposition of the beads was modeled by free convection. Radiation as a cooling mechanism was not taken into account.

The commercially available code ANSYS was used for these assessments. Keppas and Katsareas did not consider creep or phase transformations in their mechanical analyses. In order to achieve acceptable computation times, they calculated 2-dimensional axi-symmetric models, which meant that the entire length of every bead was deposited instantaneously.

Two different models were analyzed. The first model applied a further simplification by lumping the beads in layers of beads. The original buttering was applied in 21 beads, which were represented by three layers. The original weld had 26 passes, which were replaced by 9 layers for this model. In the second, more detailed calculation, the 21 + 26 beads were deposited individually, but still in the form of the 2-dimensional axi-symmetric model.

Figure 5.14 shows the circumferential stresses along line A as measured by neutron diffraction compared to the three numerical assessments presented so far. Although the more detailed analyses of Keppas and Katsareas still contain considerable simplifications, their results along line A are in much better agreement with the measurements than those of the simplified analysis.

The simplified analysis does not provide a sufficiently accurate prediction of the residual stresses. The calculated stresses along line A close to the outer component surface are consistently much lower than the measured stresses; in the fusion zone the calculated axial stresses are even compressive, while the measured stresses are tensile and range between 50 and 200 MPa.

In the more detailed assessment there is almost no under-prediction of stresses. The layered and the bead-by-bead approach render relatively similar results for the circumferential stresses. For the axial direction the two approaches provide stronger differences in their results, see Fig. 5.15. Generally the more detailed bead-by-bead model results are in better agreement with the measurements.

The third group, Gilles and Nouet also from AREVA NP [79], have in principle followed a similar approach in their analysis. However, unlike Keppas and Katsareas they modeled a three dimensional heat source and calibrated the heat input by the

size of a fusion boundary shown in a weld macrograph. Consequently their thermal analysis was 3-dimensional, while the subsequent mechanical analysis was again 2-dimensional. They employed the code SYSWELD, which allowed them to include phase transformations and tempering effects. They also included creep in their calculations. Unlike Keppas and Katsareas they used isotropic hardening. They have also added a post-weld heat treatment to their analysis, which in reality had not taken place for this component.

Figure 5.15 shows the axial stresses along line A derived by all of the above FEM analyses compared to the neutron diffraction measurements. Although the model by Gilles and Nouet includes more detail in the thermal part of the analysis than that by Keppas and Katsareas, it does not agree as well with the measurements. The use of isotropic hardening instead of kinematic hardening is likely to be the most important difference. Isotropic hardening assumes the same yield levels in tension and compression in a cyclic loading test, while upon load reversal; *e.g.*, tension to compression, a lower stress is normally reached in compression than was previously reached in tension. Only kinematic hardening laws can describe this behaviour. Mechanical models of welding using isotropic hardening tend to render conservative stress levels and this is reflected in Fig. 5.15.

The comparisons between the different numerical approaches and the neutron diffraction data lead to the following conclusions:

- The most simplified approach where the mechanical problem was reduced to the effects of cooling from elevated temperatures did not lead to acceptable stress predictions.
- A detailed bead by bead approach to model the weld process itself rendered the best results when a kinematic hardening law was used.
- Using an isotropic hardening law, even when modeling the deposition of the individual beads, produced a conservative prediction of the welding stresses.

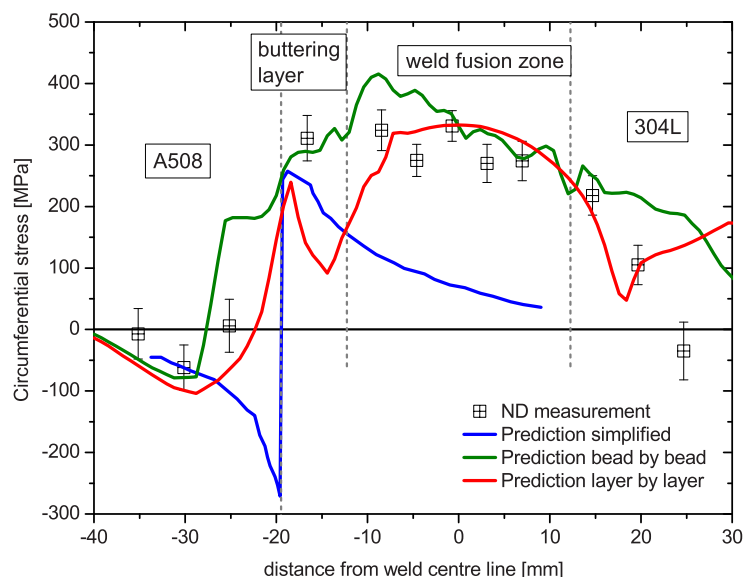


Figure 5.14: Circumferential stresses 3 mm from outer piping surface as measured by neutron diffraction compared to three different FEM approaches: simplified [76], 2-D layering and 2-D bead-by-bead [77; 78].

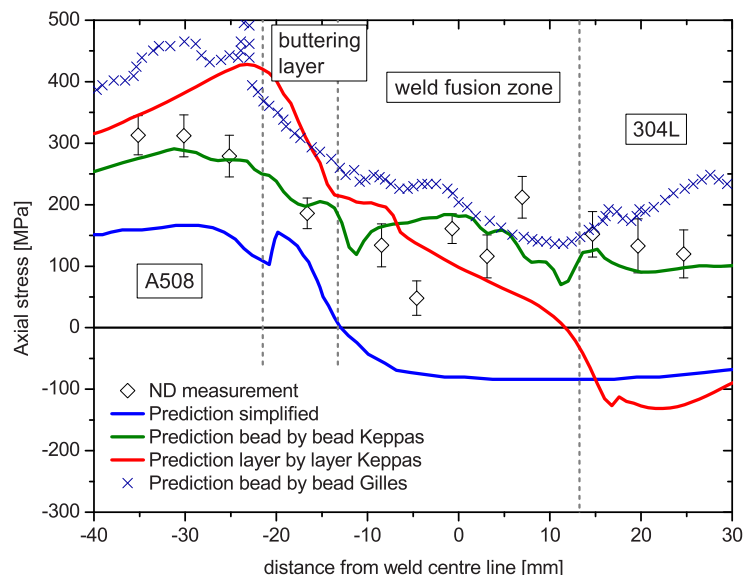


Figure 5.15: Axial stresses 3 mm from outer piping surface as measured by neutron diffraction compared to four different FEM approaches: simplified [76], 2-D layering, 2-D bead-by-bead [77; 78] and 2-D bead-by-bead by Gilles and Nouet [79].

Chapter 6

Residual stresses in a clad component

6.1 Introduction

The term "cladding" in the most general sense means covering of a material with another material exhibiting different properties. Such a cover would normally be applied using physical, chemical or thermal processes, or combinations of these, in such a way that a bonding force holds the materials together. Reasons for the application of a clad layer include:

- Protection of the environment against a potentially harmful substance
- Protection of a component against a potentially aggressive environment
- Adjustment of mechanical properties of a component
- Improvement of wear resistance
- Improvement of the optical appearance of a component
- Reduction of cost, weight, *etc.*

It was already stated in chapter 5, that joining dissimilar materials generally causes problems arising from the mismatch of their thermo-mechanical properties. Among these problems are residual stresses, which can be near the elastic limit of the constituents. They can lead to severe structural integrity problems, when the component is subjected to thermal and/or mechanical loads.

As described in chapter 2, residual stresses add up with mechanical service loads, while their interaction with thermal loads depends on the particular situation. For prediction of the behaviour of a component under service loads, accurate knowledge of the residual stresses present is essential. The generation of this knowledge by numerical or experimental means is not always easily achieved.

This chapter describes residual stress measurements in a ferritic steel block with a welded austenitic stainless steel clad layer. The test component used was repre-

Table 6.1: *Typical chemical composition ranges of 15Kh2MFA steel (in weight-%, rest Fe) [80].*

	C	Mn	Si	P	S	Cr	Ni	Mo	V	Cu	Co	As
15Kh2MFA	0.13 0.18	0.3 0.6	0.17 0.3	≤ 0.025	≤ 0.025	2.5 3.0	≤ 0.4	0.6 0.8	0.25 0.35	≤ 0.15	≤ 0.02	≤ 0.04

representative of the pressure vessel wall of a pressurized water reactor of the Russian VVER-440 type. The aim of the investigations was to quantify the residual stresses in the component and to characterize the residual stress gradient near the material interface where the stresses were expected to change from tensile in the clad layer to compressive in the ferritic steel substrate.

6.2 Description of the component

The component under investigation was a 136 mm thick low alloy steel substrate covered by a 10 mm thick welded stainless steel clad layer consisting of three layers of beads with individual beads estimated to have widths of 10 to 20 mm and heights of about 3.5 mm. The main technical reason for the application of such a clad layer is to protect the low alloy steel against corrosion. Typical applications for this type of cladding are pressure vessels in the chemical and energy sectors.

In these investigations, the component was a rectangular block, 450 mm long, 200 mm wide and 146 mm thick. The welding direction of the clad layer was parallel to the long side of the block. The substrate material was an austenised and tempered Russian steel, grade 15Kh2MFA. The typical chemical composition is given in table 6.1. The clad block had undergone a series of thermal and mechanical loads consistent with the intended application prior to residual stress measurements; however, details about these treatments are not in the public domain.

Ferritic and austenitic steels have different thermo-mechanical properties. In addition, the application of a welded clad layer involves steep temperature gradients in such components during manufacture. For these reasons, residual stresses of considerable magnitude were expected to be present. The general objective of this exercise was to experimentally determine the residual stress distribution.

As the residual stresses were to be measured by three different methods, namely neutron diffraction, deep hole drilling and the ring core method, it was decided to cut the original block into three sections. The section used for neutron diffraction testing was 225 mm long, 200 mm wide and 146 mm thick; *i.e.*, half of the original block. The other half was used for ring core measurements, and finally a block of 110 mm length, 190 mm width and 146 mm thickness was cut from the latter half for the deep hole drilling tests.

6.3 Experimental approach

The measurements were taken along lines running through the thickness of the component, in a direction normal to the nominal substrate-cladding interface. Each measurement line was located at mid-length and mid-width of the corresponding test piece. Particular attention was given to measurement locations near the interface as, based on earlier work [81; 82], it was not obvious which kind of stress distribution was to be expected there. For example, both Bertram [81] and Hofer/Bender [82] found tensile stresses in the clad layer continuing to be tensile in the heat-affected zone of the substrate material before changing to compression deeper inside the substrate. Bertram also investigated stress relieving heat treatments and found that after post weld heat treatment the transition from tension to compression occurred at the weld substrate interface. Hence in the present case, measurement locations as close as possible to the interface location were selected, taking into account the size of the nominal sampling volume, in order to establish the point of transition from tension to compression as accurately as possible.

With respect to the thickness of the specimen, the following aspects were taken into account. The specimen thickness needed to be substantially reduced for neutron diffraction measurements. Unfortunately on the one hand, cutting the specimen would alter the residual stresses to be measured in an unknown way, hence as little material as possible should be removed. On the other hand, only a limited thickness could be accommodated, at least at the test location, so that a high spatial resolution would be achieved in these tests.

The following compromise was adopted. The material thickness at the test location was reduced from 146 mm to 25 mm; *i.e.*, 10 mm cladding plus 15 mm remaining ferritic steel substrate. This was a substantial reduction in thickness, but in this way, the size of the gauge volume could be kept small and measurements relatively close to the interface were feasible. In order to reduce the impact of the cutting, only the material necessary for access of the neutron ducts was removed. Figure 6.1 shows the design of the experiment and the material removal (dashed lines), and Fig. 6.2 shows the machined component at the neutron diffractometer.

With the remaining material thickness of 25 mm it was possible to apply a match-stick shaped gauge volume of $2 \times 2 \times 20 \text{ mm}^3$ for all measurement directions. Such gauge volumes with a vertical dimension significantly larger than the horizontal dimensions, are frequently applied in neutron diffraction stress analysis as a means to enlarge the gauge volume and thus to shorten the measurement times or to facilitate the penetration of thicker specimens. In order to render valid results it is necessary that no significant strain gradients are present along the extended gauge dimension. Here, this approach allowed for measurement locations a little closer than 1 mm to the interface.

Clad layers are fully welded material. In this case the 10 mm layer consisted of 3 layers of individual beads. This material could be expected to exhibit variations in the stress free reference peak position (see also chapter 3). It was chosen to address these by testing specially cut reference specimens from the same component in parallel to

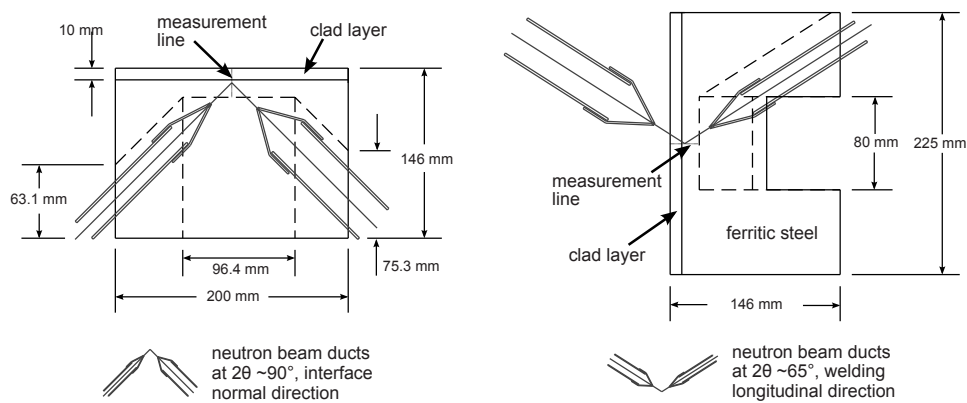


Figure 6.1: Cutting scheme to allow the neutron diffraction measurements on the clad component; left: set-up for interface normal direction, right: set-up for welding longitudinal direction.

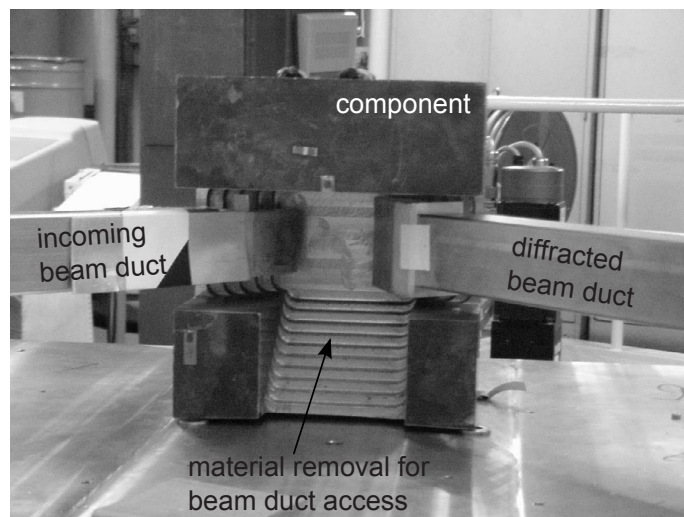


Figure 6.2: The machined clad component at the neutron diffractometer, measurements in the interface normal direction are shown here.

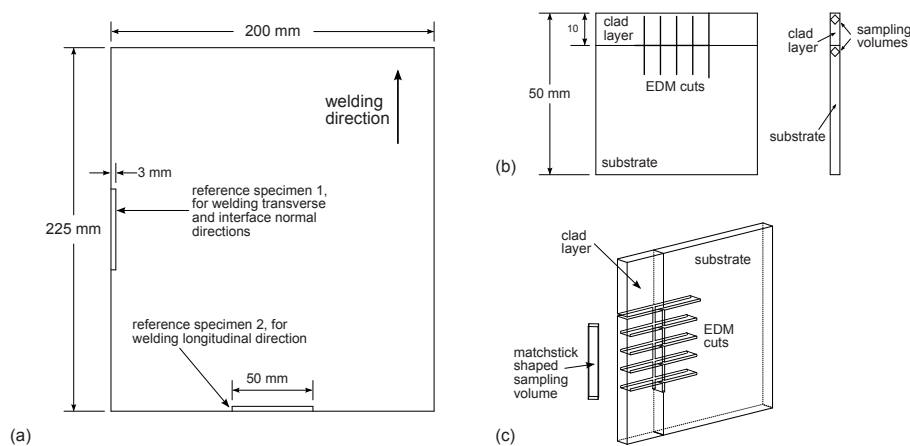


Figure 6.3: Cutting of the specimens for measurement of the reference peak positions in the clad component; a) top view of neutron diffraction component indicating the locations, where reference slices were cut, b) sketch of the system of EDM cuts indicating positions of sampling volumes within the reference specimens, c) isometric view of the reference specimen and the system of EDM cuts, and of the matchstick shaped gauge volume.

the stress measurements.

Variations of the stress free reference lattice spacing in the welded clad layers were measured at two companion specimens cut from the same component. These were prepared in the form of slices, each 3 mm thick. At reference specimen no. 1 the reference peak positions in the welding transverse and interface normal directions were measured. At reference specimen 2 the peak positions for the welding longitudinal direction were measured. In order to mechanically relieve the residual stresses in these specimens a grid of cuts was applied by EDM, such that the maximum length of uncut material was about 5 to 10 mm. It was assumed that no type I residual stresses could be sustained in the cut region of such a specimen. Figure 6.3 illustrates where these specimens have been extracted from the original component, how a grid of EDM cuts has been applied in the region of interest and how the matchstick shaped gauge volume would be positioned inside these reference specimens.

The measurements were performed at the Large Component Neutron Diffraction Facility at beam tube HB4 at the HFR. For each measurement direction the detector position was chosen such that the neutron beam defining masks could be optimally inserted into the excavated specimen. The neutron wavelength was subsequently chosen to render a diffraction peak at the selected detector positions. In the ferritic steel substrate, measurements were obtained from the crystallographic (110) diffraction plane. Because austenitic welds tend to exhibit strong (200) textures, the clad layer was investigated using diffraction from this crystallographic plane. The parameters for these measurements are presented in Table 6.2.

Table 6.2: *Instrument settings for neutron diffraction measurements.*

Nominal gauge volume:		$2 \times 2 \times 20 \text{ mm}^3$
Detector beam opening to test location:		$\sim 35 \text{ mm}$
Lattice plane used in ferrite:		{110}
Lattice plane used in clad layer:		{200}
Testing times:		600 to 8000 s
Material and measurement direction:	Nominal neutron wavelength:	Nominal diffraction angles:
Ferrite weld longitudinal:	0.2304 nm	67.95°
Ferrite weld transverse:	0.2400 nm	71.25°
Ferrite interface normal:	0.2956 nm	91.90°
Cladding weld longitudinal:	0.2000 nm	65.92°
Cladding weld transverse:	0.2300 nm	77.90°
Cladding interface normal:	0.2300 nm	77.90°

Measurements were performed at locations on the line through thickness located at the centre of the specimen as described above. In both substrate and cladding, the distance between test locations was 1 mm for locations away from the interface and 0.5 mm for locations closer than 3 mm to the interface.

Specimen alignment was performed by optical means (theodolite) and by monitoring the intensity of the ferrite diffraction peak when the sampling volume moves across the interface [26].

Individual measurements; *i.e.*, the recording of the diffraction peak for one measurement location in the component lasted from 600 to 8000 seconds, depending on material and neutron path length through the component. Figure 6.4 shows the situation for a measurement in the welding longitudinal direction, while the picture in Fig. 6.2 represents a measurement in the substrate in the interface normal direction.

6.4 Results

6.4.1 Peak positions

For the analysis of the experimental results, Gaussian functions were fitted to the raw data using PeakFit [74], whereby weighting of the data was applied. In accordance with equation (3.3) the fitted peak positions obtained for different test locations in the component, together with the corresponding reference peak positions are necessary for the calculation of strains and stresses (eq. 3.4). The peak positions found for the three measurement directions, for the component itself as well as for the corresponding reference specimen are presented in Figs. 6.5 (a) to (c).

The data are presented as measured peak position versus location of measurement. The location is measured as distance from the clad surface of the component in

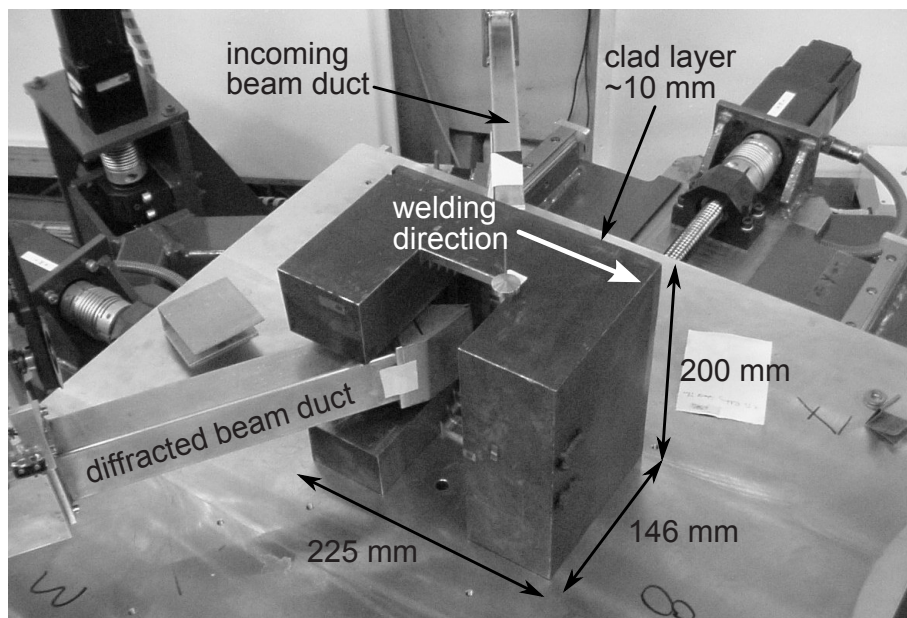


Figure 6.4: *The clad component during measurement in the welding longitudinal direction.*

millimeters. Solid symbols represent measurements from within the clad layer, open symbols show results from the substrate material. A break has been applied to the vertical axes in Figs. 6.5 (a) to (c) in order to present clad layer and substrate data in the same figure.

Several observations can be made based on the peak positions found. Firstly, considerable variations of the reference value are found in the clad layer, while the reference data for the ferritic steel substrate exhibit only small variations from an average taken over the region of measurement. Furthermore, the scatter of the data is generally smaller in the substrate than it is in the clad layer. This is likely to be related to the inhomogeneity of the weld material and to the fact that at many test locations the fusion boundaries between the individual weld beads cut through the sampling volume.

Secondly, the reference values in the clad layer for the welding transverse and interface normal directions, both measured on reference specimen 1, do not differ much. The reference data for the welding longitudinal direction, obtained from specimen no. 2, have been collected at a different detector position; nevertheless they clearly show a different behaviour. Finally, the differences between component and reference are larger for the clad layer than for the substrate.

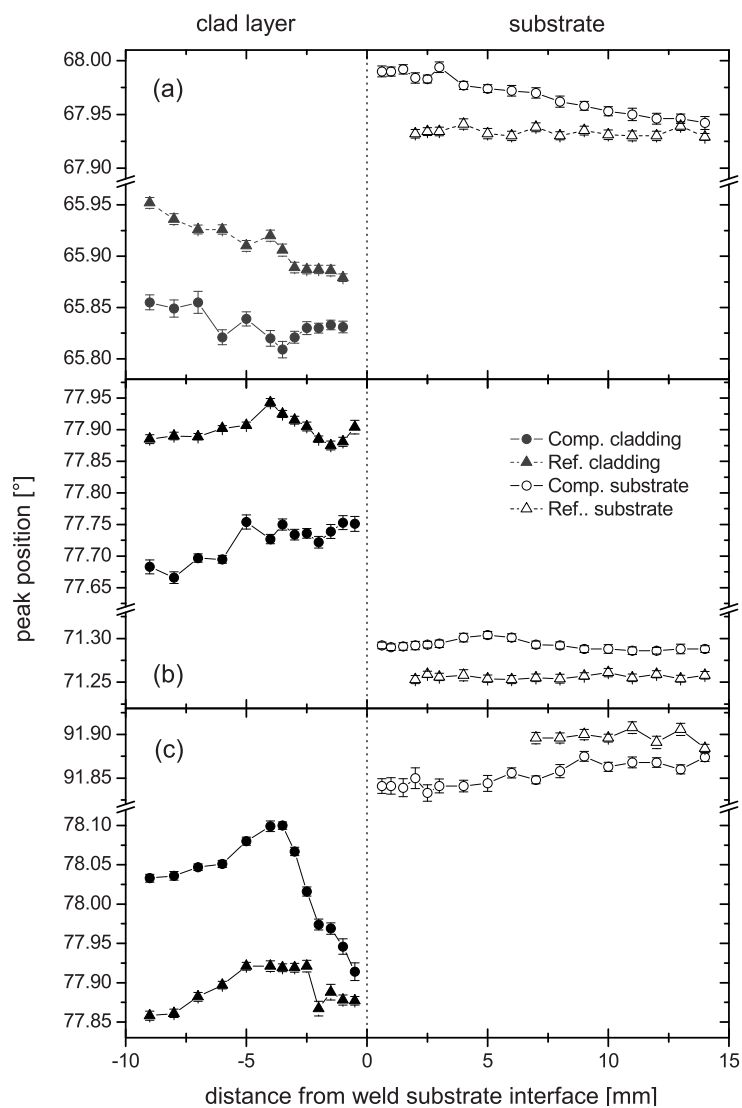


Figure 6.5: Peak positions from the measurements in the welding longitudinal direction (a), the welding transverse direction (b), and the interface normal direction (c).

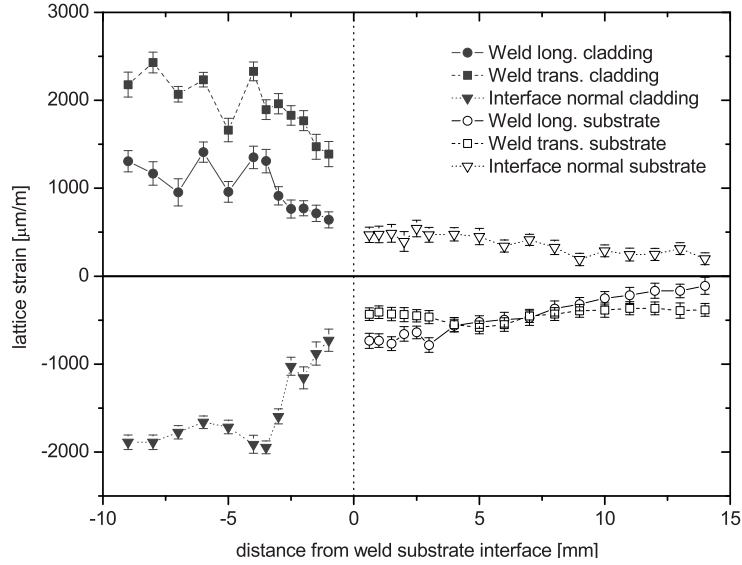


Figure 6.6: Strains derived from the peak positions presented in fig. 6.5.

6.4.2 Residual strains

Based on eq. (3.3), strains were derived from the fitted peak positions. For the clad layer, locally determined reference values were used for every test location, while for the substrate, the average of the measured reference values was applied for all test locations in a given direction. The results are presented in Fig. 6.6.

It can be observed that the clad layer exhibits significantly higher strains than the substrate. One of the reasons for this is that measurements in the clad layer have been obtained from the (200) reflection plane, which in cubic lattices normally is the "softest" crystallographic plane; *i.e.*, it responds with the biggest strain to a given external or internal load. A larger scatter, already observed for the cladding data in the peak positions, is also found in the strains.

6.4.3 Residual stresses

The strain data were finally converted to residual stresses using eq. (3.4). Diffraction elasticity constants for this calculation were taken from the literature [38]. The applied elasticity constants were the same as the ones used for the bi-metallic weld specimen, namely:

For the clad layer:

$$E_{200} = 139 \text{ GPa}$$

$$\nu_{200} = 0.35$$

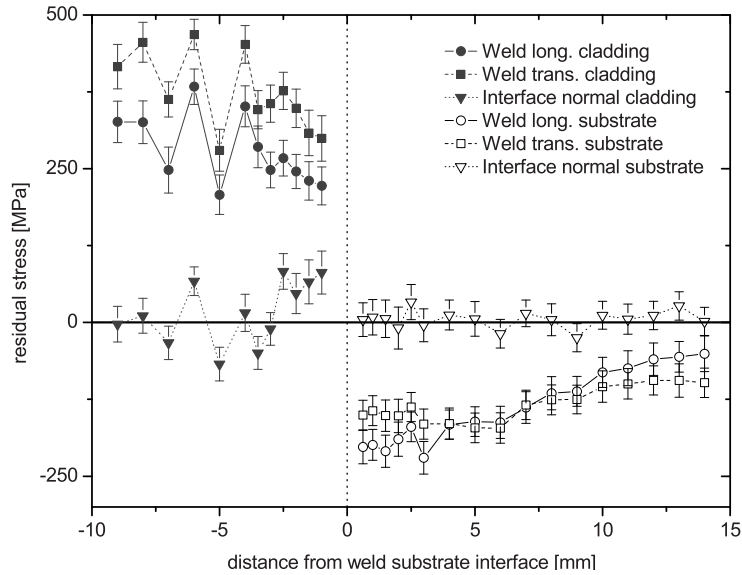


Figure 6.7: Residual stresses measured in the clad component by neutron diffraction.

For the substrate:

$$E_{110} = 220 \text{ GPa}$$

$$\nu_{110} = 0.28$$

The resulting stresses are presented in Fig. 6.7.

The austenitic clad layer exhibits high tensile stresses in the welding longitudinal and transverse directions. Average levels vary between 300 and 400 MPa. Welding transverse stresses were found to be about 50 MPa higher than the welding longitudinal stresses. Compressive stresses in the substrate balance the tension in the clad layer. The compression reaches about -200 MPa near the interface in the welding longitudinal and about -160 MPa in the welding transverse directions. Residual stresses in the interface normal direction vary around 0 MPa, both in the clad layer and in the substrate, with significantly higher scatter in the cladding. This is a strong indicator for consistency of the results. A check of stress balance is not possible in this case as neutron measurements have only been taken along a short line within an irregularly shaped specimen.

In principle, the stress distribution found resembles the case of the 25 mm thick bi-metallic piping weld (chapter 5), as tensile stress is found in the weld material and compressive stress in the ferritic steel. For the weld material, the maximum stress is in a similar range (300 to 400 MPa).

The geometry of the specimen and the geometry of the weld lead to a distribution of the stresses different from the situation in the bi-metallic girth weld specimen. In

the bi-metallic piping joint there are significant stress gradients, both in the parent materials and in the fusion zone.

An additional geometry related difference between the two specimens is that for the clad layer specimen the maximum stress values for the transverse direction, which corresponds to the axial direction in the pipe, are higher than for the welding longitudinal direction (circumferential in the case of the pipe). The main reason for this lies in the different welding and restraint geometries. While the piping girth weld is essentially a weld filling a long groove joining two separated parts, the clad layer is a weld applied over a large surface area of a massive steel block. This steel block restrains the shrinkage of the weld material in both the welding longitudinal and transverse directions in a similar way. Conversely, for the girth weld the parts to be joined do not provide any restraint for the shrinkage in the transverse direction. The stress distribution shows compression near the inner surface, tension near the outer surface, suggesting that the previously deposited inner beads provide a restraint to the shrinkage of the outer beads, deposited later.

Within the limitations of the spatial measurement resolution the neutron data for the clad layer specimen suggest a sharp transition from tension to compression at the interface. It must be noted that tests performed by neutrons closer than ~ 0.7 mm to the interface, with the gauge volume applied here, would be influenced by surface effects [83; 84]. This means that when the sampling volume is not completely filled by the material that is being measured; *e.g.*, because it is cutting across a specimen surface or across a material interface, the measurement geometry is changed. This influences the measurement of the peak position. Experience shows that the effect is non-linear; *i.e.*, small fractions of the sampling volume outside the material do not cause significant changes in the measurements. Fractions in the order of several tens of percent are known to lead to errors in the order of 10^2 $\mu\text{m}/\text{m}$. Therefore no neutron measurements have been obtained from a zone 1 to 1.6 mm wide around the interface. The data that are available show that the transition from tension to compression takes place entirely within this zone.

6.4.4 Consistency assessment of the results

In analogy with the previous chapter, a consistency check is undertaken for the observed residual stress distributions. For the clad layer component this check is limited to the residual stresses found in the interface normal direction. In common with the thin walled piping specimen, these stresses are not expected to deviate strongly from 0 MPa. The criteria stress balance and yield stress limit are not applied. A stress balance check is not possible because the small measurement region cannot represent any full cross section of the component. Yield stress data for comparison with the measurement results have not been made available.

The interface normal residual stresses are indeed not varying strongly from 0 MPa as can be seen in Fig. 6.7. In the substrate material the average value for the stress in this direction is 5 MPa and the average uncertainty is 26 MPa. The standard deviation of the stress values for these data points is 14 MPa.

In the clad layer the scatter of the interface normal stresses is bigger than in the ferritic substrate. Here the average of the residual stresses is 17 MPa, with an average uncertainty of 29 MPa. In this case however, the standard deviation of the stress values is 52 MPa, almost 4 times the value found for the data points in the substrate.

Therefore, in agreement with the expectations, the interface normal residual stresses are close to 0 MPa. The data scatter, expressed in terms of the standard deviation is significantly larger in the clad layer than in the substrate material. This is an indication for less homogeneity and a larger grain size within the welded clad layer material.

6.5 Comparison with other stress measurement techniques and modeling

In this section additional assessments of residual stresses in the clad layer component are described. The methods used for this component are deep hole drilling, the ring core method and numerical modeling. The main purpose of this section is to provide a comparison with the results obtained by neutron diffraction. This comparison provides an additional means for assessing the quality of the neutron data.

It should be noted that, in common with the work presented in section 5.5, the author of this thesis has not been involved in the additional investigations presented here.

6.5.1 Deep hole drilling

The principle of the deep hole drilling technique has already been introduced in section 3.1.1. As stated, the method belongs to the strain relaxation techniques, for which it is necessary to relax the residual stresses in the measurement area by cutting into the material and to record the resulting relaxation strains.

Unlike other related methods, which rely on strain gauges attached to the component surface, deep hole drilling takes strain measurements by means of an airprobe at the depth below the surface, where the stresses are to be measured. Because of this difference, the deep hole drilling technique can be used for residual stress analyses at substantial depths. The technique actually is the deepest penetrating method for residual stress measurements currently in existence (known to the author). However, the method is normally only applied to measure stresses in the in-plane directions; *i.e.*, it is then a 2-dimensional rather than a 3-dimensional technique.

As the original clad component of 450 mm length, 200 mm width and 146 mm thickness was shared for the application of three different measurement techniques, all of which involve a certain amount of cutting in the component, only a small section of the original specimen, 190 × 110 mm wide and 146 mm thick, was available for deep hole drilling measurements.

A reference hole of 3.18 mm diameter was gun drilled through the entire thickness of this section from the centre of the clad surface. The diameter of the reference hole was then measured in several orientations every 0.2 mm along the axis of the hole by means of the airprobe. Next a 10 mm core around the hole was removed from the test piece by EDM, after which the dimensions of the reference hole were re-measured with the airprobe. Based on the change in dimensions and based on the assumption of a plane stress state existing throughout the thickness, residual stresses were derived using bulk material elasticity constants. The chosen values were:

For the clad layer:

$$E = 188 \text{ GPa}$$
$$\nu = 0.3$$

For the substrate:

$$E = 211 \text{ GPa}$$
$$\nu = 0.3$$

Figure 6.8 shows the welding longitudinal and welding transverse stresses derived by the deep hole drilling method. These measurements, like those performed by neutron diffraction, show tensile residual stresses in the clad layer and compressive residual stresses in the ferritic steel substrate near the interface. Beyond ~ 60 mm from the clad layer surface only small stresses have been found in these measurements. Bertram found a distribution of stresses in good agreement with these DHD results [81], but only for a thermally stress relieved component. For as received clad layer components both Bertram and Hofer/Bender [82] observed completely different distributions with high tensile residual stresses of up to 400 MPa in the substrate for the first 20 to 30 mm beneath the interface. This suggests that the component investigated here has been subjected to a stress relieving heat treatment as well.

Figure 6.9 shows a comparison between the neutron diffraction and the deep hole drilling measurements over the 25 mm depth that have been probed by neutrons. A reasonable qualitative agreement has been achieved, but the quantitative agreement is not excellent. This may be explained by the different component geometries tested; *i.e.*, the stress redistribution caused by the substantial material removal in the neutron diffraction specimen and by the width reduction of the deep hole drilling specimen. A remarkable difference between the neutron and deep hole drilling data is the stress gradient across the material interface. Neutron diffraction suggests a steeper gradient than deep hole drilling. It is likely that this difference is caused by the characteristics of the measurement methods, and is not related to the difference in test piece dimension. However, in lieu of acceptable reference stress measurements, there is insufficient data to determine, which method rendered the more realistic stress distribution.

6.5.2 Ring core method

The ring core method is in principle similar to the deep hole drilling technique. The most important difference is that with this method relaxation strains are recorded

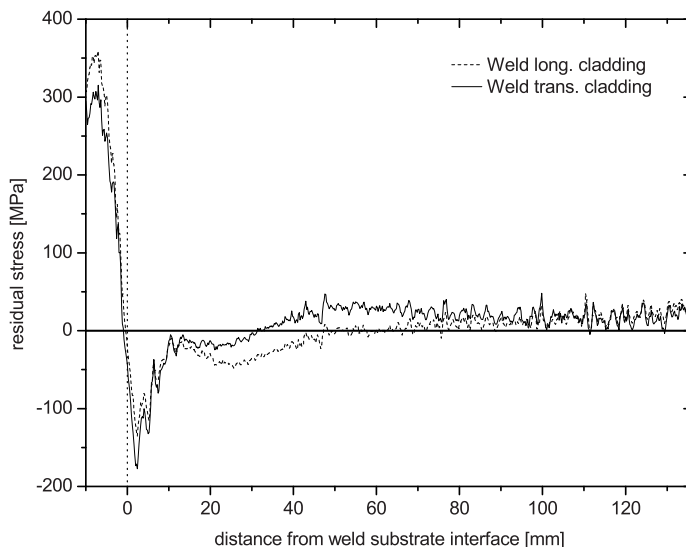


Figure 6.8: Residual stresses measured in the clad component by deep hole drilling - the nominal interface position is indicated by a dotted line (from [85]).

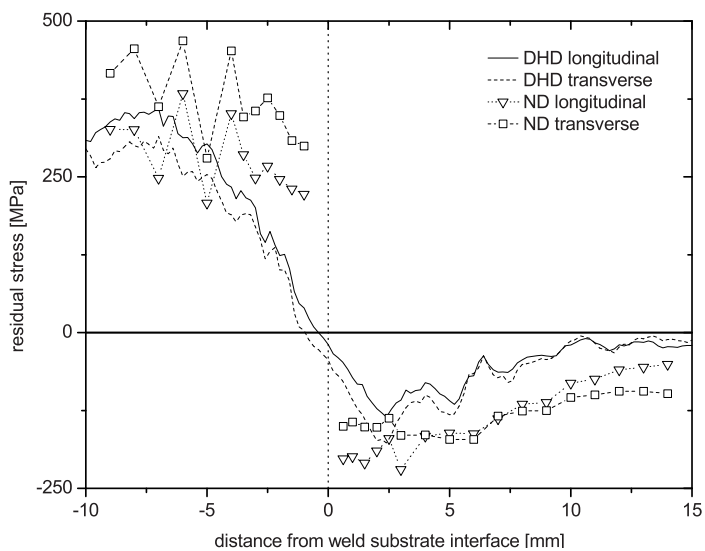


Figure 6.9: Residual stresses measured in the clad component by deep hole drilling (DHD) compared to the residual stresses obtained by neutron diffraction (ND).

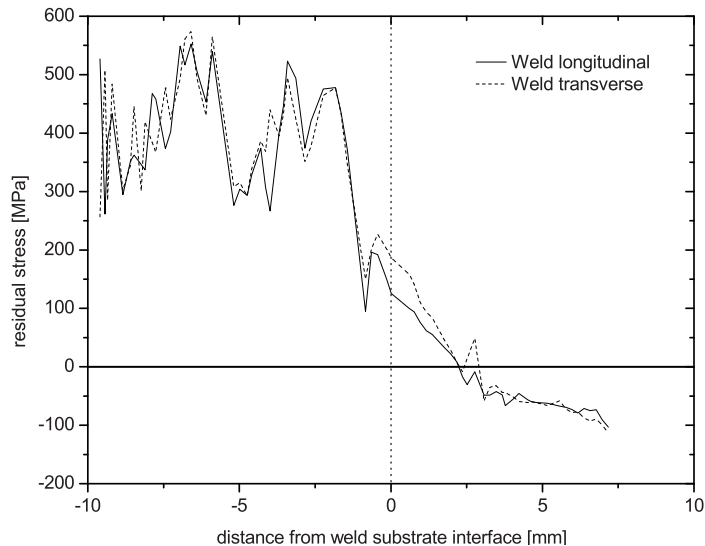


Figure 6.10: Residual stresses measured in the clad component by the ring core method - the nominal interface position is indicated by a dotted line (from [85]).

by means of strain gauges attached to the specimen surface within the perimeter of an annular groove cut by EDM machining. This difference, however, is a strong limitation to the depth below a specimen surface, to which the method can be applied. In this particular case a depth of about 4.5 mm was reached before the material core inside the annular groove was machined away and a new strain gauge rosette was attached to the bottom of the hole. The process was repeated for another ~ 4.5 mm. This was done 4 times whereby a total measurement depth of 17.2 mm was reached; *i.e.*, ~ 7 mm beyond the clad layer substrate interface. Plane stress was assumed in this case, in common with the deep hole drilling technique. Ten measurements per millimeter were taken. The test component for the ring core method was a block, 225×200 mm wide and 146 mm thick, without any material removal on its back. More details can be derived from [85]. Figure 6.10 shows the residual stress distribution measured by the ring core method.

The stress levels obtained from the ring core measurements are comparable to those measured by neutron diffraction; *i.e.*, 300-500 MPa in the clad layer. The ring core method produced data with significant scatter in the weld material, in common with the neutron diffraction results. Unlike neutron diffraction, the ring core method measured similar stress distributions for the welding longitudinal and transverse directions. The neutron diffraction results showed consistently higher stresses for the welding transverse direction. From Fig. 6.11 it is evident that the ring core measurement results in the clad layer are similar to the neutron diffraction results for the

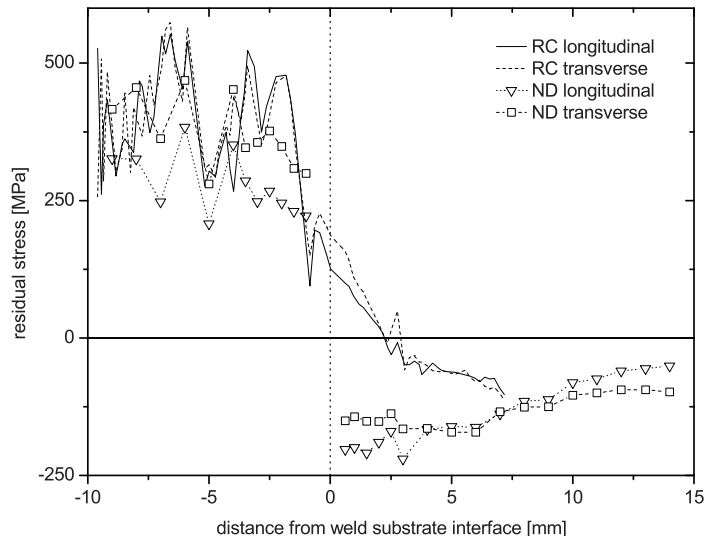


Figure 6.11: Residual stresses measured by the ring core method (RC) [85] compared to the residual stresses obtained by neutron diffraction (ND).

transverse direction. The neutron diffraction longitudinal stresses in the clad layer have a slightly lower average value. Obviously the results do not compare well in the substrate layer.

Like the deep hole drilling technique, the ring core method does not show a steep gradient of stress at the interface. Moreover, the ring core measurements do not place the transition from tension to compression around the interface. At the assumed interface location 10 mm below the clad surface, the ring core measurements still find substantial tensile stresses between 100 and 200 MPa. The transition from tension to compression in this case is measured about 2 to 2.5 mm into the ferritic steel. Deeper into the substrate material compressive stresses of 100 MPa are measured at the end of the measurement range for the ring core measurements. The stress distribution in the substrate therefore does not compare well with the neutron diffraction and deep hole drilling results as in the range of the ring core measurements within the substrate only small compressive stresses are found.

6.5.3 Numerical modeling

A simplified three-dimensional FE-model of the full size component prior to any cutting was prepared using ABAQUS 5.8-14. The model did not address the welding of the clad layer itself, but rather started from a postulated stress relieving temperature of 675 °C. After cooling to room temperature, 3-point bending was simulated,

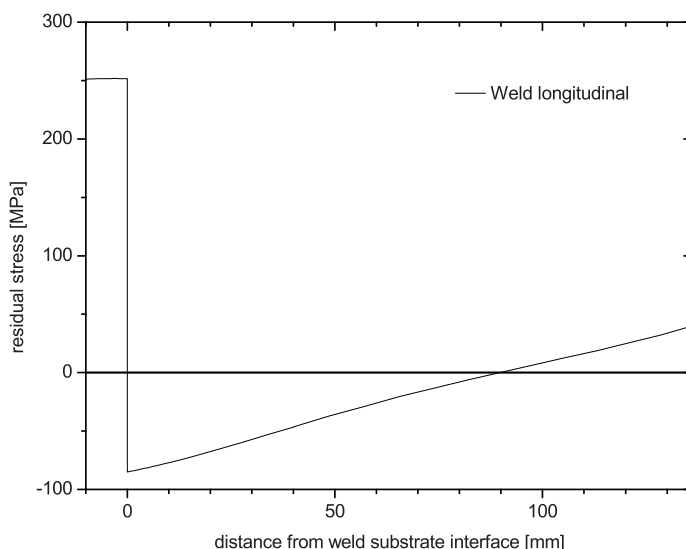


Figure 6.12: Calculated final welding longitudinal stresses across the thickness of the clad component (from [85]).

and subsequently a postulated operation at 246 °C was modeled and finally a heat treatment at 475 °C was included, before returning the component to room temperature [85]. Figure 6.12 presents the final residual stress distribution through the full thickness of the component found by FE modeling taking into account the described mechanical and thermal treatments. A sharp transition from tensile to compressive stresses at the material interface is shown in the figure.

In Fig. 6.13 the predicted residual stresses in the welding longitudinal direction are compared to the experimental results obtained by neutron diffraction, the ring core and deep hole drilling methods. On average, the longitudinal stresses measured by neutron diffraction are only slightly higher than those predicted. The compressive stresses measured by neutron diffraction near the interface are higher than those predicted, but at 14 mm from the interface the neutron diffraction results are at a level similar to that obtained from the calculations. However, no conclusions should be drawn from this similarity because of the different component shapes investigated.

Generally, the stress distribution calculated compares best to the deep hole drilling data. All measurement techniques found higher maximum tensile stresses in the clad layer than were predicted by this model.

Neutron diffraction measured the highest levels of compressive stresses in the ferritic steel substrate. This can be explained by the fact that a substantial amount of material carrying compressive residual stresses has been removed. Stress redistribution may have resulted in higher compressive stresses in the remaining material in order to maintain the stress balance.

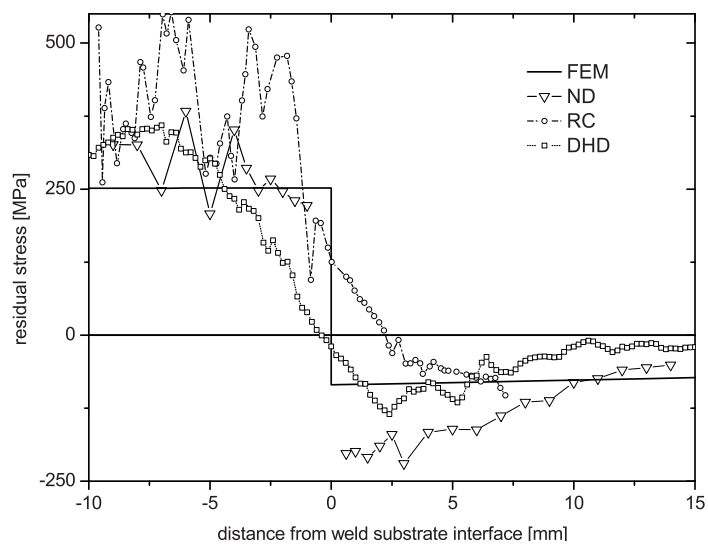


Figure 6.13: *Welding longitudinal residual stresses as calculated for the clad component by finite element modeling (FEM) compared to the corresponding measurements by neutron diffraction (ND), and the ring core (RC) and deep hole drilling (DHD) methods (data from [85]).*

Chapter 7

Residual stresses in a thick dissimilar metal pipe weld

7.1 Introduction

The investigations presented in this chapter concern a component similar to the one discussed in chapter 5. However, in this case the bi-metallic piping component is substantially thicker than the one presented earlier, being a full-scale replica of a 16-inch nozzle in a pressurizer, connected to an austenitic piping section of the same diameter. Not only the dimensions, but also the manufacturing process replicated the situation of a real plant application. [86]

The concerns about the structural integrity of such components are similar to those presented in chapter 5, hence similar objectives were pursued. As these investigations took place several years later, better capacities for numerical analyses; *e.g.*, for residual stress calculations, had become available and have been used. Similar to the 25 mm thick component of chapter 5, on one of the mock-ups an artificial crack was introduced in the heat affected zone in the ferritic part, near the ferrite-buttering interface. The mock-up was subsequently subjected to four-point-bending in order to study the crack opening behaviour.

Residual stresses were investigated by means of neutron diffraction, numerical modeling, surface hole drilling and the crack compliance method.

For the application of neutron diffraction the material thickness was a limiting factor. The component had a wall thickness of 51 mm, which, unlike in the case of the clad layer specimen, could not be reduced prior to measurements. Steel components of such a thickness had not been tested successfully at the time of the present experiment.

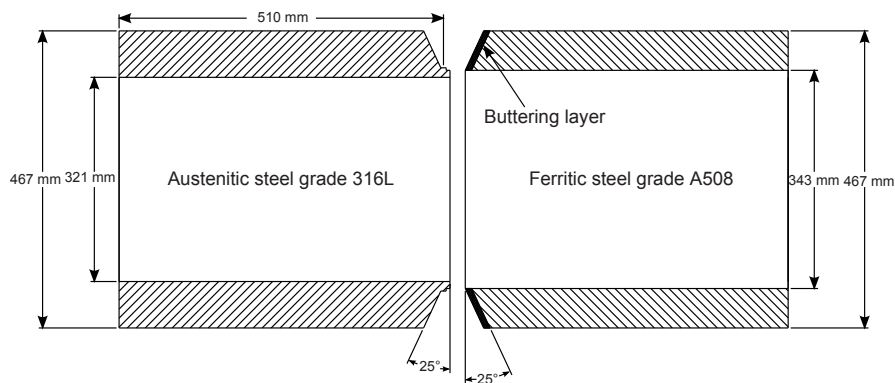


Figure 7.1: Geometry of the austenitic and ferritic pipe sections before welding; the location of the buttering layer on the ferritic section is indicated.

7.2 The component and the reference specimens

7.2.1 The component and its manufacturing

The component was a pipe cut to about 500 mm length, 453 mm outer diameter and 51 mm wall thickness. It was originally fabricated from two parts each of ~ 525 mm length, one of ferritic steel grade A508cl.3 (corresponding classification: 16MND5) and the second one of stainless steel grade 316L. These were joined by means of a circumferential butt weld using stainless steel as a filler material.

The manufacturing process for this component [86] deviated slightly from the one used for the thinner walled pipes. The ferritic pipe section as delivered had an outer diameter of 473.5 mm and an inner diameter of 335 mm, which corresponds to a wall thickness of almost 70 mm. The austenitic section had an outer diameter of 467 mm, an inner diameter of 321 mm, and a wall thickness of 73 mm. Prior to welding they were both machined to an outer diameter of 467 mm. The ferritic section was machined to an inner diameter of 343 mm while the austenitic section was left at 321 mm. Both pipe sections were then prepared for welding by beveling their edges to 25° , similar to the process for the thinner pipe. Figures 7.1 and 7.2 show the edge preparation in more detail.

The first difference compared to the manufacturing process of the thinner tube is the small lip with a land of 8.5 mm width machined on the austenitic steel pipe. The land held the filler material in place during deposition of the first beads of the root of the weld. In addition, the lip prevented relative movements of the pipe sections in the radial direction during welding. The beveling of the half pipe faces generated a V-groove weld preparation, as can be seen in Fig. 7.2.

On the ferritic half pipe a buttering layer was applied consisting of 4 individual weld layers. Before application of the first buttering layer the ferritic pipe was pre-heated to 150°C , which for the ferritic material reduced the risk of hydrogen embrit-

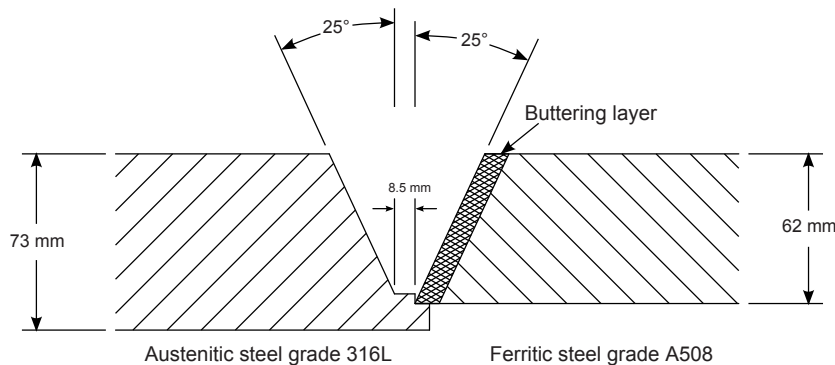


Figure 7.2: Magnified view of the "groove" preparation of the two pipe sections for welding.

Table 7.1: Chemical composition of weld consumables [in wt%].

Consumable	C	Mn	Si	P	S	Cr	Ni	Mo	Co	Nb	N
Soudrocom L309L Q5	0.016	1.21	0.60	0.014	0.011	23.55	12.66	0.04	0.056	0.012	0.052
OK 61.30 N 308L, 4 mm	0.017	1.39	0.58	0.018	0.006	19.87	9.91	0.1	0.03	0.018	0.054
OK 61.30 N 308L, 5 mm	0.019	1.34	0.55	0.015	0.007	19.68	10.0	0.07	0.03	0.018	0.046

Remainder is assumed to be Fe

tlement. The welding electrodes had been subjected to a heat treatment beforehand. Shielded metal arc welding using coated electrodes was applied. The first buttering layer was applied using a 4 mm electrode type Soudrocom 309L Q5. The interpass temperature near the weld was 215 °C. The welding current was maintained between 135 and 145 A. For the second buttering layer a 4 mm electrode type OK 61.30 N was used. The same interpass temperature was maintained and the current was kept at 135 A. For the third and fourth buttering layers again an electrode of type OK 61.30 N was used, but with a diameter of 5 mm. With this larger diameter the welding current was 180 A. For all electrodes an arc voltage of 24 V was set and the electrode travel speed was about 20 cm/min. [86; 69]

In common with the thinner bi-metallic weld, the electrodes used for the first buttering layer had an increased Cr and Ni content in order to reduce the risk of martensite formation at the interface [72]. The chemical compositions of the electrode materials are given in Table 7.1.

After application of the buttering layer a heat treatment was performed, whereby the pipe was kept between 300 °C and 340 °C for 4 hours and 15 minutes.

After the heat treatment, the surface of the buttering layer was ground to facilitate ultrasonic inspection of the weld. No defects were found during this inspection. Finally, the four layer buttering was machined down to about 8 mm.

For butt-welding the two pipes were aligned with respect to one another in ac-

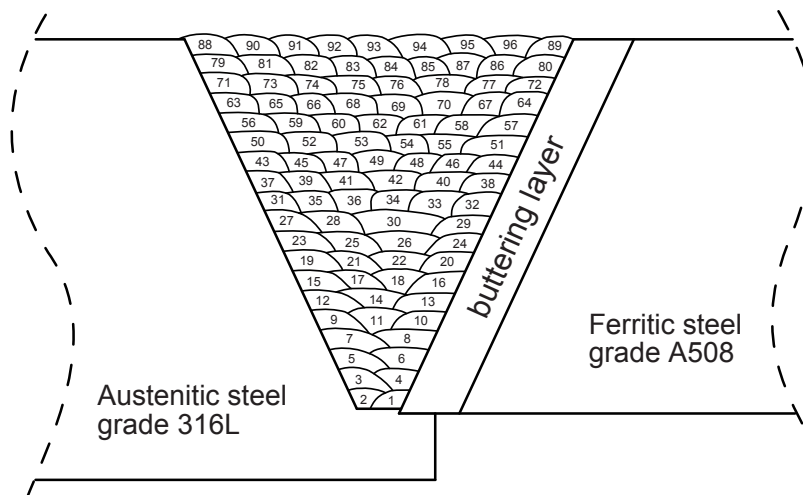


Figure 7.3: Sequence of passes for butt-welding the thick dissimilar metal weld component.

cordance with Figs. 7.1 and 7.2. They were placed on motorized rollers in order to facilitate the circumferential welding process. Shielded metal arc welding was applied here as well. The OK 61.30 N 4 mm and 5 mm electrodes (see Table 7.1) were used as filler material. The welding parameters were almost identical to those used for the buttering; *i.e.*, arc voltage 24 V, travel speed 20 cm/min, current 135 A for the 4 mm and 185 A for the 5 mm electrode. There was no preheating applied and the interpass temperature was kept below 100 °C; 91 weld beads were applied in 18 layers. Figure 7.3 shows a similar bead sequence applied in a second mock-up used for this research programme. This second mock-up was welded with 96 passes in 19 layers. The mock-up with 91 passes was used for neutron diffraction and materials characterizations while the mock-up with 96 passes was used for the large scale fracture test that has been briefly described earlier.

A stress relieving post weld heat treatment was performed, whereby the entire component was kept at 600 °C for more than 6 hours, with controlled heating and cooling rates (max 40 °C/h) above 350 °C. Because of the differences in thermo-mechanical properties of the materials involved, the component could not be expected to be free of stress after this heat treatment.

7.2.2 Preparation of the neutron diffraction specimens

a) The pipe

After heat treatment the pipe was trimmed on a turning lathe to its final inner and outer diameters of 351 mm and 453 mm, respectively. The pipe was now about 1 m long. As this length did not fit on the diffractometer for the neutron measurements, about 250 mm were cut from either end of the pipe so that its final length was 500 mm

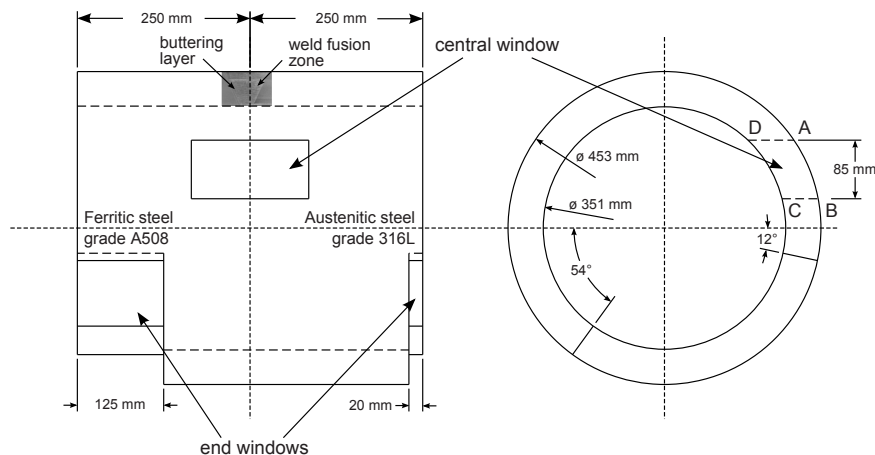


Figure 7.4: *Machining of the component to allow positioning of the neutron ducts for access to the measurement locations.*

with the fusion zone at mid-length.

Ultrasonic, dye-penetrant and X-ray radiographic inspections of the weld and the buttering layer were performed at various stages of the process to insure an acceptable quality of the specimen. Only two minor inclusions were found in this component after welding and machining.

For the neutron diffraction measurements additional material had to be removed, similar to the case of the thin walled pipe. Two sectors of base material were removed from the pipe ends by milling, and afterwards a window was cut in the middle of the pipe by EDM, whereby copper plates were driven through the material. Figure 7.4 shows the parts that have been milled away and the size and location of the central window. Figure 7.5 shows a snapshot of the EDM-process to cut the central window.

For this component an opportunity existed to measure surface strains developing during the cutting process using strain gauges attached to the surface before cutting of the central window. The rationale behind this was that the residual stresses present in the component would be partially relieved through the cutting, and it was not known to what distance from the cut this stress relief would be significant. To this end two-directional strain gauges were fixed on the surface in the weld region at several distances from the envisaged cut. The strain gauges were oriented in the welding longitudinal (piping circumferential) direction and the welding transverse (piping axial) direction. Figure 7.6 shows the surface strains for the strain gauges in the welding longitudinal direction measured during the entire cutting process. Strain gauges have been located within a few centimetres from the cut, at the location of the neutron diffraction measurements, at a distance of about 40 cm from the cut on the outer surface, and in between at about 20 cm distance.

It can be seen that, while the change in strain for the black line indicated a sub-



Figure 7.5: EDM cutting of the central window with the L-shaped electrode after having performed one of the two cuts required for the rectangular window.

stantial relief of stresses near the cut, hardly any change was observed for the locations half way between the cut and the neutron measurement location and at the neutron measurement location. This was an experimental confirmation that the impact of cutting the window on the residual stresses at the measurement location was negligible.

b) The reference specimens

The EDM cutting of the window caused only a minor loss of material and therefore a block of material became available for further analyses. This block is shown in Fig. 7.7. One cut surface of the block has been etched in order to make the fusion zone and the individual weld beads visible.

As in the case of the thinner component, this material was used to provide the reference specimen. A slice of 10 mm thickness oriented in the piping radial direction was cut. Figure 7.8 shows the location of this slice within the block. The remainder of the block material was returned to the manufacturer for materials characterization.

It has been outlined earlier that when measuring welding residual stresses by diffraction methods, potential variations of the stress free reference lattice parameter (or scattering angle) have to be taken into account. In chapters 5 and 6 two different approaches for this have been presented. A combined approach has been chosen for these investigations.

The slice described above was polished and etched to render the fusion zone and the buttering layer visible. The cutting scheme for the reference specimen was established based on the shape of the fusion zone and the thickness of the buttering layer. The

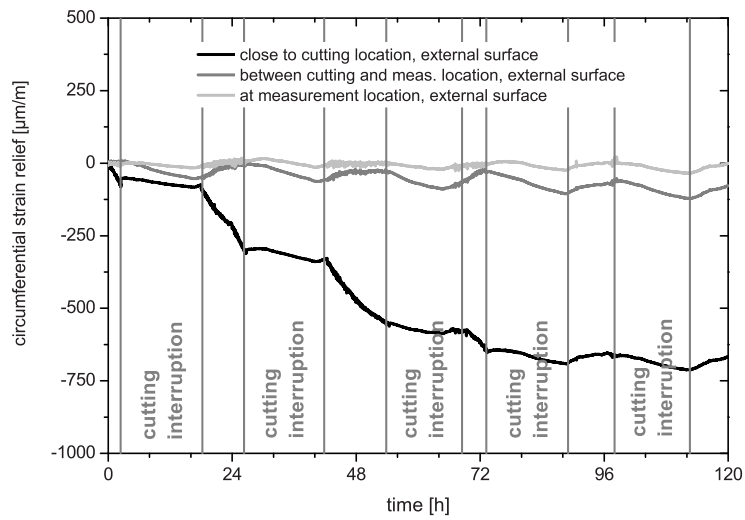


Figure 7.6: Relief of surface strains in the welding longitudinal direction as measured by strain gauges during EDM cutting of the central window (black line: strain gauge next to the cut; dark grey line: strain gauge half way between the cut and the neutron measurement location; light grey line: strain gauge at the neutron measurement location).

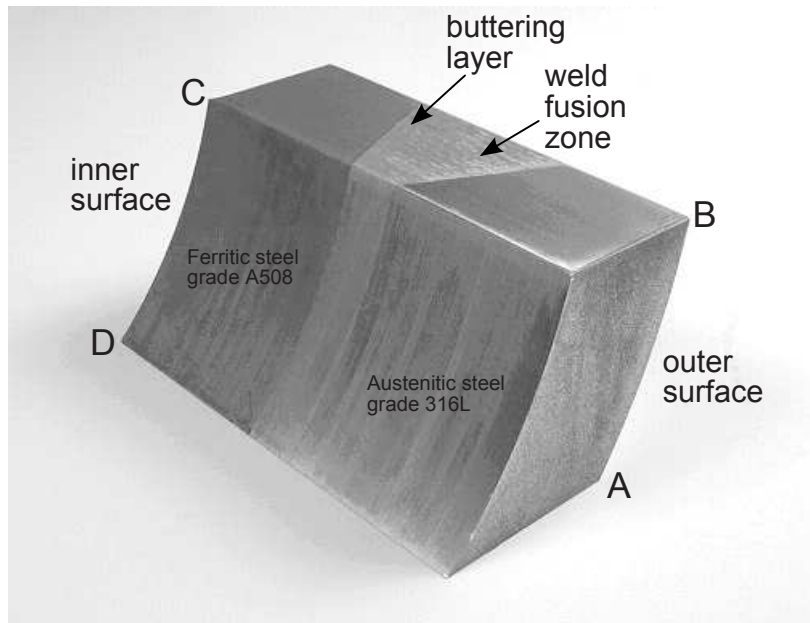


Figure 7.7: Block of material removed from the component to open a window for the neutron diffraction measurements; after etching of the surface the cross section of the fusion zone can be clearly seen.

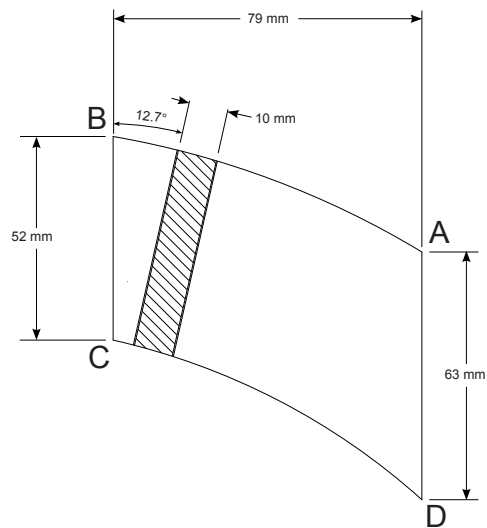


Figure 7.8: Location of the 10 mm thick slice cut by EDM from the steel block in Fig. 7.7.

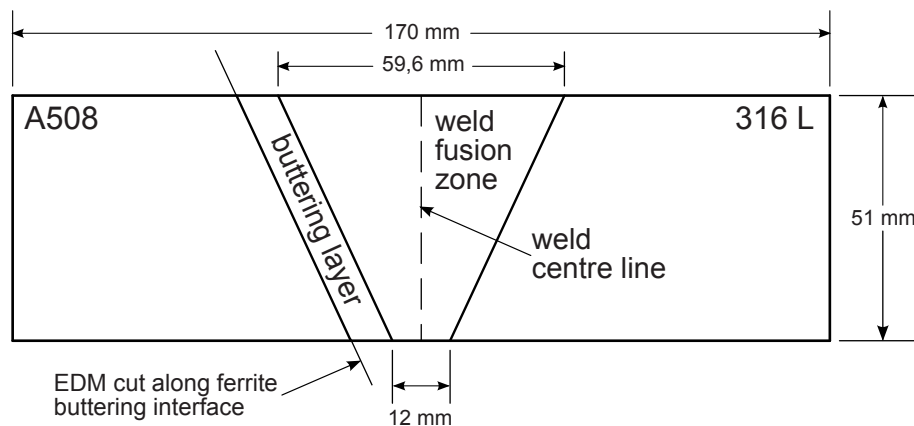


Figure 7.9: Sketch of the material slice with the weld fusion zone, the buttering layer and the location of the first cut.

specimen was then cut into two pieces by wire erosion along the ferrite-buttering interface.

The detailed design of the reference specimens depended on how the actual stress measurements would be executed in terms of the size of sampling volume, the locations of measurement and the number of measurement lines. Based on the thickness of the component, the possible size of a sampling volume and the time available for the tests, it was chosen to distribute the locations of measurements over six lines through the thickness of the piping wall. This was facilitated by five equidistant cuts in the piping axial direction for each reference specimen. A system of cuts was applied in the near-radial direction as well, in order to facilitate stress relief also in the piping axial direction. These cuts were oriented such that a grid reflecting the orientation of the edges of the fusion zone and the buttering layer was generated. The size of the elements corresponded to the size of the sampling volume chosen, and in order to keep the slices in one piece, each coupon remained connected by a material bridge of no more than 1 mm thick.

Figures 7.9 to 7.11 illustrate how the slice has been split into two parts, and how the additional cuts have been applied by means of a programmable EDM machine.

7.3 Neutron diffraction measurements

Within the greater context of this activity, residual stresses were to be determined by measurement and finite element modeling. Neutron diffraction was chosen as the method for measurements, as there was no other technique available that had the potential to do such measurements quasi non-destructively within the bulk of such a component. The Large Component Neutron Diffraction Facility at the HFR was a suitable instrument for these investigations as it could carry and accurately position

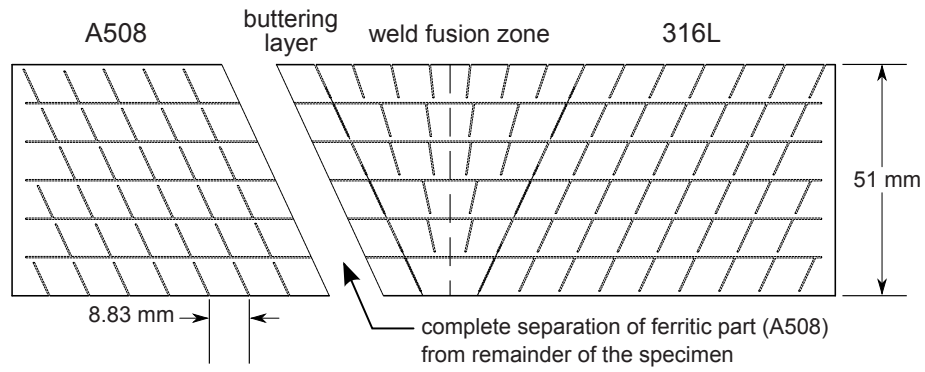


Figure 7.10: Sketch of the reference specimens; the dotted double lines represent the EDM cuts; each coupon represents a test location.

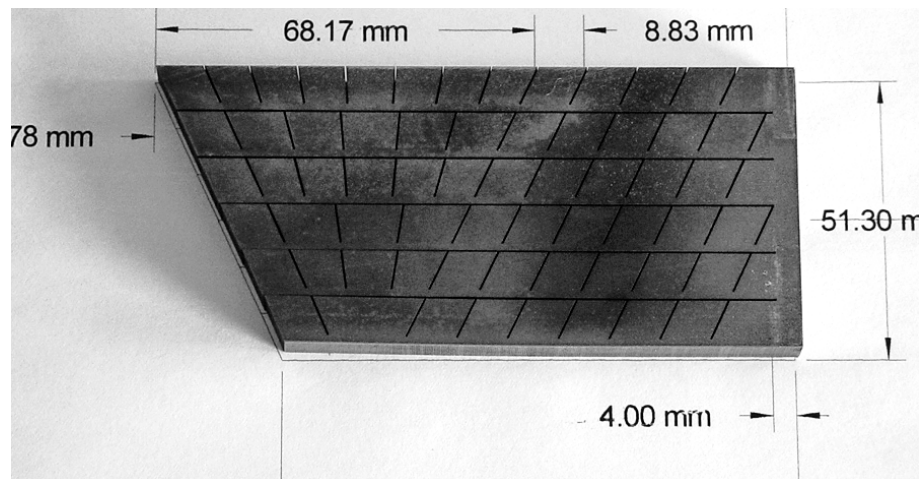


Figure 7.11: Photograph of the reference slice with the buttering layer, the weld fusion zone and the austenitic base material.

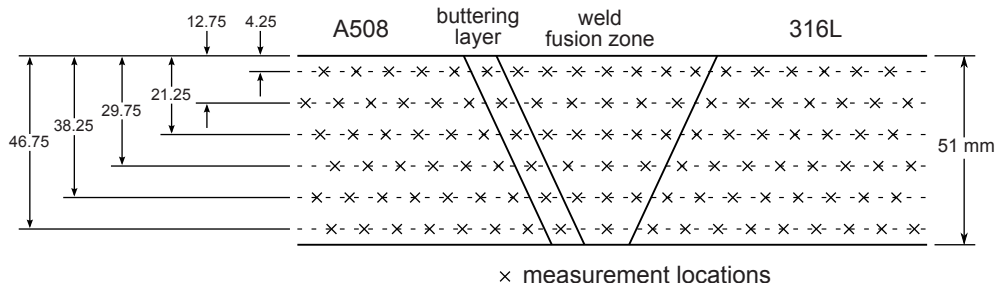


Figure 7.12: Cross sectional drawing of the wall of the thick dissimilar metal weld component in the axial direction of the piping showing the locations of the neutron diffraction measurements in and around the fusion zone.

the component, which was estimated to weigh about 250 kg.

The sampling volume size was determined based on considerations similar to those for the thinner pipe. In this case however because of the pipe thickness a significantly larger sampling volume was needed. Beam defining masks of 8 mm and 6 mm width were placed in the incoming and diffracted beams, respectively. For the piping axial and radial directions an elongated sampling volume was used with a sampling volume height of 25 mm, rendering a sampling volume of $8 \times 6 \times 25 \text{ mm}^3$. This way the spatial resolution was low, but compared to the size of the component this was considered acceptable.

Measurements in the circumferential direction again required a smaller sampling height than those in the axial and radial directions for the same reason as given in chapter 5. A sampling volume of 25 mm height would cut across the interfaces at many test locations. Hence, for this measurement direction a volume of $8 \times 6 \times 10 \text{ mm}^3$ was selected.

As mentioned earlier, it was decided to obtain measurements along lines at six distances from the outer specimen surface, namely 4.25 mm, 12.75 mm, 21.25 mm, 29.75 mm, 38.25 mm and 46.75 mm.

Figure 7.12 shows the distribution of measurement locations over the fusion zone and base materials.

In order to reduce the length of the neutron path through the material as much as possible for every measurement, it was decided to use a low diffraction angle of 65° for the welding longitudinal and welding transverse directions. For the piping radial direction a higher diffraction angle was chosen in order to reduce the path length for these reflection mode measurements as well.

Because of the three different crystallographic reflections used in the measurements, namely the (111)-reflection in the stainless steel base material (316L), the (200)-reflection in the fusion zone incl. the buttering layer (rendering at most measurement locations a strong (200) diffraction peak in the circumferential direction, which corresponds to the welding direction), and the (110)-reflection in the ferritic steel base material (A508), and the two diffraction angles used, it was necessary to

Table 7.2: *Important parameters of neutron diffraction measurements.*

Gauge volume:	$8 \times 6 \times 25 \text{ mm}^3$ (radial and axial) $8 \times 6 \times 10 \text{ mm}^3$ (circumferential)
Detector position:	65° (circumferential and axial) 81.5° (radial)
Crystallographic reflections:	ferrite $\{110\}$ in base material A508 austenite $\{200\}$ in fusion zone and buttering austenite $\{111\}$ in base material 316L
Neutron wavelengths:	0.269 nm for $\{110\}$ -ferrite at 81.5° 0.223 nm for $\{110\}$ -ferrite at 65° 0.234 nm for $\{200\}$ -austenite at 81.5° 0.198 nm for $\{200\}$ -austenite at 65° 0.275 nm for $\{111\}$ -austenite at 81.5° 0.229 nm for $\{111\}$ -austenite at 65°
Counting times:	between ~ 5 minutes and 10 hours

work with 6 different neutron wavelengths. Experience at the Large Component Neutron Diffraction Facility using the adjustable double-monochromator had shown that neutron wavelengths between 0.2 nm and 0.29 nm render an acceptable beam intensity and measurement resolution. This wavelength range covers roughly the range of scattering angles chosen for the measurements in the three material zones. Table 7.2 gives an overview of the measurement parameters chosen for the individual tests.

Measurements were performed in all three directions for most of the test locations shown in Fig. 7.12. Figure 7.13 depicts the sampling volume and neutron beam orientations for measurements in the three different directions. In order to avoid measurement errors due to inaccurate re-setting of the neutron wavelength, it was chosen to obtain measurements from the component and the corresponding reference specimen in the corresponding orientation in direct succession.

Figures 7.14 to 7.16 show the measurement set-ups in the circumferential, welding transverse and piping radial directions. These figures also give an impression of how the sampling volumes are positioned within the material for the three measurement directions.

Figures 7.17 to 7.19 show photographs of the measurement arrangements for this component during measurements in the three directions. Figure 7.17 shows the duct of the incoming beam passing through the window at mid-length of the component.

7.4 Neutron diffraction results

The results of the neutron diffraction measurements are presented here. The raw data were evaluated in the same way as it had been done for the other two components. Strains were calculated by inserting the peak positions for the component and the

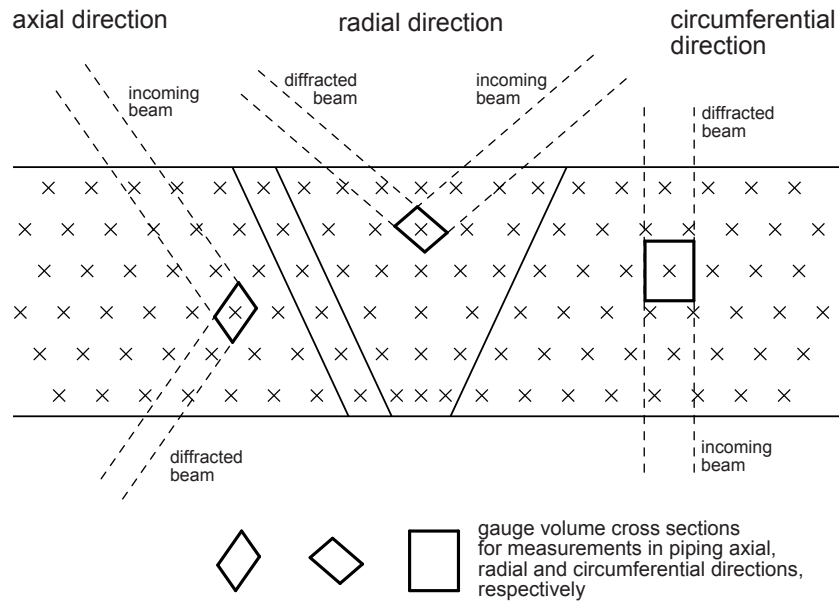


Figure 7.13: Orientation of the gauge volumes and beam paths for the three measurement directions.

reference into equation (3.3).

7.4.1 Residual strains

Figures 7.20 through 7.22 show the residual strains and their uncertainties for the piping circumferential, axial and radial directions, respectively.

As for the thinner walled bi-metallic weld pipe, the left hand sides of the plots correspond to the test locations in the ferritic steel, while the measurements in the stainless steel part of the pipe are shown on the right hand side of the plots.

Again the circumferential strains measured in ferrite are compressive, but in this case a smaller strain gradient was observed between the outer and the inner surface. In common with the thinner bi-metallic welded pipe, a steep gradient from compressive to tensile strains marks the transition from the ferrite into the buttering layer. Close to the outer surface the buttering layer and the weld exhibit tensile strains reaching higher values than observed in the thinner wall case. The strains decrease toward the inner surface, but they stay tensile over the measurement range. In the austenitic pipe smaller tensile strains have been found reaching a maximum level of about $1500 \mu\text{m}/\text{m}$ near the outer surface and near the fusion zone, decreasing to values between 0 and $500 \mu\text{m}/\text{m}$ near the inner surface of the pipe. When moving away from the fusion zone, the strain levels clearly decrease. However, the measurements did not extend far enough away from the fusion zone in order to see whether the strains actually

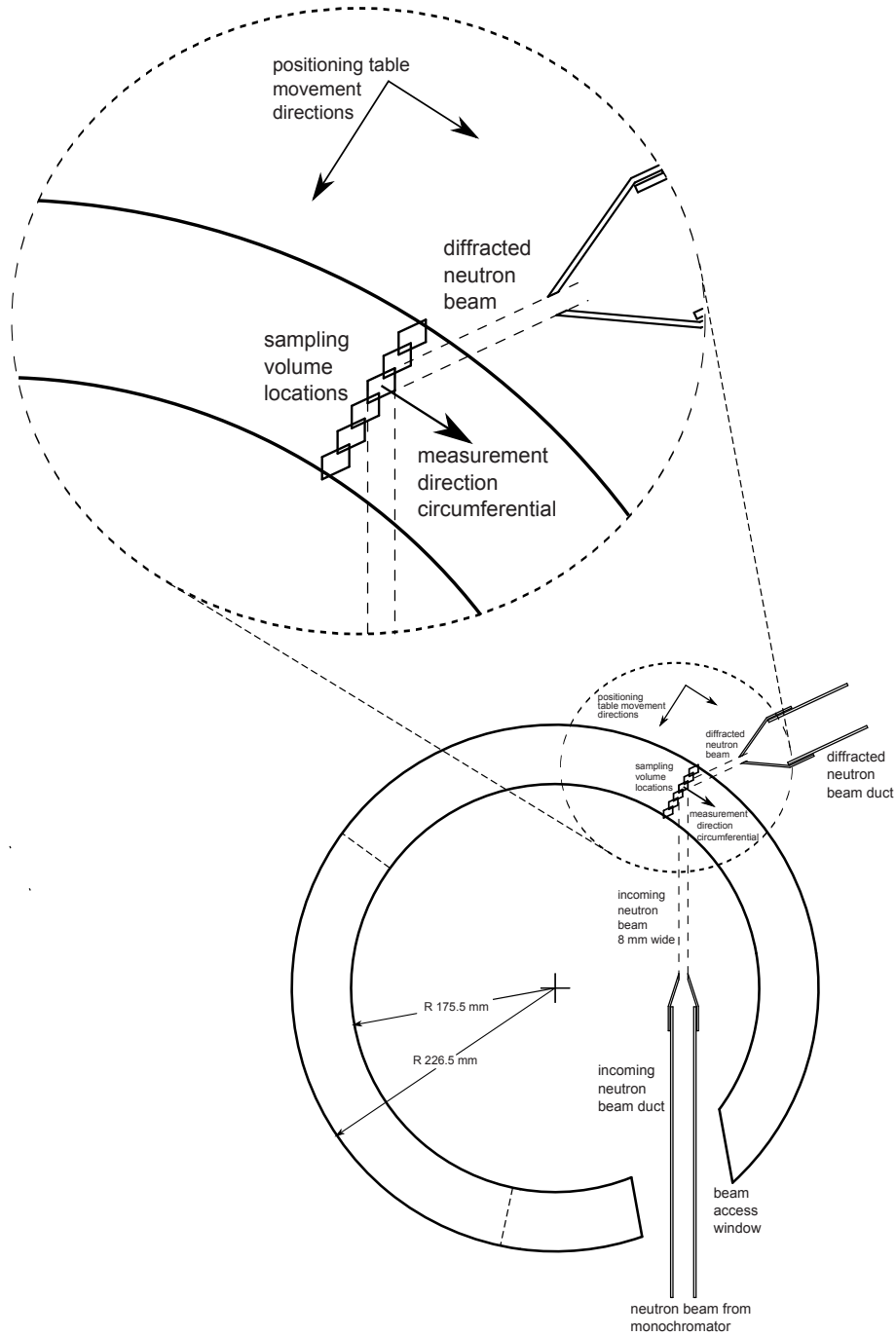


Figure 7.14: Set-up for the measurements in the piping circumferential direction; diffraction angle $2\theta = 65^\circ$, sampling volume $8 \times 6 \times 10\ \text{mm}^3$.

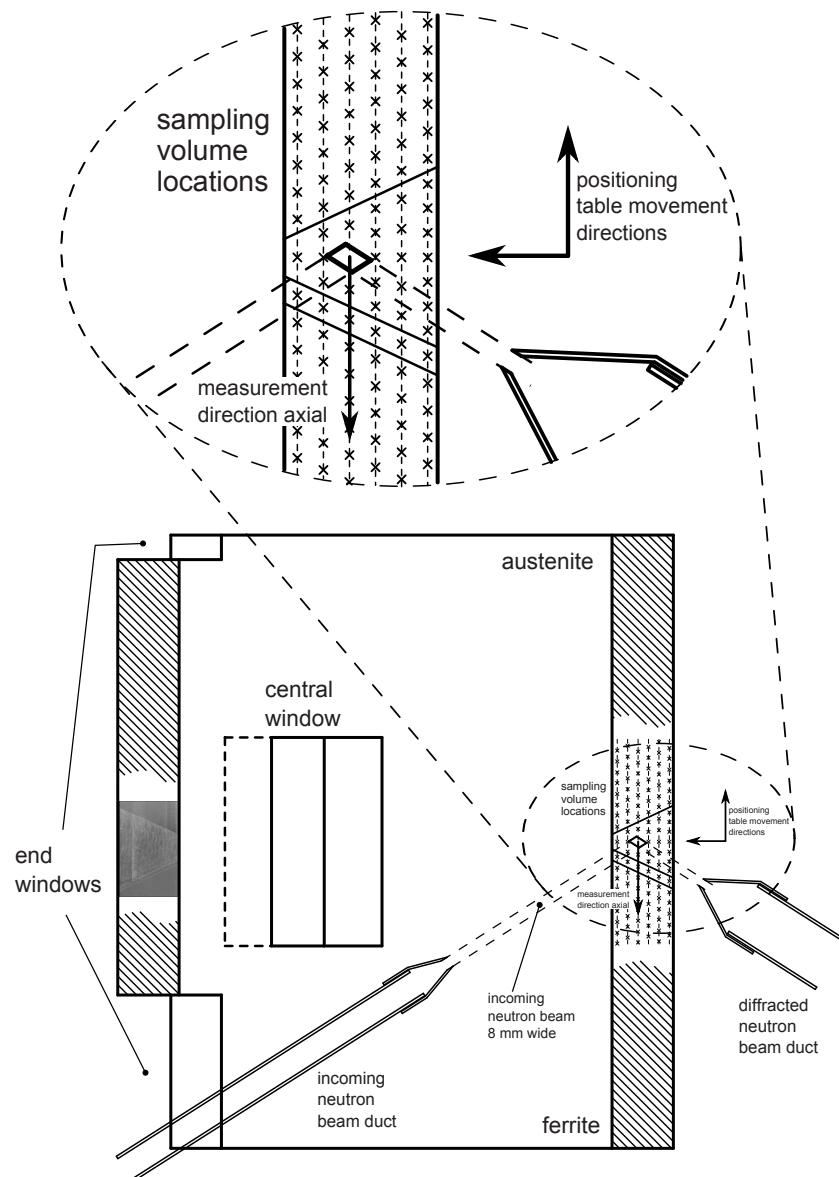


Figure 7.15: Set-up for the measurements in the piping axial direction; diffraction angle $2\theta = 65^\circ$, sampling volume $8 \times 6 \times 25 \text{ mm}^3$.

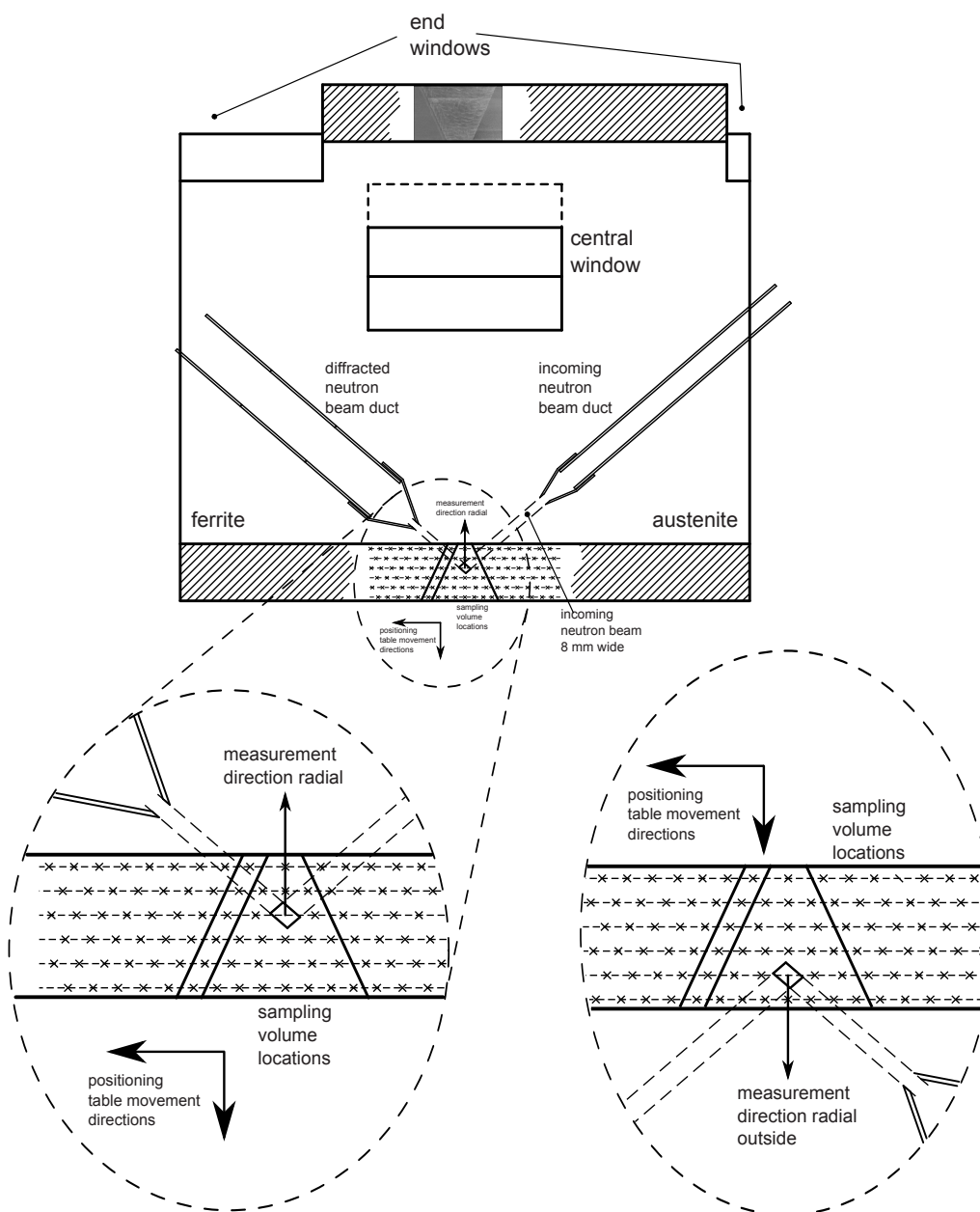


Figure 7.16: Set-up for the measurements in the piping radial direction; diffraction angle $2\theta = 81.5^\circ$, sampling volume $8 \times 6 \times 25 \text{ mm}^3$.

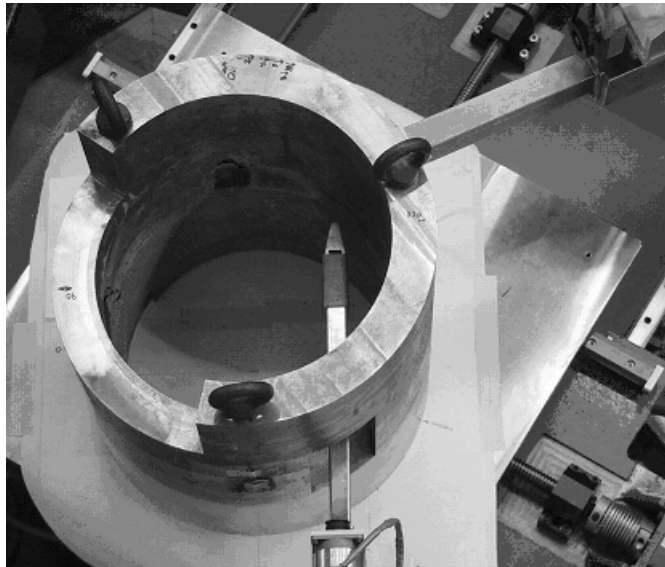


Figure 7.17: Dissimilar metal weld component with 51 mm wall thickness during the neutron diffraction measurements in the circumferential direction. Cf. Fig. 7.14.

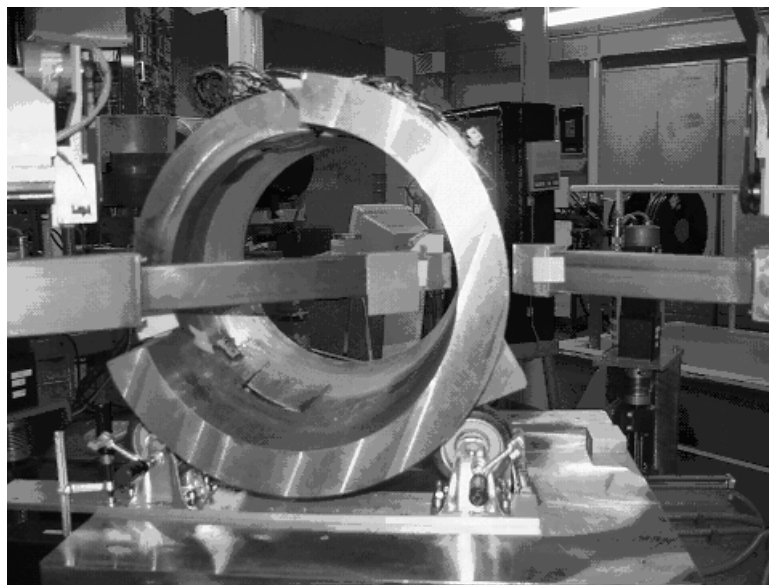


Figure 7.18: Dissimilar metal weld component during the neutron diffraction measurements in the piping axial direction. Cf. Fig. 7.15.

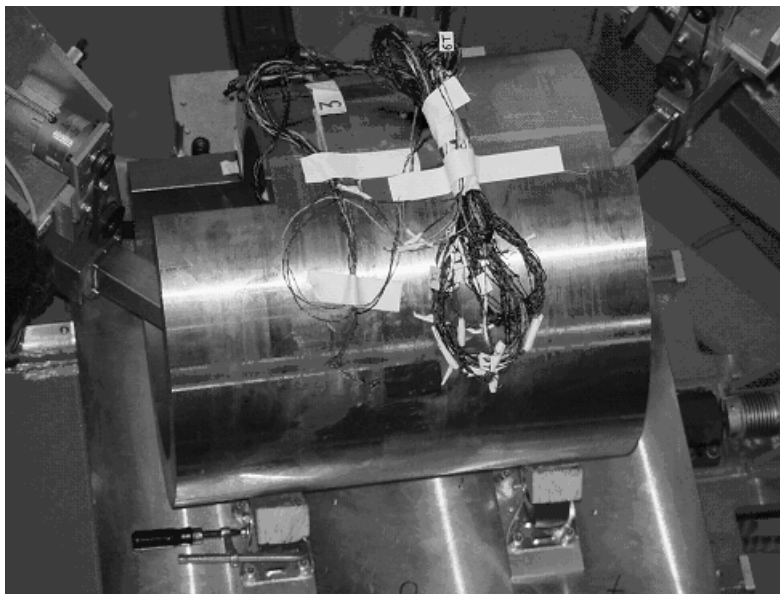


Figure 7.19: *Dissimilar metal weld component during the neutron diffraction measurements in the piping radial direction: measurements on the inner wall; the duct of the incident beam is shown on the right, the duct of the diffracted beam on the left; the cables that can be seen are attached to the strain gauges that were used to measure the relaxation strains during the cutting of the window. Cf. Fig. 7.16.*

become compressive in the far field.

The strain levels observed in the axial and radial directions, Figs. 7.21 and 7.22, are somewhat lower than those found in the circumferential direction. Most of the results do not exceed $1000 \mu\text{m}/\text{m}$ in tension or compression. In the axial direction, mainly tensile strains have been measured in the ferrite, in most cases not exceeding $500 \mu\text{m}/\text{m}$. Closer to the interface with the buttering layer, small compressive strains were found. The uncertainty levels are relatively high because of the component wall thickness. In the fusion zone at some locations measurements in the axial direction were not possible, because of an insufficient diffraction intensity obtained from the (200)-lattice plane. At the remaining locations the data exhibit a significant amount of scatter, sometimes large uncertainties, and no clear trend from the outer to the inner surface can be observed.

Relatively small axial strains were found in the austenitic steel base material. The scatter of these data is much smaller than that observed in the fusion zone and the error levels are reasonable. However, nearly all measurement locations rendered tensile strain values in the axial direction, while tensile strains would be expected near the outer surface and compressive strains near the inner surface.

The strain distributions in the radial direction are similarly confusing. In the base materials on both sides of the fusion zone small strains, both tensile as well as compressive, were measured. In the fusion zone, however the data again exhibit significant scatter. Also here some measurements are missing because the intensity at these locations did not suffice to obtain a useful measurement. One can also see some large error bars.

The difference in the accuracy of the fusion zone measurements between the circumferential and the other two directions is surprising. In the circumferential direction, the sampling volume used was 2.5 times smaller. The more pronounced (200) texture in this direction, corresponding to the welding direction, has apparently over-compensated the smaller sampling volume.

The absence of some data points in the axial and radial directions indicates that at those locations in these directions the population of contributing grains in the sampling volume is low; *i.e.*, the (200)-orientation of grains is less favoured in these directions.

In most of the measurements in the buttering layer relatively strong diffraction peaks have been observed. Figure 7.23 shows the strains in the circumferential direction measured in the thick piping component as compared to those found in the thin walled bi-metallic weld. In order to make the data comparable the positions of the measurement through the thickness have been normalized with respect to the wall thickness. It can be seen that both measurements exhibit similar trends in the strain distribution. However, in the thick walled component significantly higher strains have been measured.

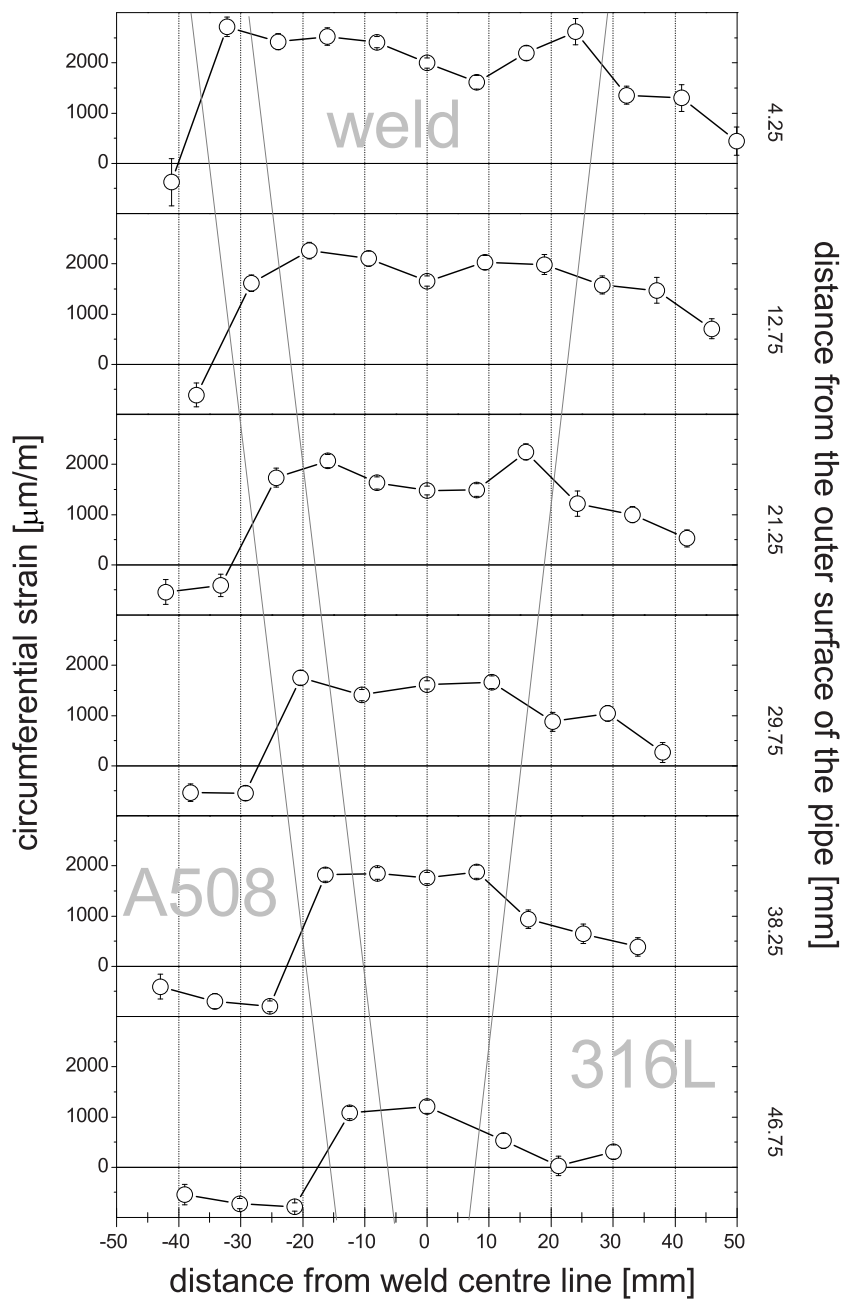


Figure 7.20: Circumferential strains at six different depths below the outer surface (cf. Fig. 7.12) in the thick bimetallic piping weld.

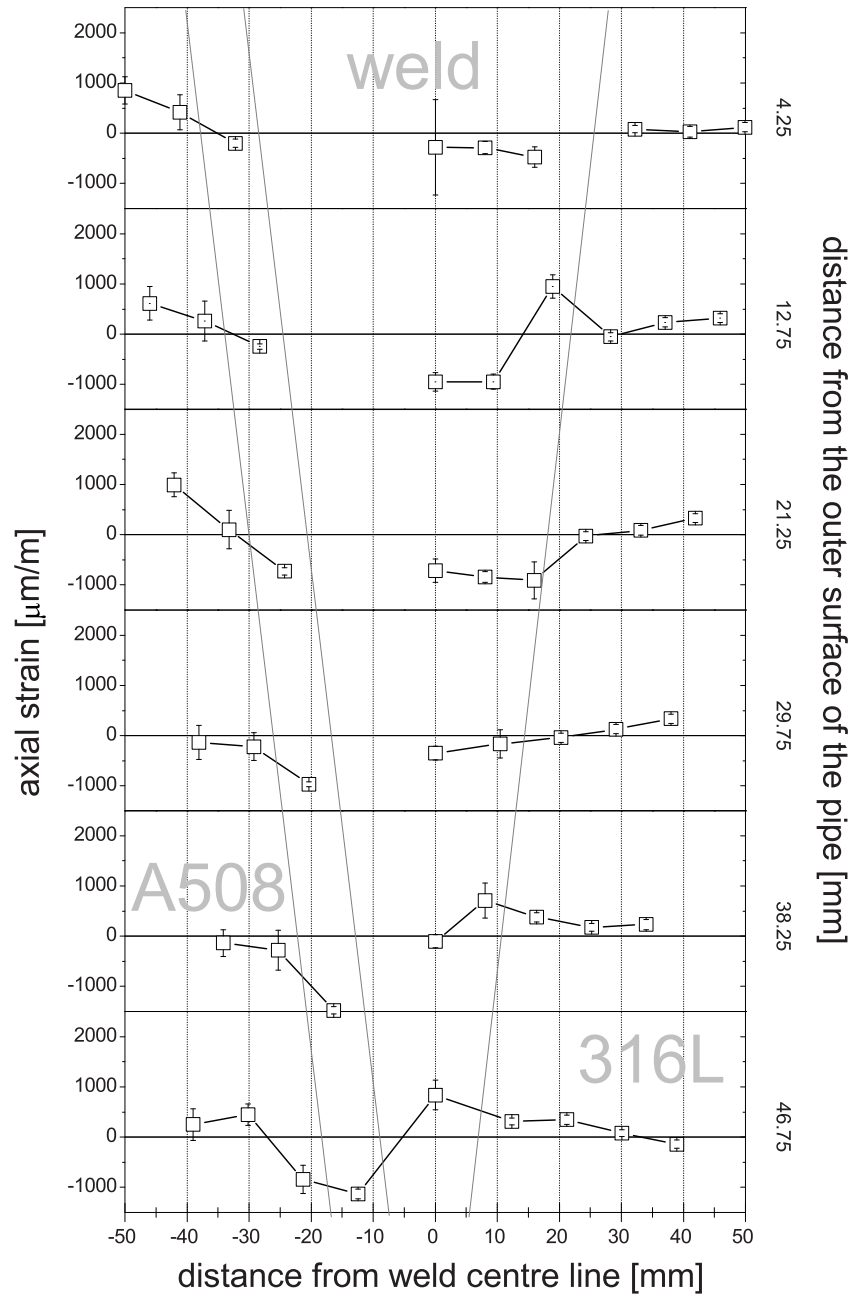


Figure 7.21: Axial strains at six different depths below the outer surface (cf. Fig. 7.12) in the thick bimetallic piping weld.

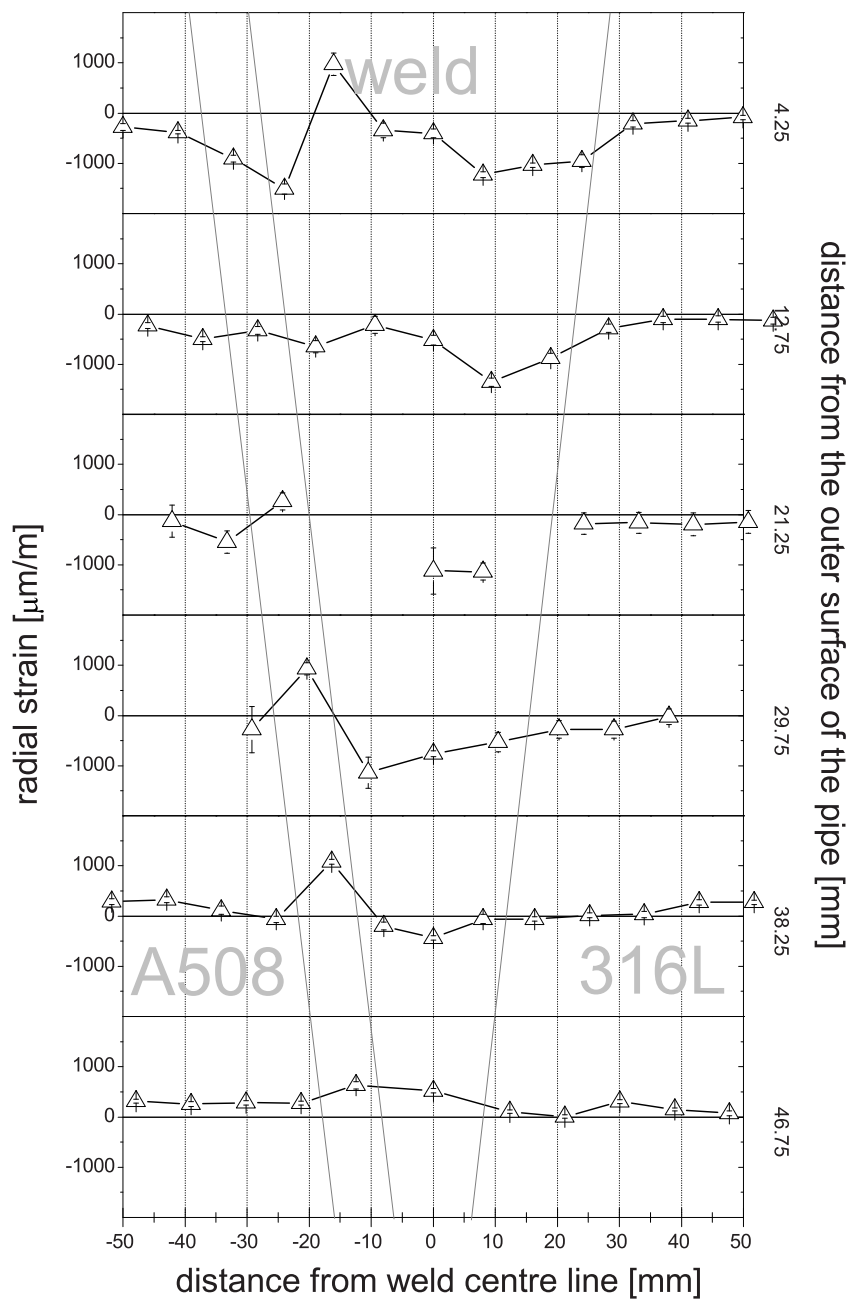


Figure 7.22: Radial strains at six different depths below the outer surface (cf. Fig. 7.12) in the thick bimetallic piping weld.

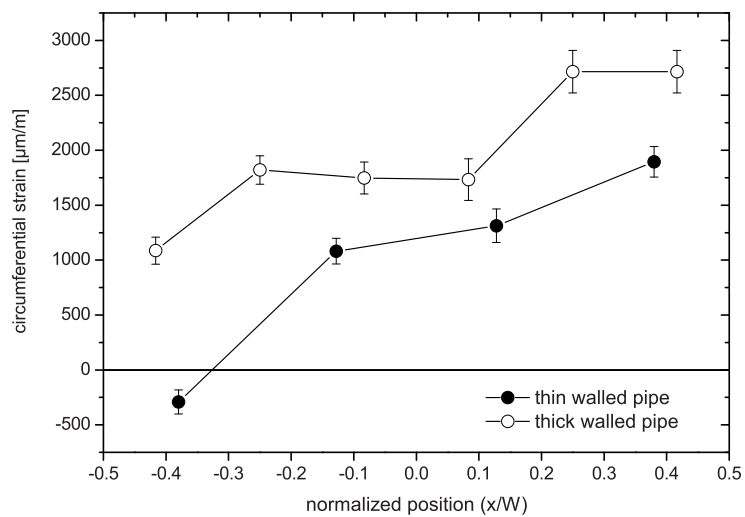


Figure 7.23: Circumferential residual strain comparison for the measurements in the buttering layer for the 25 mm dissimilar metal weld pipe (solid symbols) and the 51 mm component (open symbols); for comparability the through thickness position has been normalized, component outer surfaces on the right, inner surfaces on the left of the graph.

7.4.2 Residual stresses

Residual stresses were calculated from the measured strains using equation (3.4). Diffraction elasticity constants were taken from the literature [38]. The applied elasticity constants were:

For the ferritic parent material:

$$E_{110} = 220 \text{ GPa}$$

$$\nu_{110} = 0.28$$

For the buttering layer and weld:

$$E_{200} = 139 \text{ GPa}$$

$$\nu_{200} = 0.35$$

For the austenitic parent material:

$$E_{111} = 247 \text{ GPa}$$

$$\nu_{111} = 0.24$$

The uncertainties presented in Figs. 7.24 to 7.26 were derived from the uncertainties of the strains based on standard error propagation [75]. No uncertainty contribution from the elasticity constants was taken into account, as this would add a relatively constant contribution to the errors indicated. Moreover, this contribution would not be related to the measurement process itself.

Residual stresses in the circumferential direction are presented in Fig. 7.24. Compressive stresses in the range -100 MPa to -400 MPa were obtained for the ferritic steel base material in the vicinity of the interface. Tensile stresses have been derived throughout the fusion zone and the area of austenitic base material covered by these measurements. In the fusion zone the data exhibit significant scatter. This prevents the identification of any clear trends concerning stress gradients in the fusion zone. In the austenitic part of the pipe, the stress levels near the fusion zone are similar to those in the fusion zone, and the stresses generally decrease when moving away from the fusion zone. Within the range covered by these measurements, the stresses remain tensile.

Obviously, no stresses could be obtained for locations where strain data were missing in the radial and/or axial directions.

Residual stresses found in the axial direction are shown in Fig. 7.25. In the ferritic base material the stresses range from -400 MPa to about +250 MPa. In view of the distribution of the test locations over the material it is not clear whether this distribution is in contradiction to balance of the stresses or not. In the buttering layer, where there were relatively strong signals in all measurement directions, the stresses range from -50 MPa to about +175 MPa. These data have to be looked at together with the data in the ferrite in view of the stress balance. In view of the data missing in the fusion zone, no firm conclusions can be drawn. For that half of the fusion zone where data have been obtained, the expected large scatter of the results can be seen. Individual stress values are in the range -200 MPa to +400 MPa, which are acceptable in view of the applicable yield levels. The available data in this case

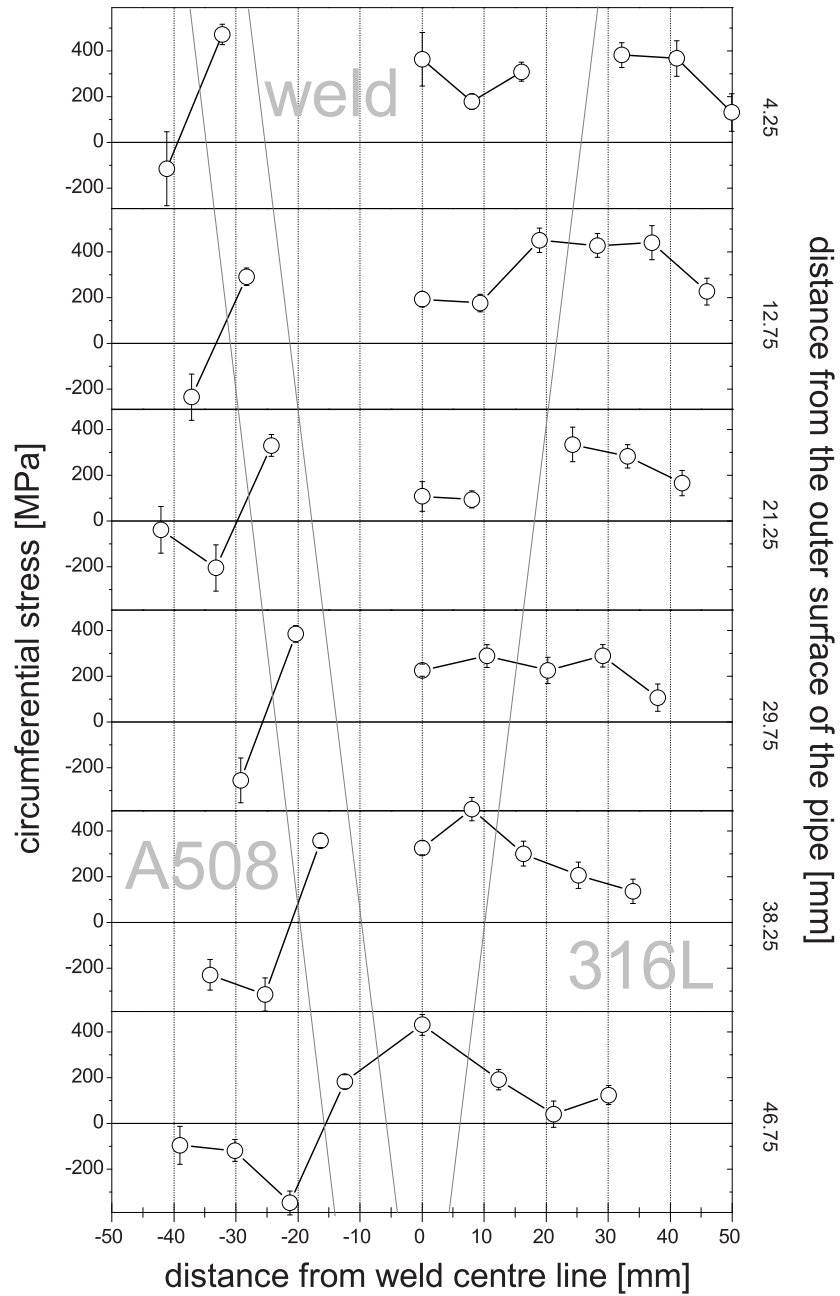


Figure 7.24: Circumferential stresses at six different depths below the outer surface (cf. Fig. 7.12) in the thick bimetallic piping weld.

clearly do not fulfill stress balance and the tensile stresses dominate. In the austenitic part of the pipe relatively little scatter in the data is obtained. All residual stresses found were in the range +50 MPa to about +150 MPa.

The radial stresses, shown in Fig. 7.26, are generally a little smaller than the axial stresses, but still reach surprisingly high levels, spanning almost the same range as the axial stresses in the fusion zone, where they exhibit a huge scatter as well. Good indicators for the quality of the radial stresses are the measurements at the near surface locations; *i.e.*, 4.25 mm from the outer and inner surfaces. These should be small in all cases (within ± 100 MPa) giving some allowance for the scatter in the data. This has only been accomplished in the austenitic part of the pipe, where all stresses found were quite small. Even in the ferritic base metal, near surface stresses outside of this range have been found, whereby the uncertainty levels are quite high because of low diffraction intensity in at least one direction of measurement. Also in the fusion zone, the near surface results are also not always within these margins. It generally appears that the radial stresses found in the bulk of the material exceed the levels that would be expected for the through thickness direction.

7.4.3 Brief assessment of the results

In analogy with chapters 5 and 6, a brief check of the consistency of the observed residual stress distributions is made here as well. Before applying the yield stress and surface normal stress criteria to the data, a general observation should be mentioned.

The data obtained for the thick walled component exhibit a larger scatter than those measured on the two thinner components. In the fusion zone, the scatter can be mainly attributed to the lack of material homogeneity; but in the case of the base materials the main reason for the scatter is the strong beam attenuation.

This scattering obscures many of the trends along the lines of measurement and through the thickness that were visible in the thin walled pipe (Figs. 5.11 and 5.12). For this reason the strains and stresses are presented in individual plots for each line of measurement in this chapter.

The yield stress levels given in Table 5.6 are 584 MPa for the ferritic base material, 370 MPa for weld material and 322 MPa for the austenitic steel base material. For all measurement locations the von Mises stresses have been derived based on eq. (2.6). In no case does the von Mises stress exceed the applicable yield level. At a few test locations, for example at the root of the weld, high tensile stresses have been derived in three directions, so that the von Mises stress still remains below yield despite the high values for the individual components. Therefore the yield stress criterion is met for all measurements in this specimen.

In common with the thin walled piping component, one should also expect low stress values for the radial direction near the surfaces. As can be seen from Figs. 7.24 and 7.26, the radial stresses along the near surface lines (4.25 mm and 46.75 mm from the outer surface) are indeed significantly lower than the circumferential stresses. However, for many measurement locations, including several in the parent materials, stresses higher than 100 MPa or lower than -100 MPa have been found. This is

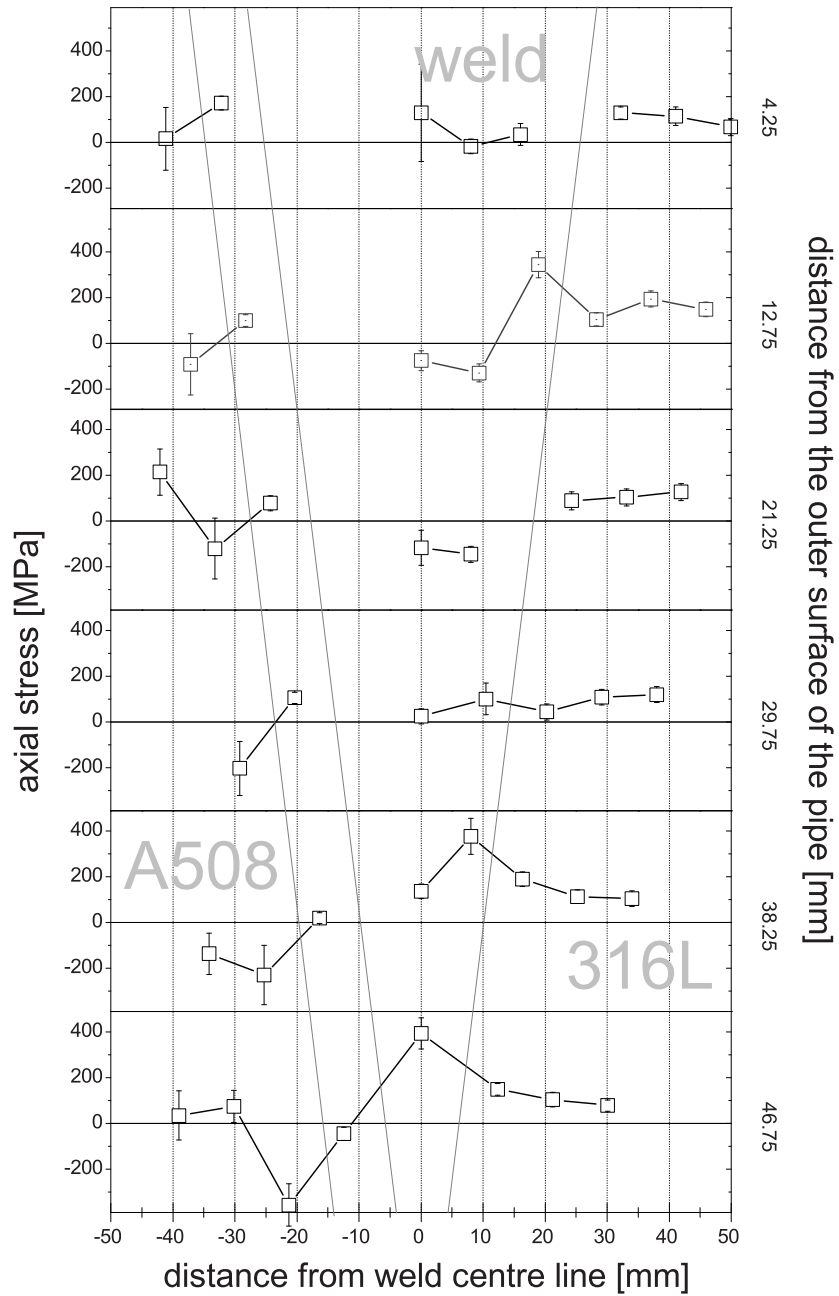


Figure 7.25: Axial stresses at six different depths below the outer surface (cf. Fig. 7.12) in the thick bimetallic piping weld.

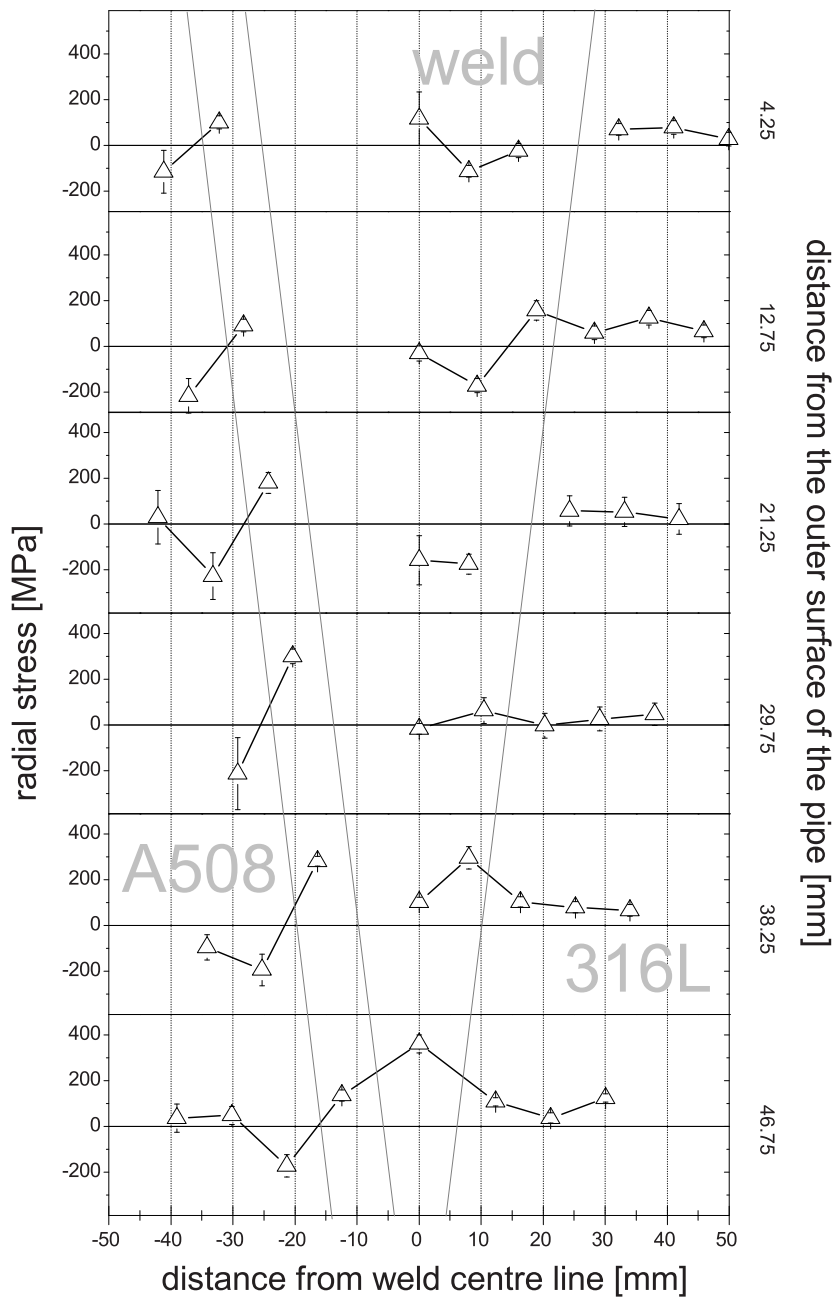


Figure 7.26: Radial stresses at six different depths below the outer surface (cf. Fig. 7.12) in the thick bimetallic piping weld.

another indicator that the data are not of excellent quality, which in relation to the surface normal stresses should be mainly attributed to the thickness of the material and the resulting strong neutron beam attenuation and therefore the compromised data quality.

7.5 Comparison with other stress measurement techniques and modeling

In this section additional assessments of residual stresses in the 51 mm thick bi-metallic piping weld specimen are described. The methods used are surface hole drilling, the crack compliance method and numerical modeling. The main purpose is again to provide a comparison with the results obtained by neutron diffraction. This comparison provides an additional means for assessing the quality of the neutron data.

It is noted that, in common with the work presented in sections 5.5 and 6.5, the author of this thesis has not been involved in the additional investigations presented here.

7.5.1 Surface hole drilling

The surface hole drilling technique [87] is a strain gauge based method for measurement of residual stresses. It is a relaxation method, similar to the ring core technique described in chapter 6. It measures the in-plane stresses at the surface of a specimen. In the application of this technique a set of three strain gauges is used to measure the relaxation strain at the specimen surface when a small hole is drilled in the centre of the strain gauge arrangement. From the combination of the relaxation strains in three directions the in-plane stress components at the surface can be obtained.

In Figs. 7.27 and 7.28 the circumferential stresses measured at the outer and inner surface of the component by surface hole drilling are compared to the neutron diffraction results obtained for the corresponding lines 4.25 mm from the surface. It can be seen that the stress levels measured by the two methods are different. The measurements can therefore not be used to validate each other. However, there are similarities in the distribution of the stresses over the fusion zone. This implies a correlation between these distributions.

The circumferential residual stress measurements by surface hole drilling at the outer and inner surfaces show similarities in the stress distributions with the near surface neutron diffraction measurements. However, at the outer surface the range of stresses found by surface hole drilling is smaller than that found by neutron diffraction (Fig. 7.27), and at the inner surface a higher peak compressive stress is found near the ferrite-buttering interface (Fig. 7.28). These differences are probably caused by plastic deformations during machining the component to its final outer and inner diameters. Normally such machining stresses do not extend to depths larger than 1 mm below the component surface and are therefore almost not seen by the neutron diffraction measurements.

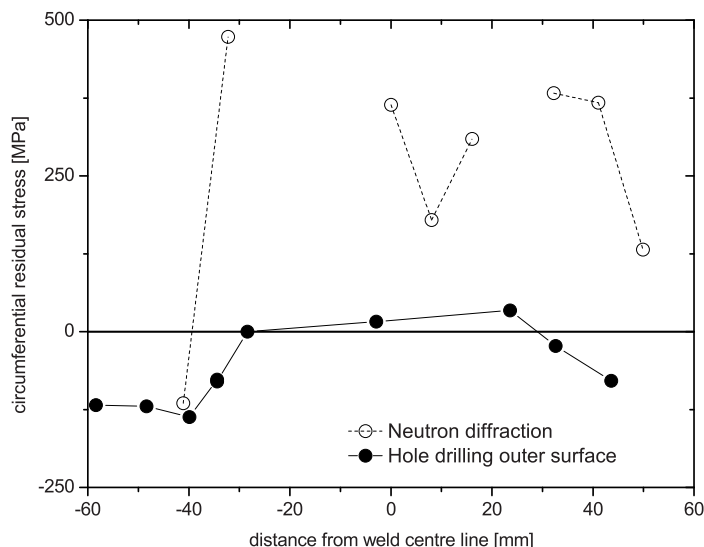


Figure 7.27: Circumferential residual stress measured at the outer component surface by surface hole drilling, compared to the corresponding neutron diffraction results at 4.25 mm from the outer surface (Cf. Fig. 7.24).

For completeness, Fig. 7.29 shows the circumferential and axial stresses obtained from the surface hole drilling at the outer surface. Comparison with the neutron data for the axial direction was not attempted because of the large scatter in the neutron data.

7.5.2 Crack compliance method

Like surface hole drilling the crack compliance method [88] is relaxation based and by means of strain gauges measures relaxation strains due to material cutting. This method operates one-dimensionally and is based on cutting a slice from the specimen. Figure 7.30 illustrates the principle of the method. While a vertical cut is machined through the slice, strain gauges at various locations record the relaxation strains due to cutting. Appropriate algorithms facilitate the calculation of the stress distribution in the direction normal to the plane of the cut.

The slice cut from the component was oriented in the piping axial direction. The remaining thickness of the slice was of the order of 10 mm. Figure 7.31 shows the slice used, where the fusion zone can be clearly seen in the picture. It can also be seen that the method has been applied at four different locations. Residual stresses were measured in the piping axial direction.

Figure 7.32 shows the axial residual stresses that have been found in the fusion zone by the crack compliance method in comparison to the corresponding neutron

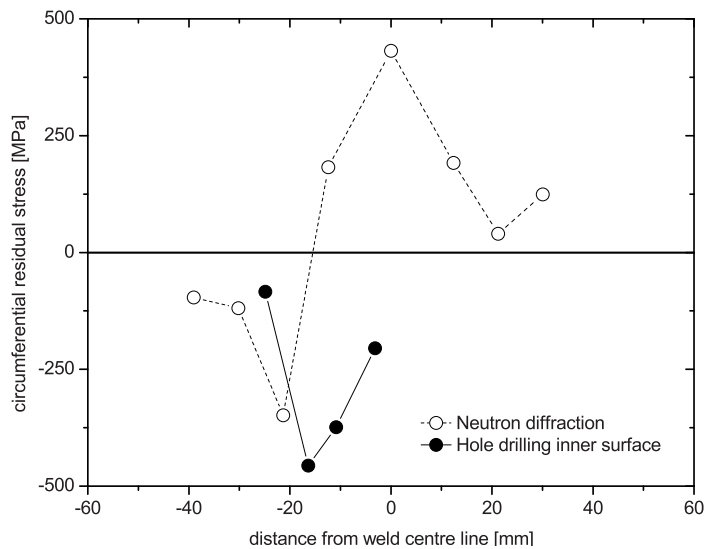


Figure 7.28: Circumferential residual stress measured at the inner component surface by surface hole drilling, compared to the corresponding neutron diffraction results at 46.75 mm from the outer surface; i.e., 4.25 mm from the inner surface.

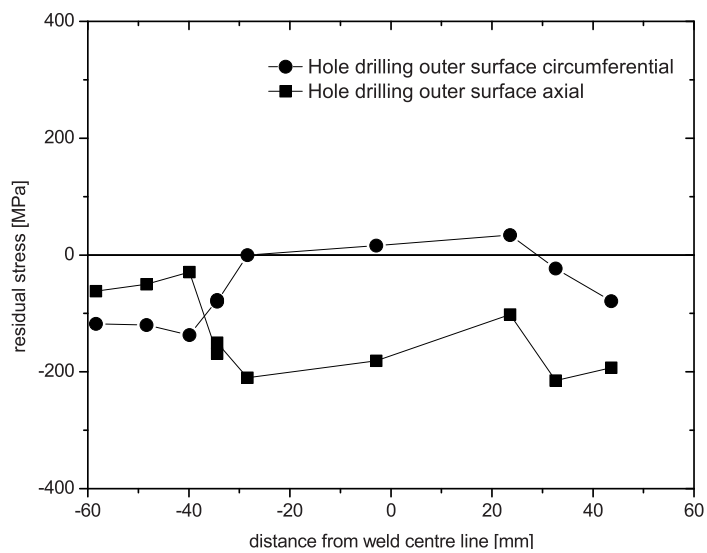


Figure 7.29: Circumferential and axial residual stress measured at the outer component surface by surface hole drilling.

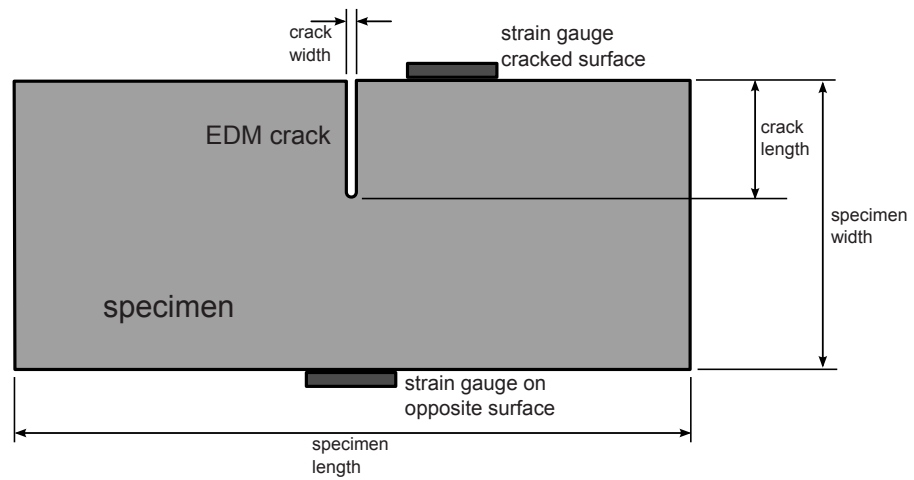


Figure 7.30: Principle of the crack compliance method.

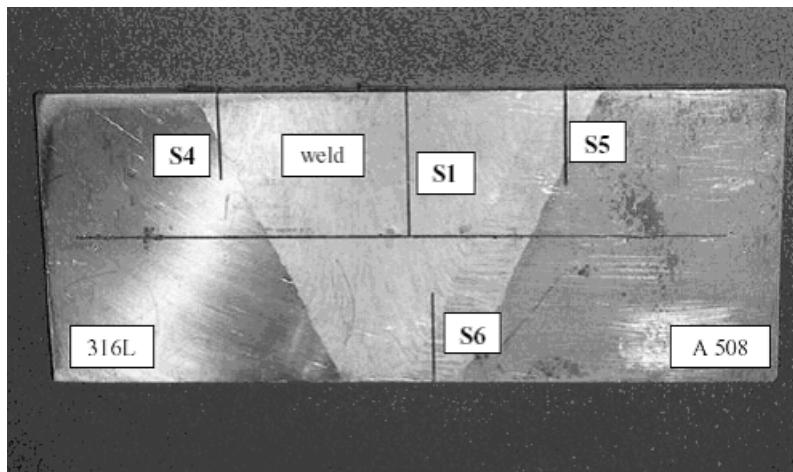


Figure 7.31: Slice from the dissimilar metal weld component after execution of the crack compliance measurements; individual measurements identified as S1, S4, S5 and S6.

diffraction data. Results are shown for measurements along lines S1 and S6 in Fig. 7.31. It can be seen that compressive stresses were found near both, the inner and outer, surfaces, and that these change to tensile stresses within a relatively short distance when moving into the bulk of the material. It should be noted that the agreement of these near surface results with the corresponding surface hole drilling data is good. This supports the argument that the machining has introduced near surface compressive stresses.

The neutron diffraction data are shown for the weld centerline (grey-solid) and for the buttering centerline (open square symbol). This way the measurement locations, for which the results are shown, fall on the corresponding lines S1 and S6 of the crack compliance measurements. The error bars indicating the stress uncertainties were derived from the fitting uncertainties of the neutron data; the error bars in distance are meant to represent the spatial extent of the sampling volumes and do not indicate an uncertainty in position.

The agreement between the neutron diffraction and the crack compliance results shown is in fact quite acceptable. However, the comparison is compromised by large uncertainties associated with the neutron measurements and the relatively small number of measurement locations. In addition, the specimens investigated by these two methods were different in size and geometry and the assumption had to be made that the cutting of the slice for the crack compliance measurements would not alter the axial residual stresses significantly.

7.5.3 Numerical modeling

In the context of the residual stress investigations in the 51 mm thick dissimilar metal weld, a number of numerical round robin exercises have been executed addressing several approaches to predict the stresses within and around this weld. More detailed information on this work is given in [89] and [69]. A brief summary including comparisons with the neutron diffraction data presented in this chapter is given here.

The different round robin exercises mainly comprise a simplified and a detailed numerical analysis of this component. Five organizations have contributed their analyses to this project.

The simplified numerical analysis in principle constitutes only the assessment of the post-weld-heat-treatment of the component. This entailed the simulation of the described heat treatment applied to the welded component, without taking into account the welding of the component itself. The simple assumption was that the entire component would be free of stress at the heat treatment temperature of 610 °C. Upon cooling the mismatch between the thermo-mechanical properties of the materials involved would lead to the built-up of strains and stresses beyond the yield strength of the materials involved. The resulting plastic deformation results in the formation of the residual stresses obtained in this analysis. Results from this simplified analysis are in general similar to the measurement results [69]. This is an indication that the post-weld heat treatment was a determining factor in the development of the stresses in this component, and that the assumption of zero stress at the heat treatment

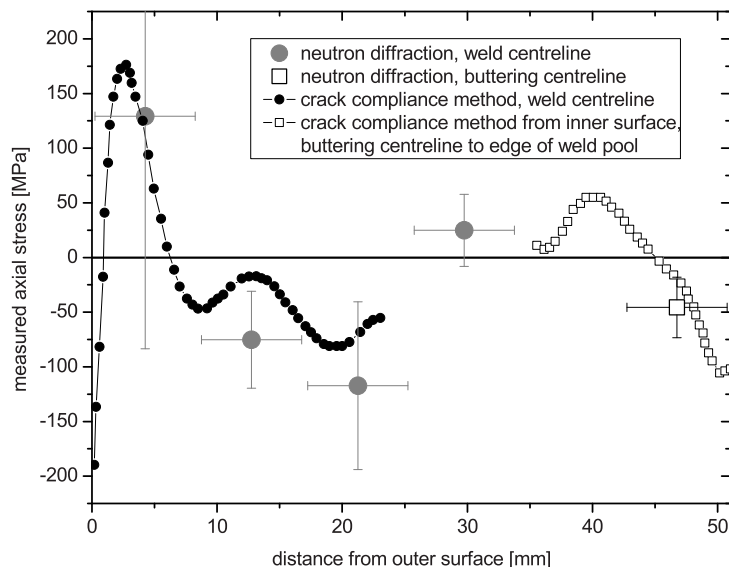


Figure 7.32: Axial stresses in the fusion zone measured by the crack compliance method in measurements S1 and S6 (cf. Fig. 7.31) in comparison with corresponding neutron diffraction results.

temperature is a good description of the real situation. Nevertheless in most cases the fusion zone residual stresses are still under predicted when compared with the neutron diffraction data.

The participants in the detailed numerical analysis undertook the modeling of the entire manufacturing process of the component including a bead-by-bead simulation of the weld. Because of the restrictions in available computation power, these analyses were executed as 2-dimensional models of the weld.

The manufacturing steps included in these analyses were (see also section 7.2): deposition of the buttering layer, ca. 70 beads in 4 layers, machining of the buttering layer, heat treatment of the ferritic part of the pipe after applying and machining the buttering layer, deposition of the weld, almost 100 beads in 18 layers, post-weld heat treatment and finally machining of the component to its final dimensions.

In Fig. 7.33 the mesh built at the JRC for the detailed analysis is shown. It consisted of more than 4000 elements with more than 13000 nodes. A prescribed temperature (1450 °C) approach was chosen in order to achieve a high heat input. The thermal and mechanical analyses were uncoupled, so that the results of the thermal analysis could be used as input into the mechanical analysis. The birth and death of element technique was used for the introduction of the consumable. Hereby the elements of the weld are defined from the beginning of the process, but they are activated, which means they are given properties that make them contribute to the component behaviour, only at the time the bead they belong to was deposited. In the prescribed temperature approach, no melting of the base material or re-melting of previously deposited beads occurred. Multi-linear kinematic hardening was applied. Creep relaxation and phase transformations were not taken into account. The analysis considered small displacements only. The final machining of the component was incorporated by simply applying death to the corresponding elements. The commercial analysis code ANSYS 8.0 was used for the analysis.

Figures 7.34 and 7.35 show the resulting distributions of the circumferential and axial stresses respectively over the thickness of the component. The neutron diffraction data are included for comparison.

For both measurement directions, there is a qualitative agreement between the experimental and the numerical results. However, only for a small number of measurement locations the numerical results agree with the measurement data to within the quoted experimental error.

It is also observed for both measurement directions that the agreement between measurement and model becomes worse toward the inner surface of the pipe. The data show that the numerical analysis predicts significantly lower residual stresses than those derived from the neutron diffraction measurements for almost all measurement locations at 38.25 mm and 46.75 mm from the outer surface of the pipe.

All data presented in Figs. 7.34 and 7.35 have been derived from strain measurements in the circumferential, axial and radial directions; *i.e.*, every data point for the circumferential direction depends on the strain measurements for the other two directions as well. In view of the large scatter and the partially significant uncertainties associated with the strain measurements in the axial and radial directions, a

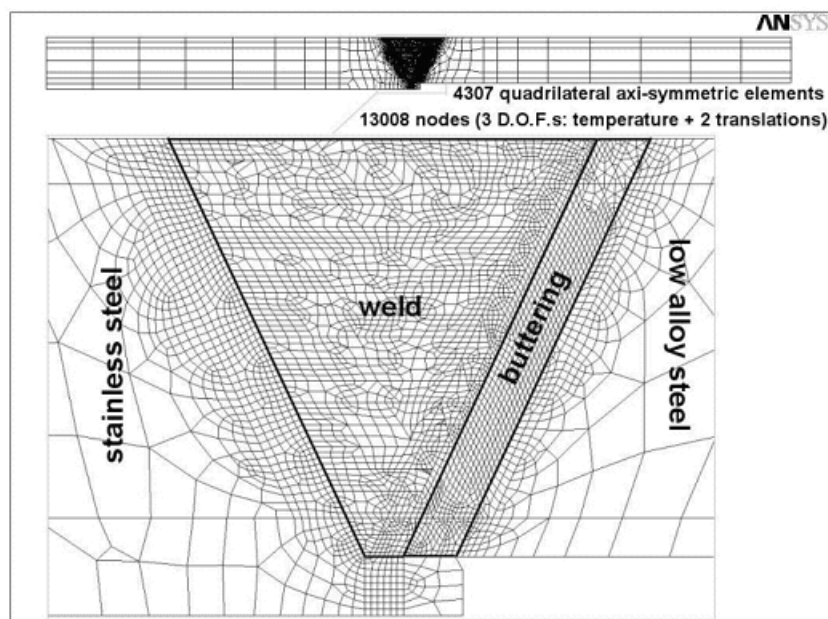


Figure 7.33: Mesh built at JRC for the detailed 2-dimensional model in the axial-radial plane of the wall of the 51 mm dissimilar metal welded pipe. From [69]

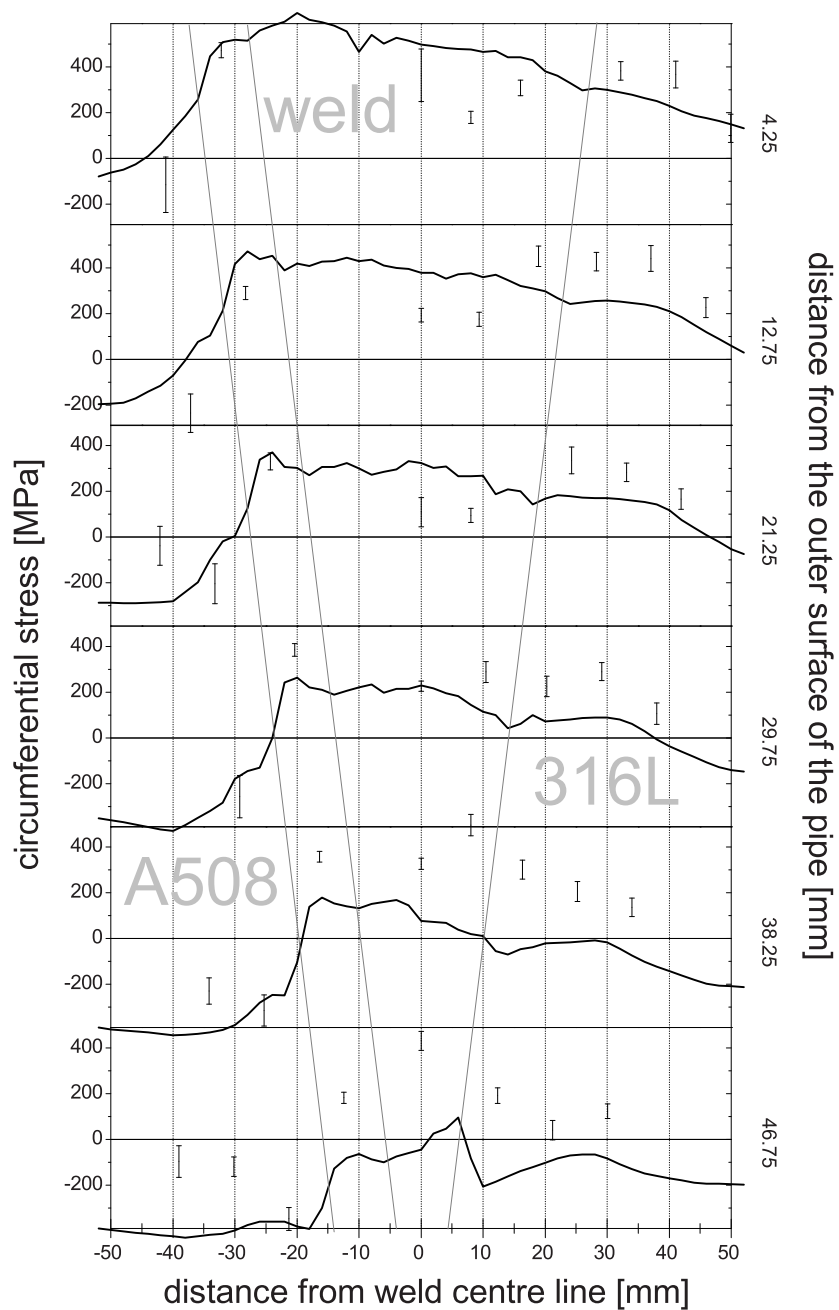


Figure 7.34: Comparison of the circumferential stresses obtained from FE modeling (black lines) with the corresponding stresses measured by neutron diffraction (error bars).

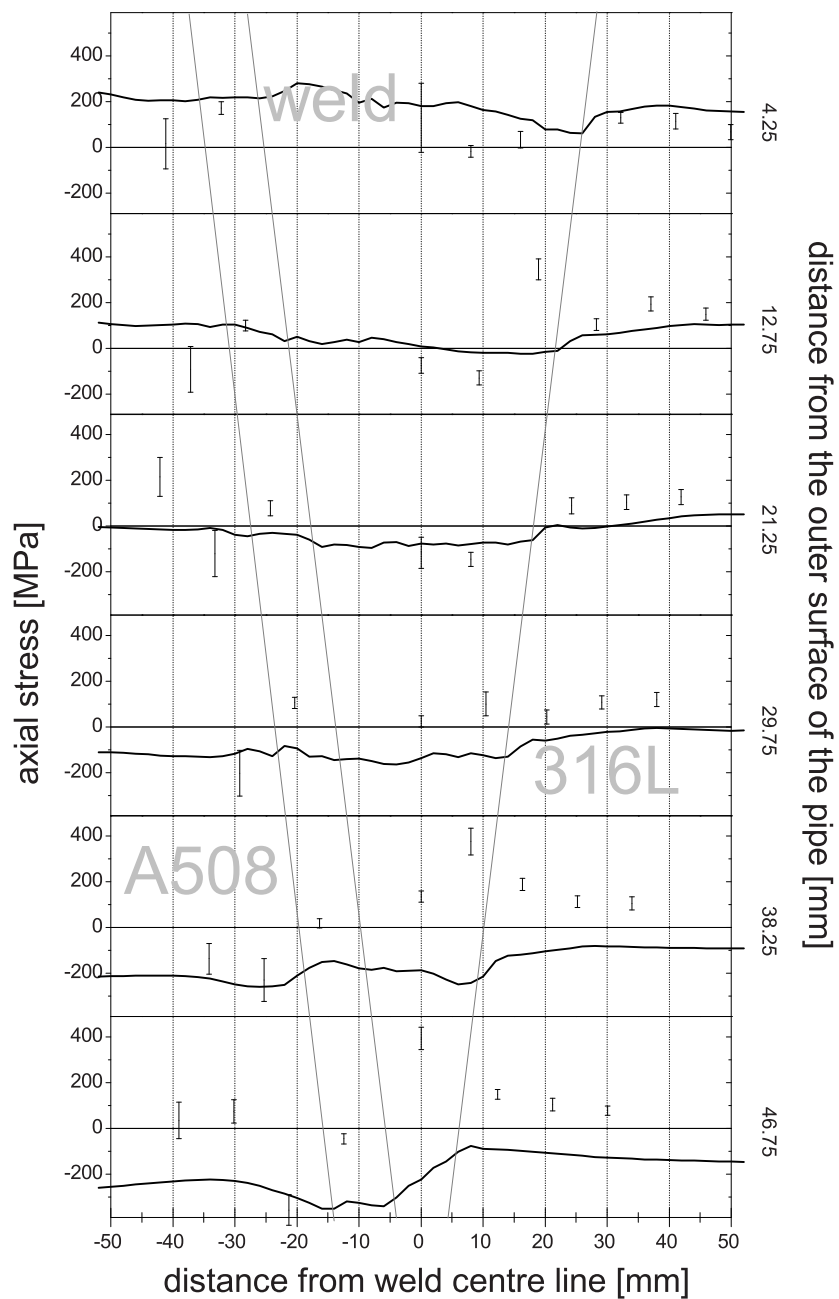


Figure 7.35: Comparison of the axial stresses obtained from FE modeling (black lines) with the corresponding stresses measured by neutron diffraction (error bars).

direct comparison between the measured strains in the circumferential direction and the corresponding strains derived from the numerical results is presented in Fig. 7.36.

Caution must be applied when comparing strains from the numerical analysis with strains from diffraction measurements. In single peak diffraction stress analysis, diffraction elasticity constants (DEC) need to be applied in the conversion of strains to stresses. In numerical analyses normally bulk elasticity constants are used. In order to visualize the resulting differences in the strain, values have been calculated from the numerical stress results based on DEC:

$$\varepsilon_{hoop,DEC} = \frac{1}{E_{hkl}}\sigma_{hoop} - \frac{\nu_{hkl}}{E_{hkl}}(\sigma_{axial} + \sigma_{radial}) . \quad (7.1)$$

and based on bulk elasticity constants:

$$\varepsilon_{hoop,bulk} = \frac{1}{E}\sigma_{hoop} - \frac{\nu}{E}(\sigma_{axial} + \sigma_{radial}) . \quad (7.2)$$

The first data set (dashed lines) in Fig. 7.36 has been obtained from the predicted stresses based on bulk elasticity constants; the second set (solid lines) has been derived by using the DEC's applicable to the respective material zone. The DEC values used are the same that had been used in the strain to stress conversion for the neutron diffraction results, which are given in section 7.4.2.

The comparison of the “diffraction strains” with the strains obtained using bulk constants shows that in particular for the fusion zone the “diffraction strains” deviate significantly from the bulk values. Throughout the fusion zone and the buttering layer the use of DEC's results in higher strains than the use of bulk constants. In the base materials the results do not differ by much.

The circumferential strains obtained using bulk constants in fact compare relatively well with the measurements except for the locations closer to the inner surface of the pipe, where the numerical analysis is apparently under predicting the strains.

When DEC's are used for the calculation of the numerical strains, an over prediction of the circumferential strains is found in the fusion zone for the locations 4.25 mm and 12.75 mm from the outer surface. Under prediction of the strains is found near the inner surface and a good agreement for the fusion zone is observed for the mid-thickness locations.

All comparisons show an under prediction of the strains and stresses near the inner surface of the pipe. From the safety point of view, under prediction of stresses is the most worrying situation; hence further improvement of the performance of the numerical models is needed particularly in this area.

Finally, Fig. 7.37 shows a comparison between the results obtained by all participants in the numerical analysis, simplified and detailed, and the stresses measured by neutron diffraction for the line 4.25 mm from the outer piping surface. Overall there is relatively good agreement between the numerical results despite some differences in the approaches followed by the various contributors.

The line presenting the lowest stresses within the fusion zone stems from a simplified analysis. It can be seen that this simplified approach was under predicting the

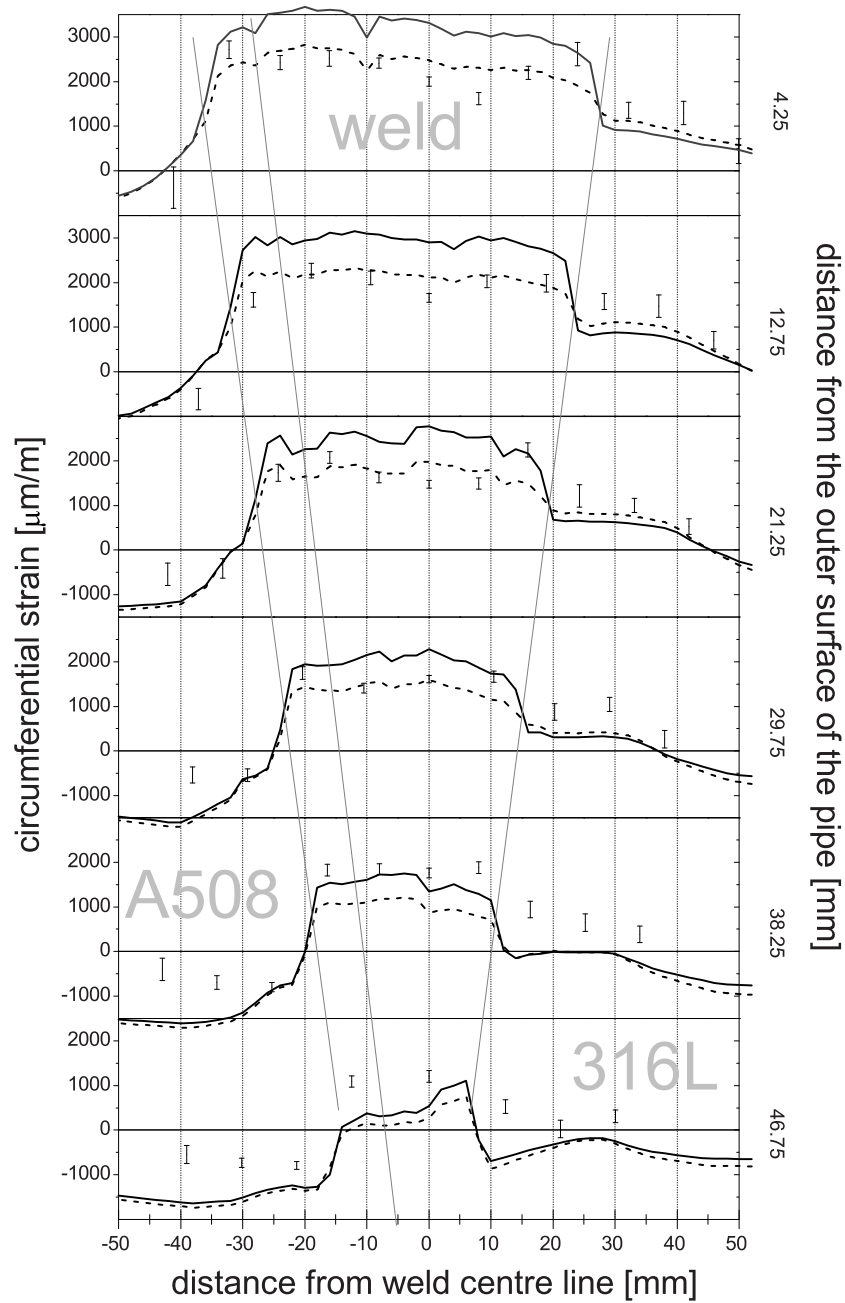


Figure 7.36: Comparison of the circumferential strains obtained from FE modeling (black lines, solid for the calculation based on DECs, dashed for the calculation based on the bulk elasticity constants) with the corresponding strains measured by neutron diffraction (error bars).

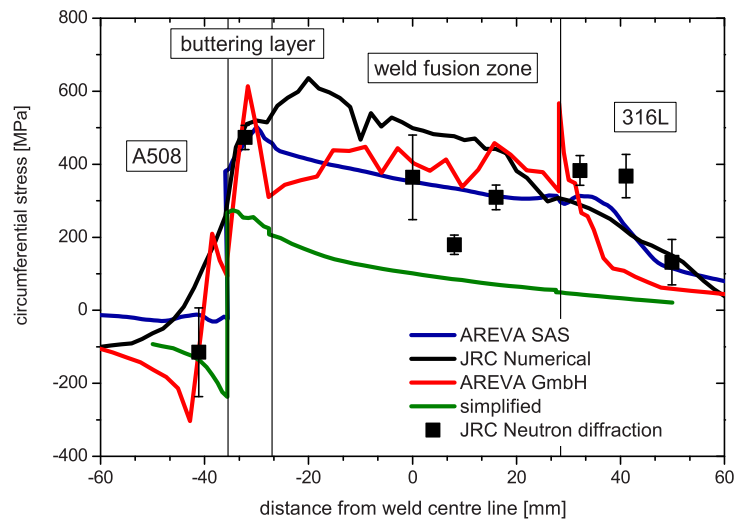
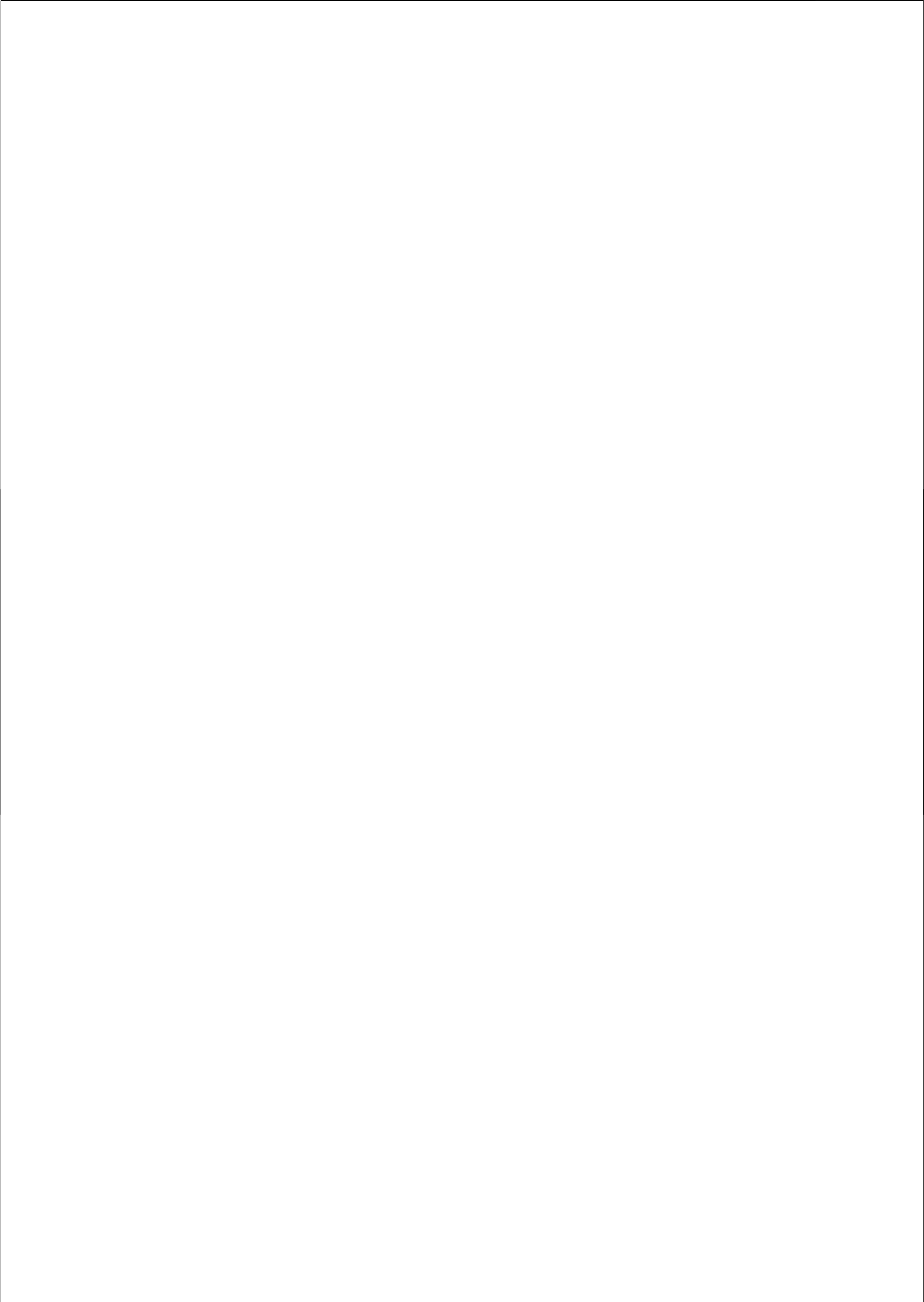


Figure 7.37: Circumferential stresses at 4.25 mm from the outer piping surface; comparison of the neutron diffraction results with simulation data from a round robin exercise within the Network for Evaluation of Structural Components. From [69]

residual stresses along this line in comparison with the experimental data and the more complex models. The detailed analyses achieved a significantly more acceptable agreement with the measurement results for these measurement locations.



Chapter 8

Comparison and assessment of methods and results

In this chapter the experimental approaches used in this work and the applied data analysis methods are critically assessed. Emphasis is given to the way the experimental uncertainties of the results are estimated. In section 8.1 the uncertainty estimation and error propagation based on the frequently applied practice of obtaining strain and stress errors exclusively from the data fitting uncertainties is outlined. The impact of the uncertainty in the elasticity constants on the errors is briefly described in section 8.2. Sections 8.3 to 8.5 address possible additional contributors to the measurement uncertainties; where possible, the magnitude of contributions is estimated in relation to the common practice approach used in chapters 5, 6 and 7. An overview of the analyzed uncertainty contributors and the relevant assessment of results is provided in section 8.6. Subsequently, the findings from the comparisons of the neutron diffraction results with data obtained by other experimental techniques and by numerical modeling are summarized in sections 8.7 and 8.8. In section 8.9 an assessment of the specific experimental approaches used in this work is presented; these include the design of the free of stress reference specimens, the cutting of the components to facilitate the neutron diffraction measurements and the application of the technique to a 51 mm thick component.

8.1 Error propagation due to fitting uncertainties

In a diffraction measurement on a monochromatic instrument the angular distribution of neutron counts exhibits a peak at an angle in accordance with the Bragg equation. The position of this peak is identified by the centroid of a Gaussian function fitted to the data (see Fig. 3.4).

From the fitted peak position 2θ for the material under stress and the position obtained for the corresponding material in a stress free state $2\theta_0$, the strain is obtained

with equation 8.1 (also presented as eq. 3.3):

$$\varepsilon_{hkl} = \frac{\sin \theta_{0,hkl}}{\sin \theta_{hkl}} - 1, \quad (8.1)$$

The reader should note that the peak positions, strains and elasticity constants in equations 8.2, 8.3 and are also meant to be *hkl*-dependent. For the sake of legibility and brevity of the equations the according indexation has been omitted.

Following standard error propagation rules, the uncertainty in the strain ε is given by

$$\Delta\varepsilon = \cot \theta_0 \cdot \sqrt{\Delta\theta^2 + \Delta\theta_0^2}. \quad (8.2)$$

This equation is an approximation, as in all trigonometric functions θ is replaced by θ_0 . For the purposes of error estimation this approximation is valid since $\theta \approx \theta_0$.

Having measured strains in three mutually orthogonal directions at a given location, the normal stresses in these directions can be calculated via Hooke's law (also presented as eq. 3.4):

$$\sigma_i = \frac{E}{1+\nu} \varepsilon_i + \frac{\nu E}{(1+\nu)(1-2\nu)} (\varepsilon_1 + \varepsilon_2 + \varepsilon_3). \quad (8.3)$$

The strain errors lead to the following uncertainty in the derived stress:

$$\Delta\sigma_i = \sqrt{\left(\frac{(1-\nu)E}{(1+\nu)(1-2\nu)}\right)^2 \cdot \Delta\varepsilon_i^2 + \left(\frac{\nu E}{(1+\nu)(1-2\nu)}\right)^2 \cdot (\Delta\varepsilon_j^2 + \Delta\varepsilon_k^2)}, \quad (8.4)$$

$$i, j, k \in \{1, 2, 3\}; \quad i \neq j \neq k.$$

The stress uncertainties presented in chapters 5, 6 and 7 have been obtained using these formulae.

8.2 Uncertainty of the diffraction elasticity constants

In order to convert strains into stresses (eq. 8.3) the values for the elasticity constants E and ν need to be known. In this work values were taken from a theoretical prediction by Eigenmann and Macherauch [38]. No data have been found concerning the uncertainty in the values. A reasonable estimate is that the constants used for the base material are inaccurate by not more than 10%. For the fusion zones, it is possible that there is a bigger deviation (see also Table 3.1). As the stresses are proportional to E , the relative uncertainty in the stresses is proportional to the relative uncertainty in E .

For Poisson's ratio the situation is mathematically more complicated; in a limited parametric study by Wimpory it was shown that the uncertainty in ν becomes increasingly important with increasing stresses [68]. Taking the measurements on the

clad layer specimen presented in chapter 6 as an example, an uncertainty in Poisson's ratio of $\pm 10\%$ results in an average increase in the uncertainty of the longitudinal stresses in the clad layer by 25%. In the substrate, an uncertainty in Poisson's ratio of $\pm 20\%$ leads to a much smaller increase of the uncertainty in the stress. The difference is caused by the different levels of stresses observed and by the differences in the elasticity constants for the different crystallographic planes. Reliable uncertainty data for the elasticity constants is unavailable and no further analysis has been made in relation to these measurements.

8.3 Instrumental and environmental uncertainty contributors

In neutron diffraction stress analysis it is common practice to take into account only the fitting uncertainties as described in 8.1. However, the experimental results presented in chapters 5, 6 and 7 indicate that this approach is not always sufficient. A preliminary standard on the neutron diffraction method for stress estimation [39] provides a list of additional contributors to the uncertainty to be considered. These include:

- a. Uncertainty in the wavelength λ of the incident beam.
- b. Variations in the temperature of the specimen as a function of time.
- c. Uncertainty in measurement position within the specimen.

In the following, the impact of these contributions to the uncertainty is examined.

a. An uncertainty in the wavelength is not considered as an independent contributing factor, because in this work the strain is derived from the peak positions and not from the lattice spacing. A stable wavelength distribution in the primary beam during measurements is a pre-requisite for this condition. This wavelength distribution is related to the size and material of the monochromating crystal used and the dimensions of the beam defining aperture(s). Instabilities of the diffractometer set-up at the HFR leading to significant variations in the neutron wavelength have never been observed.

Ambient temperature variations and grain size effects have an influence on the effective wavelength, but these effects are covered by separate accounts given below.

b. At the HFR the temperature inside the reactor building is continuously recorded by sensors distributed throughout the building. Based on these records, a maximum day-night variation of temperature at the sample location of 3 °C is observed. In stainless steel the resulting thermal expansion corresponds to an additional strain of about 50 $\mu\text{m}/\text{m}$. The same temperature change of the neutron monochromator renders a different wavelength distribution in the incoming neutron beam partly compensating

for the thermal expansion of the specimen. The potential temperature effect should therefore be considered to be smaller than the value quoted above. The additional uncertainty of not more than $50 \mu\text{m}/\text{m}$ for stainless steel and not more than $30 \mu\text{m}/\text{m}$ for ferritic steel does not constitute a significant contribution to the uncertainty at the levels that are generally considered in this work (often $> 100 \mu\text{m}/\text{m}$). However, contributions of temperature variations should be considered in case of smaller fitting uncertainties obtained.

c. The positioning of the sampling volume within a specimen with spatial variation of stress and strain forms an additional source of uncertainty.

The positioning uncertainty is estimated to be $\pm 0.1 \text{ mm}$ in the case of the clad layer specimen (discussed in chapter 6) and $\pm 0.3 \text{ mm}$ in case of the thick bi-metallic piping weld (discussed in chapter 7). In both cases the positioning uncertainty is small with respect to the dimension of the sampling volume. The largest strain gradients observed in these samples are near the interface in the clad layer, where it amounts to $300 - 400 \mu\text{m}/\text{m}/\text{mm}$ in the interface normal direction. With a positioning uncertainty of $\pm 0.1 \text{ mm}$ in the direction of the strain gradient, this corresponds to an additional strain uncertainty of about $30-40 \mu\text{m}/\text{m}$. Everywhere else in this specimen, gradients of $100 \mu\text{m}/\text{m}/\text{mm}$ or less have been observed, leading to an additional uncertainty of $10 \mu\text{m}/\text{m}$ or less. This is again negligible compared to the uncertainties resulting from the data fitting, which in all cases exceed $70 \mu\text{m}/\text{m}$.

For the thick bi-metallic weld a similar situation exists. When only looking at the circumferential strain measurements (Fig. 7.20) and ignoring the strain gradient at the interface because it is assumed to be locally concentrated such that no neutron measurements were taken on this gradient, areas with gradients higher than $100 \mu\text{m}/\text{m}/\text{mm}$ are not found. Because of the larger positioning uncertainty, which results from the larger wall thickness (51 mm) and sampling volume size, the resulting additional strain uncertainty is $30 \mu\text{m}/\text{m}$ at maximum. In view of the higher uncertainties in the peak positions for this component, this contribution is again low; *i.e.*, an uncertainty of $100 \mu\text{m}/\text{m}$ is increased by less than 10%. In terms of the uncertainty in the residual stresses, for a ferritic steel with bulk elasticity constants, strain uncertainties of $\pm 100 \mu\text{m}/\text{m}$ in three measurement directions correspond to about $\pm 30 \text{ MPa}$.

8.4 Specimen dependent uncertainty contributions

The angular position of a neutron diffraction peak is determined by a number of factors. These include the average lattice spacing; *i.e.*, lattice strain, at the measurement location and the counting statistics, which are the factors that have been considered in the assessment of the experimental data presented in this work.

Other aspects influencing the peak position are: a. local chemistry variations of the material under investigation, b. intergranular strains and c. material inhomogeneities and large grain sizes within the sampling volume that indirectly result in variations of the effective measurement geometry.

In this section these effects are described and in the case of the material inhomogeneities an attempt is made to quantify their contribution to the uncertainty in the measurement of strain.

8.4.1 Chemistry variations and intergranular strains

Spatial variations in the chemical composition of the material and in intergranular strains result in changes of the lattice spacing between measurement locations not associated with the macroscopic mechanical strain. Nevertheless, they affect the position of the diffraction peak in an identical manner to macroscopic strains.

The reference specimens described in chapters 5, 6 and 7 were meant to correct for the influence on the measurement of macroscopic strain, as the macroscopic strains are relaxed, whereas chemistry variations and intergranular strains are assumed to remain unaltered.

Unlike changes caused by macroscopic or intergranular strains the effect of chemistry variations should be independent of measurement direction. The reference measurements in the clad layer presented in Figs. 6.5 (b) and (c) are an example where only small differences have been observed between two measurement directions and where therefore the variations in the diffraction peak positions can be attributed mainly to chemistry variations.

In all cases presented here, the reference test pieces have been cut from different locations within the welds than those used for the measurements of the strained samples. It can occur that a reference peak position obtained from a different location than the location of the strain measurement is not a good representation of the reference lattice spacing at the measurement location. Dedicated investigations to study the influence of such effects on the measurement error have not been made.

8.4.2 Grain size effects

Metals used in engineering applications are mostly polycrystalline aggregates consisting of many individual crystallites that generally differ from each other in terms of their crystallographic orientation in the specimen and often in size and/or shape.

In accordance with the previous chapters, a diffraction signal originates from a volume in space defined by the intersection of the incoming and diffracted beams. Naturally, there will be a finite number of grains present inside or intersecting with this sampling volume. Normally only a small fraction of these grains is oriented such that a lattice plane normal to the direction of measurement fulfils the Bragg condition (3.1). Only these grains will contribute to the diffraction signal recorded by the detector. The neutron peak shown in Fig. 3.4 has been obtained from such a polycrystalline material.

It can happen that the material contributing to the diffraction signal is not homogeneously distributed within the sampling volume. This can be because of a large grain size of the material, as larger grains result in a higher probability that those contributing to the diffraction signal are not homogeneously distributed within the

sampling volume. A diffraction peak position shift resulting from the presence of large grains in the material is thus called a grain size effect. An inhomogeneous distribution of the diffracting material can also be caused by surfaces/interfaces cutting through the sampling volume and by variations in the preferred crystallographic orientation of the material within the sampling volume.

An inhomogeneous distribution of the diffracting material has an impact on the distribution of the scattered neutrons because it changes the effective geometry of the measurement, and the angular position of the diffraction peak obtained will be affected, which in turn influences the measured strain. Unlike in the case of chemistry variations and intergranular strains, this effect is not associated with a change in lattice spacing.

An explanation of this effect is provided by Webster *et al.* [83]. They identify three contributing causes, namely: a. the variation of the wavelength across the incident beam, b. an asymmetric clipping of the diffracted peak profile, and c. the lateral displacement of the 'effective centre' of the gauge volume relative to the detector.

a. Figure 8.1 (a) illustrates how the wavelength variation in the incident beam affects the observation of the distribution of the diffracted neutrons. The instrument geometry generates a narrow band of neutron wavelengths impinging on the specimen and different sectors of this wavelength band impinge on grains at different positions within the sampling volume. The measured diffraction peak represents the sum of the contributions from these individual grains, each seeing a slightly different wavelength distribution. For a coarse grained material, when the measurement location in the specimen is changed, this is likely to result in a shift of peak position on the detector in addition to the shift associated with the inherent lattice strain because of the small number of grains contributing to the peak signal and their inhomogeneous distribution within the sampling volume.

b. Different parts of the sampling volume contribute signals to different locations on the detector as shown in Fig. 8.1 (b). In the case of peak clipping the beam aperture can block some of the diffracted neutrons from reaching the detector. In a coarse grained material it is likely that the effect of peak-clipping on the observed neutron distribution on the detector is non-symmetric, resulting in an effective shift of the peak position and an error in the determined strain. For a fine grained material, peak clipping will be nearly symmetrical, the contribution from any individual grain will be small and the influence of clipping on the peak position will be negligible.

c. The impact of the lateral displacement of the centre of the gauge volume as "seen" by the detector is illustrated in Figure 8.2. An uneven distribution of large grains in the sampling volume can shift the diffraction peak position on the detector without this shift being associated with a change in lattice spacing.

8.4.3 Magnitude of grain size effects

The magnitude of grain size effects can be significant. For example, in a coarse grained stainless steel an effect has been observed that exceeded the maximum real lattice strains present [90]; the open symbols in Fig. 8.3 represent this data set. These

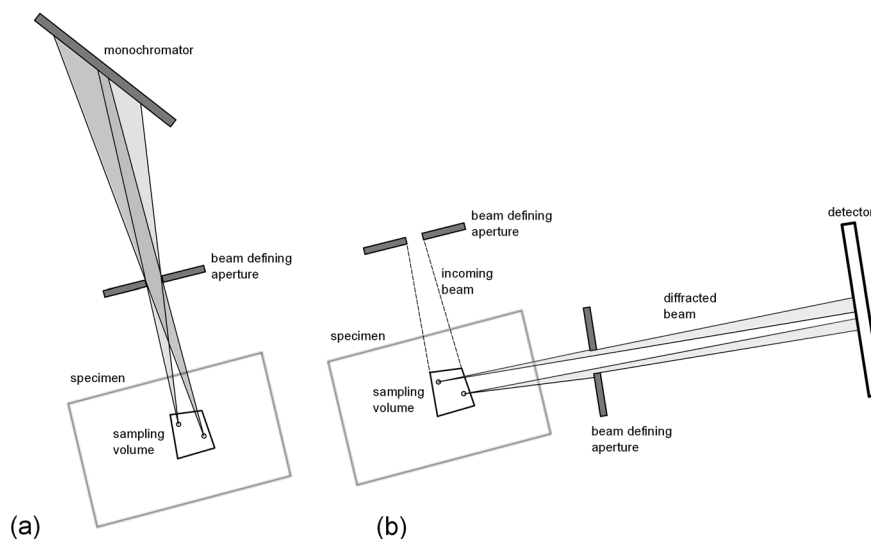


Figure 8.1: (a) Illustration how different sectors of the wavelength band impinge on different locations within the sampling volume. (b) Illustration of an asymmetric peak clipping effect. Sketches not to scale.

measurements have been taken on a welded stainless steel (grade SS347) specimen. The tensile strain peak around position 0 is associated with the welding stresses. The data on the right hand side of the plot are significantly affected by the grain size within that plate. Measurement artifacts of up to $1100 \mu\text{m}/\text{m}$ are observed exceeding the maximum real strains measured in this case by a factor of almost 2. Rocking of the sample led to the sampling of more grains from within a given gauge volume and to the measurement of a more realistic strain distribution (filled symbols in Fig. 8.3).

Pirling [84] has provided an estimation for the possible magnitude of the effect caused by the shift of the position of the effective centre of the sampling volume (as shown in Fig. 8.2). According to this assessment in the case of a $2 \times 2 \text{ mm}^2$ cross section of the sampling volume at a diffraction angle around 90° , the maximum conceivable shift of the diffraction peak would correspond to $400 \mu\text{m}/\text{m}$ in terms of apparent strain. This extreme case corresponds to the situation that all diffracting material is concentrated in one of the outermost corners of the sampling volume. The data presented in Fig. 8.3, which have been collected using a measurement geometry similar to that studied by Pirling, exhibit a grain size effect more than two and a half times this number. It may therefore be concluded that the effective shift of the neutron wavelength impinging on the sampling volume and/or peak-clipping, are the main factors contributing to the effect in this case.

Establishing the presence of a grain size related problem in a strain/stress measurement is normally not possible based on an individual diffraction peak. A number

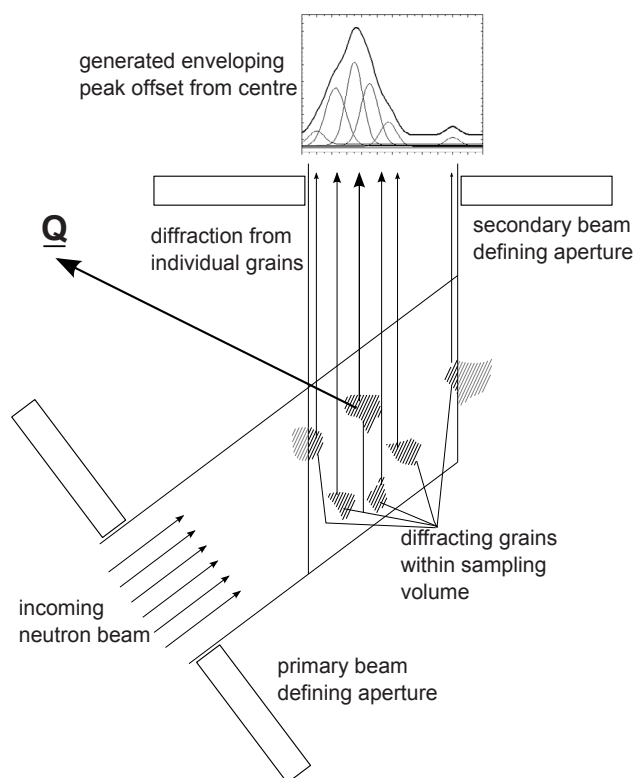


Figure 8.2: Sketch of a polycrystalline aggregate, where only grains within the sampling volume, having a set of lattice planes oriented normally to the scattering vector Q , that fulfils the Bragg condition (3.1), contribute to the diffraction signal recorded on the detector. An effective shift of the centre of gravity of the sampling volume results when the distribution of the diffracting grains is not homogeneous.

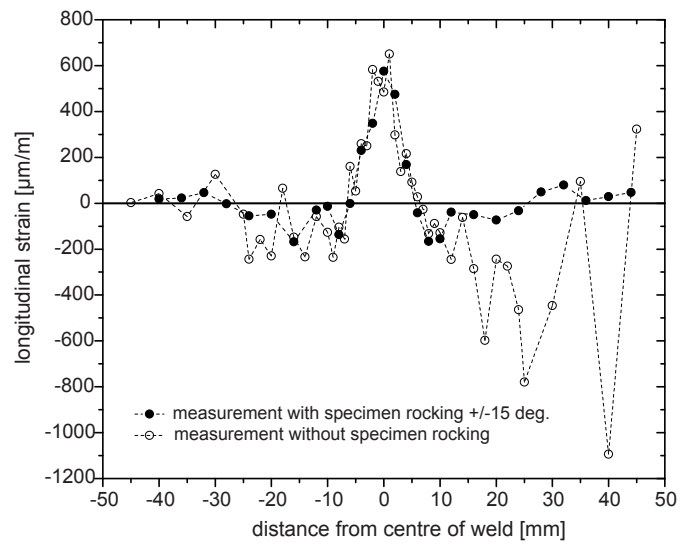


Figure 8.3: Measured longitudinal strains in a welded stainless steel specimen with and without rocking of the specimen; the right hand side of the graph exhibits a significant grain size effect in the measurement without rocking.

of possibilities for showing the presence of grain size problems in diffraction measurements are described in [6]. With a one-dimensional detector, significant variations in peak intensities between measurements from different positions or different specimen orientations indicate that a grain size problem is present. On a two-dimensional detector a grain size problem often can be seen from a single measurement through a non homogeneous (spotty) distribution of the diffraction signal on the detector surface.

Wimpory *et al.* [68] have provided suggestions for analyzing the average grain size in a welded steel specimen directly from neutron diffraction data. They also proposed a method for assessing the additional contribution to uncertainty in strain measurement stemming from the grain size effect. The application of these methods, however, requires additional neutron measurements that are not performed in the context of a normal series of strain/stress measurements such as those reported in the present work.

In order to mitigate grain size effects in diffraction based strain measurements, it is necessary to increase the number of grains contributing to the diffraction signal. This can be achieved by increasing the sampling volume, or by increasing the number of grains contributing from within the same sampling volume through rotation of the specimen about the axis perpendicular to the diffraction plane and passing through the sampling volume during the measurement; *i.e.*, rocking of the specimen. There are, however, limits to the application of these mitigation techniques. A minimum resolution in space (sampling volume) and diffraction angle (specimen rocking) is required for every investigation of residual stresses, and this means that depending on the requirements associated with a stress investigation, there is a limiting grain size, above which these effects can no longer be experimentally overcome.

For the experimenter it is always necessary to be aware of possible grain size related problems and where necessary to apply the appropriate experimental techniques to minimize the impact of grain size effects on the measurement of strain.

8.4.4 Analysis of the scatter in the measured data

In order to determine whether the impact of grain size and/or lack of material homogeneity on the uncertainties of the measurements is significant in relation to the quoted uncertainties based on the fitting errors, the results for the clad layer specimen and the 51 mm bi-metallic piping weld presented in chapters 6 and 7 are examined.

For the residual stress distribution in the clad layer specimen, stresses in the interface normal direction are scattered around 0 MPa in the clad layer and in the substrate material (see Fig. 6.7).

The average deviation of the plate normal residual stresses in the ferritic steel substrate from 0 MPa is found to be in good agreement with the average uncertainty of the stresses quoted for these measurements. This implies that the uncertainties derived solely by using the fitting uncertainties of the neutron data in eq. (8.2) and (8.4) reasonably reflect the real measurement uncertainties of the stresses in the ferritic part of this specimen.

Following the same approach for the normal stresses in the clad layer, a standard

deviation of the measured stress values of 52 MPa is found, while the average quoted uncertainty based on the fitting errors only is 29 MPa. These numbers suggest that the use of fitting uncertainties alone did not suffice to obtain appropriate stress measurement uncertainties for the clad layer.

For this particular case these numbers give an indication of the extent to which the fitting uncertainties do not comprehensively reflect the uncertainty of the stress measurements in weld material. However, it is not possible to quantitatively determine the individual contributions of the different factors.

For the measurements reported in chapter 7 there are no areas and measurement directions in the fusion zone for which the assumption of a constant strain or stress value could be made *a priori*; thus a similar simple assessment as for the clad layer specimen is not feasible. In order to provide some quantitative information on the validity of the quoted errors, an analysis of the distribution of the fitted peak positions in the fusion zone is performed. The following data plots show peak positions measured at the locations in the buttering layer and the weld fusion zone as shown in Fig. 7.12.

Figures 8.4 to 8.6 show examples of the measured peak positions, in the pipe as well as in the reference specimens, including their fitting uncertainties. The data plots presented here suffice to derive a few qualitative statements about the measured data.

Figure 8.4 shows the peak positions measured in the circumferential direction along the line 4.25 mm from the outer piping wall. Figure 8.5 shows measurement results in the axial direction along a line 12.75 mm from the outer wall and Fig. 8.6 shows radial measurement results, again from locations 4.25 mm from the outer piping wall.

It can be seen from these plots that the difference between reference and component measurements; *i.e.*, the strain measured, has the highest amplitudes in the circumferential direction. For the radial and axial directions the measured strains are generally smaller (see also Figs. 7.20, 7.21 and 7.22), and in the examples presented here, even changes between tensile and compressive strains occur along the lines of measurement.

In all data plots it can be seen that the variation of the reference peak position along the corresponding line of measurement appears to be larger than the fitting uncertainties of these measurements.

It is also seen from the data plots that the reference peak position variation is larger in the piping radial and axial directions than it is in the circumferential direction.

Tables 8.1 to 8.3 give an overview of the average uncertainties and standard deviations of the reference peak positions, when building the averages along the lines of measurements in the buttering layer and the weld fusion zone. Next to the average of the fitting uncertainties shown in the data plots (Figs. 8.4 to 8.6), the corresponding standard deviations of the fitted values are given. The tables show that the standard deviation of the reference peak positions is significantly larger than their fit uncertainties. When making the simplifying assumption that the reference peak positions should be constant along each individual line of measurement it is possible to estimate the uncertainties based on the standard deviation of the data.

For the circumferential direction, where the scatter of the reference data is by far

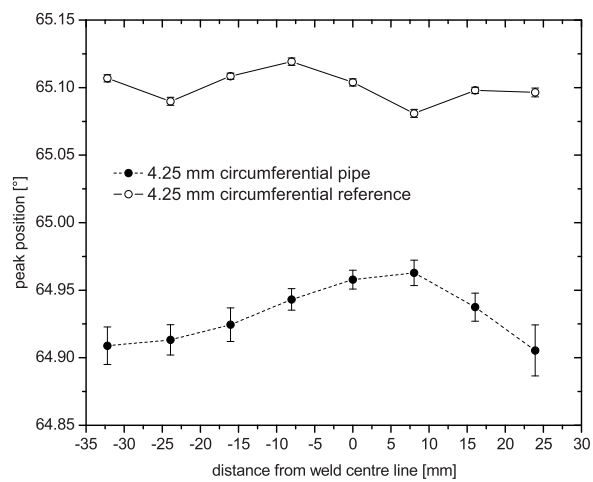


Figure 8.4: Peak positions measured in the circumferential direction at positions in the buttering layer and weld fusion zone, 4.25 mm from outer surface.

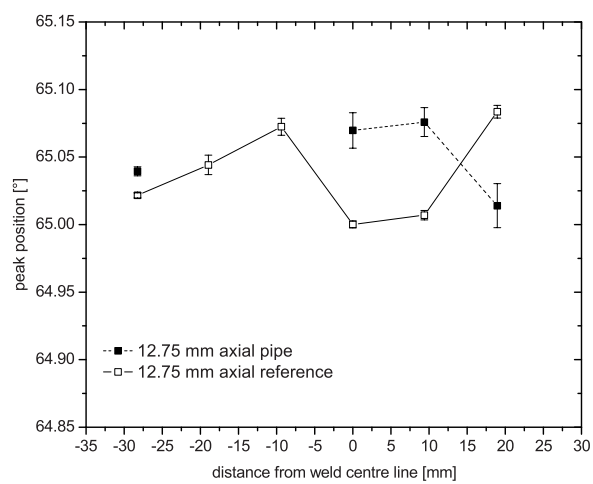


Figure 8.5: Peak positions measured in the axial direction at positions in the buttering layer and weld fusion zone, 12.75 mm from outer surface.

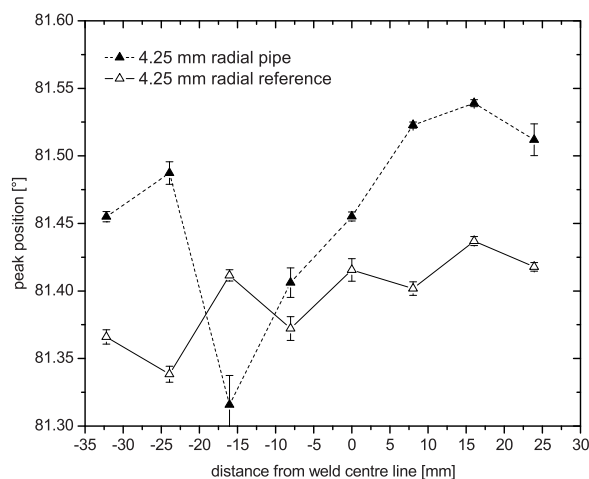


Figure 8.6: Peak positions measured in the radial direction at positions in the buttering layer and weld fusion zone, 4.25 mm from outer surface.

the smallest, this analysis results in an increase of the strain uncertainties by a factor of 1.2 to 2 compared to the values obtained from the fitting uncertainties alone. The range of the circumferential strain measurement uncertainties would then increase to ± 200 to $\pm 300 \mu\text{m}/\text{m}$. While representing a considerable increase in the uncertainty of the measurement, these figures have to be compared to the strains measured in the circumferential direction. These are mostly in the range 2000 to 3000 $\mu\text{m}/\text{m}$. Therefore reasonable strain measurements in this direction have still been obtained even when considering such increased uncertainty levels.

For the axial and radial directions, where the scatter of the reference data was found to be larger than in the circumferential direction, this analysis results in an increase of the reference peak position uncertainties by factors in the range 2 to more than 10. In most cases the resulting strain uncertainties increase to more than $\pm 500 \mu\text{m}/\text{m}$; as this number is mostly in the order of or larger than the strains actually measured, this analysis suggests that the measurements in these directions have limited value.

A further assessment of the above findings is of a more qualitative nature. One conclusion from the analyses presented is that chemistry variations within the fusion zone are not the main contributor to the variation in reference measurements as these variations would normally be expected to be independent of the measurement direction. This leaves the following aspects as the main factors impacting on the scatter in the data: the material grain size and variations in preferred crystallographic orientation within the sampling volume.

Table 8.1: Average reference peak positions and fitting uncertainties for the circumferential direction, plus standard deviations of the peak positions calculated for measurement locations at the same depth (cf. Fig. 7.12).

Averages of the reference peak positions in the circumferential direction						
	weld fusion zone & butt. layer			weld fusion zone		
Depth [mm]	Average peak pos. [°]	Average \pm uncert. [°]	Standard deviation [°]	Average peak pos. [°]	Average \pm uncert. [°]	Standard deviation [°]
4.25	65.1004	\pm 0.0027	0.0119	65.0995	\pm 0.0027	0.0125
12.75	65.0908	\pm 0.0035	0.0086	65.0936	\pm 0.0031	0.0086
21.25	65.0859	\pm 0.0033	0.0096	65.0881	\pm 0.0031	0.0089
29.75	65.0809	\pm 0.0038	0.0043	65.0793	\pm 0.0036	0.0036
38.25	65.1000	\pm 0.0041	0.0082	65.1015	\pm 0.0039	0.0094
46.75	65.0823	\pm 0.0031	0.0011	65.0831	\pm 0.0031	

Table 8.2: Average reference peak positions and fitting uncertainties for the axial direction, plus standard deviations of the peak positions calculated for measurement locations at the same depth (cf. Fig. 7.12).

Averages of the reference peak positions in the axial direction						
	weld fusion zone & butt. layer			weld fusion zone		
Depth [mm]	Average peak pos. [°]	Average \pm uncert. [°]	Standard deviation [°]	Average peak pos. [°]	Average \pm uncert. [°]	Standard deviation [°]
4.25	65.0414	\pm 0.0048	0.0453	65.0444	\pm 0.0049	0.0481
12.75	65.0382	\pm 0.0063	0.0376	65.0415	\pm 0.0049	0.0376
21.25	65.0281	\pm 0.0051	0.0344	65.0278	\pm 0.0055	0.0385
29.75	65.0560	\pm 0.0039	0.0338	65.0660	\pm 0.0046	0.0332
38.25	65.0211	\pm 0.0051	0.0126	65.0230	\pm 0.0059	0.0148
46.75	65.0624	\pm 0.0043	0.0088	65.0687	\pm 0.0058	

Table 8.3: Average reference peak positions and fitting uncertainties for the radial direction, plus standard deviations of the peak positions calculated for measurement locations at the same depth (cf. Fig. 7.12).

Averages of the reference peak positions in the radial direction						
	weld fusion zone & butt. layer			weld fusion zone		
Depth [mm]	Average peak pos. [°]	Average \pm uncert. [°]	Standard deviation [°]	Average peak pos. [°]	Average \pm uncert. [°]	Standard deviation [°]
4.25	81.3950	\pm 0.0055	0.0329	81.3992	\pm 0.0055	0.0333
12.75	81.3681	\pm 0.0066	0.0114	81.3681	\pm 0.0083	0.0114
21.25	81.3438	\pm 0.0192	0.0227	81.3327	\pm 0.0265	0.0171
(different measurement settings for inner three and outer three depths in the radial direction measurements are responsible for the significant differences in the observed averages)						
29.75	81.5120	\pm 0.0043	0.0635	81.4933	\pm 0.0049	0.0630
38.25	81.5118	\pm 0.0038	0.0659	81.4934	\pm 0.0038	0.0669
46.75	81.5248	\pm 0.0040	0.0075	81.5195	\pm 0.0034	

In view of the relatively low scatter in the circumferential data, the conclusion is that in this direction, which corresponds to the welding direction, the number and distribution of diffracting grains is satisfactory for reliable measurements. For the other two directions, this analysis suggests that the grain size distribution and the distribution of favourably oriented: *i.e.*, diffracting, material within the fusion zone are so inhomogeneous that the measurements of the peak positions are strongly affected. The effects of this are enhanced by the thickness of the component, leading to the measurement of relatively weak diffraction peaks in many cases.

In conclusion, strain measurements in the axial and radial directions in the case of the 51 mm bi-metallic weld have proven to be difficult to analyze, interpret and to associate with realistic measurement uncertainties. For the measurements in the circumferential direction, the additional uncertainties caused by large grain sizes and texture variations remain within an acceptable range in view of the magnitude of the strains measured and because the data scatter is significantly lower than in the other two directions.

8.4.5 Variability of grain size effects along the weld

There are some locations where the variations in the reference and the component measurements appear to be highly correlated, despite the large point-to-point variations in the observed peak positions. The most prominent examples are the piping axial and radial directions at 21.25 mm and 38.25 mm from the outer piping wall, respectively (Figs. 8.7 and 8.8). This indicates that the cause of the variation in the measurements has been maintained nearly constant over a relatively large distance along the weld; that is to say, a distance corresponding to about one third of the piping circumference; *i.e.*, ca. 450 mm.

While it is interesting to make this observation, it needs to be stated also that this clearly does not happen at every location. In the majority of the data sets from the fusion zone, such similarities are not found; moreover, in some cases also opposing trends are seen (*e.g.*, Fig. 8.5). This may be related to the numerous occurrences of start-stop positions within the fusion zone. The weld has been applied using stick electrodes of 350 mm length [91], suggesting that the electrode was changed every ~300 mm. With an estimated total bead length of ~190 m this results in some 600 arbitrarily distributed start-stop locations within the fusion zone.

The factors impacting on the measured peak position should be expected to be different for a start/stop location compared to a location in the middle of a bead length. This suggests that in order to obtain a better quality of strain measurement the reference specimen should be cut at or very near to the actual strain/stress measurement location within a specimen.

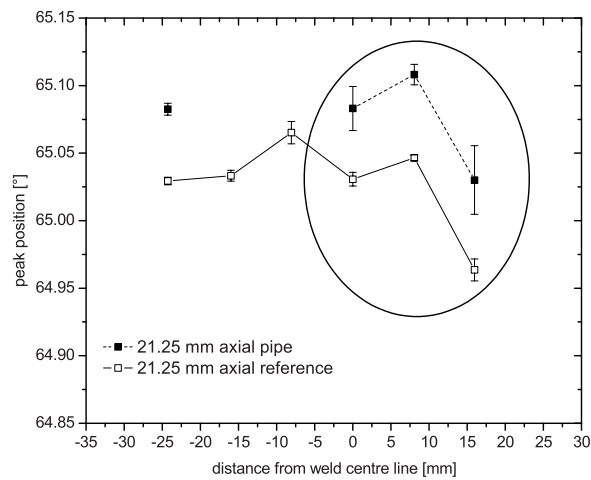


Figure 8.7: Peak positions measured in the axial direction at several positions in the buttering layer and weld fusion zone, 21.25 mm from outer surface.

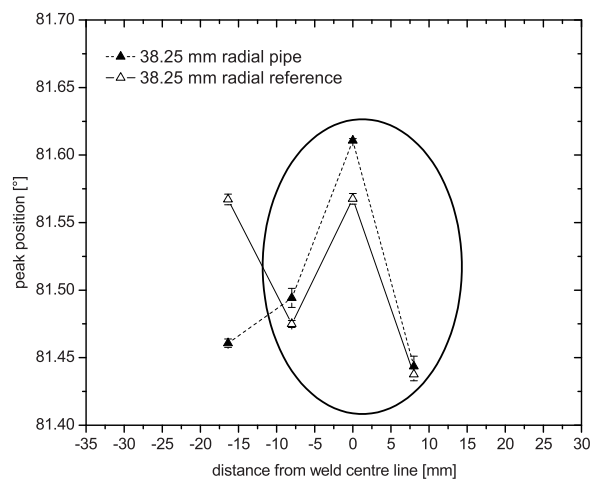


Figure 8.8: Peak positions measured in the radial direction at several positions in the buttering layer and weld fusion zone, 38.25 mm from outer surface.

8.5 Significance of instrument calibration

8.5.1 Uncertainty due to lack of calibration

All neutron diffraction measurements presented in this work have been performed on a facility that had not been calibrated prior to measurement. The main reasons for this were as follows:

- a. Waiving of instrument calibration generated economies in total measurement time. All measurements presented here went along with frequent changes of the instrumental settings; *i.e.*, of the neutron wavelength and the detector angle used. Working with a calibrated instrument would have meant recalibration with every change of the settings, often while a big specimen was mounted on the instrument table.
- b. At the time of these measurements, the opinion prevailed that calibration would not add to the accuracy and reliability of the strain measurements. This was based on the assumption that the main contributor to the strain measured through 8.1 would be the difference between the measured Bragg angles θ_{hkl} and $\theta_{0,hkl}$. The accuracy of the absolute values of these angles was believed to play a minor role. These strain measurements were considered to be “self-calibrating” to a certain degree for this reason.
- c. Equation (8.1) does not call for the determination of the lattice spacing in order to calculate the strain in accordance with eq. (3.2). Determination of lattice spacing using Bragg’s equation (3.1) does necessitate the calibration of the facility, as otherwise neither a correct value of the lattice spacing nor its uncertainty can be obtained. Strain measurement using eq. (8.1), on the other hand, seemed to be feasible using equipment that is not accurately calibrated.

The purpose here is to assess the impact of using a non-calibrated diffractometer, as described in chapter 3, on the uncertainty of strain measurements. The applicable experimental pre-requisites for working with a non-calibrated instrument are mentioned in chapter 3 and it is not the intention to discuss these here.

The purpose of diffractometer calibration for residual stress/strain measurement

The basis for measurements of strains and stresses by (neutron) diffraction is the Bragg principle as expressed in eq. (3.1). This principle facilitates the absolute determination of the lattice spacing, d_{hkl} , provided that the wavelength, λ , is known and the angular response of the detector is correct; *i.e.*, provided that the instrument is properly calibrated.

As the lattice spacing does not appear in eq. (8.1), it is not necessary to determine the lattice spacing for the measurement of strain provided that the conditions given in chapter 3 are fulfilled for the measurement.

Nevertheless, calibration does fulfill several important functions:

- It facilitates reproducibility.
- It facilitates transferability of results between instruments.
- It facilitates relating results between measurements with the same instrument, but with different settings or circumstances.
- Last, but not least, it generates additional confidence in the results produced.

As demonstrated by the following considerations, calibration contributes to the accuracy of the measurements.

Assessment of the uncertainty contribution of a non-calibrated diffractometer to the measurement of strain

For this discussion it is assumed that the requirements for the application of eq. (8.1) are fulfilled in a given measurement, namely that strain and reference measurements are performed with the same instrument settings on a stable instrument (see chapter 3) and using identical materials. Furthermore it is assumed that, through the lack of calibration, the value of the wavelength λ is not known and that the detector position is subject to an unknown, but constant, offset $2\theta_{offset}$.

For measurements of strain in accordance with eq. (8.1), the wavelength does not play a role. It does not appear in (8.1), and therefore, under the given conditions, the measurement of strain would be possible and the strain uncertainty would be independent of the uncertainty in the neutron wavelength.

In the following discussion the impact of the unknown offset in the detector position is examined. One should keep in mind that in many cases, operator experience and/or optical means facilitate the determination of the detector position to a certain degree of accuracy. As the measured Bragg angles, $\theta_{observed}$, appear in eq. (8.1), it is to be assumed that any difference between these observed Bragg angles, and the real ones; *i.e.*, the observed angles corrected by the offset of the detector position as given by

$$\theta_{real} = \theta_{observed} + \theta_{offset} , \quad (8.5)$$

would have a certain impact on the accuracy of the strain measurement as

$$\frac{\sin \theta_{real,0,hkl}}{\sin \theta_{real,hkl}} - 1 \neq \frac{\sin(\theta_{real,0,hkl} - \theta_{offset,0,hkl})}{\sin(\theta_{real,hkl} - \theta_{offset,hkl})} - 1 = \frac{\sin \theta_{observed,0,hkl}}{\sin \theta_{observed,hkl}} - 1 , \quad (8.6)$$

even though the error in strain is reduced as the error in angle impacts in a similar way on the numerator and the denominator of eq. (8.6).

The question remains to be answered, how much of an error through an unknown offset of the detector position is admissible before the additional uncertainty in strain becomes significant. For the purpose of the discussion a set of values for an assumed $2\theta_{real}$ and $2\theta_{offset}$ are chosen. The values for the real peak positions are chosen as 60° , 65° and 75° , which are settings that are typically applied at the neutron

diffraction facility mainly used for the investigations presented in this work. For the following discussion the term $\Delta\theta_{hkl}$ is defined as

$$\Delta\theta_{hkl} = \theta_{hkl} - \theta_{0,hkl} , \quad (8.7)$$

which is the same number in the system of real Bragg angles and in the system of observed Bragg angles. The strain (eq. 8.1) is closely approximated for the real angles by

$$\varepsilon_{hkl} = -\cot\theta_{0,hkl} \cdot \Delta\theta_{hkl} . \quad (8.8)$$

Therefore the deviation in strain caused by incorrect assumption of the detector offset can be obtained from

$$\frac{\varepsilon_{hkl,observed}}{\varepsilon_{hkl,real}} \cong \frac{\cot\theta_{observed,0,hkl}}{\cot\theta_{real,0,hkl}} = \frac{\cot(\theta_{real,0,hkl} - \theta_{offset,0,hkl})}{\cot\theta_{real,0,hkl}} . \quad (8.9)$$

From (8.7), (8.8) and (8.9) it can be seen that the error introduced by ignorance of the detector position is a figure relative to the strain that is actually measured.

For this analysis, the range of assumed offsets of the detector position ($2\theta_{offset}$) is limited to $\pm 30^\circ$. The relative error in strain introduced by such detector offsets is calculated for the real 2θ -values given above and plotted for the range $\pm 30^\circ$ in Fig. 8.9. It can be seen that on the outer ends of the range, highly unacceptable relative strain errors are produced by not knowing the detector position sufficiently well. When underestimating the detector angle by 30° relative strain uncertainties in the vicinity of 100% are introduced.

It is normally feasible for the experimenter to spot a detector mispositioning of 30° by simple observation. Therefore in Fig. 8.10 the plotting range is reduced to $\pm 3^\circ$. The resulting range of error in strain is now in the range 6% to -6% and in this range the relationship between detector position uncertainty and resulting strain uncertainty is almost linear. Therefore, for 1° and 2° deviation of the detector position, the resulting strain uncertainty would be around 2% and 4%, respectively. On $2500 \mu\text{m}/\text{m}$ a detector position uncertainty of $\pm 1^\circ$ introduces an additional strain uncertainty of $\pm 50 \mu\text{m}/\text{m}$, $\pm 2^\circ$ would add $\pm 100 \mu\text{m}/\text{m}$.

It follows that for measurements of high strains only small uncertainties of the detector position are admissible. In cases like those presented here the uncertainty should be of the order of $\pm 1^\circ$ or less.

8.5.2 Example

As the measurements presented in this work have been performed without calibrating the instrument, a possible uncertainty contribution related to the detector position has to be considered. The question would be whether one could claim to have worked with assumed detector positions that have been close enough to reality.

A likely error in this case is revealed when looking at the data used in chapter 6 on the clad layer specimen. An overview of the nominal wavelengths and detector angles

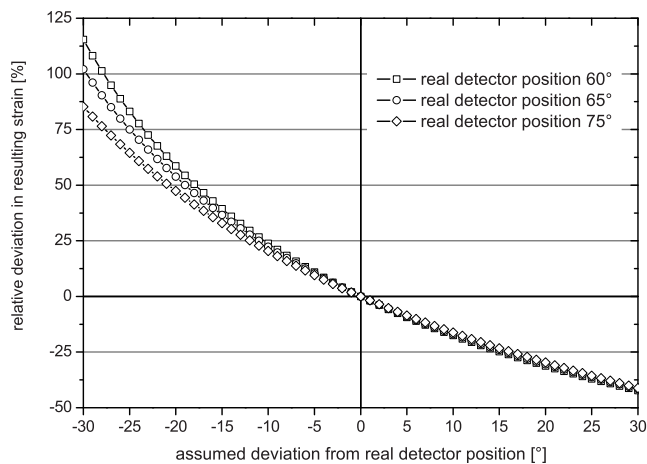


Figure 8.9: Relative error in calculated strain caused by an incorrect estimation of the detector position, range -30° to $+30^\circ$.

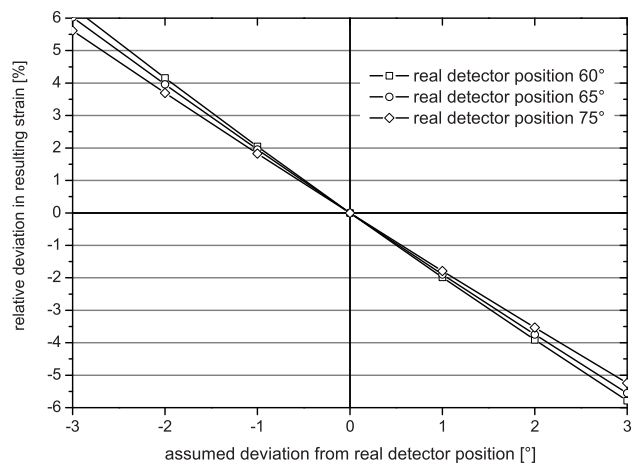


Figure 8.10: Relative error in calculated strain caused by an incorrect estimation of the detector position, range -3° to $+3^\circ$.

Table 8.4: Important parameters of the neutron diffraction measurements from Table 6.2

Lattice plane used in ferrite:	(110)		
Corresponding lattice spacing:	~ 0.203 nm		
Lattice plane used in austenite:	(200)		
Corresponding lattice spacing:	~ 0.18 nm		
Nominal neutron wavelengths used:			
Ferrite weld longitudinal:	0.2304 nm		
Ferrite weld transverse:	0.2400 nm		
Ferrite plate normal:	0.2956 nm		
Cladding weld longitudinal:	0.2000 nm		
Cladding weld transverse:	0.2300 nm		
Cladding plate normal:	0.2300 nm		
Diffraction angles :	Set for measurement:	Calculated:	Difference:
Ferrite weld longitudinal:	67.95°	69.15°	1.2°
Ferrite weld transverse:	71.25°	72.47°	1.2°
Ferrite plate normal:	91.9°	93.45°	1.55°
Cladding weld longitudinal:	65.92°	67.5°	1.6°
Cladding weld transverse:	77.9°	79.42°	1.5°
Cladding plate normal:	77.9°	79.42°	1.5°

used was given in Table 6.2. The nominal neutron wavelengths and the detector positions from this table relevant for this discussion are presented again in Table 8.4 together with estimated values for the spacing of the ferrite (110) and the austenite (200) lattice planes. Based on Bragg's equation (3.1), the lattice spacings and the nominal wavelengths, the expected detector positions have been calculated. These expected positions are also shown in Table 8.4. From this assessment one can see that all set values of the detector position have been 1.2° to 1.6° too low. It is considered likely that this error of about 1.5° on the average is indeed an error of the zero-position of the detector, which had not been detected because a) nothing had been calibrated, b) none of the settings in these measurements was performed for the standard austenitic (111) reflection and the standard detector angle of $\sim 76^\circ$ and c) a check of the numbers had not been performed during the measurements. Based on Fig. 8.10 this error in detector position of about 1.5° means that all strain measurements presented in chapter 6 carry a systematic error of about 3%.

The consequences of this have been analysed in order to show the real impact of this error, of which the direction; *i.e.*, the sign, and magnitude could be more or less determined. Figures 8.11 and 8.12 show the correction of the strains and stresses resulting from a shift of the assumed detector position by 1.5° in the analysis of these data.

The strains and stresses show that for this particular case, although a visible deviation in the measured strain and stress values resulted from this correction, the

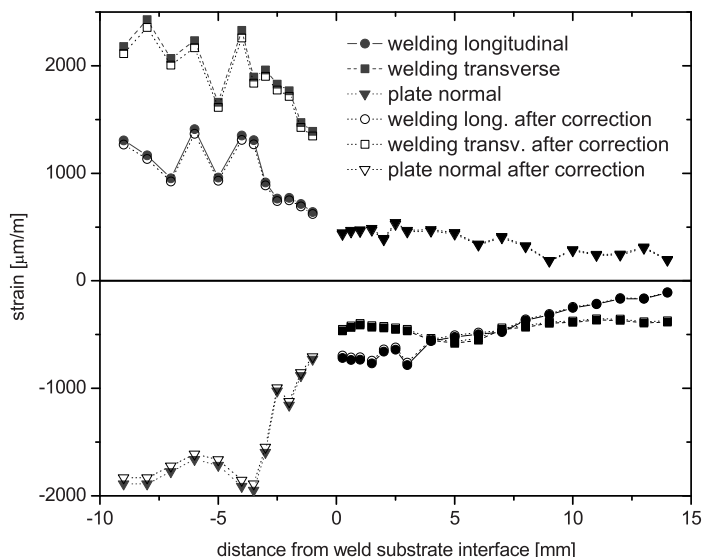


Figure 8.11: Shift of the strains measured in a clad component based on a correction of the detector position by 1.5° .

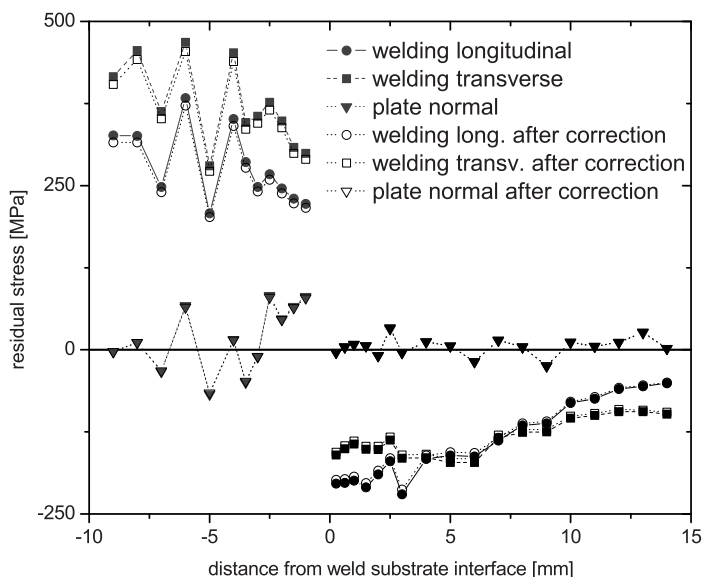


Figure 8.12: Shift of the stresses measured in a clad component based on a correction of the detector position by 1.5° .

conclusions derived from these measurements as far as the measured strain and stress distributions are concerned are not affected by the 3% change. Nevertheless, for the high strain levels of 2500 $\mu\text{m}/\text{m}$ or more an additional error of 75 $\mu\text{m}/\text{m}$ has been introduced by lack of calibration.

In this particular case a systematic error was present, such that the direction of the shift was known and a correction of the data was possible. While the situation in general would always represent a systematic error, it would normally have to be included in the uncertainty analysis of the strains when the direction of the deviation of the detector position from the real value is not known.

It has been shown that for measuring high strains and consequently high stresses, the detector angle should be known to within $\pm 1^\circ$ in order to avoid excessive additional measurement uncertainties. As it is not possible to position the neutron detector that accurately by naked eye, some kind of measurement should normally be used to demonstrate the "correctness" of the detector position. It would not necessarily have to be a full calibration, but it should be good enough for the required accuracy. The detector position uncertainty, if more than $\pm 1^\circ$, should be included in any complete assessment of the measurement uncertainty.

8.6 Overview of the uncertainty contributors

The measurement uncertainties for strain and stress that have been presented in this work were based exclusively on the fitting uncertainties of the neutron diffraction data. This is a commonly used approach in neutron diffraction stress measurement.

In the previous sections several other potential contributors to measurement uncertainty have been analyzed in relation to their possible importance for these measurements. Table 8.5 provides an overview of these sources. The column "Dependence on strain value" indicates whether or not the magnitude of the uncertainty from a given source is dependent on the magnitude of measured strain. In the column "Quantifiable" statements are made on how easily the associated uncertainty can be quantified. Finally in the column "Magnitude" quantitative estimates are provided, where possible, of the strain uncertainties associated with the different sources for the measurements presented in this work.

In summary it can be said that for these measurements the fitting uncertainties and the material inhomogeneities/grain size effects are the most important contributors to the measurement uncertainty. In the fusion zones the latter often generated the larger uncertainty contribution.

8.7 Comparison with other experimental methods

In order to set the stage for this short analysis of the comparison of the neutron diffraction results presented in chapters 6 and 7 with corresponding results obtained by other experimental methods, a few fundamental statements about residual stress measurements should first be made.

Table 8.5: Overview of uncertainty contributors.

Source of uncertainty	Dependence on strain value	Quantifiable	Magnitude
Fitting	No	Yes	70 - 300 $\mu\text{m}/\text{m}$ in these measurements
Wavelength			Not considered here
Temperature	No	Yes, temperature range needs to be estimated	10 - 50 $\mu\text{m}/\text{m}$ in these measurements
Chemical composition	No	Difficult	Not assessed here because of reference variation measurements
Measurement position (on a strain gradient)	No	Yes	10 - 30 $\mu\text{m}/\text{m}$ in these measurements
Diffraction elasticity constants	Yes	Mathematically yes; however, not many data available	Most significant for high strains and stresses as found in the fusion zones
Material inhomogeneities - grain size effects	No	Data scatter analysis needed; not always possible	2 to 10 times larger than fitting uncertainty for some of the measurements in Chapter 7
Instrument calibration	Yes	Yes	Can be equal to fitting uncertainty with 1° or 2° uncertainty in detector position

a. There is no method that measures (residual) stresses directly [10]. As the dimension of a stress in this context is basically the dimension of force divided by unit area, experimental access is only possible to effects of the stress. Strain is the property that is in most cases measured. For example, diffraction methods measure strains in order to ultimately determine stresses.

b. Different methods of stress measurement actually do (slightly) different things - as mentioned in the previous sections. This is particularly relevant in terms of measurement geometry and spatial or strain resolution. These are different for the neutron diffraction and the strain relaxation methods used here in the comparisons. On top of these principal differences between methods, in many cases different test pieces have been investigated by the different methods. Nevertheless, it is possible that such different measurement methods can produce residual stress distributions that are very similar. Traore *et al.*, for example, achieved an agreement between neutron diffraction, the crack compliance technique and the contour method on a compact tension weld specimen to within 50 MPa for most test locations where a comparison was made [92].

c. "There is no reference measurement method for residual stresses." [93] - this statement follows to a certain extent from a. and b. Since all measurement methods are based on somewhat different principles and therefore they are in most cases applicable for different situations/cases; there is no standard method, against which the results of a stress measurement can be calibrated. Hence no claims can be made as to which of the different stress measurements presented has rendered the true stress values.

Different stress measurement methods have been applied in the case of the clad layer component (chapter 6) and the 51 mm dissimilar metal piping weld (chapter 7).

In the case of the clad layer component the ring core method and the deep hole drilling method have been applied next to neutron diffraction for stress determination. For each of the methods a test piece of a different size and shape was made available. The 2-dimensional strain relaxation methods worked on the assumption that the interface normal stress would be 0 MPa. Neutron diffraction does not make this assumption, but the neutron diffraction measurements (see Fig. 6.7) confirmed the correctness of this assumption for most of the measurements.

All measurement methods have found tensile residual stresses in the range 250 to 500 MPa in the clad layer in the welding and welding transverse directions. The neutron diffraction and the ring core data exhibited significant scatter unlike the deep hole drilling data. There seem to be three different answers to the question, which of these two directions exhibits higher stresses. Neutron diffraction found higher stresses in the welding transverse direction, deep hole drilling measured the welding direction stresses to be higher and the ring core method found the stresses in both directions to be at the same level. The available information in this case does not provide the arguments to decide which of the three sets of measurements gives the closest representation of the real stress distribution in the clad layer.

Unlike the other two methods, neutron diffraction suggested a steep stress gradient at the material interface. It is possible that the relaxation behaviour during cutting across the tension to compression transition prevents such a steep gradient from being picked up by the strain relaxation methods. Neutron diffraction is not influenced by such effects. Because of the finite sized sampling volume the neutron measurements have a blind spot of a width of about 1 mm at the interface in question. Even when taking into account this blind spot, the neutron diffraction data still show the steepest gradient of stress at the interface.

For the substrate material, a quantitative comparison of the results is not possible. The neutron diffraction component had been substantially cut prior to measurement, whereby the residual stresses in the substrate have almost certainly been significantly altered. Furthermore, the ring core measurements appear to be insufficiently reliable at this depth. Finally, the deep hole drilling measurements have been taken from a test piece that had been cut to less than half the size of the specimen used for the ring core measurements. Also in this case it is not possible to know whether the cutting had an impact on the original stress field. Nevertheless, there is a qualitative agreement between the neutron diffraction and the deep hole drilling results in the substrate. Both data sets show the highest compressive stresses near the interface with the level of compression decreasing when moving away from the interface.

Finally, one should add that the choice of elasticity constants for the strain stress conversion, might also play a role in the differences between the results. The diffraction results were converted to stress based on diffraction elasticity constants whereas the strain relaxation data were translated using bulk elasticity constants. The impact of the choice of elasticity constants has been briefly discussed in the previous section.

In the case of the thick walled dissimilar metal piping weld even fewer alternative measurements are available for comparison with the neutron diffraction data. In this case a number of surface hole drilling measurements have been made as have a small amount of crack compliance method measurements in the axial direction.

The surface hole drilling measurements (Figs. 7.27 to 7.29) show stresses measured at the surface only. Surface locations were not accessible with neutron diffraction measurements in such a thick walled component, and here the stresses were obviously severely influenced by the surface machining of the component. Actually almost all stresses measured by this method were compressive. Therefore no quantitative comparison with neutron diffraction data is possible. Qualitatively, Figs. 7.27 and 7.28 show comparable trends in the circumferential stress distributions found by neutron diffraction and surface hole drilling. It is possible that (additional) compression introduced by surface machining, when superimposed on the stress distribution suggested by the neutron measurements, results in the surface stresses shown in these figures. Nevertheless, the two methods have different domains of application, namely the surface and the bulk of a component, and they cannot be applied for intercomparison of measurement data in cases like this, in particular, when the component has been subject to surface machining or other surface finishing processes.

The crack compliance measurements made in the axial direction only, confirmed that short range surface compressive stresses as found by the surface hole drilling

method exist. The crack compliance tests were performed on a long axial slice cut from the original specimen, based on the assumption that this cutting would not alter the axial stresses significantly. Measurement results were presented along a line from the centre of the fusion zone at the outer surface through the thickness for about 20 to 25 mm and another line from the centre of the buttering layer at the inner surface through the thickness for about 15 mm. Figure 7.32 shows the axial stresses from the crack compliance measurements together with the corresponding results from the neutron diffraction investigations.

There is only a limited number of measurement locations in the weld centre and in the buttering layer near the inner surface, where comparison between the data is possible because of the small number of neutron measurements and because of the large sampling volume. At these locations, the neutron diffraction data are in acceptable agreement with the crack compliance results when taking into account the measurement uncertainty. The situation for the measurements in the buttering layer from the inner surface is similar. In order to put this agreement between the data into perspective, one has to take into account that the number of neutron measurements available for comparison was low, the measurement geometries were extremely different and so were the test pieces used. The use of circumferential stresses for comparison would be more meaningful because of the higher absolute values of strain and stress. Most of the axial stresses compared here were in fact measured to be not very far from 0 MPa.

The comparison of the neutron diffraction measurements presented in this work with results obtained by other measurement methods shows more about the differences between different methods than it does about the neutron diffraction results and the validity of the methods presented here. Different component geometries, different measurement areas (volumes), different measurement resolution and differences in the underlying principles become apparent in these results. Nevertheless, good qualitative agreement between neutron diffraction and deep hole drilling and the ring core method (chapter 6) and between neutron diffraction and the crack compliance method (chapter 7) has been found.

Only in the case of the clad layer in the clad component (chapter 6) is it possible to make a quantitative statement about the comparison between results. Here, all measurement methods found tensile stresses in the same order of magnitude (250 to 500 MPa), with the neutron diffraction results fitting in between the results provided by the other two methods. However, the comparison does not permit any conclusion about which direction exhibits the highest stresses, or which method has the greater accuracy.

For the 51 mm dissimilar metal weld, only a few measurements additional to neutron diffraction have been made. These measurements were based on techniques with a different domain of application than neutron diffraction, namely surface stress measurement by hole drilling and axial, one-dimensional, stress measurements by the crack compliance method. This illustrates the uniqueness of neutron diffraction as a method for this kind of problem; that is, through thickness 3-dimensional measurements on a piping geometry. Nowadays one would also consider deep hole drilling

as an alternative method, but this was not available at the time the specimen was examined.

The qualitative agreement between neutron diffraction residual stress measurements and other methods as presented in chapters 6 and 7 shows at least that neutron diffraction provides a good overview of the stress distribution across the weld zones assessed here. This holds in particular for the fusion zones themselves. Neutron diffraction identifies zones of tensile and compressive stresses, provided the absolute stress values are significant. In addition the stresses measured by neutron diffraction are mostly of the same order of magnitude as those measured by other methods.

8.8 Modeling of residual stresses in welds

Numerical prediction of the performance or behaviour of an engineering component is an indispensable tool, useful for several purposes; design, decision making in manufacturing, but also prediction of remaining life or ex-post assessments after failure *etc.* Numerical analyses are often more economical and flexible than manufacturing and testing of real components. However, in order to verify the validity of a chosen modeling approach, it is at some point always necessary to compare the modeling results against a corresponding measurement. Such experimental validations are even formally required for fracture assessments based on the R6 procedure (section III.15 of [2]).

With the advancement of computation technology, modeling of welding processes has progressed significantly. One would assume that the quality of a model improves with the detail, to which the model describes a process. While the data presented in chapters 5, 6 and 7 show a significant progress in modeling capability, the computation possibilities available today still do not allow for representation of a multi-pass welding process to the finest detail.

The modeling detail presented here ranges from an estimation of the impact of a stress relieving heat treatment in a bi-metallic component while ignoring the welding process itself completely to a 2-dimensional bead-by-bead simulation of the welding process.

In the simple approach the assumption is made that the bi-metallic component at about 600 °C does not contain any residual stresses. This assumption in all probability is not correct. Remaining residual stresses have been reported even in a monolithic material after a stress relief heat treatment at such a temperature [26].

Upon cooling to room temperature, residual stresses are formed due to the thermo-mechanical mismatch of the constituent materials. In directions (quasi-)parallel with the interface the ferritic part is left in compression and the austenitic part is left in tension near the interface. In the cases presented here, the simple approach tended to under predict the tensile stresses in the weld (Figs. 5.14, 5.15, 6.13, 7.37). The comparison with the measurements and the results of more detailed modeling efforts (5.14, 5.15 and 7.37) shows that this approach in these cases has been insufficient.

Figures 5.14 and 5.15 include a comparison between bead lumping and bead-by-

bead modeling results. While they produced similar results in the welding direction, in good agreement with the measurements, there is a difference in the welding transverse direction and the more detailed model is in better agreement with the measurements.

Also in the most complicated case of the thick walled bi-metallic piping weld presented in chapter 7, where more than 100 individual beads had to be taken into account, several groups performed 2-dimensional bead-by-bead modeling of the welding process. Figure 7.37 shows how similar the results of their analyses are and that along the line 4.25 mm from the outer surface they all agree reasonably well with the measurements. Figures 7.34 and 7.35 show that the agreement becomes worse toward the inner surface.

As stated before, numerical models for residual stress analyses need experimental validation at some stage to establish their accuracy or degree of credibility. The results presented here suggest that these welding procedures require modeling of the welding process to a high level of detail in order to obtain results similar to the measurements. Good agreement has been accomplished already with detailed 2-dimensional mechanical analyses. The detail of the thermal analysis decoupled from the mechanical one apparently played a minor role. Simplified models and lumping of beads have produced less reliable results here.

In residual stress modeling the choice of parameters, hardening law *etc.* is paramount. In this work no parametric studies are shown, therefore no statement is possible. From the data shown it can be concluded that good choices have been made here.

By default numerical modeling results should not be used to validate the corresponding measurements. It is not appropriate to draw firm conclusions, and in particular, a quantitative assessment of the accuracy of the neutron diffraction measurements cannot be made based on the numerical data. On the contrary, the above analysis shows how the neutron diffraction data can facilitate the validation of different modeling approaches.

8.9 Validity of the experimental approaches presented

8.9.1 Introductory remarks

In this section the findings of the research are briefly summarized to provide an assessment of the validity of the experimental approaches presented. The main question that has to be addressed is to what extent it has been possible with these methods to produce reliable measurements of residual stress or strain in the components investigated.

The following measurement techniques and challenges have been examined:

- Addressing reference variation related problems for the weld material by using dedicated specimens cut from the original welds. For each of the three components a slightly different reference specimen design has been considered.

- Preparation of the components by removing material to facilitate neutron diffraction measurement. The geometry of all three components tested here necessitated material removal in order to make neutron diffraction stress measurements possible.
- Residual stress measurement has been attempted in a very thick component (51 mm wall thickness). In this case an unusually large sampling volume had to be used, and two questions arise from this: are measurements possible at all and does the unusual size of the sampling volume have an impact on the results?

There are a number of applicable criteria, which can be used to assess the credibility of residual stress or strain distributions that have been experimentally determined. The following criteria have been applied in this assessment:

- Balance of the normal residual stresses over any complete cross section of a component under investigation (eq. 2.4). While this is a prominent criterion for the judgement of residual stress measurements, its application to the present work is limited because in no cases could complete cross sections be subjected to measurement.
- The magnitude of residual stresses found in the through thickness direction of the component should be relatively low for “thin” components or for components where the production process would not be expected to cause stress formation in this direction. This criterion is applicable for two of the cases investigated.
- The comparison with the results of other experimental techniques or of numerical assessments. This has been considered in the previous sections and chapters and is only briefly addressed here.
- The presence of strong point-to-point variations of the peak positions observed in reference and strain measurements away from internal interfaces. Such point-to-point variations are likely to be measurement artifacts and not likely to reflect real variations of the lattice spacing. This aspect has been extensively discussed in section 8.4.

Before assessing the methods listed above, the stress and strain distributions that have been found and presented in chapters 5, 6 and 7 are tested with respect to the criteria listed here. An important criterion concerning the residual stresses that can be directly applied, for the 25 mm bi-metallic piping weld and the clad layer specimen, is the magnitude of the through thickness stresses. In the case of the clad layer specimen (Fig. 6.7) normal stresses scattering about 0 MPa have been found in the ferritic steel substrate as well as in the larger part of the clad layer. In the substrate the scatter of these data about 0 MPa, expressed in terms of a standard deviation, agrees well with the reported measurement uncertainty. In the clad layer the scatter of the data goes beyond the reported fitting uncertainty. In the 25 mm piping weld, through thickness residual stresses significantly lower than those in the

other two directions have been found (Fig. 5.13). In almost all cases these are within ± 100 MPa. This is the strongest “direct” indicator for the relatively good quality of these measurements. The criterion of stress balance cannot be applied to the clad layer specimen at all, and only within limits to the 25 mm piping weld, because a rigorous stress balance check would require stress data from a complete cross section of the specimen (see section 2.4). In the case of the clad layer specimen measurements have only been obtained along one line across an awkwardly shaped cross section. For the piping weld where the axial stress measurements would have to be examined in the context of stress balance, the data, while overall tending from tension at the outer surface to compression at the inner surface, as they should throughout the zone investigated, seem to be slightly out of balance, with a weighting toward the tensile stresses. While this in the present case is a weaker indicator than the through wall stresses, this finding indicates that the measurement approach chosen leaves room for improvement.

A sensible comparison with other experimental methods is only possible in the case of the clad layer specimen, where two alternative stress measurement methods have been applied, albeit on differently cut sections of the component. The comparison shows that all methods give the same order of magnitude for the residual stresses in the clad layer. The results quantitatively and qualitatively do not agree in detail, as the magnitudes of the residual stresses found differ to some degree and the reproduction of the stress gradient at the interface is different for every measurement. This in part has to be attributed to the different shape of the specimens tested, but in part certainly also to the differences in the measurement techniques. For the two bi-metallic piping welds no directly comparable measurements with other techniques are available. In the case of the 51 mm pipe there are crack compliance measurements in the axial direction, which qualitatively agree with the neutron measurements (Fig. 7.32), but the component shapes are very different and so are the measurement geometries and the axial stresses measured are quite low in most places.

Significant point-to-point variations in the experimental data have been found in all three components. They are shown in the residual strains and stresses presented in chapters 5, 6 and 7 and with additional detail in the measured peak positions for the 51 mm pipe shown in section 8.4. An analysis of the potential causes of these variations has also been given in section 8.4. However, the alternative measurement methods presented for the clad layer specimen have shown similar variations in the clad layer to the neutron measurements. From this point of view it cannot be excluded that the scatter of the data, shown for example in Fig. 6.7, also reflects a real variation of the stresses, although the data available do not facilitate conclusive statements about the stress state.

Based on the above comments, the particular neutron diffraction techniques that have been applied for these investigations can now be assessed.

8.9.2 Efficiency of reference specimen design

For these investigations, specifically cut reference specimens have been used for the measurement of the point-to-point variations of the peak positions in weld material free of macroscopic stress. Some of the reference specimens that have been used are shown in Figs. 5.4, 6.3, 7.10 and 7.11. Basically, these designs reflect three slightly different approaches. For the 25 mm piping weld, a so-called comb specimen has been used. For the clad layer there were two specimens, cut from different edges of the original component. These specimens were thin and the distribution of cuts within them was such that the matchstick shaped sampling volume would cross these cuts. For the 51 mm pipe a further development of the comb specimen was chosen. In this case the comb teeth were further sectioned into coupons, whereby the integrity of the slice was maintained by retaining 1 mm long bridges to keep the coupons attached to each other. In none of the cases have the reference specimens been cut from the location of the actual strain measurement, but rather from a different location within the same component.

The results obtained from these reference specimens in some cases; *e.g.*, the clad layer specimen, indicate that there are variations in the reference values in the fusion zones that are larger than the variations found in the parent materials (see Fig. 6.5). In another case, the 51 mm bi-metallic piping weld, the observed reference variations even differ in magnitude between measurement directions (see Tables 8.1 to 8.3).

Particularly the measurements in the clad layer, however, leaves open the question, whether it is necessary to take these variations into account to obtain the correct values of stresses, because the variations were in general much smaller than the strains that were finally measured (see Fig. 6.5). This has been observed in the 51 mm piping weld (see section 8.4) in the circumferential direction as well. In addition, in the case of the clad layer the two reference specimens showed differing distributions of these variations.

Contrary to this reservation, the peak position data presented in section 8.4 for the 51 mm piping weld on occasion shows a strong correlation between the variations found in the reference specimens and those found in the component itself. These data imply the necessity of taking the reference variations into account. However, such correlations have certainly not been found at all measurement locations.

For the comb specimen used for the 25 mm piping weld, the teeth of the comb were left unsectioned over their length, which is oriented in the piping axial direction. In addition, the final residual stresses appeared to be slightly unbalanced in the axial direction. This is not conclusive, but it has been considered possible that these observations are related; *i.e.*, the comb type reference specimen might not have been free of axial residual stresses in this case. Ganguly *et al.* found remaining residual stresses of considerable magnitude in a comb type reference specimen with even finer teeth than applied in this study, albeit that they investigated and aluminium alloy weld [94].

In summary, the following recommendations emerge from the observations made in the investigations concerning the use and design of reference specimens.

- Reference specimens should ideally be cut from the test location itself. This has not been done in this case, and is very often not done in welding residual stress analysis, for procedural reasons and the economy in time of the total measurement process. The detailed analysis of the peak positions presented in section 8.4 has demonstrated the need for executing measurements this way. Because of the numerous start-stop locations, the structure of the piping welds varies significantly around its circumference. The same argument also holds for the clad layer specimen.
- Reference specimens should be cut to as small a size as possible to really ensure the complete relaxation of the macro-stresses. The data presented for the clad layer specimens in chapter 6 suggest that the reference specimens used in this case fulfill this requirement. The comb type specimen described in chapter 5 leaves open questions in this respect. Comb type reference specimens are in fact often used, albeit involving a length to thickness ratio different to the one applied here. For the design reported in chapter 7 the results do not support any conclusions on the completeness of the macro-stress relaxation. It is recommended that solutions involving relatively large individual coupons as described in chapter 7 be accompanied by corresponding numerical analyses. There are various other approaches in existence in parallel to those presented here. The most advanced approach in terms of coupon size involves the cutting of very small size (1 - 2 mm across) individual coupons that are reassembled after cutting into larger coupons by adhesively bonding them together [95]. However, this is labour intensive and can also induce additional residual stresses.
- Reference variations are important and should be taken into account in particular when relatively small strains are measured.
- Observed variations in the reference diffraction peak position should be representative of the reference variations in the region of strain measurement, ideally by extracting the reference specimen from the strain measurement location directly. The data analyses in this chapter show that this representativeness could not in all cases be accomplished. Particular attention should be given to cases where the location of the reference specimen is different from the strain measurement location and cases where large point-to-point variations in the reference peak positions are obtained.

8.9.3 Cutting of components prior to measurements

The components investigated needed to be cut in order to facilitate three-dimensional neutron diffraction measurements. For the clad layer component a substantial amount of substrate material needed to be removed in order to reduce the effective thickness to 25 mm. Hence, at the measurement location more than 80% of the substrate had been milled away. In the piping specimen, windows had been cut to facilitate access

of the neutron beams. As stated in section 2.4, cutting of the specimen generally leads to a redistribution of the residual stresses throughout the remaining material.

In the case of the clad layer specimen it was known and accepted from the onset that this cutting would alter the residual stresses significantly. No experimental measures were taken to assess the impact of cutting. The results obtained are considered to be strongly influenced by the cutting, and this is corroborated by the difference in the stresses found in the substrate between neutron diffraction and deep hole drilling (Fig. 6.9). There is no other way to conduct stress measurements by neutron diffraction in such a component, and if the original residual stresses are to be reconstructed afterwards, accompanying measures (*e.g.*, numerical models) are always necessary. For the case presented here, it was however not possible to establish the impact of cutting on the residual stress distribution exactly; and a number of questions remain open, in particular regarding the real magnitude of the stresses in the clad layer in the two main stress directions. Here the stress levels observed by three different methods applied to the machined and as received components varied between 250 MPa and 500 MPa (see Figs. 6.9, 6.11 and 6.13). The origin of the differences can be in the cutting of the test pieces as well as in the particulars of the different measurement methods.

For the 51 mm piping weld, the impact of window cutting had been measured by strain gauges and accompanying numerical assessments. The strain gauge data are presented in Fig. 7.6, and it is shown that the cutting of the central window did not have a significant impact on the residual stresses at the measurement location.

As in the cases presented here, cutting of a specimen for neutron diffraction stress analysis is sometimes unavoidable. Accompanying measures are necessary to either demonstrate that the stress redistribution at the measurement location is small, or to afterwards reconstruct the original stress field. Otherwise only an altered residual stress distribution can be determined.

Based on the lessons learned from the present work it is thus recommended that one or more of the following three steps are included in the measurement process for neutron diffraction investigations where the specimen needs to be cut:

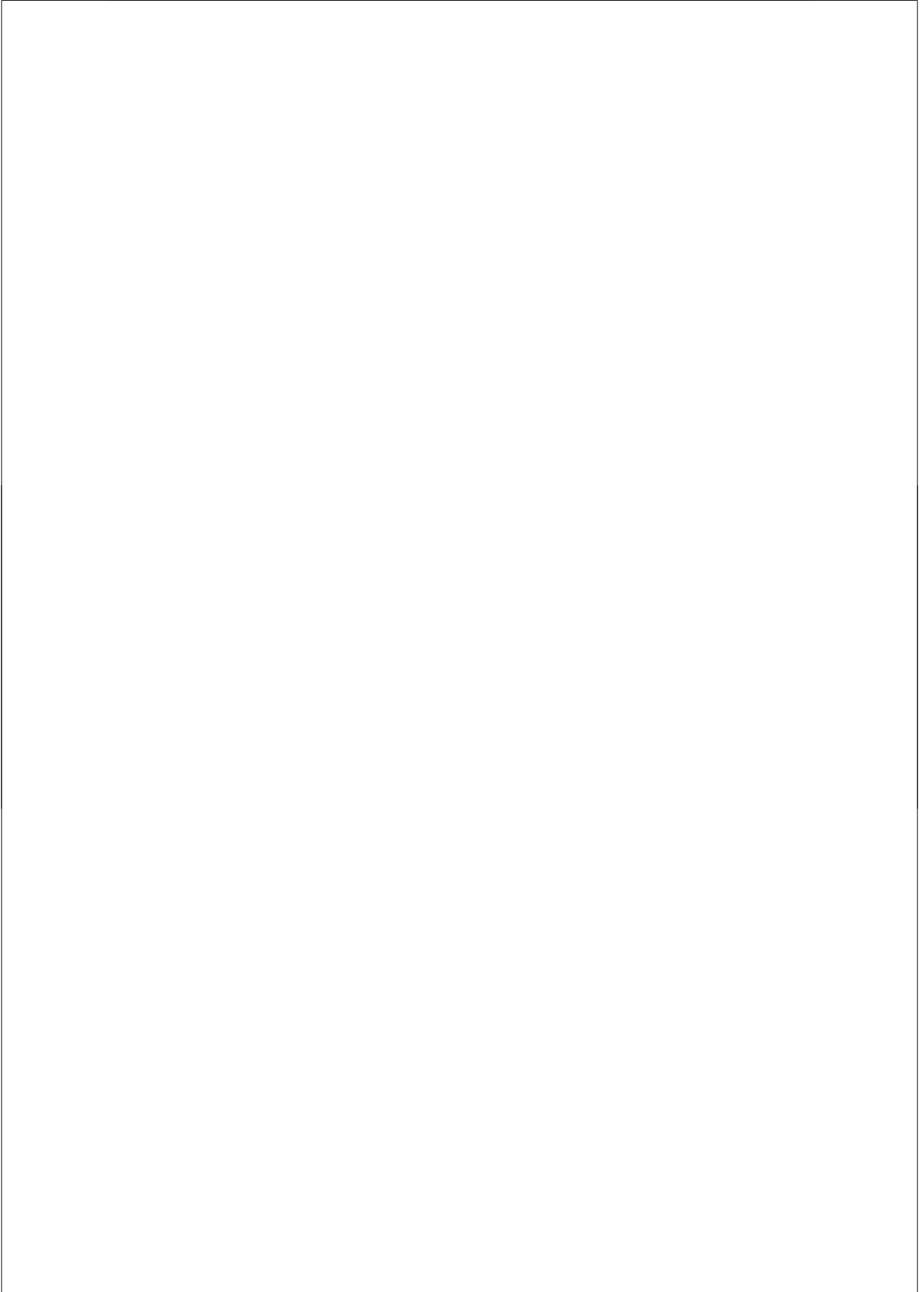
- Performance of a series of surface normal neutron diffraction strain measurements, which are basically always possible, before and after cutting, and comparison of the results.
- Measurement of the relaxation strains at the surface during cutting by means of strain gauges. If possible, establishment of these relaxation strains close to the location of neutron measurements.
- Accompany, if possible, the two other steps with a corresponding numerical analysis.

Taking these steps would at least provide the experimenter with an indication of the extent to which cutting of the specimen influences the stresses under investigation. In favourable circumstances it might even be possible to reconstitute the original stress field prior to cutting after the measurements are completed.

8.9.4 Measurements through 51 mm of steel

In chapter 7 residual stress investigations by neutron diffraction in a 51 mm thick steel component are presented. This wall thickness was at the time of the measurement close to the limits of this technique. In order to make these measurements at all feasible, large sampling volumes were used (see Table 7.2). With these large sampling volumes it has been possible to obtain diffraction peaks for most of the measurements attempted in this specimen. In section 8.4 an analysis of the results is made and significant point-to-point variations have been found particularly for the piping axial and radial directions. These variations are attributed to grain size effects and variations in the preferred crystallographic orientation within the sampling volumes. The exact causes could not be established with the data available, and it can be assumed that the huge size of the sampling volume could have an impact on the magnitude of the variations. The validity of this assumption cannot be determined with the available data. Therefore the applicability of such large volumes should be investigated prior to using, and they should only be used with great care.

The measurements that have been made on this component have demonstrated that neutron diffraction stress measurement through 51 mm of steel is possible. Such measurements could therefore be performed with smaller sampling volumes, at instruments with higher neutron beam intensity.



Chapter 9

Conclusions

The main purpose and result of the present work is the experimental determination of the residual strains and stresses within and around the fusion zones of three different *multi-pass fusion welded* specimens. Two of these were bi-metallic ferritic to austenitic steel piping girth welds, with 25 mm and 51 mm wall-thickness, respectively. The third specimen comprised a welded austenitic steel clad layer on a block of ferritic steel.

The main experimental technique applied in these investigations is neutron diffraction. Because of the high penetration of neutrons this technique is most suited to providing non-destructive 3-dimensional mapping of strains and stresses in the bulk of the specimens described above.

The size and shape of all three components was initially prohibitive for the 3-dimensional neutron diffraction measurements intended. Hence all components needed alterations by machining and cutting in order to facilitate the measurements. Moreover, dedicated reference specimens were cut from each component in order to correct for variations in diffraction peak position due to inhomogeneities in the fusion zones.

Based on the experimentally obtained results and the discussions presented in chapters 5 to 8, the following conclusions are drawn:

- Neutron diffraction strain/stress measurements through 51 mm of steel are feasible using a facility with a low intensity neutron beam.
- The measurements show that the residual stresses reach high levels in tension and compression in and around the fusion zones in all three components. At some locations, mostly near a material interface, stresses near the yield level of the material have been observed. The stresses in the welding direction exhibit steep gradients at the interfaces.
- In the austenitic steel fusion zones, high tensile residual strains/stresses are found in the welding direction. Accordingly, the ferritic steel part of the specimens close to the interface with the fusion zone exhibits compressive stresses

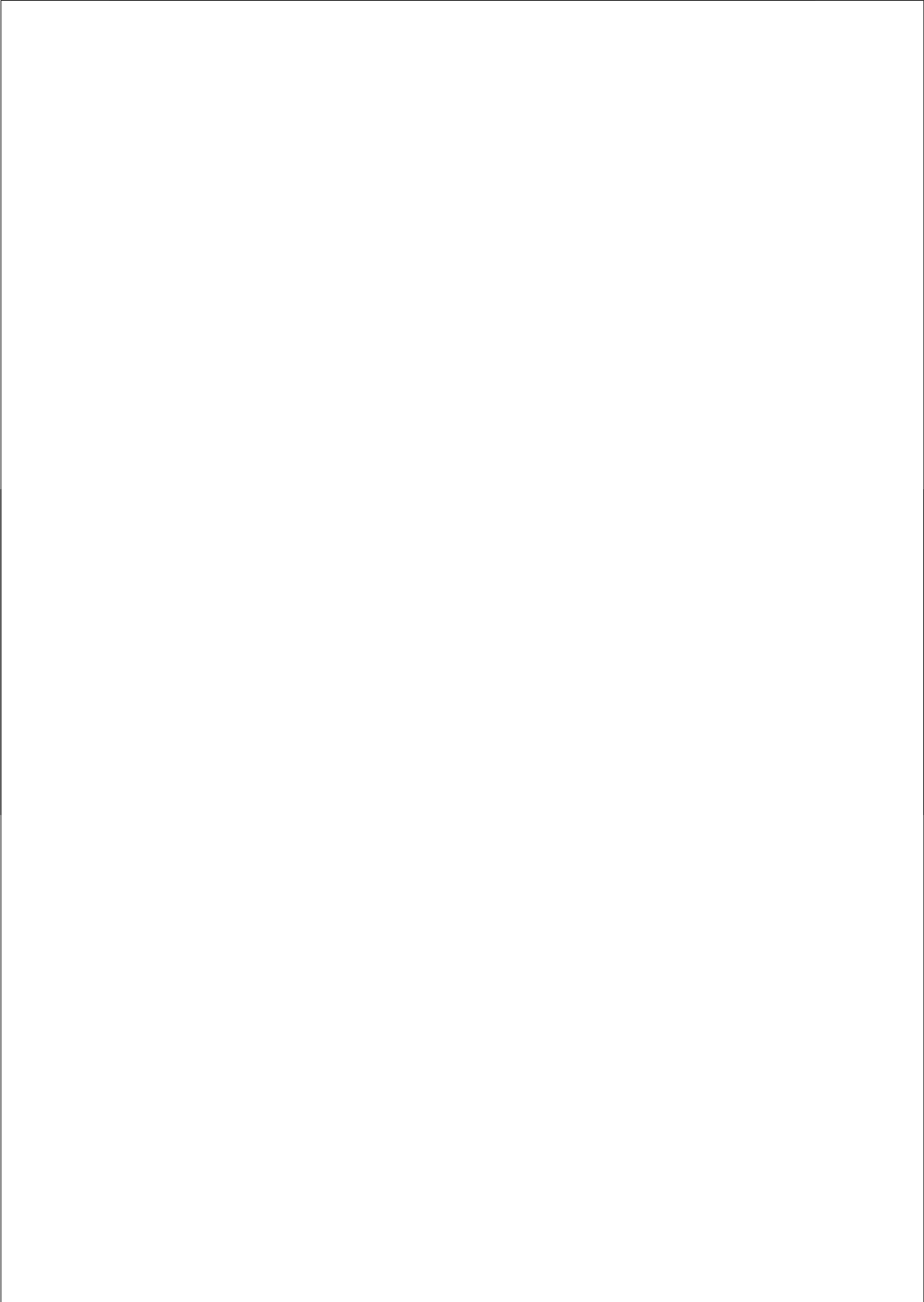
in the welding direction. Closer to the inner wall of the piping specimens these compressive strains/stresses are higher.

- In the clad layer component, the stress distribution in the welding transverse direction resembles that of the welding direction. In the thin bi-metallic piping weld the stress distributions in the two directions are completely different. This demonstrates that different constraints related to the geometries of the components and the fusion zones lead to differences in the stress distributions in the welding transverse direction.
- The stresses found in the through-thickness directions of the 25 mm piping and the clad layer specimens are significantly smaller than those found in the other directions. This is in agreement with what is expected in relatively thin specimens.
- Material inhomogeneities and large grain sizes rendered significant contributions to the uncertainty in strain in addition to the uncertainty associated with peak fitting. In particular, this is observed for the strains in the welding transverse and piping radial directions for the thick bi-metallic piping component where the estimated total strain uncertainties are in the same order as the observed strains for many measurements.
- The uncertainty contributions associated with inhomogeneities and large grain sizes limit the reliability of the strain measurements in the welding transverse and piping radial directions for the thick bi-metallic piping component.
- The position of the diffraction peak for a stress free reference specimen depends on the location of measurement in the fusion zones. The experimental data show that the peak positions do not only depend on variations in lattice spacing, but also on large grain sizes and/or texture gradients within the sampling volume.
- The observed high degree of correlation between point-to-point variations of the peak positions measured in the thick bi-metallic welding component and its reference specimen suggests the occurrence of quasi-invariant microstructures along this weld.
- The presence of many weld start/stop locations probably has an impact on the residual stress determination by neutron diffraction.
- In the cases presented here only qualitative agreement between neutron diffraction stress/strain data and the corresponding numerical predictions is observed. The simplified modeling approaches generally under-predict the magnitudes of the tensile residual stresses observed in the fusion zones.
- The magnitude of strain/stress relaxation at the measurement locations induced by cutting material from the specimen should be determined by measurement or prediction.

- For high strains of the order of 2000 to 3000 $\mu\text{m}/\text{m}$, an uncertainty in the detector position as low as $\pm 1^\circ$ translates into an additional uncertainty contribution for the measured strain comparable in magnitude to the fitting uncertainty.

From the work presented and the conclusions drawn several recommendations have been derived for potential improvements in future residual stress measurements in *inhomogeneous materials*; *e.g.*, *fusion welds*, and *“grainy” materials* similar to those investigated here.

- Reference specimens should be cut as close as possible to the location in the component where the actual strain measurements will be made (see section 8.4.5). Extracting the reference specimens exactly from the location of strain measurements would be ideal, but may not always be possible in practice. This experimental approach can help to mitigate the impact on the measured strain data by composition variations; *e.g.*, originating from the thermal history at and near to the measurement location and by grain size and texture effects.
- The use of specimen rocking during measurements should always be considered in order to reduce grain size effects, because it increases the number of diffracting grains.
- Time-of-flight techniques can make neutron diffraction measurements less susceptible to grain size effects. This is because they sample a larger fraction of the grains within the gauge volume through employing an increased the detector opening angle, which can be considered as “intrinsic rocking”, and through using a wide range of neutron wavelengths enabling the recording of multi-peak diffraction patterns.



References

- [1] B. HAYES, “Six case histories of pressure vessel failures”, *Engineering Failure Analysis*, 1996, 3, pp. 157–170
- [2] EdF Energy Ltd., Gloucester, UK, *R6 Revision 4. Assessment of the integrity of structures containing defects*, 2012
- [3] British Energy Generation Ltd., Gloucester, UK, *R5. Assessment procedure for the high temperature response of structures*, 2003
- [4] P. WITHERS, M. TURSKI, L. EDWARDS, P. BOUCHARD and D. BUTTLE, “Recent advances in residual stress measurement”, *International Journal of Pressure Vessels and Piping*, 2008, 85, pp. 118–127
- [5] A. KRAWITZ, “The Early History of Neutron Stress Measurements”, *Materials Science Forum*, 2008, 571-572, pp. 3–11
- [6] M. HUTCHINGS, P. WITHERS, T. HOLDEN and T. LORENTZEN, *Introduction to the Characterization of Residual Stress by Neutron Diffraction*, Taylor & Francis, CRC Press, Boca Raton, London, New York, Singapore, 2005, ISBN 0-415-31000-8
- [7] M. FITZPATRICK and A. LODINI (eds.), *Analysis of Residual Stress by Diffraction using Neutron and Synchrotron Radiation*, Taylor & Francis, London, New York, 2003, ISBN 0-415-30397-4
- [8] D. SMITH, P. BOUCHARD and D. GEORGE, “Measurement and prediction of residual stresses in thick section steel welds”, *Journal of Strain Analysis for Engineering Design*, 2000, 35, pp. 287–305
- [9] M. PRIME, “Cross-sectional mapping of residual stresses by measuring the surface contour after a cut”, *Journal of Engineering Materials and Technology*, 2001, 123, pp. 162–168
- [10] I. NOYAN and J. COHEN, *Residual Stress - Measurement by Diffraction and Interpretation*, Springer Verlag, New York, Berlin, Heidelberg, London, Paris, Tokyo, 1987, ISBN 0-387-96378-2

- [11] K. KANG and L. KUPCA (eds.), *Integrity of Reactor Pressure Vessels in Nuclear Power Plants: Assessment of Irradiation Embrittlement in Reactor Pressure Vessel Steels*, no. NP-T-3.11 in IAEA Nuclear Energy Series, International Atomic Energy Agency, Vienna, Austria, 2009, ISBN 978-92-0-101709-3
- [12] F. GILLEMOT, *Information sheet, Mock-up of VVER Pressure Vessel Nozzle Dissimilar Metal Girth Weld*, KFKI Atomic Energy Research Institute, Budapest, Hungary, 2010, unpublished Project Documentation within EU FP7 Project STYLE
- [13] J. NYE, *Physical Properties of Crystals: Their Representation by Tensors and Matrices*, Oxford University Press, first edn., 1957, ISBN 0-19-851165-5
- [14] N. JIA, R. LIN PENG, G. CHAI, S. JOHANSSON and Y. WANG, “Direct experimental mapping of microscale deformation heterogeneity in duplex stainless steel”, *Materials Science and Engineering A*, 2008, 491, pp. 425–433
- [15] J. ODDERSHEDE, S. SCHMIDT, H. POULSEN, H. OSHOLM SORENSEN, J. WRIGHT and W. REIMERS, “Determining grain resolved stresses in polycrystalline materials using three-dimensional X-ray diffraction”, *Journal of Applied Crystallography*, 2010, 43, pp. 539–549
- [16] R. VON MISES, “Mechanik der festen Körper im plastisch deformablen Zustand”, *Nachrichten von der Gesellschaft der Wissenschaften zu Göttingen, Mathematisch-Physikalische Klasse*, 1913, pp. 582–592
- [17] K. KLOOS and B. KAISER, “Residual stresses induced by manufacturing”, in: V. HAUKE, H. HOUGARDY and E. MACHERAUCH (eds.), “Residual Stresses - Measurement, Calculation, Evaluation”, DGM Informationsgesellschaft, Oberursel, Germany, 1991, ISBN 3-88355-169-4, pp. 205–226
- [18] B. EIGENMANN and E. MACHERAUCH, “Röntgenographische Untersuchung von Spannungszuständen in Werkstoffen - Teil II”, *Mat.-Wiss. u. Werkstofftech.*, 1995, 26, pp. 199–216
- [19] E. MACHERAUCH, H. WOHLFAHRT and U. WOLFSTIEG, “Zur zweckmässigen Definition von Eigenspannungen”, *Härtereitechnische Mitteilungen*, 1973, 28, pp. 201–211
- [20] T. HOLDEN, R. HOSBONS, S. MAC EWEN, E. FLOWER, M. BOURKE and J. GOLDSTONE, “Comparison between finite element calculations and neutron diffraction, measurements of residual stress in a diametrically compressed ring”, in: M. HUTCHINGS and A. KRAWITZ (eds.), “Measurement of Residual and Applied Stress using Neutron Diffraction”, NATO ASI Series, Kluwer Academic Publishers, Dordrecht, Netherlands, 1992, ISBN 0-7923-1809-9, pp. 93–112

- [21] G. WEBSTER (ed.), *Neutron Diffraction Measurements of Residual Stresses in a Shrink-fit Ring and Plug*, VAMAS report no. 38, National Physics Laboratory, Teddington, UK, Jan 2000
- [22] J. MOYER and G. ANSELL, “The Volume Expansion Accompanying the Martensite Transformation in Iron-Carbon Alloys”, *Metallurgical Transactions A*, 1975, 6A, pp. 1785–1791
- [23] J. FRANCIS, H. STONE, S. KUNDU, R. ROGGE, H. BHADSHIA, P. WITHERS and L. KARLSSON, “Transformation temperatures and welding residual stresses in ferritic steels”, in: D. LIDBURY (ed.), “Proceedings of the ASME Pressure Vessels and Piping Division Conference 2007, Volume 6: Materials and Fabrication”, ASME, New York, 2008, ISBN 0-7918-4284-3, pp. 949–956
- [24] H.-J. HÄNSCH and J. KREBS (eds.), *Eigenstressen und Formänderungen in Schweißkonstruktionen*, *Fachbuchreihe Schweißtechnik*, vol. 138, DVS-Verlag GmbH, Düsseldorf, 2006, ISBN 978-3-87155-183-3
- [25] A. EZEILO, “Shot peening”, in: M. FITZPATRICK and A. LODINI (eds.), “Analysis of Residual Stress by Diffraction using Neutron and Synchrotron Radiation”, Taylor & Francis, London, 2003, ISBN 0-415-30397-4, pp. 251–262
- [26] C. OHMS, “Untersuchung des Verfahrens zur Spannungsreduktion durch Vibration mittels hochauflösender Neutronendiffraktometrie”, Master’s thesis, Christian-Albrechts University, Kiel, Germany, 1995
- [27] K. KANG and L. KUPCA (eds.), *Stress Corrosion Cracking in Light Water Reactors: Good Practices and Lessons Learned*, no. NP-T-3.13 in IAEA Nuclear Energy Series, International Atomic Energy Agency, Vienna, Austria, 2011
- [28] W. DIETZEL, “Fracture Mechanics Approach to Stress Corrosion Cracking”, *Anales de Mecánica de la Fractura*, 2001, 18, pp. 1–7
- [29] M. TURSKI, P. BOUCHARD, A. STEUWER and P. WITHERS, “Residual stress driven creep cracking in AISI Type 316 stainless steel”, *Acta Materialia*, 2008, 56, pp. 3598–3612
- [30] J. FRANCIS, W. MAZUR and H. BHADSHIA, “Type IV cracking in ferritic power plant steels”, *Material Science and Technology*, 2006, 22, pp. 1387–1395
- [31] W. BRAGG, “The reflection of X-rays by crystals”, *Proceedings of the Royal Society*, 1913, 88, pp. 428–438
- [32] W. BRAGG, “The reflection of X-rays by crystals”, *Proceedings of the Royal Society*, 1913, 89, pp. 246–248, 248–277
- [33] W. SOETE and R. VANCROMBRUGGE, “An Industrial Method for the Determination of Residual Stresses”, in: “Proceedings of SESA 8”, Society for Experimental Stress Analysis, 1950, pp. 17–28

- [34] K. MILBRADT, “Ring Method Determination of Residual Stresses”, in: “Proceedings of SESA 9”, Society for Experimental Stress Analysis, 1951, pp. 63–74
- [35] R. KELSEY, “Measuring Non-Uniform Residual Stresses by the Hole Drilling Method”, in: “Proceedings of SESA 14”, Society for Experimental Stress Analysis, 1956, pp. 181–194
- [36] M. PRIME, “Residual Stress Measurement by Successive Extension of a Slot: The Crack Compliance Method”, *Applied Mechanics Reviews*, 1999, 52, pp. 75–96
- [37] C. OHMS, in: “Proceedings of 4th NeT Enlargement and Integration Workshop”, EUR23571EN, Joint Research Centre, Petten, The Netherlands, 2008
- [38] B. EIGENMANN and E. MACHERAUCH, “Röntgenographische Untersuchung von Spannungszuständen in Werkstoffen - Teil III”, *Mat.-Wiss. u. Werkstofftech.*, 1996, 27, pp. 426–437
- [39] *Non-destructive testing - Standard test method for determining residual stresses by neutron diffraction*, ISO, Geneva, Switzerland, Jul 2005, Technical Specification ISO/TS 21432:2005(E)
- [40] W. VOIGT, *Lehrbuch der Kristallphysik*, Teubner-Verlag, Berlin, 1928
- [41] A. REUSS, “Berechnung der Fließgrenze von Mischkristallen aufgrund der Plastizitätsbedingung für Einkristalle”, *Z. für angew. Math. und Mech.*, 1929, 9, pp. 49–58
- [42] R. HILL, “The Elastic Behaviour of a Crystalline Aggregate”, *Proc. Phys. Soc.*, 1952, A65, p. 349 ff.
- [43] E. KRÖNER, “Berechnung der elastischen Konstanten des Vielkristalls aus den Konstanten des Einkristalls”, *Zeitsch. für Physik*, 1958, 151, pp. 504–518
- [44] N. KOCH, U. WELZEL, H. WERN and E. MITTEMEIJER, “Mechanical elastic constants and diffraction stress factors of macroscopically elastically anisotropic polycrystals: the effect of grain-shape (morphological) texture”, *Philosophical Magazine*, 2004, 84, pp. 3547–3570
- [45] B. CLAUSEN, T. LORENTZEN, M. BOURKE and M. DAYMOND, “Lattice strain evolution during uniaxial tensile loading of stainless steel”, *Materials Science and Engineering A*, 1999, 259, pp. 17–24
- [46] C. KITTEL, *Einführung in die Festkörperphysik*, R. Oldenbourg Verlag, Munich, sixth edn., 1983, ISBN 3-486-32766-6
- [47] L. DE BROGLIE, “Researches on the quantum theory”, Ph.D. thesis, Faculty of Science, Paris University, Paris, France, 1924

- [48] M. DAYMOND, P. WITHERS and M. JOHNSON, “The expected uncertainty of diffraction-peak location”, *Applied Physics A: Materials Science and Processing*, 2002, 74, Suppl. I, pp. S112–S114
- [49] A. ALLEN, C. ANDREANI, M. HUTCHINGS and C. WINDSOR, “Measurement of internal stress within bulk materials using neutron diffraction”, *NDT International*, 1981, 14, pp. 249–254
- [50] D. EMENDÖRFER and K. HÖCKER, *Theorie der Kernreaktoren, Band 1: Der stationäre Reaktor*, Bibliographisches Institut AG, Zürich, Switzerland, 1982, ISBN 3-411-01599-3
- [51] B. WILLIS and C. CARLILE, *Experimental Neutron Scattering*, Oxford University Press, Oxford, UK, first edn., 2009, ISBN 978-0-19-851970-6
- [52] P. BRANDT, “Stress Measurement by Means of Neutron Diffraction”, Ph.D. thesis, University of Twente, Enschede, Netherlands, 1991
- [53] J. SANTISTEBAN, M. DAYMOND, J. JAMES and L. EDWARDS, “ENGIN-X: a third-generation neutron strain scanner”, *Journal of Applied Crystallography*, 2006, 39, pp. 812–825
- [54] “Schweißen und verwandte Prozesse - Begriffe - Teil 1: Metall-Schweißprozesse”, Standard, DIN ISO 857-1, Deutsches Institut für Normung e.V., Berlin, Germany, 1998
- [55] A. FRITZ and G. SCHULZE (eds.), *Fertigungstechnik*, VDI-Verlag, Düsseldorf, Germany, third edn., 1995, ISBN 3-18-401394-4
- [56] G. LINNERT, *Welding Metallography, Carbon and Alloy Steels, Volume I*, American Welding Society, Miami, USA, fourth edn., 1994, ISBN 0-87171-457-4
- [57] A. O’BRIEN (ed.), *Welding Handbook, Vol. 2, Welding Processes, Part 1*, American Welding Society, Miami, USA, ninth edn., 2004, ISBN 0-87171-729-8
- [58] G. DEN OUDEN, *Lasttechnologie*, Delftse Uitgevers Maatschappij b.v., Delft, The Netherlands, 1987, ISBN 90-6562-087-7
- [59] M. SMITH and A. SMITH, “NeT bead-on-plate round robin: Comparison of transient thermal predictions and measurements”, *International Journal of Pressure Vessels and Piping*, 2009, 86, pp. 96–109
- [60] K. DECROOS, “The Influence of Anisotropy due to Crystallographic Texture on Residual Stresses in Welds”, Ph.D. thesis, University of Ghent, Ghent, Belgium, 2011
- [61] E. VAN DER AA, “Local cooling during welding: Prediction and control of residual stresses and buckling distortion”, Ph.D. thesis, Delft University of Technology, Delft, The Netherlands, 2007

- [62] M. SMITH and A. SMITH, *NeT Task Group 1 Single Bead Weld on Plate: Review of Phase 1 Weld Simulation Round Robin*, Tech. Rep. E/REP/BDBB/0089/GEN/05, British Energy Generation Ltd, United Kingdom, 2006
- [63] D. HUGHES, P. WEBSTER and G. MILLS, "Ferritic Steel Welds - A Neutron Diffraction Standard", *Materials Science Forum*, 2002, 404-407, pp. 561-566
- [64] J. LANCASTER, *Metallurgy of Welding*, Abington Publishing, Abington, UK, sixth edn., 1999, ISBN 1-85573-428-1
- [65] H. GRANJON, *Fundamentals of welding metallurgy*, Abington Publishing, Woodhead Publishing Ltd, Abington, Cambridge, UK, 1991, ISBN 1-85573-019-7
- [66] K. EASTERLING, *Introduction to the Physical Metallurgy of Welding*, Butterworths & Co Ltd., 1983, ISBN 0-408-01351-6
- [67] J. MOYSAN, A. APFEL, G. CORNELOUP and B. CHASSIGNOLE, "Modelling the grain orientation of austenitic stainless steel multipass welds to improve ultrasonic assessment of structural integrity", *International Journal of Pressure Vessels and Piping*, 2003, 80, pp. 77-85
- [68] R. WIMPORY, C. OHMS, M. HOFMANN, R. SCHNEIDER and A. YOUTSOS, "A Step Towards a Complete Uncertainty Analysis of Residual Stress Determination using Neutron Diffraction", *Materials Science Forum*, 2010, 638-642, pp. 2487-2492
- [69] N. TAYLOR, C. FAIDY and P. GILLES (eds.), *Assessment of Dissimilar Weld Integrity: Final Report of the NES-C-III Project*, EUR 22510 EN, European Communities, Luxembourg, 2006
- [70] C. FAIDY, G. CHAS, S. BHANDARI, M. VALETA, R. HURST, A. YOUTSOS, P. NEVASMAA, W. BROCKS, D. LIDBURY and C. WIESNER, "BIMET: structural integrity of bi-metallic components", *Nuclear Engineering and Design*, 2001, 209, pp. 79-85
- [71] *Butt Weld between SA508 CI3 Base Material with Austenitic Buttering and Stainless Steel A182 F304L. Equipos Nucleares SA*, Tech. Rep. No. 910, BIMET Project, Dec 1997
- [72] P. NEVASMAA, A. LAUKKANEN and U. EHRNSTÉN, "The role of metallurgy and micro-mechanisms of fracture in assessing structural integrity of bi-metallic ferrite-austenite pipeline welds", in: R. DENYS (ed.), "Pipeline Technology: Proceedings of the 3rd International Pipeline Technology Conference, Brugge, Belgium, May 21-24, 2000", Elsevier Science BV, Amsterdam, The Netherlands, 2000, ISBN 0-444-50271-8, pp. 253-268

- [73] L. METTEN, A. VAN DE SANDE and J. OUDAERT, *Radiographic examination of BIMET W-8583, W-8636 and W-8635*, Tech. rep., JRC, Petten, The Netherlands, Jul 1999
- [74] *PeakFit - Peak separation and analysis software, User's Manual*, SeaSolve Software Inc., Framingham, MA, USA, 2003, ISBN 81-88341-07-X
- [75] *Uncertainty of measurement - Part 3: Guide to the expression of uncertainty in measurement*, ISO, Geneva, Switzerland, 2008, ISBN 92-67-10188-9
- [76] C. FAIDY, *BIMET - Synthesis report*, Tech. rep., EdF-Septen, France, Sep 2001
- [77] L. KEPPAS, D. KATSAREAS and N. ANIFANTIS, *Finite Element Simulation and Residual Stress Prediction in Multi-Pass Joint Welds of Bi-Metallic Pipes - Part 1: Report on Bibliographical Research and Preliminary 2-d Simplified Analysis of Bimetallic Pipe Welded Joints*, Tech. rep., University of Patras and Joint Research Centre, Sep 2006
- [78] L. KEPPAS, D. KATSAREAS and N. ANIFANTIS, *Finite Element Simulation and Residual Stress Prediction in Multi-Pass Joint Welds of Bi-Metallic Pipes - Part 2: Report on Detailed 2-d Bead-by-Bead Simulations of Bimetallic Multipass Welded Joints*, Tech. rep., University of Patras and Joint Research Centre, Mar 2007
- [79] P. GILLES and L. NOUET, "Residual stress numerical simulations of two dissimilar metal weld junctions", in: A. YOUTSOS (ed.), "Residual Stress and its Effects on Fatigue and Fracture - Proceedings of a Special Symposium held within the 16th European Conference of Fracture, Alexandroupolis, July 2006", Springer, Dordrecht, The Netherlands, 2006, ISBN 1-4020-5328-2 (HB), pp. 3-13
- [80] M. BRUMOVSKY, V. PISTORA and I. KUPKA, "Residual Stresses in Austenitic Cladding", in: "Proceedings of the ASME 2007 Pressure Vessels and Piping Division Conference and Eighth International Conference on CREEP and Fatigue at Elevated Temperature", ASME, New York, 2007, ISBN 0-7918-3804-8
- [81] W. BERTRAM, "Eigenspannungen in austenitisch plattiertem dickwandigem Feinkornbaustahl", *Archiv für das Eisenhüttenwesen*, 1977, 48, pp. 623-628
- [82] G. HOFER and N. BENDER, "The Measurements of Residual Stresses in Claddings", in: "Proceedings of the International Conference on Residual Stresses in Welded Construction and their Effects", The Welding Institute, London, UK, 1977, pp. 89-95
- [83] P. WEBSTER, G. MILLS, X. WANG, W. KANG and T. HOLDEN, "Impediments to Efficient Through-Surface Strain Scanning", *Journal of Neutron Research*, 1996, 3, pp. 223-240

- [84] T. PIRLING, “Neutron Strain Scanning at Interfaces: An Optimized Beam Optics to Reduce the Surface Effect”, *Materials Science Forum*, 2000, 347-349, pp. 107–112
- [85] H. GRIPENBERG, H. KEINÄNEN, C. OHMS, H. HÄNNINEN, D. STEFANESCU and D. SMITH, “Prediction and Measurement of Residual Stresses in Cladded Steel”, *Materials Science Forum*, 2002, 404-407, pp. 861–866
- [86] M. CIPIERE, *ADIMEW Mock-up - Manufacture of two mock-ups with bimetallic weld of austenitic stainless steel, representing a pressurizer surge nozzle*, Tech. Rep. no. NFEMT.02.0341, Framatome-ANP, France, Sep 2002
- [87] J. WINTLE, R. SANDERSON and S. GREEN, *ADIMEW Project: Residual Stress Measurements by Hole Drilling of AD01 Dissimilar Metal Weld*, Tech. Rep. TWI report no. 13219/3/03, The Welding Institute, UK, Nov 2003
- [88] C. OHMS, R. WIMPORY, D. KATSAREAS, P. HORNAK and A. YOUTSOS, *ADIMEW - Assessment of aged piping DIssimilar MEtal Weld integrity, Contract FIKS-CT-2000-00047, Work Package 3, Deliverable D3.1-a: Report on Residual Stress Measurements*, Tech. rep., Joint Research Centre, Petten, The Netherlands, Nov 2003
- [89] D. KATSAREAS and A. YOUTSOS, *NESC III Project TG6: Finite Element Simulation and Residual Stress Prediction of a Dissimilar Metal Pipe Welded Joint*, Tech. Rep. NESCDOC TG6 (04)03, Joint Research Centre, NL, Nov 2004
- [90] D. NEOV, C. OHMS, R. WIMPORY and A. YOUTSOS, “Residual stress analyses by neutron diffraction in irradiated double-V butt welded steel plates”, *Materials Science Forum*, 2008, 571-572, pp. 381–386
- [91] ESAB Welding & Cutting, *Information sheet on welding consumable ESAB OK61.30*, product specifications published online
- [92] Y. TRAORE, S. PADDEA, P. BOUCHARD and M. GHARGHOURI, “Measurement of the Residual Stress Tensor in a Compact Tension Weld Specimen”, *Experimental Mechanics*, 2013, 53, pp. 605–618
- [93] M. HILL, “Computational and experimental methods for residual stress engineering”, Statement during Presentation at Workshop WONERS 2007, Golden, Colorado, USA, 21-22 July 2007
- [94] S. GANGULY, L. EDWARDS and M. FITZPATRICK, “Problems in Using a Comb Sample as a Stress Free Reference for the Determination of Welding Residual Stresses by Diffraction”, *Materials Science and Engineering A*, 2011, 528, pp. 1226–1232
- [95] T. HOLDEN, H. SUZUKI, D. CARR, M. RIPLEY and B. CLAUSEN, “Stress Measurements in Welds: Problem Areas”, *Material Science and Engineering A*, 2006, 437, pp. 33–37

Summary

Welding is applied in many industrial sectors to join components, and has become an important manufacturing process because it enables the fabrication of structures that could not otherwise be constructed.

Weld regions have inhomogeneous microstructures and are more susceptible to crack initiation and crack propagation than the surrounding base material regions. Residual stresses are also formed, which superimpose with applied loads, resulting in a reduction of the maximum applied load a component can sustain.

In particular for nuclear installations, the limited failure tolerance and the relative abundance of rather large welds require a reliable assessment of component integrity for lifetime management. Residual stresses need to be considered in such assessments because they can contribute to initiation and propagation of defects. Commonly, residual stresses are more difficult to determine experimentally or to predict by numerical methods than stresses resulting from applied loads; hence residual stress assessment in welded nuclear components is an important area of research.

The present work concerns the experimental determination of residual stresses by neutron diffraction in three full-scale mock-ups of components found in nuclear power installations. Two of these mock-ups represent dissimilar metal girth welds joining ferritic steel pressure vessel nozzles to austenitic stainless steel primary piping sections. The third represents a welded clad layer on a section of a reactor pressure vessel wall.

In this work neutron diffraction has been used as the technique for residual stress determination. This technique is based on the principle of Bragg diffraction and measures changes in lattice spacing; *i.e.*, strain. Residual stresses can be determined in three directions in the bulk of a component at a spatial resolution of typically 1-5 mm. Such a resolution is appropriate in view of the distances over which the residual stresses normally vary in welded metallic components.

There are a number of challenges associated with neutron diffraction measurements addressed in the current study. One of these is that component dimensions and geometries necessitate machining to facilitate access of the neutron beams to the measurement locations. Neutron diffraction measurements are also known to be sensitive to the inhomogeneity in the microstructure and to local variations in chemical composition in the weld region; therefore dedicated reference specimens are needed in order to calibrate the strain determinations.

Prior to the description of the experimental work undertaken, background information is provided on the main aspects of the work. Definitions are given for residual stresses and strains and their main characteristics are explained (chapter 2). A short overview of the most important techniques for strain and stress measurement being used today is given in chapter 3. These are the relaxation techniques, where the relaxation of strains due to material removal is measured; and the diffraction techniques, where lattice deformations caused by stresses are observed through Bragg diffraction. A detailed account of residual stress determination based on neutron diffraction is followed by a description of the facility at the Joint Research Centre that was used for the present investigations. An overview of the industrially relevant welding techniques is given in chapter 4, where additional detail is provided on the arc welding methods used for the manufacture of the components investigated in this study. The mechanism responsible for residual stress formation in welds, namely local plastic deformation caused by steep temperature gradients, and the dendritic microstructure of stainless steel fusion welds similar to those investigated here are discussed based on a few examples.

The experimental work and the results obtained are described in chapters 5, 6 and 7 with each chapter covering one of the three components. The first component is a "thin" walled (25 mm wall thickness) bi-metallic girth welded pipe. The second component is a ferritic steel block with a 10 mm thick welded stainless steel clad layer applied to one of its surfaces. This component represents a nuclear reactor pressure vessel wall with a thickness of 146 mm. The third component is a thick walled (51 mm wall thickness) bi-metallic girth welded pipe. Both, the thin and the thick walled bi-metallic pipes, represent joints between ferritic steel pressure vessel nozzles and austenitic stainless steel pipes.

For each component, details are provided concerning the manufacturing techniques employed, including the welding processes, the associated heat treatments and the final machining applied to the thick walled pipe. For the access of the neutron beams in three measurement orientations windows and access slots were cut into each of the bi-metallic piping weld specimens. The clad layer specimen thickness was locally reduced from 146 mm to 25 mm. This significant reduction was necessary to achieve a high spatial resolution in the measurements. The alterations described lead to stress relaxation and stress redistribution within the components. For the thick bi-metallic pipe the relaxation of strains was monitored by strain gauges during cutting showing negligible impact at the location of the neutron diffraction measurements. All component modifications are described in detail as well as the design and manufacture of the reference specimens needed for the calibration of the strain measurements. The measurement procedures and the data analyses are explained, and for each specimen the neutron diffraction results are presented in terms of residual strains and the derived stresses.

In the thin walled bi-metallic pipe, tensile residual stresses have been found in the welding direction within the fusion zone. These tensile stresses reach values not far below the yield level of the material near the outer surface; and they decrease to almost 0 MPa toward the inner surface of the pipe. In the ferritic part of the pipe compressive

residual stresses have been found near the austenitic-ferritic material interface. Here, the highest compression is observed close to the inner surface, decreasing toward the outer surface. In the welding transverse direction, tensile stresses have been obtained near the outer surface changing gradually to compressive stresses near the inner surface. The maximum stress levels attained in tension and compression are slightly lower than those in the welding direction. The piping radial direction exhibits overall the lowest stress levels in this component with values varying between +100 MPa and -100 MPa.

The stainless steel clad layer of the clad component exhibits high tensile stresses in the welding longitudinal direction as well as in the welding transverse direction. The stress level ranges between 250 and 500 MPa with a considerable scatter of the data. The ferritic steel substrate is found to be in compression in both directions with minimum stress levels between -150 and -200 MPa near the austenitic-ferritic material interface. The stresses in the interface normal direction observed in this component scatter about 0 MPa.

In the fusion zone of the thick walled bi-metallic piping component, tensile residual stresses have been found in the welding direction. In the ferritic part compressive residual stresses have been found in this direction near the austenitic-ferritic interface. Both of these observations are similar to those made for the thin walled component. The maximum stress levels observed are slightly higher than in the thinner component; the tensile stresses in the fusion zone reach the nominal yield level. No clear trend is observed for the welding longitudinal stresses between the outer and the inner surface. For the other two measurement directions the scatter of the data is so high that the magnitude of the stresses cannot be determined with sufficient accuracy.

For all three components the data recorded from the fusion zones exhibit higher scatter than those from the base materials.

The neutron diffraction results have been compared to third party numerical predictions of the residual stresses and to stress measurements by strain relaxation techniques. The numerical predictions have been performed by finite element analyses. Simplified and more detailed approaches have been applied. In the simplified approaches the welding process itself has been neglected unlike in the detailed models. In all cases the detailed numerical assessments produced a better agreement with the neutron diffraction results than the simplified ones. In particular, in the fusion zones the simplified numerical approaches under predict the residual stresses found by neutron diffraction.

The applied third party strain relaxation techniques were the ring core method and deep hole drilling for the clad layer component, and surface hole drilling and the crack compliance method for the thick walled bi-metallic pipe. Most comparisons with the neutron diffraction data show a qualitative, but not a close quantitative agreement. The discrepancies are attributed to the use of differently extracted test pieces from the original components and to the differences in the measurement geometries that apply to the different methods used.

Subsequent to the presentation of the measurements and their results, an assessment of the experimental methods and the analysis of the results is performed. In

particular attention is given to the method of obtaining the measurement uncertainties. In stress determination by neutron diffraction it is common practice to calculate the uncertainties solely from the fitting uncertainties of the neutron data; a practice that has been applied in this work as well.

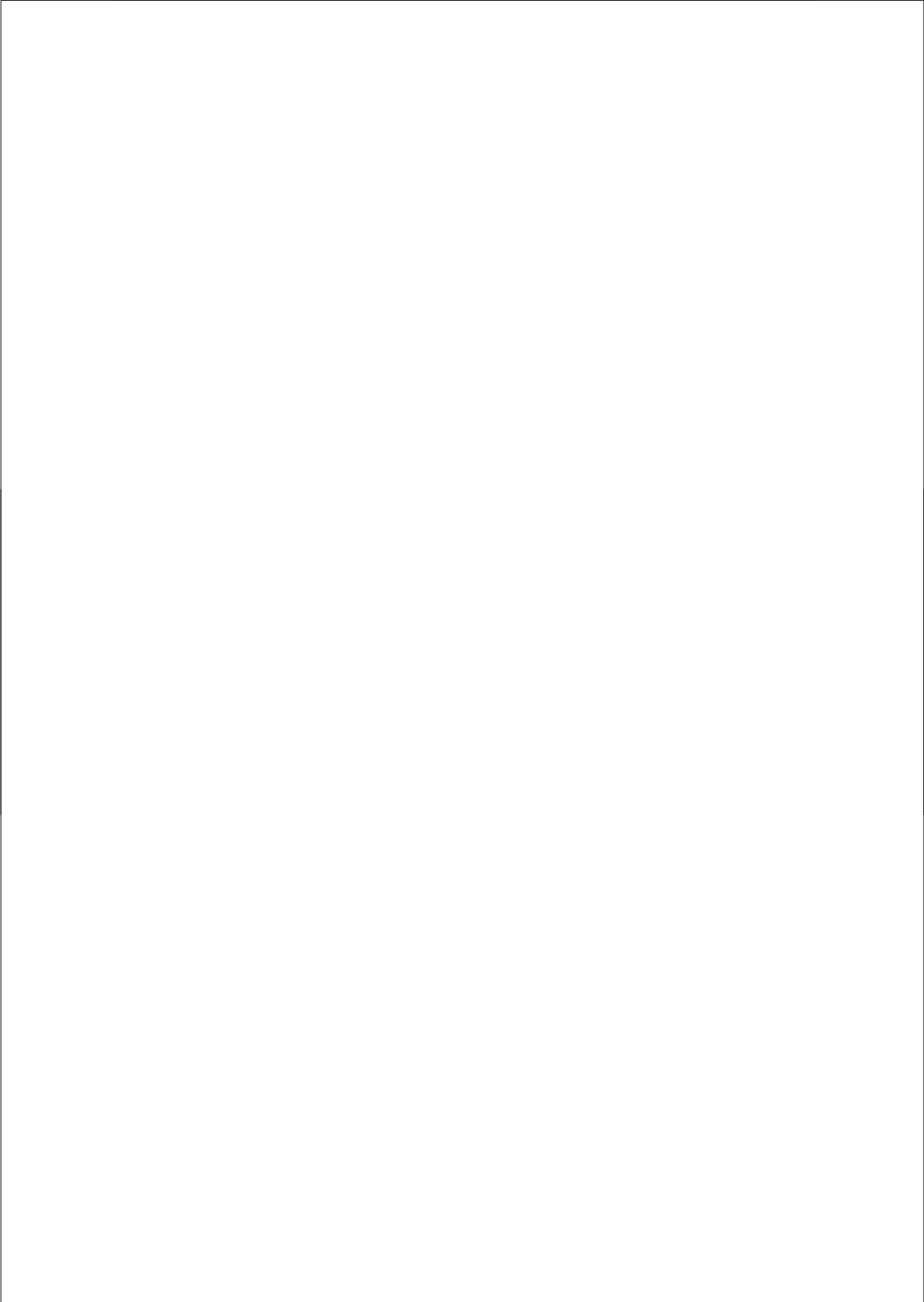
The detailed assessment of the results indicates that this approach can provide appropriate uncertainty values only for materials that are sufficiently homogenous. This is the case, for example, for the ferritic steel substrate of the clad layer component. For the less homogeneous regions, like the welds in these components, it is observed that the experimental data exhibit larger scatter than one would expect on the basis of the counting statistics. The analysis of the effect suggested that the uncertainty is underestimated by a factor of up to 10 in the worst case presented. The second uncertainty contributor analysed in more detail is the uncertainty in the detector position. The analysis shows that, for the highest strains measured, an uncertainty in detector position as small as 1° or 2° results in an additional strain uncertainty comparable to that stemming from the fitting uncertainties. Other sources of uncertainty, such as possible errors in specimen positioning or variations of the specimen temperature, are also briefly analysed. It is found that these do not produce significant additional uncertainty contributions in these investigations.

Based on the observations and subsequent analyses of the findings and comparisons several conclusions are derived. The most significant conclusions can be summarized as follows:

- The applied cutting schemes for the specimens and the use of the dedicated reference specimens have made the neutron diffraction measurements possible. The necessary alterations to the specimens have an impact on the stresses under investigation. It is demonstrated that the impact should be quantified through experiments or modelling, in order to relate the stresses measured to the original stresses present in the test piece.
- It is shown that for a material like the welds studied in this work, the impact of the material inhomogeneity on the neutron diffraction measurements must be considered in a complete uncertainty analysis. It is found that this uncertainty contribution can be larger than the contribution from the fitting uncertainty of the neutron data.
- The neutron diffraction stress measurements can be used for the validation of numerical stress prediction methods. It is demonstrated that the simplified numerical approaches for these specimens are not sufficient.

Following from the above, a number of recommendations are formulated for further improvements in the application of neutron diffraction for future residual stress measurements in large welded components. In similar cases it is recommended to apply experimental techniques capable of mitigating the problem of the high scatter in the results obtained for the fusion zones. The time-of-flight technique is presented as

one option, or where possible, rocking of the specimen during measurements could be applied to increase the number of grains sampled during a diffraction measurement. Furthermore, the importance of quantifying the stress relaxation due to modifications of the specimens is pointed out. This quantification could be achieved by numerical simulation, but preferably by measurement, in particular when the recommendations just mentioned are followed.



Samenvatting

Lassen wordt toegepast in veel industriële sectoren om componenten te verbinden, en is een belangrijk proces geworden omdat het toelaat structuren te maken die anders niet gemaakt zouden kunnen worden.

Lasgebieden hebben een inhomogene microstructuur en zijn meer vatbaar voor scheurvorming en -uitbreiding dan het omliggende basismateriaal. Er ontstaan ook restspanningen, die opgeteld worden bij externe belastingen, hetgeen resulteert in een vermindering van de maximale externe belasting waaraan een component kan weerstaan.

In het kader van lifetime management van nucleaire installaties in het bijzonder zorgen de beperkte marge voor falen, en het relatief groot aantal grote lassen, voor de noodzaak om tot betrouwbare inschattingen van de integriteit van componenten te komen. Daarin moeten restspanningen in beschouwing genomen worden omdat ze kunnen bijdragen tot het ontstaan en de groei van defecten. In het algemeen zijn restspanningen moeilijker experimenteel of numeriek te bepalen dan spanningen ten gevolge van externe belastingen. Daardoor is het bepalen van restspanningen in gelaste nucleaire componenten een onderzoeksdomein van cruciaal belang.

Dit proefschrift gaat over de experimentele bepaling van restspanningen door middel van neutronendiffractie toegepast op drie replica's op ware schaal van componenten uit nucleaire installaties. Twee daarvan zijn lassen van verschillende metalen die een pijp uit het drukvat, bestaande uit ferritisch staal, verbindt met een pijp uit de primaire kring, bestaande uit austenitisch staal. De derde is een gelaste bekleding op een deel van de wand van een reactorvat.

In dit werk is neutronendiffractie gebruikt als techniek voor het bepalen van restspanningen. Het principe is gebaseerd op de wet van Bragg en meet veranderingen in roosterafstand, of rek. Restspanningen kunnen in 3 richtingen bepaald worden in de bulk van een component met een ruimtelijke resolutie van 1-5 mm. Een dergelijke resolutie is aanvaardbaar wanneer men de lengteschalen beschouwt waarover restspanningen normaal variëren in metallische lassen.

In dit werk worden enkele uitdagingen in verband met neutronendiffractie bestudeerd. Een ervan is dat dit soort grote componenten bewerkt moeten worden om toegang van de neutronenbundels tot de meetlocaties mogelijk te maken. Een andere is dat neutronendiffractiemetingen gevoelig zijn voor inhomogeniteiten van de microstructuur, en voor schommelingen in chemische samenstelling in en in de buurt van de

las. Daardoor zijn speciale referentiemonsters nodig om de rekmetingen te kalibreren.

Alvorens het experimentele werk toe te lichten wordt achtergrondinformatie over de belangrijke aspecten van het werk besproken. Begrippen als restspanning en rek en hun belangrijkste karakteristieken worden uitgelegd in hoofdstuk 2. Een kort overzicht van de belangrijkste technieken voor het bepalen van deze spanningen en rekken wordt gegeven in hoofdstuk 3. Deze technieken zijn op te splitsen in 2 categorieën: de relaxatietechnieken waar de relaxatie van rekken ten gevolge van het verwijderen van materiaal wordt gemeten, en de diffractietechnieken, waar roostervervormingen ten gevolge van spanningen worden gemeten door middel van Braggreflecties. Een gedetailleerd overzicht van spanningsmetingen door middel van neutronendiffractie wordt gevolgd door een beschrijving van de meetapparatuur van het JRC, die gebruikt is voor dit onderzoek. Een overzicht van de relevante industriële lastechnieken wordt gegeven in hoofdstuk 4, waar bijkomende informatie wordt gegeven over de booglasmethodes die gebruikt zijn in de bestudeerde componenten. Het mechanisme verantwoordelijk voor het ontstaan van restspanningen in lassen, namelijk de inhomogene plastische vervormingen door de grote temperatuursgradinten, en de dendritische microstructuur van lassen van roestvrij staal, wordt besproken aan de hand van enkele voorbeelden.

Het experimentele werk en de verkregen resultaten worden besproken in hoofdstukken 5, 6, en 7 met een apart hoofdstuk toegewijd aan elke component. De eerste component is een bimetallische gelaste pijp met een dunne wand (wanddikte van 25 mm). De tweede is een blok uit ferritisch staal met gelaste bekleding van 10 mm dikte uit austenitisch staal op een van zijn oppervlaktes. Deze component stelt een stuk van de wand van een reactorvat van 146 mm dikte voor. De derde component is een bimetallische gelaste pijp met een dikke wand (wanddikte 51 mm). De bimetallische pijpen met dikke en dunne wand stellen verbindingen voor tussen een ferritische pijp uit het reactorvat en een austenitische pijp uit de primaire koelkring.

Voor elke component worden details gegeven over de technieken die gebruikt zijn bij het fabriceren, zoals het lasproces, de warmtebehandelingen, en het verspanen. Opdat de neutronenbundel toegang zou hebben voor alle 3 meetrichtingen, werden vensters gesneden uit elk van de bimetallische pijpen. Het specimen met de bekledingslas werd rondom de meetlocatie gefreesd van 146 mm tot 25 mm dikte. Deze significante reductie was noodzakelijk om een hoge ruimtelijke resolutie in de metingen te bereiken. De gemaakte aanpassingen leiden tot een spanningsrelaxatie en een spanningsherverdeling in alle componenten. Voor de dikke bimetallische pijp werd de relaxatie van rekken opgevolgd door middel van rekstroken, en er werd aangetoond dat de impact op de aanwezige spanningen op de plaats waar gemeten werd via neutronendiffractie verwaarloosbaar was. Alle modificaties aan de componenten, samen met het maken van de referentiemonsters, worden in detail beschreven. De procedures voor het meten en het verwerken van data worden beschreven, en voor elk monster worden de resultaten van de neutronendiffractiemetingen gepresenteerd in de vorm van restrekken, en de daaruit afgeleide restspanningen.

In de dunne bimetallische pijp werden binnen de las restspanningen onder trek waargenomen in de lasrichting. Deze trekspanningen bereiken dicht bij het buitenste

oppervlak waarden niet ver onder de vloeigrens, en ze dalen tot ongeveer 0 MPa aan het binnenste oppervlak. In het ferritisch deel van de pijp werden drukspanningen waargenomen in de buurt van de ferritisch-austenitische interface. Hier wordt de grootste drukspanning waargenomen dichtst bij het binnenste oppervlak, en daalt de drukspanning in de richting van het buitenste oppervlak. In de transversale richting ten opzichte van de las worden trekspanningen waargenomen in de buurt van het buitenste oppervlak die geleidelijk overgaan naar drukspanningen in de buurt van het binnenste oppervlak. De hoogste trek- en drukspanningen zijn een beetje lager dan in de lasrichting. De radiale richting vertoont in het algemeen de laagste spanningsniveaus, gaande van +100 MPa tot -100 MPa.

De lasbekleding uit austeniet vertoont een hoge trekspanning zowel in de longitudinale als in de transversale richting ten opzichte van de las. De spanning varieert tussen 250 en 500 MPa met een aanzienlijke spreiding van de data. Het substraat uit ferritisch staal bleek in druk belast te zijn in beide richtingen met de laagste spanningsniveaus tussen -150 en -200 MPa in de buurt van de interface. De spanningen in de richting loodrecht op het interface schommelden rond het niveau van 0 MPa.

Binnen de las van de bimetallische pijp met dikke wand waren de restspanningen positief (trek) in de lasrichting. In het ferritische gedeelte waren de restspanningen in die richting negatief (druk) in de buurt van de austenitisch-ferritische interface. Dit werd ook waargenomen in de pijp met dunne wand. De maximale spanningen waren hoger dan in de dunne pijp. De trekspanningen in de fusiezone bereiken het niveau van de vloeispanning. Er is geen duidelijk trend waar te nemen voor de longitudinale spanningen tussen het binnenste en het buitenste oppervlak. Voor de andere twee meetrichtingen is de spreiding van de data zo hoog dat de spanningen niet kunnen bepaald worden met de nodige accuraatheid.

Voor alle drie de componenten vertoont de data uit het lasgebied een hogere spreiding dan de data uit het basismateriaal.

De resultaten van de neutronendiffractie werden vergeleken met externe numerieke voorspellingen en metingen door middel van relaxatietechnieken. De numerieke berekeningen werden uitgevoerd met behulp van de eindige elementen methode. Het model werd zowel vereenvoudigd als gedetailleerd berekend. In de vereenvoudigde benaderingen werd het lasproces zelf genegeerd. De gedetailleerde modellen vertonen in alle gevallen een betere overeenkomst met de neutronendiffractiemetingen. In het bijzonder worden de spanningen in de lasgebieden onderschat door de vereenvoudigde aanpak.

De extern uitgevoerde relaxatie technieken waren de ring core methode, en de deep hole drilling (DHD) methode voor de bekledingslas, en de surface hole drilling methode en de crack compliance methode voor de dikke pijp. In het algemeen is er een kwalitatieve, maar geen excellente kwantitatieve overeenkomst met de resultaten van de neutronendiffractie. De verschillen zijn vermoedelijk te wijten aan de verschillen in meetmonsters die gemaakt werden uit de originele componenten, en aan het verschil in meetgeometrie gebruikt bij de verschillende meettechnieken.

Volgend op het voorstellen van de metingen en de resultaten, komt een beoordeling en een bespreking van de resultaten. Er wordt bijzondere aandacht gegeven aan het

omgaan met meetonzekerheden. In restspanningsbepalingen door neutronendiffractie worden onzekerheden meestal berekend alleen op basis van de onzekerheden van de fit van de data. Zo is het ook toegepast in dit werk.

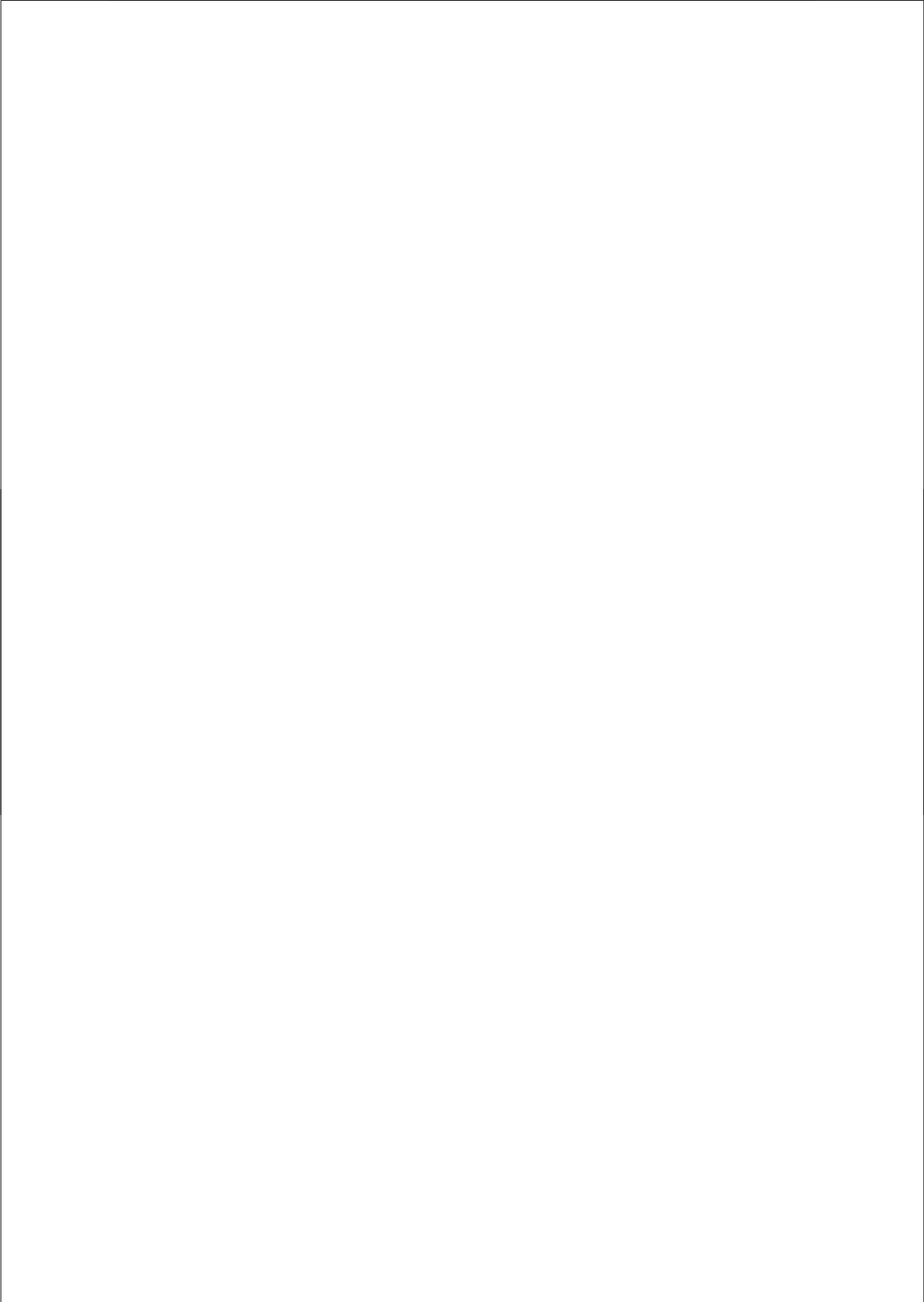
Een gedetailleerde analyse van de resultaten leert echter dat deze aanpak enkel een accurate onzekerheidsbepaling toelaat wanneer het materiaal voldoende homogeen is. Dit is bijvoorbeeld het geval voor het ferritisch substraat in de component met een bekledingslas. Voor de minder homogene materialen, zoals bijvoorbeeld de lassen, vertoonden de meetresultaten een grotere spreiding dan verwacht enkel op basis van de telstatistieken. Analyse daarvan leert dat de onzekerheid onderschat wordt met een factor 10 in het slechtste besproken geval. De tweede bijdrage tot onzekerheid, die in detail wordt besproken, is de onzekerheid van de positie van de detector. Deze analyse leert dat voor de hoogste rekken een onzekerheid in positie van de detector van slechts 1° of 2° aanleiding geeft tot een additionele onzekerheid in rek vergelijkbaar met diegene die komt uit de fitonzekerheid. Andere oorzaken van onzekerheid, zoals bijvoorbeeld fouten ten gevolge van het positioneren van het specimen of variaties in temperatuur van het specimen worden ook kort besproken. Er kon geconcludeerd worden dat deze geen significante extra onzekerheid veroorzaakten.

Gebaseerd op de waarnemingen, analyses, en vergelijkende studies konden verschillende conclusies getrokken worden uit dit werk. De belangrijkste worden als volgt samengevat:

- De toegepaste modificaties aan de monsters en het gebruik van goedgekozen referentiemonsters maakten deze diffractiemetingen met neutronen mogelijk. De noodzakelijke aanpassingen aan de monsters hebben een impact op de restspanningsvelden. Er werd aangetoond dat die impact zou moeten gekwantificeerd worden door experimenten of modelleren om de gemeten spanningen te relateren aan de originele spanningen in het monster.
- Er werd aangetoond dat voor materialen als gebruikt in de bestudeerde lassen de onzekerheid van de neutronendiffractiemetingen tengevolge van inhomogeniteit in het materiaal in beschouwing moet genomen worden in een onzekerheidsanalyse. Er werd aangetoond dat deze bijdrage aan de onzekerheid groter kan zijn dan die van de statistische onzekerheid van de neutronendata.
- De spanningsmetingen met neutronendiffractie kunnen gebruikt worden ter validatie van de numerieke methodes. Er is aangetoond dat vereenvoudigde modellen niet voldoen voor de bestudeerde monsters.

Uit dit alles kan een aantal aanbevelingen geformuleerd worden voor verdere verbeteringen in het toepassingsveld van spanningsmetingen door middel van neutronendiffractie in grote gelaste componenten. In gelijkaardige gevallen wordt aanbevolen om experimentele technieken toe te passen om het probleem van de hoge spreiding in meetdata komende uit de fusiezone van de las aan te pakken. De time-of-flight techniek wordt genoemd als een mogelijke oplossing. Indien mogelijk zou het monster

ook heen en weer geroteerd kunnen worden tijdens de meting om het aantal korrels dat deelneemt aan de diffractie van de inkomende bundel te doen toenemen. Daarenboven wordt het belang van het kwantificeren van de spanningsrelaxatie ten gevolge van aanpassingen aan het specimen benadrukt. Dit zou kunnen gebeuren door numerieke simulatie, maar bij voorkeur door een meting, in het bijzonder wanneer de net vermelde aanbevelingen gevolgd zijn.



Acknowledgements

The development of this thesis has been an exceptionally long process from my first arrival at the JRC in Petten in 1995 until today, a bit more than 18 years later. These have been challenging, but mostly also very enjoyable years. I have been and I still am privileged to pursue fascinating research activities in collaboration with colleagues and friends from all over the world.

It is my wish to express my sincere gratitude to all those who have directly or indirectly contributed to the conception of this thesis.

I would like to start with expressing my gratitude to my parents. Of course, I have to thank them for so many things, but in this context it must be stated that without their support it would not even have been possible for me to come to the JRC in the first place. Unfortunately my mother is not with us anymore, but I hope to be enjoying a moment of celebration with my father and the rest of my family on this occasion soon.

My supervisors at the TU Delft, Prof. Ian Richardson, Dr. Henk Schut and Dr. Rob Delhez have made contributions to this work beyond measure. I admit that I have tested their patience over the last years a lot, but they have always been ready to provide excellent advice both on the conception of the thesis and the way I presented my ideas. I think that I have learned a lot from them; and I certainly enjoyed our numerous discussions and exchanges of views.

Tassos Youtsos, my supervisor at the JRC for more than 10 years, really stands at the very basis of this work. He has invited me to come to Petten for this research, and he has never allowed me to give up on drafting my thesis. He has presented me with many technical, scientific challenges that by myself I would not even have considered tackling. The thick bi-metallic weld in this thesis is one of these. Without him, this thesis would certainly still be waiting to be written.

During the first 6 years at the JRC, I had the pleasure to work on the diffractometers with my colleagues Theo Timke and Paul van den Idsert. They have been directly involved in the execution of most of the measurements presented here, but also in their conception and in the development of this indispensable instrument that allowed us to do all of these measurements on these large components.

I am very grateful to Dr. Muru Amirthalingam from the TU Delft who has helped me with the set-up of this thesis using \LaTeX on so many occasions. He has always been ready to help when I asked him. Without his advice, often also on scientific questions,

it would have been significantly more difficult for me to complete this work.

I have been collaborator and friend with Dr. Robert Wimpory for many years. During his time at the JRC he contributed a lot to the measurements in the thick piping component; and he identified several flaws in the way we used to analyse our data that without him would probably not have been eliminated from this work.

Koen Decroos has been the first and so far the only PhD student whom I had the pleasure to supervise at the JRC. I think one can say that it has been a motivating "competition"; and I have certainly also benefited from his research for my work. I am particularly grateful that Koen has allowed me to be a member of his promotion committee in 2011.

I would also like to thank my other collaborators at the JRC over the past years, namely, Dr. René Martins, Dr. Dimitris Katsareas, Dr. Dimitar Neov, Dr. Oktay Uca, and Dr. Peter Horňák. They may have more indirectly contributed to this work, but I have always appreciated our stimulating discussions and I think I have learned a lot from all of them.

Prof. Don Kearley was the first to accept the supervisor role for me at TU Delft. Therefore without him this would also not have been possible. He has moved to Australia though when I was still in the early stages of the write-up.

Prof. H.-G. Priesmeyer has been my supervisor for my Diploma-Thesis when I graduated from University. He has introduced me to residual stress measurements by neutron diffraction, but he has also allowed me at this early point in my career to participate in an international project collaboration, which until today I continue to appreciate very much. After I had graduated it was thanks to Prof. Priesmeyer's contact with Dr. Tassos Youtsos that I found the assignment at the JRC.

I am grateful to all the other colleagues and friends at the JRC who kept pushing me - and teasing me - in order to motivate me to finish my thesis one day. I would of course also be grateful if the teasing could become less in the future, but I fear that the "record time" in which I completed my thesis will continue to be remembered.

During the time that I have been drafting my thesis under TU Delft supervision I have been in contact with a number of colleagues at JMB and at 3mE. I have been allowed to give several presentations and I would like to thank the colleagues for all the advice and support they have given to me.

I would also like to express my gratitude also to my employer, the Joint Research Centre. The JRC has continuously been supporting these nuclear safety related activities; and my supervisors over the years have allowed for the continuation of my PhD work using a small portion of my time, and they kept stimulating me to complete it.

Finally, I would like to thank all the partners and the collaborators in the projects that my specimens belonged to. Many of these colleagues I actually do not even know, but also without their contributions this work would not exist.

List of publications

Journal Publications

1. A.G. Youtsos, C. Ohms, T. Timke, *Residual stress investigations by neutron diffraction at the JRC-Petten*, PHYSICA B: Physics of Condensed Matter, Vol. 234-236 (E), 1997, pp. 959-961.
2. C. Ohms and A.G. Youtsos, *Residual stress measurements in structural components by neutron diffraction*, Journal of Textures and Microstructures, Vol. 33, 1999, pp. 243-262.
3. A.G. Youtsos, C. Ohms, C. Hubbard, *VAMAS TWA 20 Workshops held at ORNL and JRC-Petten*, Neutron News, No. 2, Vol. 11, 2000, pp. 2-4.
4. C. Ohms, A.G. Youtsos, A. Bontenbal, F.M. Mulder, *Neutron Diffraction Facilities at the High Flux Reactor, Petten*, PHYSICA B: Physics of Condensed Matter, Vol. 276-278, 2000, pp. 160-161.
5. C. Ohms, A.G. Youtsos, P. v.d. Idsert, Th. Timke, *Residual Stress Measurements in Thick Structural Weldments by Means of Neutron Diffraction*, Materials Science Forum, Vol. 347-349, 2000, pp. 658-663.
6. A.G. Youtsos, C. Ohms, *Residual Stresses in Interface Controlled Materials by Neutron Diffraction*, Materials Science Forum, Vol. 347-349, 2000, pp. 524-529.
7. D. Gigout, A. Baczmanski, C. Ohms, A.G. Youtsos, A. Lodini, *Residual Stresses in Austeno-Ferritic Steel - Neutron Diffraction and Modelling*, Journal of Neutron Research, Vol. 9, 2001, pp. 65-70.
8. A.G. Youtsos, C. Ohms, *European Standardization Activities on Residual Stress Analysis by Neutron Diffraction*, Applied Physics A, Vol. 74, Supplement 1, 2002, pp. 1716-1718.
9. C. Ohms, A.G. Youtsos, P. v.d. Idsert, *Structural Integrity Assessment based on the HFR Petten Neutron Beam Facilities*, Applied Physics A, Vol. 74, Supplement 1, 2002, pp. 1443-1445.

10. H. Gripenberg, H. Keinänen, C. Ohms, H. Hänninen, D. Stefanescu and D. Smith, *Prediction and Measurement of Residual Stresses in Cladded Steel*, Materials Science Forum, Vol. 404-407, 2002, pp. 861-866.
11. C. Ohms, P. Horňák, R. Wimpory, A.G. Youtsos, *Residual stress analyses based on neutron diffraction in double-V butt welded steel plates*, Journal of Neutron Research, Vol. 11, No. 4, Dec 2003, pp. 273-276.
12. O. Uca, C. Ohms, A.G. Youtsos, *Flux calculations for the upgrade of the SANS facility at the Petten-reactor*, Nuclear Instruments and Methods in Physics Research Section A: Accelerators, Spectrometers, Detectors and Associated Equipment, Vol. 558, 2006, pp.367-372.
13. R.C. Wimpory, C. Ohms, P. Horňák, D. Neov, A.G. Youtsos, *Residual Strain measurement of C/C-SiC tubes at high temperature*, Materials Science Forum, Vol. 524-525, 2006, pp. 665-670.
14. C. Ohms, D. Neov, *Residual Stress Analysis by Neutron Diffraction: Current Possibilities and Outlook to the Future - Involvement of JRC-IE in the Context of the ERA*, in: "Selected Topics on Nuclear Methods for Non-Nuclear Applications", Ch. Stoyanov (ed.), supplement to Bulgarian Journal of Physics, vol. 34 (s1), Heron Press Ltd., Sofia, 2007, ISBN: 978-954-580-209-6, pp. 226-240.
15. R.C. Wimpory, C. Ohms, M. Hofmann, R. Schneider, A.G. Youtsos, *Problems in the averaging of neutron diffraction stress data from round-robin campaigns*, Materials Science Forum, Vol. 571-572, 2008, pp. 283-288.
16. D. Neov, C. Ohms, R.C. Wimpory, A.G. Youtsos, *Residual stress analyses by neutron diffraction in irradiated double-V butt welded steel plates*, Materials Science Forum, Vol. 571-572, 2008, pp. 381-386.
17. O. Uca, C. Ohms, *Monte Carlo Simulations of the SANS Instrument in Petten*, Physica B - Condensed Matter, Vol. 403, 2008, pp. 3892-3895.
18. C. Ohms, R.C. Wimpory, D.E. Katsareas, A.G. Youtsos, *NET TG1: Residual Stress Assessment by Neutron Diffraction and Finite Element Modeling on a Single Bead Weld on a Steel Plate*, International Journal of Pressure Vessels and Piping, Vol. 86, No. 1, 2009, pp. 63-72.
19. R.C. Wimpory, C. Ohms, M. Hofmann, R. Schneider, A. G. Youtsos, *Statistical Analysis of Residual Stress Determinations using Neutron Diffraction*, International Journal of Pressure Vessels and Piping, Vol. 86, No. 1, 2009, pp. 48-62.
20. C. Ohms, R.C. Wimpory, D. Neov, *Residual Stress Measurement by Neutron Diffraction in a Single Bead on Plate Weld - Influence of Instrument and Measurement Settings on the Scatter of the Results*, Materials Science Forum, Vol. 638-642, 2010, pp. 2452-2457.

21. R.C. Wimpory, C. Ohms, *A Step Towards a Complete Uncertainty Analysis of Residual Stress Determination using Neutron Diffraction*, Materials Science Forum, Vol. 638-642, 2010, pp. 2487-2492.
22. R.V. Martins, C. Ohms, K. Decroos, *Full Depth-Resolved Strain Mapping of a Three-Pass Slot Weld Specimen in Austenitic Stainless Steel Using the Spiral Slit Technique*, Materials Science Forum, Vol. 652, 2010, pp. 74-79.
23. R.V. Martins, C. Ohms, K. Decroos, *Full 3D Spatially Resolved Mapping of Residual Strain in a 316L Austenitic Stainless Steel Weld Specimen*, Materials Science and Engineering A, Vol. 527, 2010, pp. 4779-4787.
24. L.K. Keppas, R.C. Wimpory, D.E. Katsareas, C. Ohms, *Combination of Simulation and Experiment in Designing Repair Weld Strategies: a Feasibility Study*, Nuclear Engineering & Design, Vol. 240, 2010, pp. 2897-2906.
25. K. Decroos, M. Seefeldt, C. Ohms, R. Petrov, F. Verhaeghe, L. Kestens, *Modelling and Characterisation of the Texture Development in the Fusion Zone of an Austenitic Weld*, Steel Research International, Vol. 82, Issue 8, 2011, pp. 911-917.
26. K. Decroos, M. Seefeldt, C. Ohms, R. Petrov, F. Verhaeghe, L. Kestens, *Calculation of macroscopic elasto-plastic anisotropy based on an analytical expression of the Orientation Distribution Function in the case of fibre textures*, Computational Materials Science, Vol. 68, 2013, pp. 263-270.
27. K. Decroos, C. Ohms, R. Petrov, M. Seefeldt, F. Verhaeghe, L. Kestens, *Automatic meshing method for optimization of the fusion zone dimensions in Finite Element models of welds*, Materials Science Forum, Vol. 768-769, 2014, pp. 597-604.

Conference Publications

1. C. Ohms, A.G. Youtsos, *Advances in Residual Stress Measurements at JRC-Petten*, Proceedings of ICRS-5 5th International Conference on Residual Stresses, T. Ericsson *et al.* (eds.), Vol. 2, Linköping, Sweden, 16-18 June 1997, pp. 738-743.
2. A.G. Youtsos, C. Ohms, *Residual Stress Measurements by Neutron Diffraction at JRC*, Proceedings of First Hellenic Conference on Composite Materials and Structures, S.A. Paipetis and E.E. Gdoutos (eds.), Xanthi, Greece, July 2-5 1997.
3. A.G. Youtsos and C. Ohms, *Residual stress in Joints by Neutron Diffraction at JRC*, Proceedings of ECCM-8 European Conference on Composite Materials, I. Crivelli Visconti (ed.), Vol. 3, Napoli, 1998, pp. 309-316.

4. C. Ohms and A.G. Youtsos, *Monitoring of Ageing Effects in Structural Components based on Neutron Diffraction*, Proceedings of the Joint EC-IAEA Specialists Meeting on NDT Methods for Monitoring Degradation, IAM-JRC, Petten, March 10, 1999.
5. C. Ohms, A.G. Youtsos, *Residual Stress Measurements in Steel Alloy Fusion Welds and Aluminum Alloy Friction Welds based on Neutron Diffraction*, Proceedings of THERMEC'2000 - International Conference on Processing and Manufacturing of Advanced Materials, Las Vegas, USA, Dec 4-8, 2000, Vol. D, T. Chandra (ed.), Elsevier Science Ltd., 2001, pp. 142-147.
6. C. Ohms, A.G. Youtsos, P. van den Idsert, *Non-destructive Measurement of Residual Stresses in Nuclear Welds by Means of Neutron Diffraction*, Proceedings of Baltica V - International Symposium on Condition and Life Management for Power Plants, S. Hietanen and P. Auerkari (eds.), VTT Technical Research Centre, Espoo, Finland, June 2001, Vol. 2, pp. 487-497.
7. K. van Thoor, A.G. Youtsos, C. Ohms, M.L. Castaño, A. Roth, D. Gavillet, S. van Dyck, *Irradiation effects on the evolution of the microstructure, properties and residual stresses in the heat affected zone of stainless steel welds (INTERWELD)*, Proceedings of FISA 2001 - EU Research in Reactor Safety, Luxembourg Nov 12-14, 2001, pp. 95-108.
8. J. Guidez, A.G. Youtsos, C. Ohms, *Role of Thermal and Sub-Thermal Neutrons in NDE Activities*, Proceedings of 3rd International Conference on NDE in Relation to Structural Integrity for Nuclear and Pressurised Components, Seville Nov 14-16, 2001, European Commission, Joint Research Centre, Report EUR 20671 EN, 2003.
9. A.G. Youtsos, C. Ohms, *NDE based on neutron techniques in support of structural integrity assessment*, Proceedings of 3rd International Conference on NDE in Relation to Structural Integrity for Nuclear and Pressurised Components, Seville Nov 14-16, 2001, European Commission, Joint Research Centre, Report EUR 20671 EN, 2003.
10. C. Ohms, A.G. Youtsos, *Neutron Diffraction assisted Residual Stress Analysis in Welded Structures*, in: "Recent Advances in Experimental Mechanics - in Honor of Prof. Isaac M. Daniel", E.E. Gdoutos (ed.), Kluwer Academic Publishers, Dordrecht, Netherlands, 2002, ISBN 1-4020-0683-7, pp. 515-526.
11. G.A. Webster, A.G. Youtsos, C. Ohms, R.C. Wimpory, *Draft Standard for the Measurement of Residual Stresses by Neutron Diffraction*, in: "Recent Advances in Experimental Mechanics - in Honor of Prof. Isaac M. Daniel", E.E. Gdoutos (ed.), Kluwer Academic Publishers, Dordrecht, Netherlands, 2002, ISBN 1-4020-0683-7, pp. 467-476.

12. D.E. Katsareas, C. Ohms, A.G. Youtsos, *Neutron Diffraction Techniques for Measuring Residual Stresses in Large Industrial Components*, Proceedings of International Symposium of Multiscale Mechanics, G.C. Sih and C.P. Spyropoulos (eds.), NTUA, Athens, Greece, Sep 2-6, 2002.
13. M.L. Castaño, K. van Thoor, A. Roth, D. Gavillet, S. van Dyck, C. Ohms, *Irradiation effect on the evolution of heat affected zone characteristics of austenitic stainless steels - the INTERWELD Project*, Proceedings of the XXIX Annual Meeting of the Spanish Nuclear Society, Paper 0207. Zaragoza, 1-3 October 2003.
14. R.C. Wimpory, P. Horňák, C. Ohms, D. Katsareas and A.G. Youtsos, *Neutron Methods for Structural Integrity Assessment*, 16th Workshop of Marie Curie Fellows: Research Training in Progress Held at the Institute for Energy, Joint Research Centre of the European Commission Petten (Netherlands), 21-22 October, 2003, EU publications, ISBN 92-894-8198-6, pp. 28-31.
15. C. Ohms, D. Katsareas, P. Horňák, R.C. Wimpory and A.G. Youtsos, *Welding Residual Stress Analysis based on Neutron Diffraction and Numerical Modelling*, Proceedings of 2nd International Conference on Integrity of High Temperature Welds, IOM Communications Ltd., London, UK, Nov, 2003, ISBN 1-86125-160-2, pp. 197-206.
16. A. Roth, B. van der Schaaf, M.L. Castaño, C. Ohms, A.G. Youtsos, D. Gavillet, S. van Dyck, *INTERWELD - European Project to Determine Irradiation Induced Material Changes in the Heat Affected Zones of Austenitic Stainless Steel Welds that Influence the Stress Corrosion Behaviour in High-temperature Water*, Amendment to Proceedings of 29th MPA Seminar, Vol. 1, Stuttgart, Oct 9-10, 2003, ISSN 0722-401X, pp. 53.1-53.28.
17. B. van der Schaaf, A. Roth, C. Ohms, D. Gavillet, S. van Dyck, M.L. Castaño, *Irradiation Effects on the Evolution of the Microstructure, Properties and Residual Stresses in the Heat Affected Zone of Stainless Steel Welds (INTERWELD)*, Proceedings of FISA 2003 - EU Research in Reactor Safety, Luxembourg Nov, 2003.
18. C. Boucher, J. Bourchard, B. Brown, D. Cardamone, D. Colchen, H. Hein, C. Ohms, M. Smith, D. Smith and A.G. Youtsos, *Management of Nuclear Plant Operation by Optimising Weld Repairs (ENPOWER)*, Proceedings of FISA 2003 - EU Research in Reactor Safety, Luxembourg Nov, 2003.
19. D.E. Katsareas, C. Ohms and A.G. Youtsos, *Structural Integrity Assessment of Nuclear Safety Related Welded Components*, Proceedings of the International Conference on "Influence of Traditional Mathematics and Mechanics on Modern Science and Technology - Fundamentals and Applications Related to Physics and Engineering Problems, G.C. Sih and C.P. Spyropoulos (eds.), Eptalofos

- S.A., Athens, Greece, ISBN 960-8360-31-5, May 24-28, 2004, pp. 111-123.
20. D.E. Katsareas, C. Ohms and A.G. Youtsos, *On the Performance of a Finite Element Code in Multi-Pass Welding Simulation*, Proceedings of ASME/JSME Pressure Vessels and Piping Conference 2004, PVP-Vol. 477, M.A. Porter and T. Sato (eds.), ASME, New York, ISBN 0-7918-4672-5, July 25-29, 2004, pp. 29-37.
 21. C. Ohms, D.E. Katsareas, R.C. Wimpory, P. Horňák and A.G. Youtsos, *Residual Stress Analysis in Thick Dissimilar Metal Weld based on Neutron Diffraction*, Proceedings of ASME/JSME Pressure Vessels and Piping Conference 2004, PVP-Vol. 479, Y.-Y. Wang (ed.), ASME, New York, ISBN 0-7918-4674-1, July 25-29, 2004, pp. 85-92.
 22. C. Ohms, D.E. Katsareas, R.C. Wimpory, P. Horňák and A.G. Youtsos, *Residual Stress Analysis in RPV & Piping Welded Components based on Neutron Diffraction*, Proceedings of 12th International Conference on Experimental Mechanics, C. Pappalettere (ed.), 29 Aug - 2 Sep 2004, Bari, Italy, ISBN 88 386 6273-8.
 23. M.L. Castaño, B. van der Schaaf, A. Roth, C. Ohms, D. Gavillet, S. van Dyck, *IASCC Susceptibility under BWR Conditions of Welded 304 and 347 Stainless Steels*, Proceedings of EUROCORR 2004 - Long Term Prediction and Modelling of Corrosion, ISBN 2-9516844-1-X, 12-16 September 2004, Nice, France.
 24. R. Stoenescu, M.L. Castaño, S. van Dyck, A. Roth, B. van der Schaaf, C. Ohms, and D. Gavillet, *Irradiation-assisted stress corrosion cracking of heat-affected zones of austenitic stainless steel welds*, Proceedings of the Twelfth International Conference on Environmental Degradation of Materials in Nuclear Power Systems-Water Reactors, 2005, T.R. Allen, P.J. King, and L. Nelson (eds.), The Minerals, Metals & Materials Society, pp. 267-276.
 25. C. Ohms, R.C. Wimpory, D. Neov, D. Lawrjaniec and A.G. Youtsos, *ENPOWER - Investigations by neutron diffraction and finite element analyses on Residual stress Formation in repair welds applied to ferritic steel plates*, Proceedings of the ASME Pressure Vessels and Piping Conference 2005, Volume 6, Materials and Fabrication, ASME, New York, 2005, ISBN 0-7918-4191-X, pp. 385-393.
 26. H. Hein, B. Brown, D. Lawrjaniec, C. Ohms, R.C. Wimpory and C. Truman, *ENPOWER - Repair Welds and Residual Stresses in Clad Plates*, Proceedings of the ASME Pressure Vessels and Piping Conference 2005, Volume 6, Materials and Fabrication, ASME, New York, 2005, ISBN 0-7918-4191-X, pp. 361-369.
 27. C. Boucher, P.J. Bourchard, B. Brown, D. Smith, D. Lawrjaniec, H. Hein, C. Truman, M. Smith, C. Ohms, T.A. Dauda, D. Cardamone and A.G. Youtsos, *Management of Nuclear Plant Operation by Optimising Weld Repairs -*

- Empower Project Overview*, Proceedings of the ASME Pressure Vessels and Piping Conference 2005, Volume 6, Materials and Fabrication, ASME, New York, 2005, ISBN 0-7918-4191-X, pp. 355-360.
28. C. Ohms, R.C. Wimpory, D. Neov, A.G. Youtsos, *Evaluation of Novel Post Weld Heat Treatment in Ferritic Steel Repair Welds based on Neutron Diffraction*, in: "Residual Stress and Its Effects on Fatigue and Fracture", Proceedings of a Special Symposium held within the 16th European Conference of Fracture - ECF16, Alexandroupolis, Greece 3-7 July, 2006, Springer, Dordrecht, 2006, ISBN 978-1-4020-5328-3, pp. 55-66.
 29. D.E. Katsareas, C. Ohms, A.G. Youtsos, *Finite Element Simulation of Welding in Pipes: a Sensitivity Analysis*, in: "Residual Stress and Its Effects on Fatigue and Fracture", Proceedings of a Special Symposium held within the 16th European Conference of Fracture - ECF16, Alexandroupolis, Greece 3-7 July, 2006, Springer, Dordrecht, 2006, ISBN 978-1-4020-5328-3, pp. 15-26.
 30. O. Uca, C. Ohms, D. Neov, A.G. Youtsos, *The Present and the New HFR-Petten SANS Facility*, in: "Residual Stress and Its Effects on Fatigue and Fracture", Proceedings of a Special Symposium held within the 16th European Conference of Fracture - ECF16, Alexandroupolis, Greece 3-7 July, 2006, Springer, Dordrecht, 2006, ISBN 978-1-4020-5328-3, pp. 97-101.
 31. C. Ohms, C.E. Truman, R.C. Wimpory, H. Gripenberg, D. Smith, A.G. Youtsos, *Measurement of Residual Stress in As Received and Repaired Clad Components*, Proceedings of ASME PVP 2006 / ICPVT-11, Vancouver, CAN, July 23-27, 2006, ASME, CD Publication, 2006, ISBN 0-7918-3782-3.
 32. C. Ohms, R.V. Martins, O. Uca, A.G. Youtsos, P.J. Bouchard, M. Smith, M. Keavey, S.K. Bate, P. Gilles, R.C. Wimpory, L. Edwards, *The European Network on Neutron Techniques Standardization for Structural Integrity - NeT*, Proceedings of ASME PVP 2008, Chicago, USA, July 27-31, 2008, ASME, CD Publication, 2008, ISBN 0-7918-3828-5.
 33. K. Decroos, C. Ohms, Y. Houbaert, *Including Elastical Anisotropy due to Texture in a Finite Element Model for the Prediction of Residual Stresses in Welds*, in: "Materials Processing and Texture", Proceedings of the 15th International Conference on the Textures of Materials (ICOTOM 15), Pittsburgh, USA, June 1-6, 2008, A.D. Rollett (ed.), Ceramic Transactions, 200, John Wiley & Sons, Inc, Hoboken, NJ, USA, 2009, ISBN 978-0-470-40834-6, pp. 115-122.
 34. C. Ohms, R.C. Wimpory, D. Neov, M. Hofmann, M. Turski, R. Haigh, M. Fitzpatrick, L. Edwards, *Residual Stress Measurements in a Three-Bead Slot Weld in a 20 mm Carbon Steel Plate*, Proceedings of ASME PVP 2009, Prague, Czech Republic, July 26-30, 2009, ASME, CD Publication, 2009, ISBN 978-0-7918-3854-9.

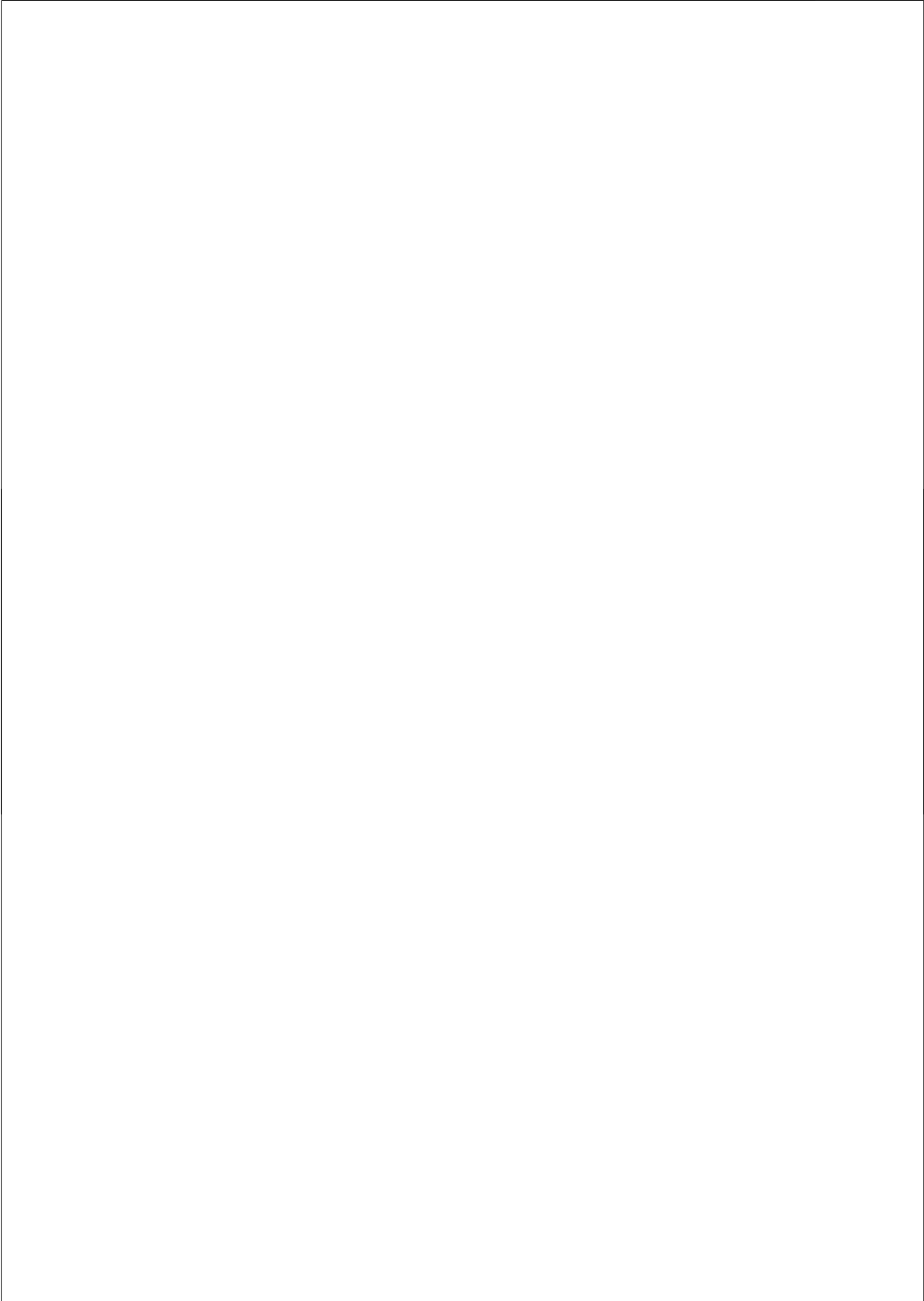
35. M. Smith, A.C. Smith, R.C. Wimpory, C. Ohms, B. Nadri, P.J. Bouchard, *Optimising Residual Stress Measurements and Predictions in a Welded Benchmark Specimen: a Review of Phase Two of the NeT Task Group 1 Single Bead on Plate Round Robin*, Proceedings of ASME PVP 2009, Prague, Czech Republic, July 26-30, 2009, ASME, CD Publication, 2009, ISBN 978-0-7918-3854-9.
36. X. Ficquet, S. Courtin, C. Ohms, D. Neov, P. Gilles, P. Joly, *Residual Stress Measurement and Finite Element Mapping on a Narrow Gap Dissimilar Metal Weld Pipe*, in: 14th International Conference on Environmental Degradation of Materials in Nuclear Power Systems Water Reactors 2009, Proceedings of a meeting held 23-27 August 2009, Virginia Beach, Virginia, USA, Curran Associates Inc. (publ.), Red Hook, NY, USA, ISBN 978-1617388538, pp. 456-469.
37. S. Courtin, Ph. Gilles, P. Joly, C. Ohms and X. Ficquet, *Numerical Welding Simulation on a 14" Narrow Gap Dissimilar Metal Weld*, Proceedings of: 20th International Conference on Structural Mechanics in Reactor Technology (SMiRT 20), CD Publication, VTT, Espoo, Finland, August 9-14, 2009.
38. S. Courtin, V. Robin, Ph. Gilles and C. Ohms, *Residual Stress and Shrinkage Predictions on 14" Narrow Gap Dissimilar Metal Welds*, Proceedings of: 9th International Seminar on Numerical Analysis of Weldability, Seggau 2009, Graz University of Technology, Graz, Austria, Sep 28-30, 2009, Title of Proceedings: "Mathematical Modelling of Weld Phenomena 9", H. Cerjak and N. Enzinger (eds.), Verlag der Technischen Universitt Graz, 2010, ISBN: 978-3-85125-127-2, pp. 651-665.
39. L. Tatár, G. Török, D. Smith, S. Do, C. Ohms, L. Kovács, *Manufacture, residual stress measurement and analysis of a VVER-440 nozzle mockup*, Proceedings of ASME PVP 2013, Paris, France, July 14-18, 2013, ASME, CD Publication, 2013.

Contributions to Monographs

1. C. Ohms, A.G. Youtsos, in "Neutron Diffraction Measurements of Residual Stress in a Shrink-fit Ring and Plug", G.A. Webster (ed.), VAMAS Report No. 38, ISSN 1016-2186, Jan 2000.
2. A.G. Youtsos, C. Ohms, in "ISO - Technology Trends Assessment: Polycrystalline materials - Determination of residual stresses by neutron diffraction", G.A. Webster and R.C. Wimpory (eds.), Reference number ISO/TTA 3 2001(E), ISO, Geneva, 2001.
3. C. Ohms, A.G. Youtsos, *Measurement of residual stresses by neutron diffraction*, in "The Orange Book - Dutch Neutron and Muon Science 2000 - 2003", Netherlands Organisation for Scientific Research (NOW), Dutch Neutron Scattering

Society (NVNV), Interfaculty Reactor Institute, Delft University of Technology (IRI-TUD), 2003, ISBN 90-70608-92-8, pp. 14-15.

4. C. Ohms, R.C. Wimpory, D. Neov, A.G. Youtsos, *Residual stress analysis by means of neutron diffraction at research reactors - facilities and applications at the HFR*, in: IAEA-TECDOC-1545: "Characterization and Testing of Materials for Nuclear Reactors, Proceedings of a technical meeting held in Vienna, May 29-June 2, 2006", International Atomic Energy Agency, Vienna, March 2007, ISBN 92-0-103007-X, ISSN 1011-4289, pp. 69-85.



Curriculum Vitae

Carsten OHMS

born on 5 February 1968 in Kiel, Germany

- | | |
|-------------|--|
| since 2004 | Scientific officer, Official of the European Commission, Joint Research Centre, Petten, The Netherlands |
| 1999 - 2004 | Scientific officer, Temporary Agent at the European Commission, Joint Research Centre, Petten, The Netherlands |
| 1996 - 1999 | Research Fellow at the European Commission's Joint Research Centre, Petten, The Netherlands |
| 1995 - 1996 | Scientific Assistant, Christian-Albrechts-University, Kiel, Germany |
| 1995 | Diploma in Physics |
| 1989 - 1995 | Student of Physics at the Christian-Albrechts-University, Kiel, Germany |
| 1987 - 1989 | Military Service at the Federal German Navy (Bundesmarine) |
| 1987 | Abitur |
| 1978 - 1987 | Secondary School Education, Gymnasium Wellingdorf, Kiel, Germany |

